PHOTOEMISSION SPECTROSCOPY AND FIRST-PRINCIPLES STUDIES OF TWO-DIMENSIONAL DIRAC AND WEYL MATERIALS

by

Qiangsheng (Johnson) Lu

A dissertation submitted in partial fulfillment of the requirements for the degree of

DOCTOR OF PHILOSOPHY

Major: Condensed Matter Physics

Department of Physics and Astronomy

University of Missouri

Columbia, MO 65201 USA

December 2022

The undersigned, appointed by the dean of the Graduate School, have examined the dissertation entitled

Photoemission Spectroscopy and First-Principles Studies of Two-Dimensional Dirac and Weyl Materials

presented by Qiangsheng Lu,

a candidate for the degree of Doctor of Philosophy,

and hereby certify that, in their opinion, it is worthy of acceptance.

Professor [David J. Singh] (Chair)

Professor [Guang Bian] (Director of Research)

Professor [Ping Yu]

Professor [Gavin M. King]

Professor [Jian Lin]

Acknowledgments

With deepest gratitude, I would like to take this opportunity to mention the names of those who helped me in researching, studying as well as everyday life over the past five and half years. It is them who turned my Ph.D. time into one of the most precious periods of my life.

First, I would like to thank my Ph.D. advisor Dr. Guang Bian. Guang is an experimental physicist with the deepest theoretic views of physics I ever know. If you ask him a physics question, he will quickly write down an equation and start deriving the Hamiltonian on a blackboard. In his opinion, only a physics theory with a well-defined equation could be a good theory. This unique characteristic is the most important reason that attracted me and helped me choose him as my advisor. I remember that day I asked my undergraduate advisor, Dr. Chang Liu, about which group I should join as a graduate student. He recommended Guang and said: Guang is the one who really understands the underneath theories of the physics phenomenon. The study process with Guang was not easy. In the beginning, there was a big gap for me to understand the equations he wrote. However, this process did push me further to understand the underneath theory. Moreover, it also helped me gain the ability to describe physical phenomena with beautiful equations. On the other hand, Guang is a good advisor and friend who helped me a lot in everyday life.

I would also like to thank my co-advisor, Dr. David J. Singh. David is a famous and knowledgeable theoretical physicist. To me, he is kind of a reversed version of Guang. He is a theorist who has the best insight into the physics phenomenon. He doesn't do experiments, but

the experiment phenomenon and results are kind of alive in his mind. He has about forty years of research experience in condensed matter physics. If you ask him any physics questions, you will feel that you are actually talking with a living dictionary. He can always give me some physics pictures explaining the tedious equations. For example, he used a picture of many balls with different colors to explain the phases of wave functions in the tight-binding model. More important, those physics pictures he taught me are not only work of understanding the hard theory but also show as toy models that help me to develop my own theory. His guidance, like warm sunlight, enlightened my world when I got stuck in some difficult theory; his way of thinking and the physics pictures gave me faith that I could also touch the very deep of physics and do the top research in the world. Guang taught me the professional methods of physics research, but David taught me the way of thinking and the feelings of physics. It is incredibly lucky for me to have the best Ph.D. advisors I can ever imagine.

My gratitude is also given to my former group mate, friend, and collaborator, Dr. Xiaoqian Zhang. She was a visiting student in Guang's group, and the two years she stayed here were the most colorful time period ever in my life. During the time she was here, I could not only discuss research with her but also share my emotion with her. Her hard-working and the spirit of "never give up" also excited my study passion. Most of the research breakthroughs were made during that time with the passion she gave me.

I also thank my present group mates in Guang's group, Jacob Cook and Clayton Conner. Not only because of their help in research but also because they gave me a sense of life in the U.S.

They helped me to understand American culture and life, and they also gave me a sense of belonging, which is precious for me as an international student.

In addition, I would like to thank all my collaborators. Dr. Peng li, Dr. Rob G. Moore, Dr. Matthew Brahlek, Dr. Tay-Rong Chang, Dr. Alessandro R. Mazza, Dr. Pawel J. Kowalczyk, Dr. Bingchao Qin, Dr. Li-Dong Zhao, Dr. Ching-Kai Chiu, Dr. Giovanni Vignale, Dr. Paul F. Miceli, Dr. Mitchel Vaninger, Dr. Shengyuan A. Yang, Dr. Suchismita Guha, and Chang Liu.

Finally, I would express my special thanks to my parents, Xin Jiang and Minghua Lu, for their unconditional belief, support, and love.

TABLE OF CONTENTS

PHOTOEMISSION SPECTROSCOPY AND FIRST-PRINCIPLES STUDIES OF TWO-DIMENSIONAL DIRAC AND WEYL MATERIALS

Abstract

Two-dimensional (2D) materials have attracted tremendous research interest since the breakthrough of graphene. As the nature of the low dimension, 2D materials are thin, flexible, and easy for fabrication. More interestingly, it emerges a lot of novel and unique properties such as 2D magnetic and 2D superconductivity, which attracts a huge amount of research and opens a door for the next generation of electronics and spintronics. Dirac and Weyl semimetals are topological matter with gapless electronic excitations protected by topology and symmetry. Their nontrivial electron band topology leads to protected surface or edge states and novel responses to applied electric and magnetic fields. Those states are described by the models of relativistic chiral fermions as quasi-particles, which raise a platform to study particle physics in condensed matter physics and lead to more possibilities for spintronics and quantum calculation. The combination of low-dimension and novel band topology would emerge a lot of novel physics properties and applications, but due to the lack of a dimensional constraint, 2D Dirac and Weyl systems are rare. In this research, we use the symmetry analysis to find the possible candidate of 2D Dirac and Weyl materials, the molecular beam epitaxy (MBE), and the in-situ scanning tunning microscopy (STM) are used to experimentally synthesize and adjust the 2D thin films, the combination of angle-resolved photoemission spectroscopy (ARPES) and first-principles calculation is used to examine the electronic properties of 2D

Dirac and Weyl matter. Specifically, there are three different 2D Dirac or Weyl systems discussed in this thesis. The first one focuses on black phosphorous structures, and symmetry-enforced Dirac states, unpinned 2D Dirac states, and 2D Weyl fermions are discussed in this system. The second one studies the interaction between Dirac states based on the Moiré lattice. The third one is mainly about the 2D magnetic material and its heterostructures which are the candidates of the 2D magnetic Weyl matters.

1. INTRODUCTION

1.1. Two-Dimensional materials

Two-dimensional (2D) materials have attracted tremendous research interest since the breakthrough of graphene. Recent research around 2D magnetic and 2D superconducting matter exhibits the novel properties of 2D material and opens a new gate to understanding the fundamental physics of magnetism and superconductivity. On the other hand, their unique electronic, optical, magnetic, and mechanical properties hold great potential for harnessing them as key components in novel applications for electronics, optoelectronics, and spintronics. In addition, the coupling between the layers in 2D materials usually is the Van der Waals force, which is easy for exfoliation and fabrication. Their atomic thickness and huge exposed surface even make them highly designable and manipulable, leading to extensive application potential.

2D superconductors: Due to the poor quality and extreme sensitivity of the samples, early research of high-Tc superconductors reported that superconductivity degradation occurs in the 2D limit [1, 2], but in recent years, the exfoliated Cu-based superconductors (Bi-2212) [3], the monolayer FeSe/$SrTiO_3$ system, [4,5] the ultrathin transition metal dichalcogenide(TMD) samples (NbSe2, TaS2, WTe2, etc.), [6-11], and the twisted bilayer graphene (TBG) systems raise different kinds of superconductors and have been experimentally achieved. As the mechanism and the physical properties of the 2D

superconducting are different from the 3D cases, the 2D superconductor attracted much attention in recent years.

2D magnetism: Ferromagnetism had long been believed to hardly survive in two-dimensional (2D) systems because of the enhanced thermal fluctuations revealed by the Mermin-Wagner theorem. The recent discovery of 2D magnetic crystals on Cr2Ge2Te6, CrI3, and Fe3GeTe2 [13-19] showed that magnetic anisotropy could stabilize the long-range magnetic order opening up an excitation gap to resist thermal agitation. Two-dimensional magnetic crystals constitute ideal platforms to experimentally access the fundamental physics of magnetism in reduced dimensions. In contrast to the traditional magnetic thin films, 2D materials largely decouple from the substrates, allow electrical control, and are mechanically flexible. [20]

1.2. Topological materials

A decade has passed since the first experimental observation of topological materials that do not require stringent experimental conditions to realize a topological state1. Topological materials are characterized by an electronic band structure that exhibits a special band topology [21-23], which is now essential to understand the physical properties of many materials. These materials possess topologically protected surface states with unique electronic properties; in topological insulators (TIs) [26-29], the surface states arise from the inversion of the bulk bandgap, which is induced by the large spin-orbit coupling of the heavy atoms in the material and is protected by time-reversal symmetry. In topological crystalline insulators (TCIs) [30,31], the surface states are protected by crystal symmetry instead. In

recent years, topological materials have expanded to include topological semimetals: Weyl and Dirac semimetals [24, 32-35] are 3D systems that possess gapless bulk states in the form of relativistic chiral fermions near nodal points and Fermi arc surface states and are described by the 3D Weyl and Dirac [25] equations, respectively. With the breaking of symmetry, either inversion symmetry or time-reversal symmetry, a Dirac semimetal can become a Weyl semi- metal, as each Dirac point splits into a pair of Weyl points. Detail discussions of topological order and topological semi-metal are in sections 2.4 and 2.5.

1.3. Structures and overview of this thesis

This thesis is organized as follows: Chapter **2** provides some background knowledge and some fundamental understanding of this thesis, and chapter **3** introduces the experimental techniques, including the principle of ARPES, MBE, and STM system.

Chapters 4 ~ 7 discuss the 2D Dirac and Weyl states on a black phosphorous structure system (α-Bi and α-Sb). We start at the non-symmorphic symmetry of these black phosphorous structures and study the symmetry-enforced Dirac fermions located at the high symmetry points (chapter 4 for α-Bi and chapter 5 for α-Sb). Next, we introduce a new 2D topological phase, unpinned Dirac fermion, which is observed on monolayer and bilayer α-Sb (chapter 6). Further, we found that substrate perturbation can modulate the α-Bi into a 2D Weyl state, which is the first observation of 2D Weyl fermion (shown in chapter 7).

Chapter 8 focused on the interaction between 2D Dirac states. We observed cloned Dirac cones on Graphene/SiC heterostructures. The Moiré modulation causes the Dirac fermions

cloning and interaction. Similar to twist bilayer graphene, we discuss the magic lattice constant and the emergent flat bands in this substrate-induced Moiré system.

Chapter 9~11 introduces the study of 2D ferromagnetic CrTe2 thin film and heterostructures, which is an ideal candidate for the 2D magnetic Weyl system. We first show the intrinsic room-temperature ferromagnetism in the CrTe2 monolayer and a few layers (in chapter 9). Then we found a giant topological Hall effect in CrTe2/Bi2Te3 heterostructures (in chapter 10). We also report the epitaxy and crystallinity engineering of CrTe2 on an amorphous substrate (shown in chapter 11)

Chapter 12 is the summary and outlook of this thesis

.

Reference

[1] K. S. Novoselov, D. Jiang, F. Schedin, T. J. Booth, V. V. Khotkevich, S. V. Morozov, A. K. Geim, Proc. Natl. Acad. Sci. USA 2005, 102, 10451.

[2] L. J. Sandilands, A. A. Reijnders, A. H. Su, V. Baydina, Z. Xu, A. Yang, G. Gu, T. Pedersen, F. Borondics, K. S. Burch, Phys. Rev. B 2014, 90, 081402.

[3] Y. Yu, L. Ma, P. Cai, R. Zhong, C. Ye, J. Shen, G. D. Gu, X. H. Chen, Y. Zhang, Nature 2019, 575, 156.

[4] Q.-Y. Wang, Z. Li, W.-H. Zhang, Z.-C. Zhang, J.-S. Zhang, W. Li, H. Ding, Y.-B. Ou, P. Deng, K. Chang, J. Wen, C.-L. Song, K. He, J.-F. Jia, S.-H. Ji, Y.-Y. Wang, L.-L. Wang, X. Chen, X.-C. Ma, Q.-K. Xue, Chin. Phys. Lett. 2012, 29, 037402.

[5] S. He, J. He, W. Zhang, L. Zhao, D. Liu, X. Liu, D. Mou, Y. B. Ou, Q. Y. Wang, Z. Li, L. Wang, Y. Peng, Y. Liu, C. Chen, L. Yu, G. Liu, X. Dong, J. Zhang, C. Chen, Z. Xu, X. Chen, X. Ma, Q. Xue, X. J. Zhou, Nat. Mater. 2013, 12, 605.

[6] J. P. Xu, M. X. Wang, Z. L. Liu, J. F. Ge, X. Yang, C. Liu, Z. A. Xu, D. Guan, C. L. Gao, D. Qian, Y. Liu, Q. H. Wang, F. C. Zhang, Q. K. Xue, J. F. Jia, Phys. Rev. Lett. 2015, 114, 017001.

[7] H.H.Sun, K.W.Zhang, L.H.Hu, C.Li, G.Y.Wang, H.Y.Ma Z.A.Xu, C.L.Gao, D.D.Guan, Y.Y.Li, C.Liu, D.Qian, Y.Zhou, L. Fu, S. C. Li, F. C. Zhang, J. F. Jia, Phys. Rev. Lett. 2016, 116, 257003.

[8] S. C. de la Barrera, M. R. Sinko, D. P. Gopalan, N. Sivadas, K. L. Seyler, K. Watanabe, T. Taniguchi, A. W. Tsen, X. Xu, D. Xiao, B. M. Hunt, Nat. Commun. 2018, 9, 1427.

[9] Y. Yu, F. Yang, X. F. Lu, Y. J. Yan, Y. H. Cho, L. Ma, X. Niu, S. Kim, Y. W. Son, D. Feng, S. Li, S. W. Cheong, X. H. Chen, Y. Zhang, Nat.Nanotechnol. 2015, 10, 270.

[10] V. Fatemi, S. Wu, Y. Cao, L. Bretheau, Q. D. Gibson, K. Watanabe, T. Taniguchi, R. J. Cava, P. Jarillo-Herrero, Science 2018, 362, 926.

[11] E. Sajadi, T. Palomaki, Z. Fei, W. Zhao, P. Bement, C. Olsen, S. Luescher, X. Xu, J. A. Folk, D. H. Cobden, Science 2018, 362, 922.

[12] D. Qiu, C. Gong, S. Wang, M. Zhang, C. Yang, X. Wang, and J. Xiong, Adv. Mater. 2021, 33, 2006124

[13] C. Gong et al., Discovery of intrinsic ferromagnetism in two-dimensional van der Waals crystals. Nature 546, 265–269 (2017).

[14] B. Huang et al., Layer-dependent ferromagnetism in a van der Waals crystal down to the monolayer limit. Nature 546, 270–273 (2017).

[15] T. Cao, Z. Li, S. G. Louie, Tunable magnetism and half-metallicity in hole-doped monolayer GaSe. Phys. Rev. Lett. 114, 236602 (2015).

[16] L. D. Casto et al., Strong spin-lattice coupling in CrSiTe3. APL Mater. 3, 041515 (2015).

[17] H. J. Deiseroth, K. Aleksandrov, C. Reiner, L. Kienle, R. K. Kremer, Fe3GeTe2 and Ni3GeTe2 - two new layered transition-metal compounds: Crystal structures, HRTEM investigations, and magnetic and electrical properties. Eur. J. Inorg. Chem. 2006, 1561–1567 (2006).

[18] B. Chen et al., Magnetic properties of layered itinerant electron ferromagnet Fe3GeTe2. J. Phys. Soc. Jpn. 82, 124711 (2013).

[19] J.-X. Zhu et al., Electronic correlation and magnetism in the ferromagnetic metal Fe3GeTe2. Phys. Rev. B 93, 144404 (2016).

[20] Cheng Gong and Xiang Zhang, Two-dimensional magnetic crystals and emergent heterostructure devices, Science 363, eaav4450 (2019)

[21] Kane, C. L. & Mele, E. J. Z2 topological order and the quantum spin Hall effect. Phys. Rev. Lett. 95, 146802 (2005).

[22] Fu, L. & Kane, C. L. Time reversal polarization and a Z2 adiabatic spin pump. Phys. Rev. B 74, 195312 (2006).

[23] Qi, X.-L. & Zhang, S.-C. Topological insulators and superconductors. Rev. Mod. Phys. 83, 1057–1110 (2011).

[24] Armitage, N., Mele, E. & Vishwanath, A. Weyl and Dirac semimetals in three-dimensional solids. Rev. Mod. Phys. 90, 015001 (2018).

[25] Dirac, P. A. M. The quantum theory of the electron. Proc. R. Soc. A 117, 610–624 (1928).

[26] Zhang, H. et al. Topological insulators in Bi2Se3, Bi2Te3, and Sb2Te3 with a single Dirac cone on the surface. Nat. Phys. 5, 438–442 (2009).

[27] Fu, L. & Kane, C. L. Superconducting proximity effect and Majorana fermions at the surface of a topological insulator. Phys. Rev. Lett. 100, 096407 (2008).

[28] Ren, Z., Taskin, A., Sasaki, S., Segawa, K. & Ando, Y. Large bulk resistivity and surface quantum oscillations in the topological insulator Bi2Te2Se. Phys. Rev. B 82, 241306 (2010).

[29] Kim, D. et al. Surface conduction of topological Dirac electrons in bulk insulating Bi2Se3. Nat. Phys. 8, 459 (2012).

[30] Fu, L. Topological crystalline insulators. Phys. Rev. Lett. 106, 106802 (2011).

[31] Hsieh, T. H. et al. Topological crystalline insulators in the SnTe material class. Nat. Commun. 3, 982 (2012).

[32] Pengzi Liu, James R. Williams, and Judy J. Cha. Topological nanomaterials, Nature Reviews Materials 4, pages 479–496 (2019)

[33] Yan, B. & Zhang, S.-C. Topological materials. Rep. Prog. Phys. 75, 096501 (2012).

[34] Müchler, L., Casper, F., Yan, B., Chadov, S. & Felser, C. Topological insulators and thermoelectric materials. Phys. Status Solidi Rapid Res. Lett. 7, 91–100 (2013).

[35] Ando, Y. & Fu, L. Topological crystalline insulators and topological superconductors: from concepts to materials. Annu. Rev. Condens. Matter Phys. 6, 361–381 (2015).

2. BACKGROUND KNOWLEDGE

2.1. Electron band structures

The basic and fundamental question we want to study is the electron properties in the material or the condensed matter in about a hundred years before Bloch raised a theorem [1] that could give the solutions of the Schrodinger equations in a periodic boundary condition or a periodic potential.

Mathematically, it is written as:

$$\psi(\boldsymbol{r}) = e^{i\,\boldsymbol{k}\cdot\boldsymbol{r}} u(\boldsymbol{r})$$

Where **r** is position, ψ is the wave function, u is a periodic function with the same periodicity as the crystal, and the wave vector **k** is the crystal momentum vector. This function serves as a suitable basis for the wave functions or states of electrons in crystalline solids, which can simplify the Schrodinger equations and make the equations solvable. Based on the Bloch theorem, the Schrodinger equations can be solved in the k space or the momentum space with the relations between energy and momentum (or k). These solutions could be found in each k point in the whole k space. By connecting all of the solutions (energy points at different k positions), we can get the electron band structures. A graphene band structure is shown in Figure 2.1. A real band structure for a 3-dimensional crystal is 4-dimension (E, k_x, k_y, k_z), and it is 3-dimension for a 2-dimensional thin film such as graphene (shown in Fig. 2.1 left). The band structures usually are drawn along high symmetry lines (shown in Fig. 2.1 right). In most cases, the band structures along high symmetry lines hold all information of the total band structures. In addition, as the electron band structures contain all the

solutions of the Schrodinger equations, almost all the electron properties in the single crystal could be realized from the band structures.

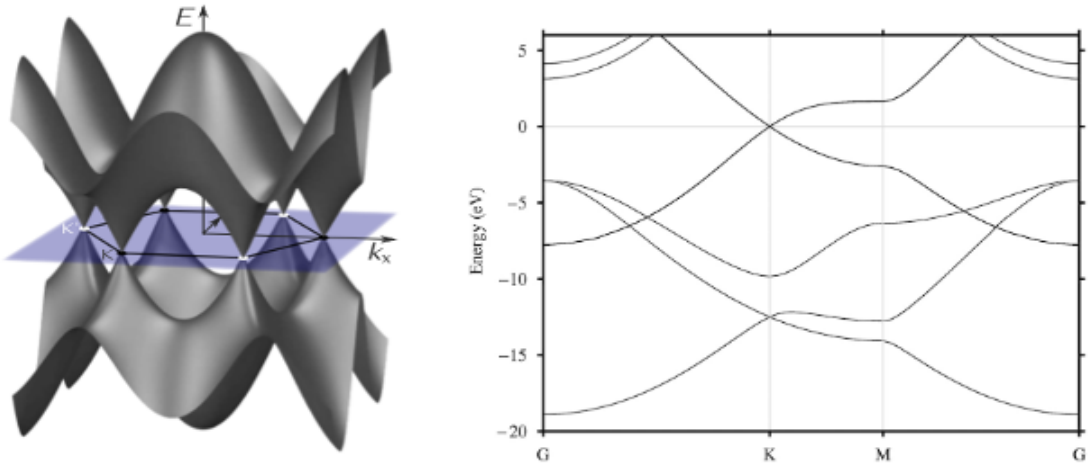

Fig. 2.1 Electron band structures of graphene, 3-dimensional band structures (left), band structures along high symmetry lines (right).

2.2. A semi-classic view of band structures

Basically, a tight-binding approximation is used with the wave function linear combination of different orbits and different sites of the atoms to build the total wave function of the crystal.[2]

We can start with a one-dimensional case and consider a series of atoms labeled by n=1, 2, 3⋯ , as shown below. There is a basis function (an H 1s orbital),χ_0, χ_1, χ_2, etc., then the appropriate symmetry-adapted linear combinations (remember that translation is as good a symmetry operation).

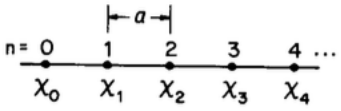

$$\psi_k = \sum_n e^{i\,kn\,a}\,\chi_n$$

Here **a** is the lattice spacing, the unit cell in one dimension, and **k** is an index that labels which irreducible representation of the translation group. Let's see what combinations are generated for two specific values of k: 0 and π/a.

$$k = 0,\ \ \psi_0 = \sum_n e^0\,\chi_n = \sum_n \chi_n = \chi_0 + \chi_1 + \chi_2 + \cdots$$

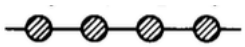

$$k = \frac{\pi}{a},\ \ \psi_0 = \sum_n e^{i\,\pi n}\,\chi_n = \sum_n -1^n\,\chi_n = \chi_0 - \chi_1 + \chi_2 - \cdots$$

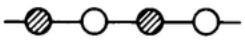

We can see that the wave function corresponding to k = 0 is the most bonding one, the wave functions of all atoms are in the same phase, so the energy would be the lowest. On the contrary, the one for k =π/a should be at the top of the band. For other values of k, we get a neat description of the other levels in the band. But one has to be careful--there is a range of k, and if one goes outside of it, one doesn't get a new wave function but rather repeats an old one. The unique values of k are in the interval -π/a≤ k ≤ π/a. This is called the first

Brillouin zone, the range of unique k. Based on the above discussion, we are already able to predict the band structure in Fig. 2.2:

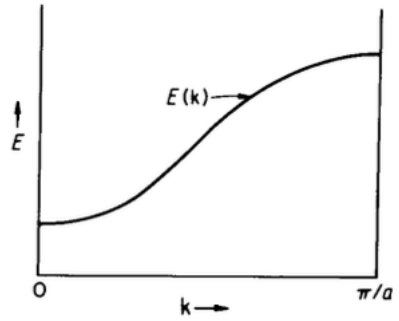

Fig. 2.2 Band dispersion from 0 to π/a formed by a 1s orbits chain. [3]

If we consider different orbits, the band dispersion could be different, for example, the p orbits. We can consider a similar case: a one-dimension chain contains all p orbits and all the p orbits connected head-to-head. The wave function and the band structure on k=0 and k=π/a drawn in Fig. 2.3.

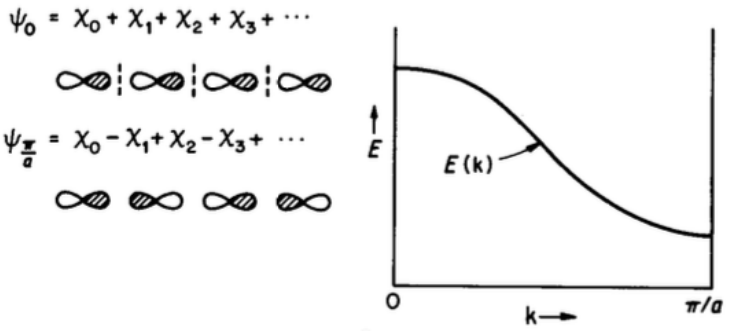

Fig. 2.3 Wave function and band dispersion from 0 to π/a formed by a p orbits chain. [3]

Now, we can move to a two-dimensional case (shown in Fig. 2.4)

Consider a squire lattice shown in Fig. 2.4. For the s orbits, at the **Γ** point(0,0), the phase of the wave function should be the same, and the energy would be the lowest. At the Y point (0, π/a), the atoms on the same horizontal line has the same phase but have the opposite phase along the vertical line. We can count the 'nodes' (number of the connecting point with the opposite phase) in the diagram, and if they are head-to-head, we can define they are σ nodes; and if they are shoulder-to-shoulder, we can define they are π nodes. We can count the number of nodes. The more nodes, the higher energy the configuration should be, and the σ nodes care a higher energy than π nodes. As a result, we can draw the energy levels at different high symmetry points so that we can have a brief band structure shown in Fig. 2.4c. The result is actually quite accurate as a result fits well with the real band structure of Sb atoms with a 2D squire lattice (shown in Fig. 2.4d).

As a summary, we can use the semi-classic view to understand the band structure formation. More important, we can tell the band orbital formation in a real system band structure based on this view. We can even predict the symmetry, the degeneracy, and even the topology of band structures just based on the lattice structure.

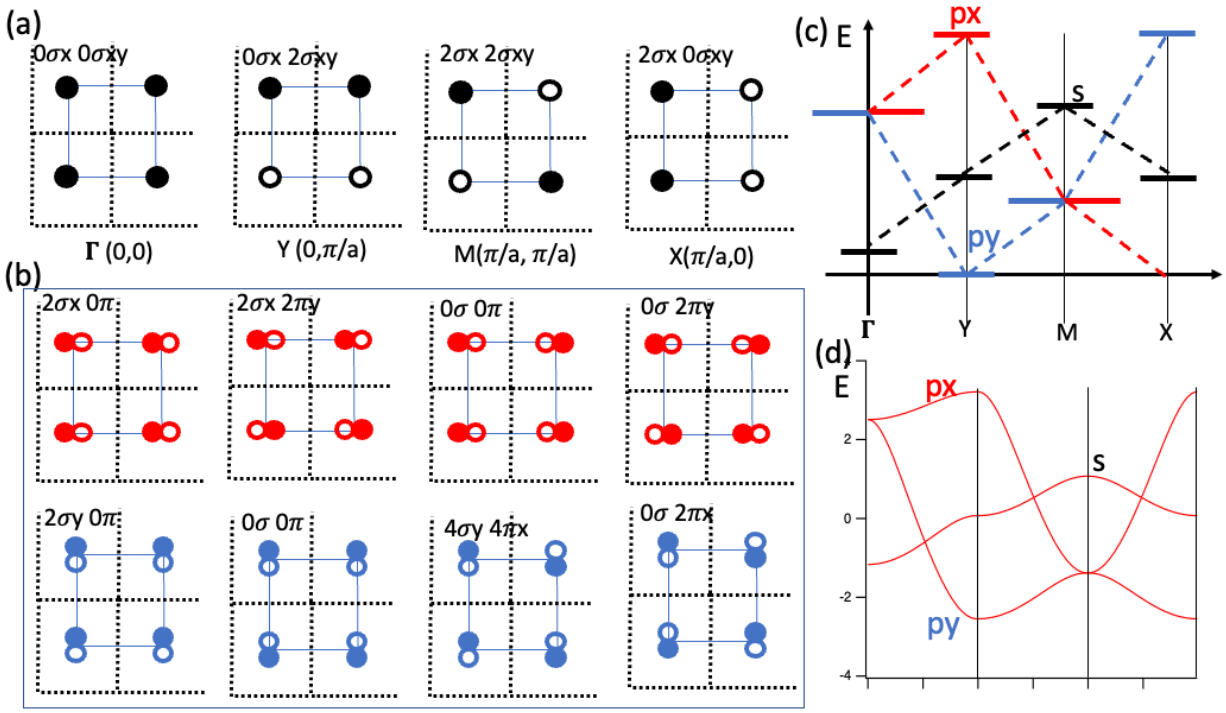

Fig. 2.4. a s orbital phase diagram in 2D squire lattice. **b** px and py orbital phase diagram, **c** a predicted band structure based on the orbital phase diagram. **d** band structure of a 2D Sb squire lattice.

2.3. Surface states (SSs), edge states (ESs) and quantum well state (QWSs).

2.3.1 Surface states and edge states

The termination of a material with a surface not only gives rise to surface relaxation and reconstruction but also strongly modifies the electronic structure at the surface. Breaking of the lattice periodicity allows the existence of new states beyond the Bloch bulk states. The wavefunctions of those new states are localized near the surface, and thus they have accordingly termed surface states [1]. Their energy levels are found in the band gaps where bulk states are not allowed. Intuitively the surface states can be viewed as electronic states

which are trapped by the band gap on one side of the surface and the surface barrier potential, which prevents electrons from escaping into the vacuum.

In order to examine the behavior of surface electrons, one needs to compare the surface bands with the bulk bands projected to the surface [4]. Fig. 2.5 gives such a comparison. [5]

Suppose the bulk band disperses along $k_{\perp}$, the wavevector perpendicular to the surface, in the manner as shown in the left upper panel of Fig. 2.5. The width of this band then gives the continuum of allowed states in the surface reciprocal space, and the projected bulk bands are widened to have the shape of, say, the hatched area along a particular $k_{\parallel}$ direction. Surface states may exist in the gap of the projected bulk bands, as shown in the upper middle panel. In such a case, the states must be localized near the surface as they are not allowed in bulk. Thus, the wavefunctions of the surface states decay rapidly towards the interior of the solid, as illustrated in the lower middle panel. If, however, a surface band stays in the band gap for only a limited range of $k_{\parallel}$ and overlaps with the projected bulk bands for other $k_{\parallel}$, as shown in the right upper panel, then the wavefunction will be gradually evanescent towards the bulk, as shown in the right lower panel. These states inside the bulk band region are called surface resonance states. Both surface state and surface resonance are experimentally observable by photoemission spectroscopy, but a clear discrimination between the two is not always accessible. Similar to the SSs, edge states (ESs) are the new states that are rising from breaking the periodic condition of a two-dimensional system. Well-defined edge states are located inside the band gap. In a topological nontrivial system, the SSs or ESs are from, as the topology is different in and out of the system. When connecting the wave function in and out of the system, a new solution will arise. This solution is the non-trivial SSs or ESs.

Because the topological SSs or ESs are derived from the non-trivial property of the 3D or 2D bulk, those SSs and ESs are robust under perturbation. This will be discussed in section 2.5.

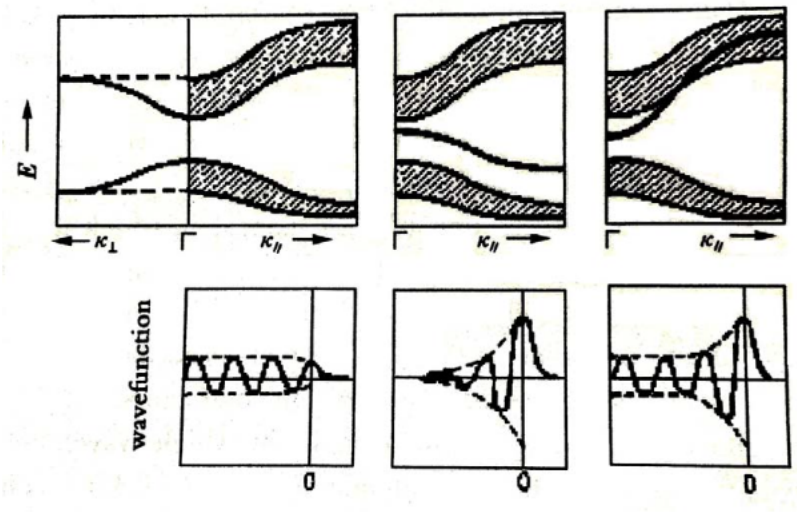

Figure 2.5. Schematic illustration of the surface states as compared with the projected bulk bands (the hatched area) [4]. Left: projected bulk bands and a bulk state. Middle: a surface band (the solid line) and a surface state. Right: a surface resonance. The "0" denotes the surface position.

2.3.2 Quantum well states

If the film thickness is comparable to the coherence length of the electron, the electrons can bounce back and forth between the two boundaries of the film and form electronic standing waves, known as quantum well states (QWS). For thin films, quantum well states are often the dominant features, giving rise to quantum size effects. As a consequence, the continuum of the valence band is quantized in the k_z direction (Fig. 2.6c). Considering the

dispersion along the k_x and k_y directions, say, free electron-like, the band structure of the thin film will consist of a set of parabolic quantum well subbands (Fig. 2.6c).

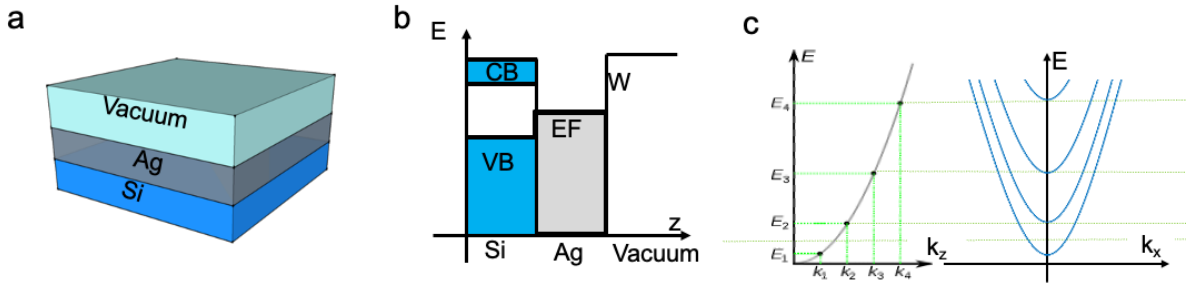

Fig. 2.6 a an Ag-Si quantum well, **b** the potential barrier of the Ag quantum well, **c** the quantization of k_z and the free electron like k_x band dispersion.

2.4. Berry phase and Topological invariants

Consider a system with a Hamiltonian that depends on a set of parameters H=H(**R**). We are interested in the adiabatic evolution of the system as **R**(t) moves slowly along path C in the parameter space. For this purpose, it is useful to introduce an instantaneous orthonormal basis so $H(R)|n(R)>=\varepsilon_n(R)|n(R)>$. According to the quantum adiabatic theorem, [6] a system initially in one of its eigenstates |n(**R**(0))> will stay as an instantaneous eigenstate of the Hamiltonian H(**R**(t)) throughout the process. Therefore, the only degree of freedom we have is the phase of the quantum state. We write the state at time t as:

$$|\psi_n(t)\rangle = e^{i\gamma_n(t)}\exp\left[-\frac{i}{\hbar}\int_0^t dt'\,\varepsilon_n(\boldsymbol{R}(t'))\right]|n(\boldsymbol{R}(t))\rangle,$$

Where the second exponential is known as the dynamical phase factor, put this into the time-dependent Schrodinger equation:

$$i\hbar\frac{\partial}{\partial t}|\psi_n(t)\rangle = H(\boldsymbol{R}(t))|\psi_n(t)\rangle$$

We can find that γ_n can be expressed as a path integral in the parameter space,

$$\gamma_n = \int_C d\boldsymbol{R}\cdot\mathcal{A}_n(\boldsymbol{R}),$$

$$\mathcal{A}_n(\boldsymbol{R}) = i\langle n(\boldsymbol{R})|\frac{\partial}{\partial \boldsymbol{R}}|n(\boldsymbol{R})\rangle.$$

Where

This vector $A_n(R)$ is called the Berry connection or the Berry vector potential. It shows that, in addition to the dynamical phase, the quantum state will acquire an additional phase γ_n during the adiabatic evolution. Consequently, the phase γ_n will be changed by $\zeta(R(0))$-$\zeta(R(T))$ after the transformation, where R(0) and R(T) are the initial and final points of path C. This shows that γ_n can be only changed by an integer multiple of 2π under the gauge transformation, and it cannot be removed. Therefore, for a closed path, γ_n becomes a gauge-invariant physical quantity, now known as the **Berry phase**.

$$\gamma_n = \oint_C d\boldsymbol{R}\cdot\mathcal{A}_n(\boldsymbol{R}).$$

In three-dimension cases, it is useful to define, in analogy to electrodynamics, a gauge-field tensor derived from the Berry vector potential:

$$\Omega^n_{\mu\nu}(\boldsymbol{R}) = \frac{\partial}{\partial R^\mu}\mathcal{A}^n_\nu(\boldsymbol{R}) - \frac{\partial}{\partial R_\nu}\mathcal{A}^n_\mu(\boldsymbol{R}) = i\left[\left\langle\frac{\partial n(\boldsymbol{R})}{\partial R^\mu}\middle|\frac{\partial n(\boldsymbol{R})}{\partial R^\nu}\right\rangle - (\nu\leftrightarrow\mu)\right].$$

This field is called the Berry curvature. Then according to Stokes's theorem, the Berry phase can be written as a surface integral

$$\gamma_n = \int_S dR^\mu \wedge dR^\nu \tfrac{1}{2}\Omega^n_{\mu\nu}(\boldsymbol{R}),$$

where S is an arbitrary surface enclosed by path C. Unlike the Berry vector potential, the Berry curvature is gauged invariant and thus observable. If the parameter space is three-dimensional, the above equations can be recast into a vector form:

$$\boldsymbol{\Omega}_n(\boldsymbol{R}) = \boldsymbol{\nabla}_{\boldsymbol{R}} \times \mathcal{A}_n(\boldsymbol{R}),$$

$$\gamma_n = \int_S d\boldsymbol{S} \cdot \boldsymbol{\Omega}_n(\boldsymbol{R}).$$

Besides the differential formula, the Berry curvature can also be written as a summation of the eigenstates: [7]

$$\Omega^n_{\mu\nu}(\boldsymbol{R}) = i \sum_{n' \neq n} \frac{\langle n|\partial H/\partial R^\mu|n'\rangle\langle n'|\partial H/\partial R^\nu|n\rangle - (\nu \leftrightarrow \mu)}{(\varepsilon_n - \varepsilon_{n'})^2}.$$

Here, we need to notice that the E, k, v change sign is under space inversion, and the k, v change sign is under time reversal. So, if the system is time-reversal invariant, then $\Omega(-k) = -\Omega(\mathrm{k})$, and if the system is space-inversion invariant, then $\Omega(-k) = \Omega(\mathrm{k})$. As a result, if the system has P and T symmetry, the Berry curvature always is 0.

2.5. Topological Semimetals

2.5.1 Weyl semimetal

Weyl semimetal is a three-dimensional (3D) topological state of matter in which the conduction and valence energy bands touch at a finite number of nodes [8, 9]. The nodes always appear in pairs. In each pair, the quasiparticles carry opposite chirality and linear

dispersion, much like a 3D analog of graphene. In the past few years, a number of materials have been suggested to host Weyl fermions [10–22]. The topological semimetals can be simply classified into Weyl semimetals and Dirac semimetals. In a Weyl semimetal, each Weyl node is non-degenerate, while in a Dirac semimetal, the Weyl nodes are degenerate due to time-reversal and inversion symmetry [17].

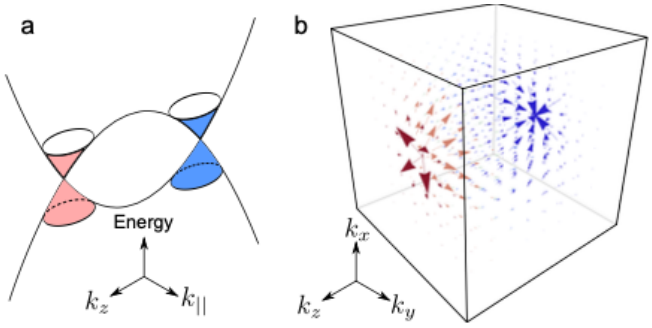

Fig. 2.7. Nontrivial band structure and Berry curvature of a Weyl semimetal. (**a**) A schematic of the energy spectrum of a topological semimetal (k_x, k_y,k_z) is the wave vector. $K_{//}^2 = k_x^2 + k_y^2$. (b) The vector plot of the Berry curvature in momentum space. The conduction and valence bands of a topological semimetal touch at the Weyl nodes, at which a pair of monopoles are hosted. The arrows show that the flux of the Berry curvature flows from one monopole (red) to the other (blue), defining the nontrivial topological properties of a topological semimetal. [23]

A minimal model for a Weyl semimetal can be written as $H = A(k_x \sigma_x + k_y \sigma_y) + \mathcal{M}_k \sigma_z$, where σ are the Pauli matrices, $M_k = M_0 - M_1 (k_x^2 + k_y^2 + k_z^2)$, $k = (k_x, k_y, k_z)$ is the wave vector, and A, $M_{0/1}$ are model parameters. This minimal model gives a global description of a pair of Weyl nodes of opposite chirality and all the topological properties. If $M_0 M_1 > 0$,

the two bands intersect at (0, 0, $\pm k_w$) with $k_w \equiv pM_0/M_1$ (see Fig. 2.7), giving rise to the topological semimetal phase. In the topological semimetal phase, the model can also be written as $H = A(k_x \sigma_x + k_y \sigma_y) + M(k_w^2 - \boldsymbol{k}^2)\sigma_z$, here A, M, and k_w are model parameters. The dispersions of two energy bands of this model are

$$E_{\pm} = \pm\sqrt{[M(k_w^2 - \mathbf{k}^2)]^2 + A^2(k_x^2 + k_y^2)},$$

which reduce to $E\pm = \pm M|k_w^2 - k_z^2|$ at $k_x = k_y = 0$. The two bands intersect at $(0,0,\pm k_w)$ (see Fig. 2.7).

The topological properties in H can be seen from the Berry curvature, $\Omega(k) = \nabla k \times A(k)$, where the Berry connection is defined as $A(k) = i \langle u(k)| \nabla k |u(k)\rangle$. For example, for the energy eigenstates for the + band $|u(k)\rangle = [\cos(\theta/2), \sin(\theta/2)e^{i\varphi}]$, where $\cos\theta \equiv M_k/E_+$ and $\tan\varphi \equiv k_y/k_x$. The three-dimensional Berry curvature for the two-node model can be expressed as

$$\boldsymbol{\Omega}(\mathbf{k}) = \frac{A^2 M}{E_+^3}\left[k_z k_x, k_z k_y, \frac{1}{2}\left(k_z^2 - k_w^2 - k_x^2 - k_y^2\right)\right]$$

There exists a pair of singularities at (0, 0, $\pm k_w$), as shown in Fig. 2.7. The chirality of a Weyl node can be found as an integral over the Fermi surface enclosing one Weyl node.

For a given k_z, a Chern number can be well defined as $n_c(k_z) = -(1/2\pi)\iint dkxdky\Omega(k) \cdot \hat{z}$ to characterize the topological property in the k_x-k_y plane, and

$$n_c(k_z) = -\frac{1}{2}[\mathrm{sgn}[M(k_w^2 - k_z^2)] + \mathrm{sgn}(M)].$$

The Chern number $n_c(k_z) = -\mathrm{sgn}(M)$ for $-k_w < k_z < k_w$, and $n_c(k_z) = 0$ otherwise [12]. The nonzero Chern number corresponds to the k_z-dependent edge states (known as the Fermi arcs) according to the bulk-boundary correspondence.

If there is an open boundary at y = 0, where the wave function vanishes, the dispersion of the surface states is finally given by

$$E_{\mathrm{arc}}(k_x, k_z) = \mathrm{sgn}(M) A k_x.$$

The corresponding wavefunction is similar to the topological insulator surface states

$$\Psi^{\mathrm{arc}}_{k_x,k_z}(\mathbf{r}) = C e^{ik_x x + ik_z z} \begin{bmatrix} \mathrm{sgn}(M) \\ 1 \end{bmatrix} (e^{\lambda_1 y} - e^{\lambda_2 y})$$

where C is a normalization factor and $\lambda_{1,2} = A/2|M| \mp \sqrt{(A/2M)^2 - \Delta_k}$, and $\Delta_k = k_w^2 - kx2 - k_z^2$. There are Fermi arcs in two cases: (i) $\lambda_{1,2} > 0$, and (ii) $\lambda_{1,2} = a \mp ib$ with a,b > 0 (Note that $\lambda_1 = \lambda_2$ corresponds to a trivial case). Also, in both cases (i) and (ii), we have $\lambda_1\lambda_2 > 0$ and henceforth $\Delta_k > 0$. Therefore the solution of Fermi surface states is restricted inside a circle defined by $k_x^2 + k_z^2 < k_w^2$.

The two-node model above provides a generic description for Weyl semimetals, including the band touching, opposite chirality, monopoles of Berry curvature, topological charges, and Fermi arcs.

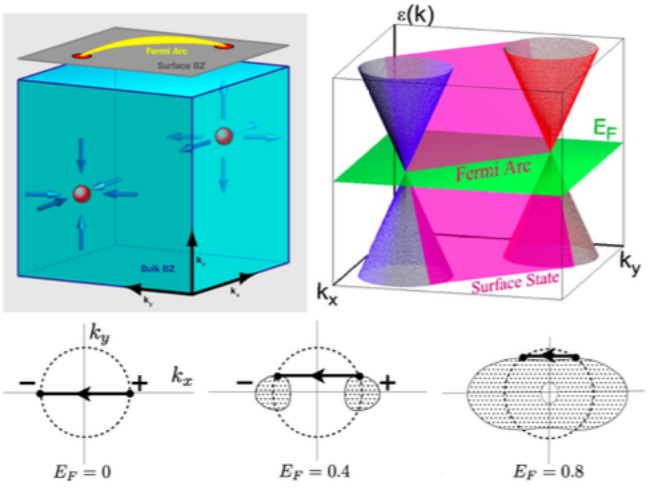

Fig. 2.8. (Top right) Connection of surface states to bulk Weyl points. (Bottom) Evolution of the Fermi arc with chemical potential in a particular microscopic model on raising the chemical potential from the nodal energy (E =0). Fermi arcs are tangent to the bulk Fermi surface projections and may persist even after they merge into a trivial bulk Fermi surface. [24]

2.5.2 Dirac semimetal

As discussed, Weyl points can occur in three-dimensional materials only when either time reversal or inversion symmetries are broken. When inversion symmetry is present, a Weyl node at k must be accompanied by a partner node at −k at the same energy that carries the opposite topological charge. Conversely, time reversal symmetry requires that nodes at these momenta are time-reversed partners which carry the same topological charge. Since the net topological charge enclosed within the Brillouin zone is zero, this latter situation further requires the existence of two additional compensating partners, Weyl nodes. The presence of both inversion and time reversal symmetries excludes the possibility of a twofold degeneracy at a Weyl point in the spectrum.

Nevertheless, when both symmetries are present, energetically degenerate Weyl nodes carrying opposite charges can be stabilized at the same crystal momentum. This produces a composite point singularity hosting a fourfold degeneracy. This degeneracy is not topologically protected since its net Chern number is zero, and residual momentum-conserving terms in the Hamiltonian projected into the degenerate sub-space can potentially mix these states and gap the electronic spectrum. However, in special situations, this mixing

can be forbidden by space group symmetries, in which case the nodes remain intact as symmetry-protected degeneracies. This is of fundamental interest since the stable merger of two low-energy Weyl nodes provides a solid-state realization of the (3+1)-dimensional Dirac vacuum, and materials that support this degeneracy are called Dirac semimetals.

Similar to the Weyl semimetal, the Hamiltonian can be treated as two pairs of Weyl fermion:

$$H(k) = H_w(k) + H_w^*(k) = A\left(k_x\sigma_x + k_y\sigma_y\right) + 2M(k_w^2 - \boldsymbol{k}^2)\sigma_z + A\left(-k_x\sigma_x + k_y\sigma_y\right)$$

However, a DSM can also appear as a robust electronic phase that is stable over a range of Hamiltonian control parameters. There are at least two different ways of accomplishing this. (Class I) One can exclude the possibility of mass terms appearing in a band-inverted Bloch Hamiltonian H(k) for k lying along a symmetry axis [24]. We refer to this as the "band inversion" mechanism. (Class II) One can search for space groups that support small groups with four-dimensional irreducible representations (FDIR) at discrete high-symmetry momenta k_n. We refer to this as the "symmetry-enforced" mechanism. In the band inversion mechanism, the Dirac semimetal is not truly a symmetry-protected state since it actually contains a pair of DPs, and one may continuously tune parameters to uninvent the bands without changing the space group. This eliminates the two DPs by their merger and pairwise annihilation. However, in the symmetry-enforced mechanism, the appearance of the DP is an unavoidable consequence of the space group of the material.

The band inversion mechanism provides perhaps the most direct route to the formation of a Dirac semimetal. The energy eigenvalues in the nth band are related by time-reversal symmetry $E_{n,\uparrow}(k) = E_{n,\downarrow}(-k)$ and by inversion symmetry $E_{n,\sigma}(k) = E_{n,\sigma}(-k)$ The combined operation of both symmetries requires that $E_{n,\uparrow}(k) = E_{n,\downarrow}(k)$ so that each band

remains doubly degenerate locally at every k. A Dirac node can occur if two such branches undergo an accidental band crossing at a point. Since the small group is trivial at a low symmetry k point in the Brillouin zone, the intersection of a pair of doubly degenerate bands is generically prevented by an avoided crossing. However, when k lies along a symmetry line, lattice symmetries intervene by constraining the possible interactions within this multiplet. For example, if the crossing states transform according to different irreducible representations of the group of the symmetry line, their hybridization is prevented, and a fourfold degeneracy at this point of intersection is symmetry protected.

Figure 2.9 illustrates how this situation can arise naturally near a band inversion transition. The uninverted [Fig. 2.9(a)] and inverted [Fig. 2.9(b)] band structures reverse the parties and band curvatures of their k = 0 eigenstates. Generally, these states are allowed to mix at $k \neq 0$, as shown in Fig. 2.9(b), which produces an avoided crossing and fully gaps the state with a "Mexican-hat" dispersion. However, if these states transform along a symmetry direction according to different irreducible representations of the group of the symmetry line, the spectrum retains a gap closure on the symmetry line, as shown in Fig. 2.9 (c). Note that this mechanism generically produces pairs of fourfold degenerate points along this line. If one tunes parameters to uninvent the bands, these two Dirac points merge and annihilate, and the system reverts to a fully gapped state shown in Fig. 2.9(a). Generally, Dirac systems are very sensitive to symmetry-breaking terms.

The band inversion mechanism can be understood more quantitatively by adopting a four-state Hamiltonian for a system near a band inversion transition

$$\mathcal{H}(\mathbf{k}) = \sum_{ij} a_{ij}(\mathbf{k})\sigma_i \otimes \tau_j,$$

where σ and τ are Pauli matrices that act in the spin and orbital spaces, respectively.

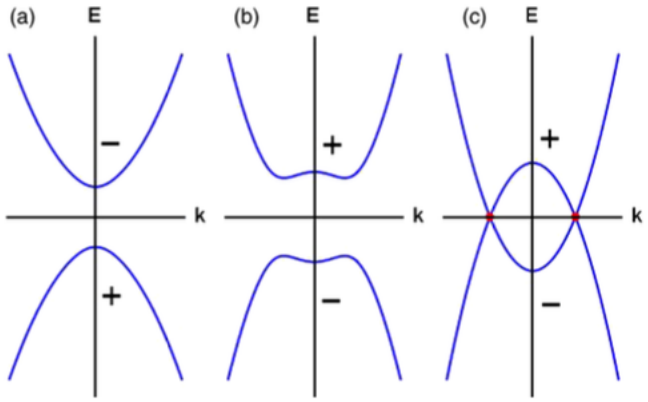

Fig.2.9. Development of a Dirac semimetal in an inverted band structure. The band inversion transition reverses the parities (±) of the k = 0 eigenstates in the (**a**) uninverted and (**b**) inverted level orderings. (**b**) The inverted bands are twofold degenerate and undergo an avoided crossing at $k \neq 0$, which gaps the spectrum. (**c**) The mixing is forbidden along a symmetry line by the different rotational symmetries of the intersecting bands. This leaves two points, each with a fourfold point degeneracy at $k = \pm k_D$ along the symmetry line that is lifted to linear order in $k - k_D$. Uninverting the bands produces a pairwise annihilation of the Dirac points, and the system reverts to the conventional insulating state, as shown in (**a**). [24]

2.6. Two-dimensional magnetism

In order to hold two-dimensional Weyl fermions, one practicable way is to break the time-reversal symmetry, which in particular, the material needs to hold two-dimensional

magnetism. Two-dimensional intrinsic magnetic materials have been discovered in recent years [22,23] and have attracted a lot of attention in the field.

Understanding the fundamental difference between 2D and 3D magnetism is instructive. The driving force underlying the ordering of electrons' spin magnetic moments in an (anti-)ferromagnet is the "exchange interaction," which was initially dubbed as a "molecular field" and was understood to be quantum mechanical (Fig. 2.10). The effect is a coulombic interaction under the Pauli exclusion principle relating to the electrons' anti-symmetric wave function. The exchange interaction has been used to estimate the Curie temperatures of 3D ferromagnets based on the argument that the short-range exchange interaction needs to be overcome by thermal energy to randomize the magnetic moments. Nonetheless, the mean-field picture suitable for 3D systems does not work for the length scale of 2D systems, in which the dimensionality effect comes into play. Magnon (i.e., quanta of a spin wave) dispersion in 2D systems is reduced with respect to that in the 3D counterparts, corresponding to an abrupt onset of magnon density of states (DOS) in 2D systems and thus ease of thermal agitations. For 2D systems without magnetic anisotropy (Fig. 2.10B), the spin wave excitation gap diminishes (Fig. 2.10C). Together with the diverging Bose-Einstein statistics of magnons at zero energy, any nonzero temperatures cause massive magnon excitations and the spin order to collapse. However, for 2D systems with uniaxial magnetic anisotropy, a magnon excitation gap opens up and resists the thermal agitations (Fig. 2.10, D and E), which then lifts the Mermin-Wagner restriction and results in finite Curie temperatures. Meanwhile, the exchange interaction, together with the dimensionality, dictates the magnon band width and profiles. Therefore, the synergy of these factors, as well

as the inter quasi-particle scattering, which potentially renormalizes the magnon spectrum, determines the upper bound temperature (i.e., Curie temperature) below which a 2D ferromagnet can be found. [27]

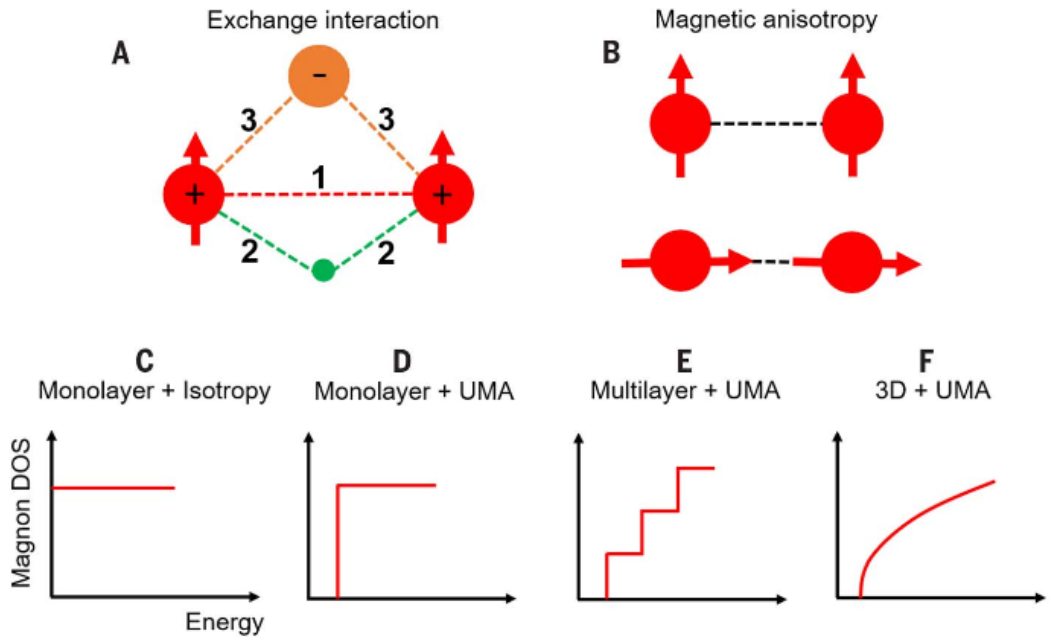

Fig. 2.10. Fundamental physical parameters and spin wave excitations in ferromagnets of different dimensionalities. (A and B) In a collinear magnet, exchange interaction and magnetic anisotropy are fundamental parameters. Exchange interaction arises from electrons' antisymmetric wave function and is governed by coulombic interaction under the Pauli exclusion principle. The exchange interaction between spins can be directly established (red dashed line 1) or indirectly mediated by conduction electrons (green ball with dashed lines labeled 2) or intermediate anions (orange ball with dashed lines labeled 3) such as O^{2-}. While spins are aligned, there is usually a preferred orientation, which means magnetic anisotropy. Magnetic anisotropy has a variety of sources, such as magnetocrystalline anisotropy, shape anisotropy, and stress anisotropy. (C to F) In a 2D isotropic Heisenberg ferromagnet, there will be massive excitations of magnons at nonzero temperatures

because of the absence of a spin wave excitation gap, the abrupt onset of magnon density of states (DOS), and the diverging Bose-Einstein statistics at zero energy; the result is the collapse of long-range magnetic order. The presence of uniaxial magnetic anisotropy (UMA) opens up the spin wave excitation gap to resist the thermal agitations of magnons, leading to the finite Curie temperature. As the system evolves from 2D to 3D, the magnon DOS spectrum changes from a step function to a gradually increasing function with zero DOS at the threshold of excitation. Therefore, in 3D systems, UMA (related to the spin wave excitation gap) is not a prerequisite for the presence of finite-temperature long-range magnetic order.

Reference

[1]. Bloch, F. (1929). Über die quantenmechanik der elektronen in kristallgittern. Zeitschrift für physik, 52(7), 555-600.

[2]. Giuseppe Grosso and Giuseppe Pastori Parravicini, Solid State Physics, Elsevier (2006)

[3]. Roald Hoffmann, Solid and Surface: A Chemist's View on Bonding in Extended Structures, VCH Publishers, (1988)

[4]. C. Kittle, Introduction to Solid State Physics (John Wiley & Sons, Inc., New York, 1986).

[5]. G. Bian, Angle-Resolved Photoemission and First-Principles Studies of Topological Thin Films, Ph.D. Thesis, University of Illinois at Urbana-Champaign, (2012)

[6]. Kato, T., 1950, J. Phys. Soc. Jpn. 5, 435.

[7]. D. Xiao, M. Chang, and Q. Niu, Berry phase effects on electronic properties, RevModPhys.82.1959 (2010)

[8]. L. Balents, Physics 4, 36 (2011).

[9]. G. E. Volovik, The Universe in a Helium Droplet (Clarendon Press, Oxford, 2003).

[10]. X. Wan, A. M. Turner, A. Vishwanath, and S. Y. Savrasov, Phys. Rev. B 83, 205101 (2011).

[11]. K. Y. Yang, Y. M. Lu, and Y. Ran, Phys. Rev. B 84, 075129 (2011).

[12]. A. A. Burkov and L. Balents, Phys. Rev. Lett. 107, 127205 (2011).

[13]. G. Xu, H. M. Weng, Z. J. Wang, X. Dai, and Z. Fang, Phys. Rev. Lett. 107, 186806 (2011).

[14]. P. Delplace, J. Li, and D. Carpentier, EPL 97, 67004 (2012).

[15]. J.-H. Jiang, Phys. Rev. A 85, 033640 (2012).

[16]. S. M. Young, S. Zaheer, J. C. Y. Teo, C. L. Kane, E. J. Mele, and A. M. Rappe, Phys. Rev. Lett. 108, 140405 (2012).

[17]. Z. Wang, Y. Sun, X. Q. Chen, C. Franchini, G. Xu, H. Weng, X. Dai, and Z. Fang, Phys. Rev. B 85, 195320 (2012).

[18]. B. Singh, A. Sharma, H. Lin, M. Z. Hasan, R. Prasad, and A. Bansil, Phys. Rev. B 86, 115208 (2012).

[19]. Z. Wang, H. Weng, Q. Wu, X. Dai, and Z. Fang, Phys. Rev. B 88, 125427 (2013).

[20]. J. Liu and D. Vanderbilt, Phys. Rev. B 90, 155316 (2014).

[21]. D. Bulmash, C.-X. Liu, and X.-L. Qi, Phys. Rev. B 89, 081106 (2014).

[22]. M. Brahlek, N. Bansal, N. Koirala, S. Y. Xu, M. Neu- pane, C. Liu, M. Z. Hasan, and S. Oh, Phys. Rev. Lett. 109, 186403 (2012).

[23]. Hai-Zhou Lu and Shun-Qing Shen, Quantum transport in topological semimetals under magnetic fields, Front. Phys. 12,127201 (2017)

[24]. N. P. Armitage, E.J. Mele and Ashvin Vishwanath, Weyl and Dirac semimetals in three-dimensional solids, RevModPhys.90.015001 (2018)

[25]. C. Gong et al., Discovery of intrinsic ferromagnetism in two-dimensional van der Waals crystals. Nature 546, 265–269 (2017).

[26]. B. Huang et al., Layer-dependent ferromagnetism in a van der Waals crystal down to the monolayer limit. Nature 546, 270–273 (2017).

[27]. Cheng Gong and Xiang Zhang, Two-dimensional magnetic crystals and emergent heterostructure devices, Science 365, 706 (2019).

3. EXPERIMENTAL TECHNIQUES

This chapter presents a comprehensive description of our main experiment system: two-dimensional material synthesizes and characterization system. This system contains a molecular beam epitaxy (MBE), a scanning tunning microscopy (STM), and an angle-resolved photoemission spectroscopy (ARPES) system. We discuss the basic principles and working process of each part.

The MBE-STM-ARPES system shown in Fig. 3.1, the MBE, STM, and ARPES systems are all connected to the same ultra-high vacuum (UHV) chamber, all the parts in the system need a UHV condition, and the basic knowledge of UHV system is discussed in section 3.1. Basically, ARPES use a photoemission process, photo in an electron out, to measure the electron band structures of the sample; MBE is a thin film synthesize method that deposit atoms or molecules on substrates under UHV condition; STM can directly measure the topography and local density of states (LDOS) on the sample surface based on quantum tunning on the tip. The principle of ARPES is discussed in sections 3.2 and 3.3, and the information on MBE and STM is in sections 3.4 and 3.5.

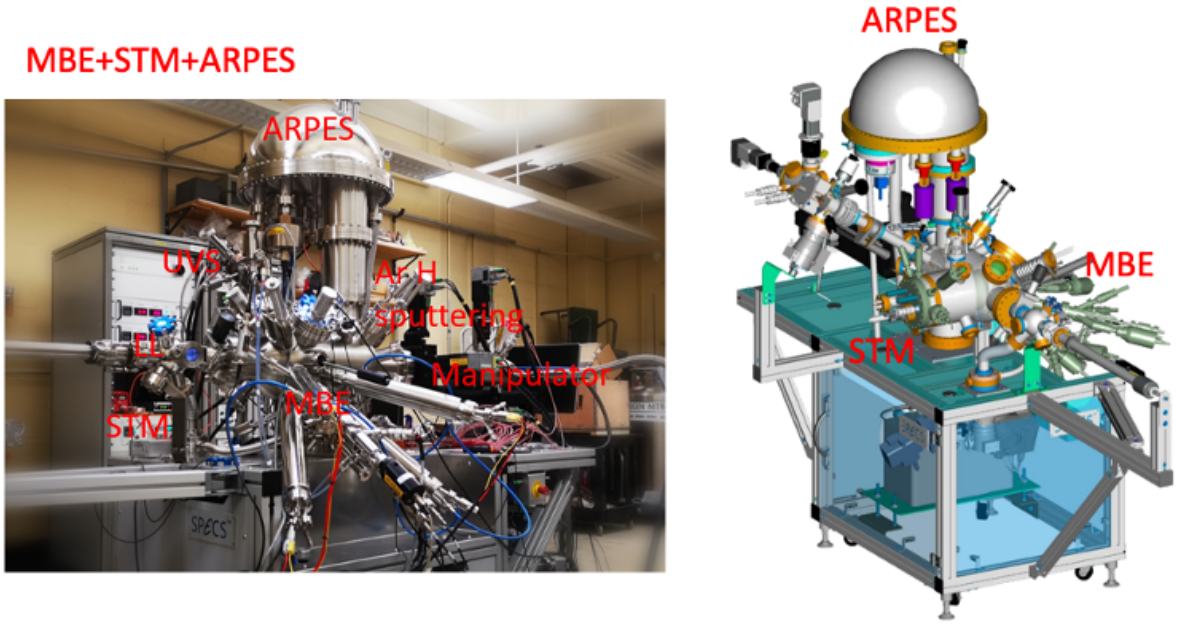

Fig. 3.1 MBE-STM-ARPES system in our lab.

3.1. Ultra-High Vacuum (UHV) systems

There are three reasons that our system needs a good vacuum condition. First, to perform an ARPES measurement, a photoelectron should be able to travel from the sample to the micro-channel plate (MCP) detector, and an electron mean free path (l) of at least 2 meters is required. According to kinetic theory, l is inversely proportional to the pressure and the scattering cross-section of the particle. l ~ 2 m thus corresponds to a vacuum better than p ~ 10^{-4} torr (1 torr = 1 mmHg = 133.3 Pa =1.333mbar =0.019psi). Second, for a reasonably long lifetime of the sample inside the chamber, the sample surface must not be covered with gas molecules too quickly. In a gas system obeying the Maxwell-Boltzmann distribution, the typical scale for particle speed is v ~ $\sqrt{pkBT/m}$. In a given time t, the number of times these molecules would hit the sample surface is given by n ~ $vts\rho$, where s is the area of the sample surface, and ρ is the density of gas molecules. Assume that all particles hitting the

surface would stick to it. The threshold pressure for the formation of a single layer of gas molecules on the sample surface within a time period t is $\rho_c \sim \sqrt{m/k_B T}/ts_0$, where s_0 is the molecule cross-section. Therefore, a sample total-loss time of 1 hour in an oxygen gas environment at T = 10 K requires a vacuum better than $p \sim 10^{-9}$ torr, which is in the range of ultrahigh vacuum. Third, in the MBE growth process, atoms or molecules require a long enough mean free path to move from the evaporator to the substrate, which also needs a UHV condition.

3.1.1 Vacuum pumps

Based on the residual pressure, vacuum condition is generally divided into three major categories: rough vacuum (ambient pressure (760 torrs) to 10^{-3} torr), high vacuum (10^{-3} to 10^{-9} torr), and ultrahigh vacuum (lower than 10^{-9} torr). Different types of pumps work in different pressure ranges and have different pumping speeds. In an operating vacuum chamber, these pumps are often arranged in series (e.g., a turbo pump backed up by a roughing pump). Ion pumps are usually directly connected to the chamber, but the chamber needs to be pre-pumped.

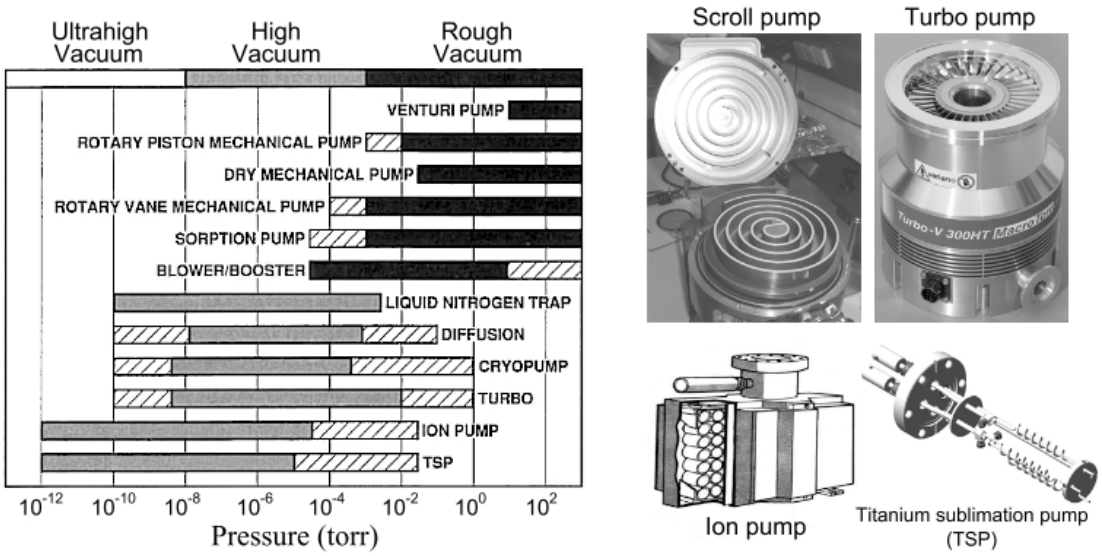

Fig. 3.2 vacuum pumps and pressure ranges. [1]

3.1.2 Vacuum gauges

Vacuum gauges are used to monitor the pressure inside a vacuum chamber. As an example, two types of gauges are used in the ARPES chamber at the Ames Laboratory: the Pirani gauge for measuring rough vacuum (10^{-3} torr to ambient pressure) in the load-lock area; and hot cathode ionization gauges (ion gauges) for measuring high to ultrahigh vacuum everywhere else. [2-5]

A routine procedure for achieving UHV in our system is as follows: First, the chamber must be made leak-tight, particularly at the joints of flanges, and the oxygen-free gas kites are used to seal at the flange. Rough and turbo pumps are connected in series and provide a high vacuum condition (10^{-5}~10^{-8} torr), then the ion pump can start the pump. In order to reach

the UHV condition, a “bakeout” process is carried out, during which the chamber is heated to ~150C for about 70 hours. In this process, most of the gas molecules that are absorbed in the chamber would be ‘pushed’ away and pumped by the ion pump. After backout, the titanium sublimation pump (TSP) is used with the ion pump to provide an even higher vacuum in the chamber.

3.2. Angle-Resolved Photoemission Spectroscopy (ARPES)

3.2.1 Principle of ARPES

Photoemission spectroscopy (PES) is a well-known technique that measures the electronic structure of a solid through the external photoelectric effect. For the PES measurement, photons excite electrons from the crystal surface by the external photoelectric effect. By fixing the energy of incident photons and observing the velocity (kinetic energy) of excited photo-electrons, it is possible to determine the density of states at a fixed binding energy of electrons in the material. [6]

Semi-classical view of the photoemission process: Three-Step Model

1. Photoexcitation of an electron inside the solid.
2. Travel of the photoelectron to the sample surface.
3. Emission of the photoelectron into the vacuum.

The electron is initially excited by absorbing a photon, in which energy conservation across the excitation is satisfied. From the observed photoelectron kinetic energy Ek,

$$E_{\mathrm{B}} = h\nu - E_k - \phi$$

where E_B is the binding energy of an electron, hν is the incident photon energy, and φ is the work function. Since hν and φ are already-known values, we can determine E_B when E_k is

identified experimentally. The PES technique is inherently surface sensitive. Figure 3.3 shows a relationship between the escape depth and the kinetic energy of photoelectrons, called the "universal curve" [7,8]. Photoelectron escape depth varies according to the energy of the photoelectrons, while it also depends on the dielectric function of the material. The escape depth of photoelectrons for the kinetic energy of 20~100 eV is only 5~10 Å. Therefore, special attention is necessary to the surface condition of the sample.

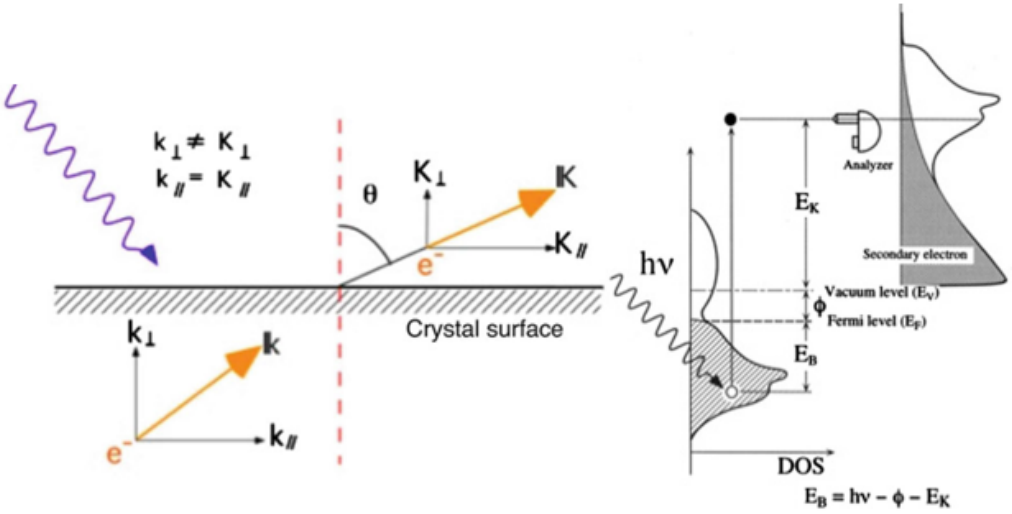

Fig. 3.3 3steps model and the photo-excitation process [7]

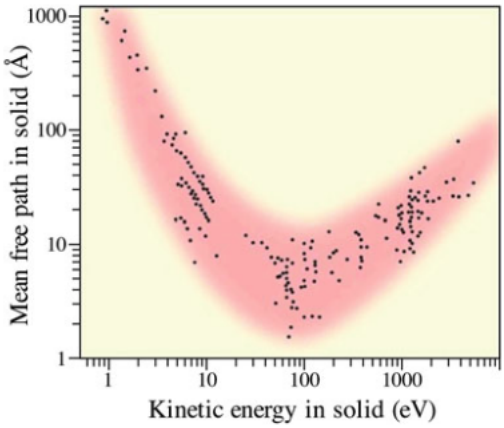

Fig. 3.4 Escape depth of electrons as a function of electron kinetic energy in a solid. [8]

In the ARPES, an initial momentum k is given by the emission polar angle θ (measured from the surface normal). The momentum of an exciting photoelectron in a crystal is expressed as the surface parallel component $\hbar k_{//}$ and the perpendicular component $\hbar k_{\perp}$. After the photoelectron is emitted from the crystal to a vacuum, the momentum is expressed as the parallel $\hbar K_{//}$ and the perpendicular $\hbar K_{\perp}$ component, respectively. The momentum of exiting electrons from a sample is altered by the crystal potential at the surface. However, the parallel component $\hbar k_{//}$ is conserved owing to the translation symmetry of the crystal surface.

$$\hbar k_{\parallel} = \hbar K_{\parallel}$$

On the other hand, the energy of photoelectrons emitted to a vacuum is given by

$$E_k = \frac{(\hbar K)^2}{2m}$$

where m is an electron mass.

$$k_{\parallel} = \frac{\sqrt{2m(h\nu - \phi - E_B)}}{\hbar}\sin\theta$$

$$\text{Or } k_{\parallel}(\text{Å}^{-1}) = 0.5123\sqrt{E_k(eV)}sin\theta$$

When the final state of the electron is assumed as the free electron, the perpendicular component $k_{\perp}$ is not conserved.

$$k_{\perp} = \frac{\sqrt{2m(h\nu - \phi - E_B)\cos^2\theta + U_0}}{\hbar}$$

where U_0 is a variable called "inner potential". Typically it is defined as the energy of the valence band bottom [9]. However, the $k_{\perp}$ value has a finite width ($\Delta k_{\perp}$) because the escape

depth of photoelectron Δz is very short. From the uncertainty principle, Due to the effect, which is called "final-state broadening" [10], the $K_{\perp}$ component in the final state also has a finite width. In the case of a 2D state like the surface, the interface, and the layered materials such as graphene, it is possible to ignore $k_{\perp}$.

3.2.2 Theory of photoemission process and matrix element effect

Here, the wave function of the initial state can be written in the form of a Slater determinant as,

$$\Psi_i^N = C\phi_i^{\mathbf{k}}\Psi_i^{N-1},$$

where ϕ_i^k is the orbital with momentum k from which the electron is excited, Ψ_i^{N-1} is the wave function of the remaining (N-1) electrons, and C is the operator that antisymmetrizes the wave function. The wave function of the final state under the sudden approximation can be written as a product of the wavefunction of the photoemitted electron ϕ_i^k and that of the remaining (N-1) electrons Ψ_i^{N-1},

$$\Psi_f^N = C\phi_f^{\mathbf{k}}\Psi_f^{N-1},$$

Therefore, the matrix element is obtained as

$$\left\langle \Psi_f^N \middle| H_{\text{int}} \middle| \Psi_i^N \right\rangle = M_{f,i}^{\mathbf{k}} \left\langle \Psi_f^{N-1} \middle| \Psi_i^{N-1} \right\rangle,$$

where $M_{f,i}^k$ is the one-electron matrix element, and the second term is the (N-1)-electron overlap integral. In the first step of evaluating the overlap integral, one can assume that the remaining orbitals are the same in the final state as they were in the initial state (frozen-orbital approximation), meaning that $\Psi_f^{N-1}=\Psi_i^{N-1}$,. This renders the overlap integral unity,

and the transition matrix element is just the one-electron matrix element. Under this assumption, the photoemission experiment probes only the one-electron state (from ϕ_i^k to ϕ_f^k), which does not interact with the remainder of the (N-1) electrons. Of course, this cannot be a very good approximation. In reality, this simple picture breaks down because the excitation of an electron from ϕ_i^k disturbs the remaining (N-1) electrons. The remaining system will readjust itself in such a way as to minimize its energy (relaxation). We now assume that the final state with (N-1) electrons have many possible excited states (labeled by s) with the wave function $\Psi_{f,i}^{N-1}$,. and energy E_s^{N-1}. Therefore, the total photoemission intensity measured as a function of electron kinetic energy at a momentum k is

$$I(\mathbf{k}, E_{\text{kin}}) = \sum_{f,i} \left| M_{f,i}^{\mathbf{k}} \right|^2 \sum_s \left| c_s \right|^2 \delta(E_K + E_s^{N-1} - E_i^N - h\nu),$$

We can see that most of the factors in the photoemission process, such as the polarization of the light, and the different reactions of different orbits, are all hidden in the matrix element. Let us consider the photoemission of an electron from a d-orbital (as in the case of the iron pnictides), whose shapes are depicted in Figure 3.5. Assume that the photon comes along the y-z plane and the detector also locates at this plane (mirror plane). In order to have nonvanishing photoemission intensity, $\langle \phi_f(\mathrm{k}) \mid e_r \cdot x \mid \phi_i(\mathrm{k}) \rangle$ has to be an even function under reflection with respect to the mirror plane. where er is a unit vector along the polarization direction of the vector potential in our approximation, electron final states are plane waves, i.e., $\langle \phi_f(\mathrm{k})|$ is always an even function. Therefore there are two possibilities. (1) Electrons are emitted from an odd orbital, e.g., d_{xz} or d_{xy}. In this case, the e_r has to be an odd function with respect to the mirror plane, i.e., perpendicular to the mirror plane. (2)

Electrons are emitted from an even orbital, e.g., d_{yz}, $d_{x2-y2,}$ or d_{z2}. In this case, e_r has to be along the mirror plane.

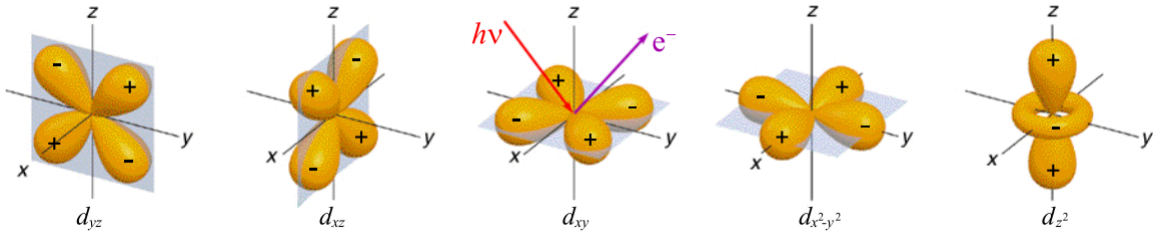

Fig. 3.5 The shapes and parity of the d-orbitals. [11]

3.3. A setup of ARPES systems

An ARPES system contains a light source, a sample stage, and an electron detector. For a light source or photo source, the commonly used types are gas discharge lamps, the synchrotron radiation source, and the laser light source. The gas discharge lamp is discussed in section 3.3.1. A sample stage usually has the ability to finely control the sample position (x, y, z) and rotate the sample in the polar axis (along x), azimuthal axis (along z), and the perpendicular polar axis (along y). A sample stage can usually also cool down the sample or heat up the sample. The last but the most important part of an ARPES system is an electron detector. Here a hemisphere electron analyzer is discussed in 3.3.2.

3.3.1 Gas discharge light source

Gas-discharge lamps are a family of artificial light sources that generate light by sending an electrical discharge through an ionized gas, i.e., plasma. In operation, the gas atoms are first ionized (excited to a quantum state with higher energy) by external means like high voltage

electro-sparks or collision with existing gas ions. In the subsequent relaxation process to the ground state, a photon with frequency characterized by the gas atom is emitted. In ARPES, these photons must have an energy higher than the work function ($\varphi = 2 \sim 5$ eV) to be able to generate photoelectrons, i.e., they are ultraviolet (UV) photons. The most commonly used lamps are the helium lamp, the xenon lamp, and so on. Below we use the helium lamp (routinely used in the present thesis) as an example to explain the principle and typical composition of a gas discharge lamp.

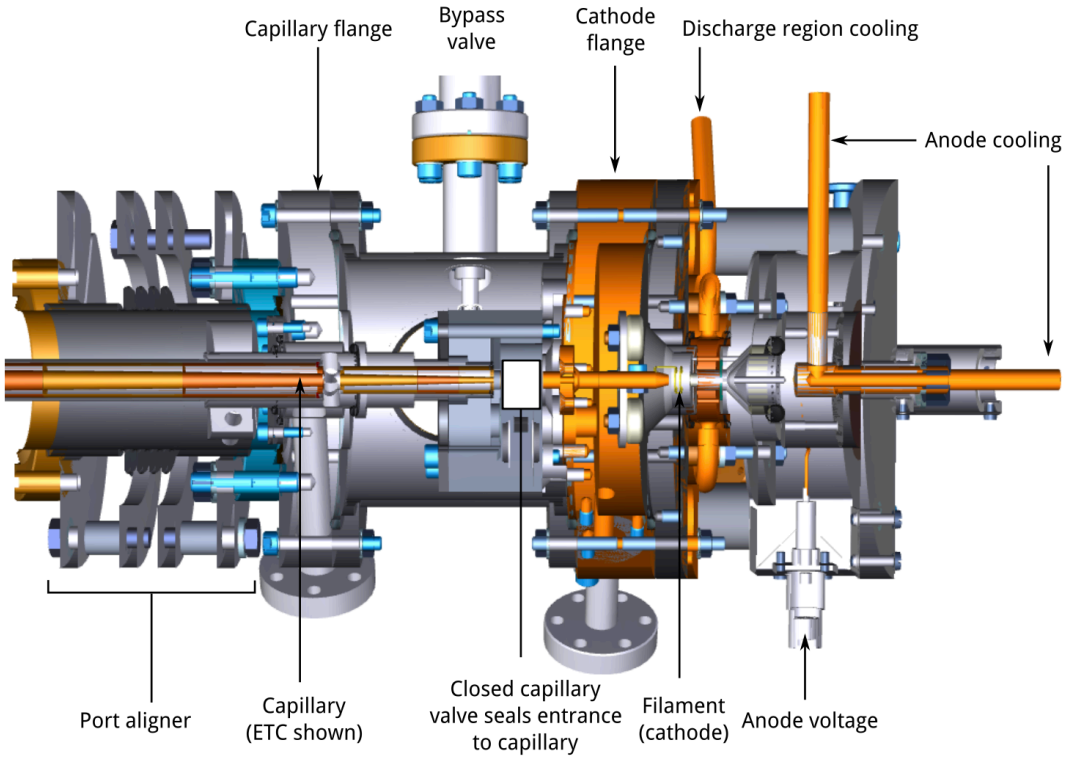

Fig. 3.6 Cross view of a helium lamp. [12]

Figure 3.6 shows the components of a typical helium lamp used in ARPES experiments. In this setup, the helium plasma is generated by electron cyclotron resonance due to external

microwave radiation. When helium gas is imported into the plasma discharge area, gas discharge is initiated by high-voltage electric sparks generated at the UV source head and the filament. More helium atoms are subsequently ionized due to collisions with existing seed ions. Using this electron cyclotron resonance technique, a total UV flux as high as 2×10^{16} photons/(s) can be obtained. The helium emission spectrum contains three major photon wavelengths functional for photoemission: the He I_α line (584 Å or 21.218 eV, ~ 82%), the He I_β line (537 Å or 23.08 eV, ~ 8%), and the He II_α line (304 Å or 40.814 eV, > 10%). Since the He I_β line is shadowed by the intense He I_α line, we normally use the He I_α and He II_α lines for the experiment. After leaving the plasma cavity, photons enter a monochromator chamber in which different wavelengths are selected. In the case of a helium lamp, this monochromatic process is optional since it will greatly reduce the photon intensity, and the He I_α line is separated sufficiently in energy from the He II_α line that the spectra from those lines will not substantially overlap in most cases even without the monochromator. On the other hand, one obtains a higher signal-to-background ratio, reduces the photon spot size, and prevents helium gas from leaking into the main chamber by using the monochromator. After the monochromator, the photons exit the photon source package via an exit capillary. The resulting beam has a typical dimension of a millimeter or so. The beam dimension is about 1 mm along the long axis of the elliptical bright spot. One of the most important advantages of using a gas discharge lamp as a photon source is the availability of large photon flux at ~ 1 meV bandwidth and unlimited machine time.

3.3.2 Hemisphere electron analyzer

Selected photoelectrons enter the hemispheric electron analyzer after traveling through the vacuum chamber. In this section, we intend to discuss the basic operating principles of the electron analyzer optimized for ARPES studies. In operation, the entire analyzer should also be kept under an ultrahigh vacuum, and the analyzer consists of two major parts: the electrostatic lens and the hemispheric capacitor.

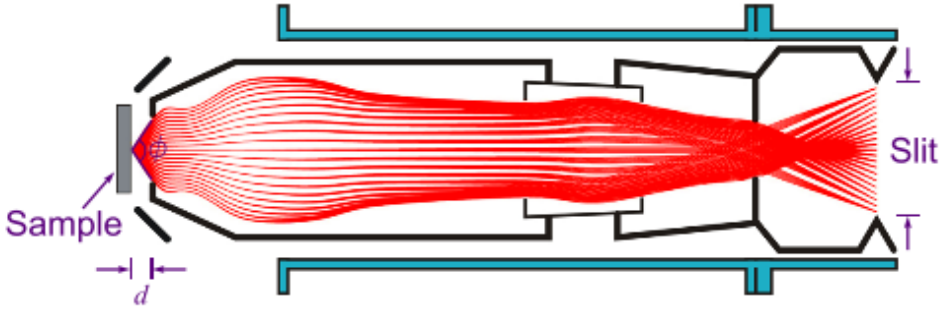

Figure **3.7** Schematics of the electrostatic lens setup. d is the working distance, φ is the acceptance angle of the analyzer. Red curves show the calculated electron trajectories for photoelectrons emitted from different angles or from the same angle with different energies.

The electrostatic lens portion of an analyzer maps the emitting angle of the photoelectrons onto different positions at the plane of the analyzer slit. After being emitted from the sample, photoelectrons enter the electron analyzer through a circular opening at the beginning of the electrostatic lenses (shown in Figure 3.7). The diameter of the circular opening and its distance from the sample (working distance d) define the acceptance angle φ of the analyzer, which in turn gives the maximum k range in the raw data. There are usually 3 or 4 lens

elements in total. [13] In what is called the "angular mode," these lenses work similarly to a regular concave lens in optics: at the focal plane of the lens set (slit plane), electrons emitted at different angles are focused to different locations, creating a one-to-one mapping from the real space to the reciprocal space. Modern analyzers also include the option of the "transmission mode", which gives information on the real space distribution: electrons that come from different parts of the sample are focused on different locations at the slit plane. The transmission mode is often used in ARPES experiments to accurately locate the sample with respect to the analyzer. It should be noted that even electrons emitting at the same angle will have different energies due to the intrinsic electronic structure.

The analyzer slit is located between the electrostatic lens and the hemispheric capacitor. The length of the slit determines the maximum k-range, whereas the width of the slit controls the electron intensity, energy, and lateral momentum resolutions of the analyzer (discussed later). In a Phobious 150 analyzer, one can choose the slit width from 0.1 mm to 2 mm. This is done by manually tuning a knob at the back of the hemispheric capacitor.

After entering the hemispheric capacitor, electrons with different energies travel along different paths due to the voltage difference between the inner and outer hemispheric plane. As shown by the red and green curves in the left panel of Figure 3.8, electrons with lower kinetic energies bend more severely by the capacitor, ending up at locations closer to the inner sphere on the MCP/CCD screen. On the other hand, electrons with higher kinetic energies end up at locations closer to the outer sphere. By this means, the axis of energy is created. A second requirement of the hemispheric capacitor is that electrons with different k but the same E_k must travel along a plane to the MCP/CCD screen that is perpendicular to

the E-axis. As shown by the yellow and blue curves in the same panel, this is done in a reversed fashion: electrons that come from the right side (top) of the slit travel to the left side (bottom) of the screen and vice versa. The "straightness" of the k-axis depends on the shape of the analyzer slit. Before a real experiment, detailed calibration must be done to determine exactly how the k-axis is curved (or simply how the chemical potential is shifted with different k's).

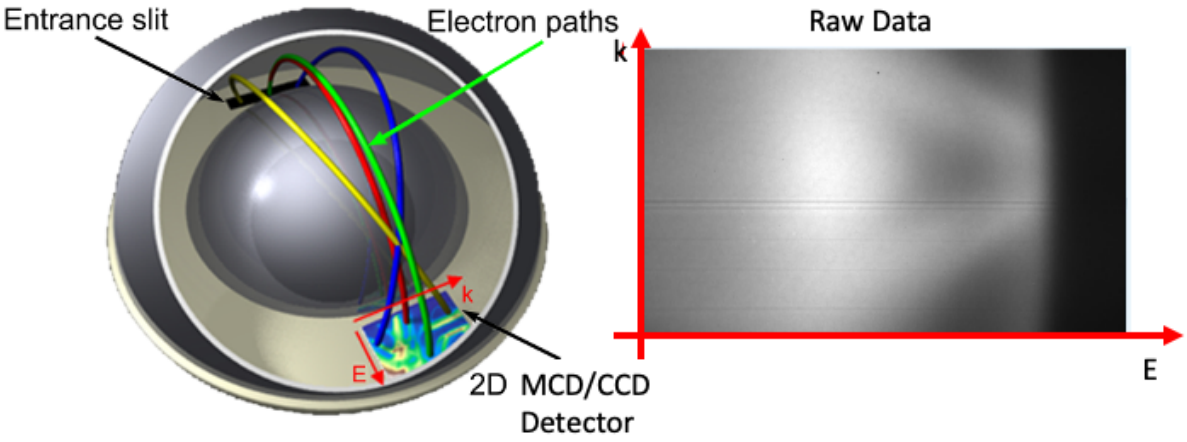

Fig. 3.8 Left: Schematics of a hemispheric capacitor and several electron paths. Yellow and blue curves denote two trajectories for electrons with the same energy but different k; Red and green curves denote two trajectories for electrons with different energies but the same k. From [57]. Right: Raw data at the MCP screen. The horizontal and vertical axes are E and k, respectively.

The final destination of the photoelectrons is the micro-channel plate (MCP) detector located at the opposite end of the hemispheric capacitor. A micro-channel plate is a slab with a regular array of tiny tubes or slots (microchannels) leading from one face to the opposite, densely distributed over the whole surface. Each microchannel works as a usual electron

multiplier, in which the number of electrons is multiplied by an electric-field-driven secondary emission process. The voltage across the MCP is generally > 1400 V. After the MCP, electrons hit a florescent phosphor screen, and images are collected by a high-speed CCD camera. A typical image of the CCD camera is shown in the right panel of Figure 3.8. It is interesting to notice that such a camera image (not even the raw data) already shows the band structure of the detected material: the brighter "band" in the image is actually an energy band in the sample, and the sudden drop of overall intensity at roughly the middle of the image comes from the Fermi cut-off.

Now we introduce the concept of pass energy which generally determines the overall transmission and the energy resolution of an electron analyzer. A measurement with pass energy E_{pass} (unit eV) is such that the electrons traveling to the central vertical line of the MCP detector have kinetic energy PE. Note that this energy is not the original kinetic energy of the photo-electrons. Photoelectrons undergo accelerating/decelerating processes within the electrostatic lens, yielding a certain range of energies with which electrons are allowed to pass through the analyzer slit. This energy range is centered at the pass energy, its width depending on the pass energy. For example, in the setting of Pass Energy 5 (PE = 5 eV) the energy range is $4.84 < E < 5.16$ eV, and the width of the energy range is 0.32 eV. Since the pixel number in the MCP is fixed, we expect a measurement of higher pass energy to have higher intensity and lower energy resolution.

Another factor that affects the intensity and the energy resolution is the slit size. The bigger the slit, the higher the number of transmitted electrons. However, in the bigger slit settings, some electrons with slightly different k's would end up in the same k-channel in the MCP

detector, rendering a lower k and E resolution. As a result, the energy resolution of an ARPES experiment is a monotonic but non-linear function of the pass energy and the slit size. The momentum resolution, on the other hand, is better defined by the ratio between the acceptance angle and the number of k-channels in the MCP.

3.3.3 Fermi-surface mapping

After confirming the quality of a sample using a single ARPES map, a common next step is to map the Fermi surface of the sample, i.e., construct a k_x-k_y-E map out of a large number of ARPES maps with different inclining angle θ (shown in the upper right panel of Fig. 3.9). In order to do this, the analyzer should be arranged such that the entrance slit (with acceptance angle φ) is perpendicular to the scanning direction. By taking consecutive ARPES maps at a series of θ angles, we obtain a three-dimensional data set with axes θ, φ, and E (See Figure 3.9). Since a fixed incoming photon energy defines a spherical surface in the k-space, such a φ-θ map covers a spherical region. The Fermi maps presented in this thesis are projections of the spherical region onto the k_x-k_y plane (Figure 3.9). As a result, the conversion from φ-θ values to k_x-k_y values requires the usage of the three Euler angles θ, φ, and ψ, which are defined as the angles for each individual data point.

3.3.4 k_z mapping

For a material whose bands are dispersive along the axis perpendicular to the cleaving plane ($k_\perp$ or k_z), the shape of the Fermi surface will depend on incoming photon energies. That is because, for different photon energies, the mapping region of the k-space intersects differently with the underlying electronic structure. Ideally, one would like to have a set of

ARPES Fermi maps for consecutive photon energies. In this way, a full three-dimensional Fermi map, as well as a full four-dimensional electronic structure (k_x, k_y, k_z, E) can be constructed. Since this procedure requires considerable machine time, a more feasible way is to make a "k_z dispersion map" by changing the photon energy while maintaining the θ angle (Figure 3.9 lower right) at a high symmetry axis. Figure 3.9 shows the principle and an example of such a map. By fixing the θ angle of the analyzer and varying the photon energy, a sector-shaped k_x-k_z cross-section of the k-space is measured. This schematic also explains the energy dependence of the momentum resolution. Since the pixel number is fixed, the higher the photon energy (hence the wider the detection range), the worse the k-resolution. On the other hand, we can find the real ARPES data of certain energy is a sphere, so we should be careful that the k_z would be slightly different for the bands coming from different binding energy.

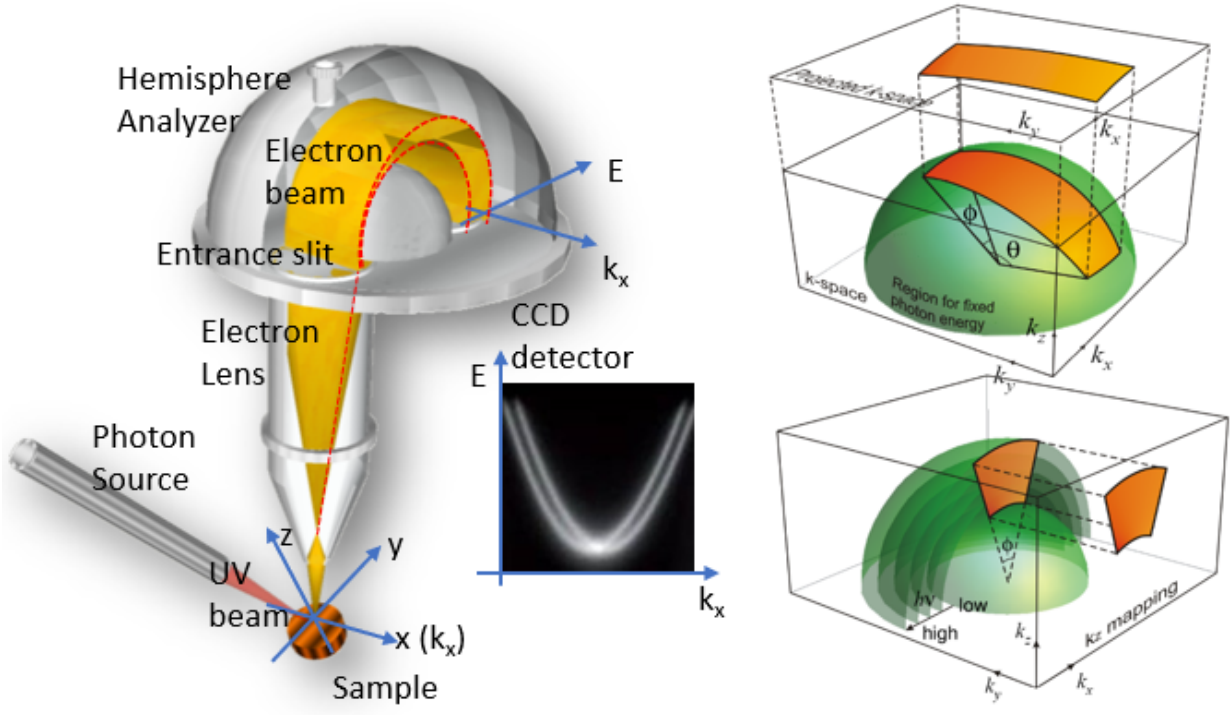

Fig. 3.9 ARPES measurement process (left), Fermi-surface mapping (upper right), and the k_z mapping(bottom right).

3.4. Spin resolved ARPES measurement

For the electron spin-polarization measurements, many kinds of spin detectors have been developed utilizing various spin-dependent scattering processes, as shown in the following Table. Common characteristics of these detectors are to use heavy elements as a target like gold (Au) and tungsten (W) owing to their large spin-orbit coupling (SOC). Recently, a spin detector that utilizes the spin exchange interaction has also been developed. Among them, the Mott detector is one of the widely used, and the principles of other spin detectors are

similar to the Mott detector. The principles and the detail of the Mott detector are introduced in this section. [15-20]

Method	Interaction	Operation voltage	S_{eff}	Figure of merit	Target
Mott	Spin-orbit	20–100 kV	0.1–0.2	$1–5 \times 10^{-4}$	Au thin film
SPLEED	Spin-orbit	150 V	0.2–0.3	$1–2 \times 10^{-4}$	W single crystal
Diffuse scattering	Spin-orbit	150 V	~0.2	$\sim 1 \times 10^{-4}$	Au thin film
VLEED	Spin-exchange	6–10 V	0.3–0.4	$\sim 10^{-2}$	Fe single crystal

3.4.1 Principle of the Mott Scattering

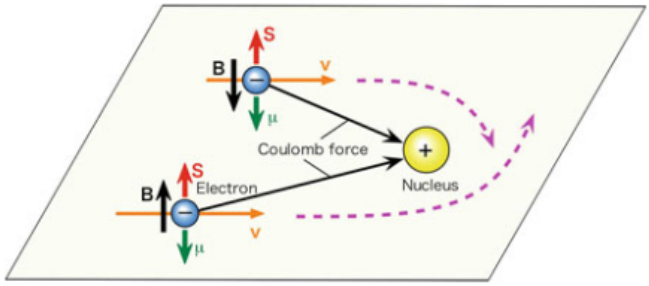

Fig. 3.10 Mott scattering process, electron experiences electric and magnetic field by scattering to a nucleus.

The asymmetry of the spin polarization in the Mott scattering arises from SOC between the electron and the nucleus. Mott spin detector is based on this scattering [16]. As seen in Fig. 3.10, in the electron's rest frame, the positively charged nucleus looks to move toward the

electron, and an effective magnetic field B is generated at the position of the electron. The magnetic field is given by

$$\mathbf{B} = -\frac{1}{c}\mathbf{v} \times \mathbf{E} = \frac{Ze}{cr^3}\mathbf{r} \times \mathbf{v} = \frac{Ze}{mcr^3}\mathbf{L}$$

Where **v** is the velocity of the electron, **r** is the distance between the electron and the nucleus, and Z is the atomic number of the nucleus. The electron orbital angular momentum about the nucleus **L** and the electric field of the nucleus **E** is given by

$$\mathbf{E} = \left(Ze/r^3\right)\mathbf{r}$$

$$\mathbf{L} = m\mathbf{r} \times \mathbf{v}$$

The magnetic moment of an electron μ_e is defined as

$$\mu_e = -\frac{g_s e}{2mc}\mathbf{S}$$

where g_s is the gyromagnetic ratio ($g_s \approx 2$), it means that; when an electron has an upward spin perpendicular to the orbital plane, μ_e points to the downward direction. Here we take into account spin precession, and the potential by the SOC (V_{LS}) that arises from the interaction between the electron magnetic moment and the B of the nucleus, as given by

$$V_{LS} = -\mu_e \cdot \mathbf{B} = \frac{Ze^2}{2m^2c^2r^3}\mathbf{L} \cdot \mathbf{S}$$

The sign of the V_{LS} is determined by whether S and L are aligned or anti-aligned. The SOC becomes the maximum when the spin direction is perpendicular to the orbital plane. It is indicated that the upward (downward) spin is easy to be scattered toward the right (left) way. In addition, V_{LS} becomes larger as the Z is larger and the **v** is faster so that the Mott detector

makes the electron collide with a target prepared by a heavy element such as Au at high speed (voltage).

Now we consider the system in Fig. 3.11a. The electron beam strikes the Au target by high voltage. Depending on the scattering angle, the differential scattering cross section σ(θ) also shows an asymmetry. σ(θ) is given by

$$\sigma(\theta) = I_0(\theta) \cdot (1 + S(\theta)\mathbf{P} \cdot \hat{\mathbf{n}})$$

Where $I_0(\theta)$ is the differential scattering cross section for an unpolarized electron beam, **P** is the polarization vector of incident electrons, $\hat{n}$ is the unit vector normal to a scattering plane, and S(θ) is the Sherman function. We notice that a vertical spin component to a scattering plane only contributes to the σ(θ). Scattering asymmetry, A(θ) is defined by the differential scattering cross section for up and down spin $\sigma \uparrow (\theta)$, $\sigma \downarrow (\theta)$

$$A(\theta) \equiv \frac{\sigma_\uparrow(\theta) - \sigma_\downarrow(\theta)}{\sigma_\uparrow(\theta) + \sigma_\downarrow(\theta)} = PS(\theta)$$

As shown in Fig. 3.11b, σ(θ) and A(θ) depend on the scattering angle, and they have a maximum value at θ = 120° [17]. S(θ) also becomes the maximum at θ = 120°. However, the S(θ) value strongly depends on the incident electron energy and Z of the target material (Fig. 3.11c, d). The absolute value of S(θ) becomes larger as Z becomes larger and v becomes faster. Since the up spin is scattered toward the −θ side and the down spin toward the +θ side, we need a pair of electron detectors that are set to ±120°.

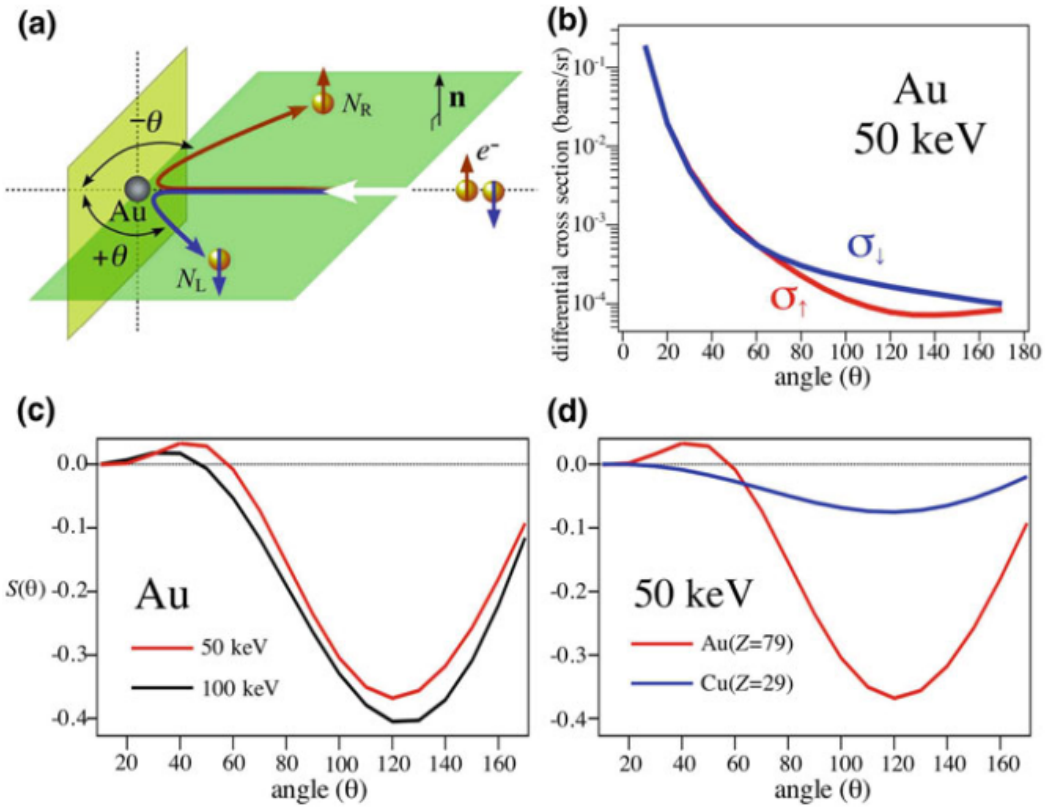

Fig. 3.11 a Schematic view of electron spin scattering for heavy atom. **b** Cross section for gold as a function of the back-scattering angle at 50 keV. **c, d** Energy and atomic-number dependence of the Sherman function, respectively [17]

3.4.2 Mott Detector

A traditional Mott detector utilizes incident electrons with high energy (~30 keV) to enhance the scattering asymmetry. Figure 3.12 shows a schematic view of the Mott detector. In this type of Mott detector, energy-reduced electrons by multiple scattering are excluded by the retarding potential. A Mott detector usually has two-pair electron detectors, such as a channeltron, in order to observe spin for two axes. Lens elements are built into the Mott detector to make a focused electron beam onto the target. Au (Z = 79) is widely used as a

target material owing to its high stability. A thin film target is used to reduce multiple and plural scatterings, which reduces the scattering asymmetry. Taking account into the multiple scatterings, the Sherman function is replaced with an "effective Sherman function S_{eff}". The value of S_{eff} is specific to each instrument. The absolute value of $S_{eff}(\theta)$ is smaller than the $S(\theta)$, while the variation of $S_{eff}(\theta)$ near 120° is milder than $S(\theta)$. The Mott detector is usually installed parallel to the MDC/CCD detector and connected to the hemisphere detector. So, after a general ARPES measurement, we can easily switch to the Mott detector and direct measure the spin polarization at the certain k position, the electron energy can be measured by the hemisphere detector, but the angular resolution is lost during the spin measurement. The electron used for the spin measurement comes from the center of the MDC detector or 0 degree, so in order to get momentum information, we have to rotate the sample and measure different EDC lines.

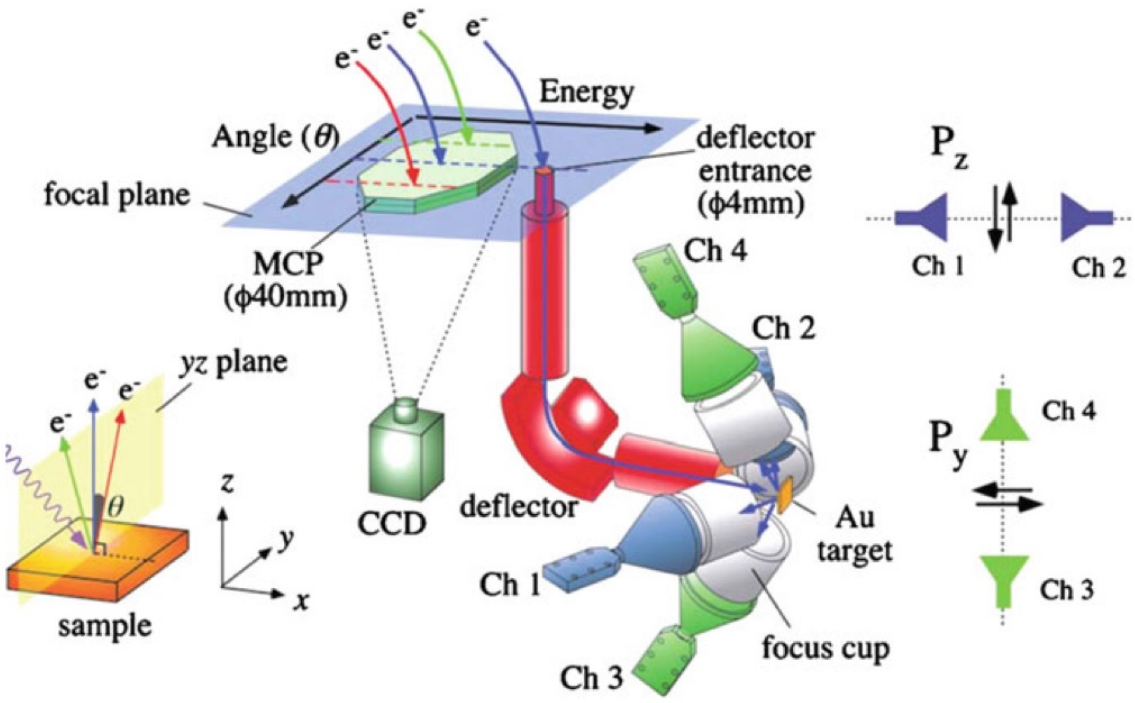

Fig. 3.12. Schematic drawing of the process of the spin measurement. An MCP/MDC and an entrance hole of the spin detector are located closer to the inner and outer spheres. [18]

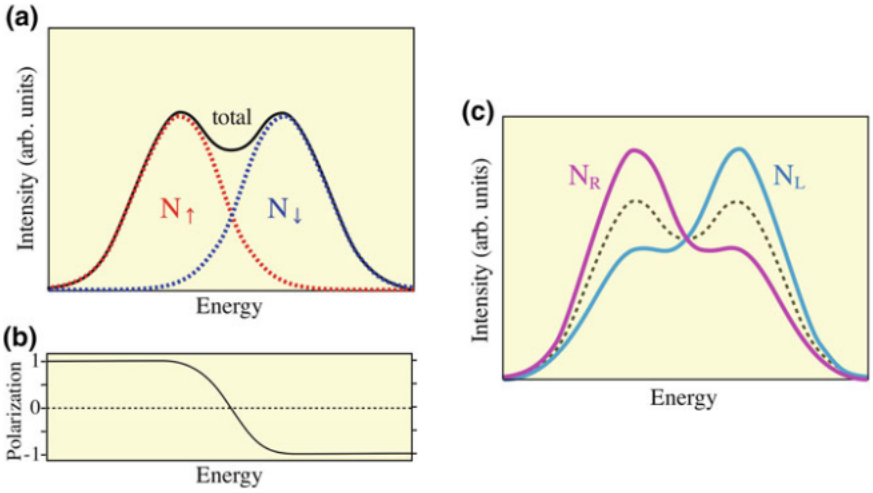

Fig. 3.13 Procedure to extract the spin-resolved spectra from the experimentally observed data. **a** N ↑ and N ↓ are intrinsic spin-polarized spectra. A solid line (Total) is a spin-integrated photoemission spectrum. **b** Spin polarization as a function of energy in **a. c** Spectra for S_{eff} = 0.3 determined from the spin-resolved photoemission experiment. [17]

Figure 3.12 and Figure 3.13 illustrates the process of spin measurement. Here the number of up or down spins is expressed as N ↑ , N ↓ respectively, and the "total" spectrum is given by N ↑ + N ↓ . As displayed in Fig. 3.13b, the spin polarization P range is $-1 \leqslant P \leqslant 1$. N_L (N_R) denotes the intensity measured in the left (right) channeltron detector at angle θ (−θ).

$$N_L = N_\uparrow I_0(\theta)(1 + S_{eff}(\theta)) + N_\downarrow I_0(\theta)(1 - S_{eff}(\theta))$$

$$N_R = N_\uparrow I_0(\theta)(1 - S_{eff}(\theta)) + N_\downarrow I_0(\theta)(1 + S_{eff}(\theta))$$

This represents the experimentally obtained spin-resolved spectra (Fig. 3.12c). Next, we calculate "$N_L + N_R$" and "$N_L - N_R$" :

$$N_{\mathrm{L}} + N_{\mathrm{R}} = 2I_0(\theta)(N_{\uparrow} + N_{\downarrow})$$

$$N_{\mathrm{L}} - N_{\mathrm{R}} = 2I_0(\theta)S_{eff}(\theta)(N_{\uparrow} - N_{\downarrow})$$

Here, P and A(θ) are defined as

$$P = \frac{N_{\uparrow} - N_{\downarrow}}{N_{\uparrow} + N_{\downarrow}}$$

$$A(\theta) = \frac{N_L - N_R}{N_L + N_R}$$

$$A(\theta) = \frac{N_L - N_R}{N_L + N_R} = \frac{N_{\uparrow} - N_{\downarrow}}{N_{\uparrow} + N_{\downarrow}} S_{eff}(\theta) \equiv PS_{eff}(\theta)$$

Thus, if the $S_{eff}(\theta)$ is known and the asymmetry is measured, the polarization can be calculated; therefore, it is essential to determine an accurate S_{eff} value of the Mott detector prior to the experiment.

3.5. Molecular beam epitaxy (MBE)

The thin films synthesized in this thesis research are produced by molecular beam epitaxy (MBE), a process in which sample layers are deposited epitaxially on a substrate in an ultra-high-vacuum (UHV) chamber. The principle behind the method is simple: a substance such as Bi or Sb is heated up in quasi-Knudsen effusion cells or electron-beam evaporators (EBE), it evaporates, and the vapor-deposited on a substrate such as Graphene. The substrate usually is a single crystal so that the crystallized surface can help the film grow as a single crystal.

A schematic diagram of our MBE system is shown in Fig. 3.14 [6]. A crucible containing high-purity materials is to be evaporated, and the evaporated molecules or atoms are bombarded to the sample surface. Evaporated atoms do not interact with each other or vacuum-chamber gases until they reach the wafer due to the long mean free paths of the atoms, which are protected by the UHV condition. The deposition rate is controlled by the temperature of the evaporate sources or the filament current and voltage of the EBE. The actual deposition rate is calibrated by a water-cooled crystal thickness monitor. The thickness monitor calibrates the deposition rate by monitoring the change in the oscillation frequency of a quartz crystal as a result of its mass change from the deposition.

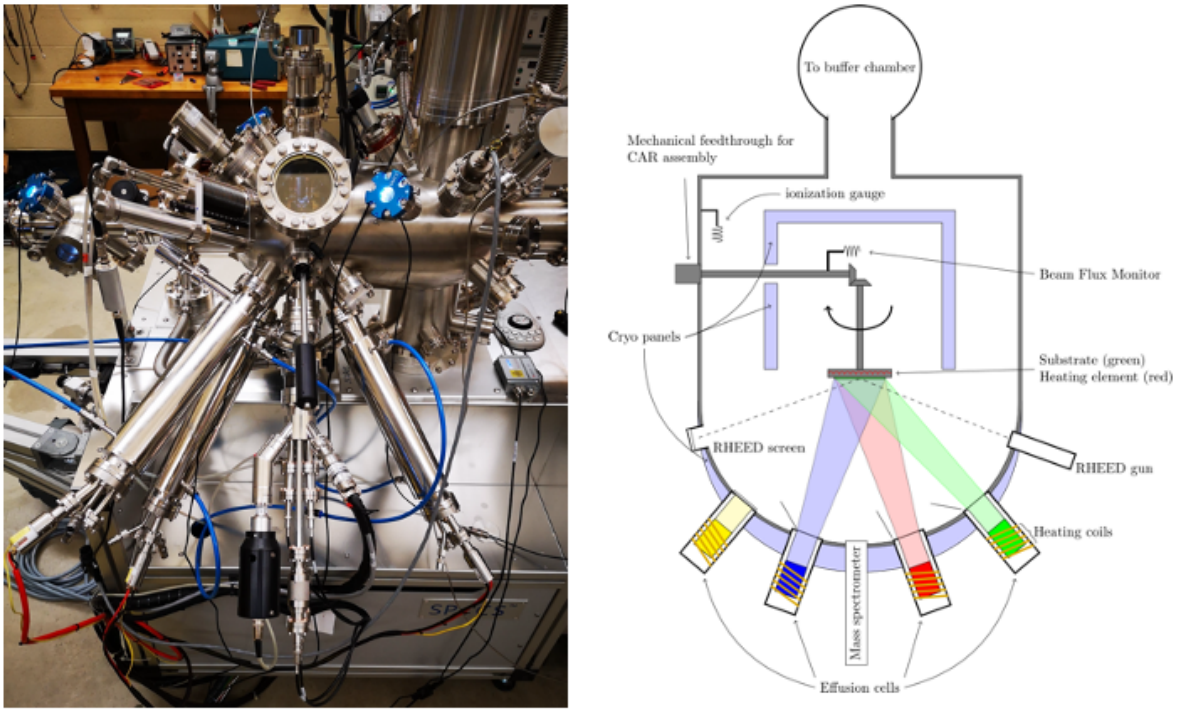

Fig. 3.14 MBE system on our chamber and a schematic diagram of MBE system.

3.6. Scanning tunning microscope (STM)

The scanning tunneling microscope (STM) is arguably the most powerful tool to directly study the electronic structure of material systems with atomic resolution. STMs can reach the resolution of sub-Angstrom lateral resolution and pm depth resolutions. With this resolution, individual atoms within materials are routinely imaged and manipulated. The STM can be used not only in ultra-high vacuum(UHV) but also in water and various other liquid or gas ambient, and at temperatures ranging from near zero Kelvin to a few hundred degrees Celsius. STMs work basically based on the tunning current, which is affected by the bias voltage and the local density of states(LDOS) of the sample. In other words, STM doesn't measure the topography but measure the surface electron states distribution.

3.6.1 Tunning current

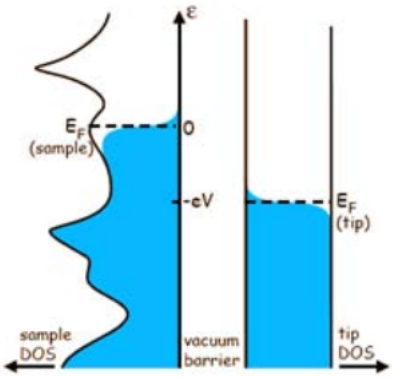

Fig. 3.15 Schematics of the electronic states of the sample-tip junction. Energy is shown on the vertical axis, and the density of states is on the horizontal axis. A negative bias is applied to the sample. As a result, the two Fermi levels are different by the amount of applied voltage (-eV). Filled states are shown in blue. Electrons from the sample, with their energy range between -eV and zero, can tunnel into the tip. [22]

Herein, we examine the case of tunneling in one dimension and consider two separate subsystems of the tip and the sample, where the electronic states can be found by using the time-independent Schr¨odinger equation. To calculate the rate of transfer of electrons from one system to the other, we can use the time-dependent perturbation theory[22] and show that the amplitude of the electron transfer is determined by the overlap of the surface wavefunctions of the two systems.

$$w_{\mu\nu} = \frac{4\pi^2}{h} \mid M_{\mu\nu} \mid^2 \delta(E_\nu - E_\mu),$$

where matrix elements are given by

$$M_{\mu\nu} = \frac{-h^2}{2m} \int (\bar{\chi}_\nu \bigtriangledown \psi_\mu - \psi_\mu \bigtriangledown \bar{\chi}_\nu).dS$$

Here, ψ and χ are the wavefunctions of the sample and the tip. To decipher useful information from STM experiments, some simplifying assumptions are commonly to be used. The matrix elements are usually assumed to be constant and not change from one energy level to the other. Since most of the tips used are metallic, the density of the states of the tip is fixed. Given the fact that experiments are usually carried out at 4 Kelvin, the Fermi distribution function can be replaced by a Heaviside step function.

To decipher useful information from STM experiments, some simplifying assumptions are commonly to be used. The matrix elements are usually assumed to be constant and not change from one energy level to the other. Since most of the tips used are metallic, the density of the states of the tip is fixed. Given the fact that experiments are usually carried out at very low temperatures (4 Kelvin), the Fermi distribution function can be replaced by a Heaviside step function. After applying these assumptions, the last equation becomes:

$$I \approx \frac{8\pi^2 e}{h} \mid M \mid^2 \rho_T(0) \int_0^{eV} \rho_S(\epsilon) d\epsilon.$$

Furthermore, we can approximate the vacuum potential barrier with a square and conclude that the wave functions decay exponentially inside this vacuum barrier. The simplified problem of finding the probability of tunneling through a square of width z_0, and the potential height of V_0, is a solvable one, and the final answer is:

$$I \propto e^{-z_0 \sqrt{\frac{8mV_0}{\hbar^2}}} \int_0^{eV} \rho_S(\epsilon) d\epsilon.$$

We can find that the tunning current is prepotential to the integral of the density states. In STM, a tunneling current is maintained between a sharp metallic tip and a sample, while the tip is held in the angstrom range above the sample. To achieve the desired control over its position, the tip is placed on a piezoelectric tube, which can extend or contract in response to an applied voltage. The piezoelectric material provides an essential ingredient for STM, namely the ability to move the sample and the tip with angstrom accuracy. There are four electrodes connected to the four quadrants of the piezoelectric tube, and by applying voltages to the different quadrants, the tube can be bent or made to vary in length (Fig. 3.16). By electrically biasing the sample with respect to the tip, electrons will tunnel into the empty states of the sample in the case of positive bias and tunnel from the occupied states of the sample to the tip in the case of negative bias. [23]

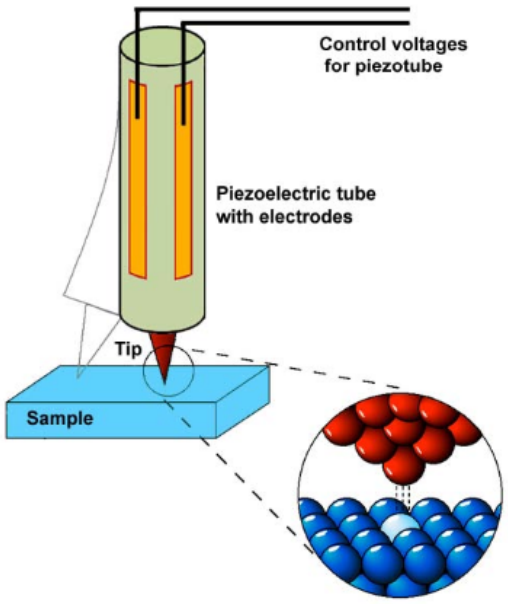

Figure 3.16: The Schematic of the STM operation. By bringing the tip (shown in red) close to the sample (shown in blue), electrons can tunnel between the two. The voltage bias applied determines the direction of the current. Applying a positive voltage to the sample gives the image of the empty states, and maps with a negative bias applied to the sample contribution of the filled states are depicted. [22]

3.6.2 Scanning Tunning Spectrum (STS) measurement

Topography. One of the most common modes of measurement in STM is the constant current mode, also known as topography. An STM topography is obtained by maintaining the tunneling current between the tip and the surface fixed. In this case, a constant voltage (V_s) is applied to the sample, and a constant current is demanded by the user (I_{set}). As the tip scans over the surface, its piezoelectric tube extends and contracts to keep the flow of current fixed,

and the height for which I_{set} was achieved is recorded. For scanning a metallic surface, the values of V_s could be as low as a few tens of millivolts and the current as high as 1 nA. The image represents a contour of constant tunneling current on a surface, approximating the integrated LDOS. Considering only elastic tunneling, the electrons with energies between Fermi energy and V_{bias} can tunnel from the filled states of the sample to the tip in the case of negative bias and from the tip to the empty states of the sample in the case of positive bias.

dI/dV. Another STM mode of measurement is measuring the differential tunneling conductance dI/dV, which is directly proportional to the LDOS. The measurement can be done at a single point in space or over an area of the sample. A general technique to obtain the energy spectrum is to add some oscillatory voltage (dV) on top of the bias voltage and measure the response (dI) by using a lock-in amplifier. Thus, dI/dV for a particular value of energy can be measured, and from equation (IV) it can be seen that it is proportional to the density of states:

$$g(V) \equiv \frac{dI}{dV} \propto DOS(V).$$

The measurement of this differential conductance as a function of energy and space is the key measurement for obtaining energy-resolved information on the electronic structure.

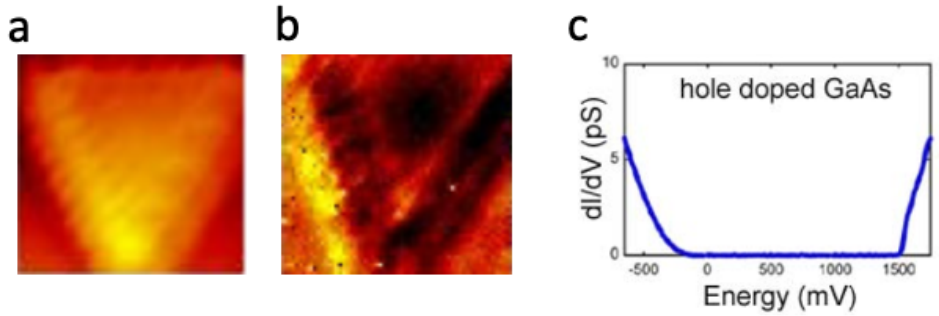

.

Fig. 3.17 a STM topography in 3*3nm area on $NbSe_2$, b STS mapping at -700meV bias voltage (the same position as STM topography), c STS spectrum on hole-doped GaAs. [22]

Reference

[1]. C. Liu, Electronic structure of iron arsenic high temperature superconductors studied by angle resolved photoemission spectroscopy (ARPES) Ph.D. thesis, Iowa State University, (2011)

[2]. Varian inc. vacuum products. Basic Vacuum Practice. 3rd ed. Varian Associates, Inc. (1992).

[3]. Oil free pumping system. http://www-app1.gfz-potsdam.de/www/pb4/pg2/equipment/sims/OilFree.html (2011).

[4]. Akari Takayama, High-Resolution Spin-Resolved Photoemission Spectrometer and the Rashba Effect in Bismuth Thin Films, Springer, (2015)

[5]. G. Bian, Angle-resolved photoemission and first-principles studies of topological thin films, Ph.D. Thesis, University of Illinois at Urbana-Champaign, (2012)

[6]. M. Date (Ed.), Kyosokan-Denshi-kei Strongly Correlated Electron System. (Kodansha, 1997)

[7]. J.J. Yeh, I. Lindau, At. Data Nucl. Data Tables 32, 1 (1985)

[8]. T. Valla, A.V. Fedorov, P.D. Johnson, B.O. Wells, S.L. Hulbert, Q. Li, G.D. Gu, N. Koshizuka, Science 285, 2110 (1999)

[9]. W. Gerlach, O. Stern, Zeitschrift für Physik 9, 353 (1922)

[10]. G.E. Uhlenbeck, S. Goudsmit, Phy. Rev. 34, 145 (1929)

[11]. d orbitals in their different orientations. http://itl.chem.ufl.edu/2045_s00/matter/FG06_023.GIF (2011).

[12]. Y. Liu, Angle-resolved photoemission studies of two-dimensional electron systems, Ph.D. thesis, University of Illinois at Urbana-Champaign, (2010)

[13]. Hong, S.-S., Shin, Y.-H. and Arakawa, I. Investigation of gas species in a stainless steel ultrahigh vacuum chamber with hot cathode ionization gauges. Meas. Sci. Technol. 15, 359 (2004).

[14]. Wannberg, B. VG Scienta AB. 2008 Joseph F. Keithley Award for advances in measurement science recipient. http://www.vgscienta.jp/wannberg-winner.html (2008).

[15]. K. Soda, Nihon Butsuri Gakkai-shi (Butsuri) 45, 804 (1990)

[16]. G.C. Wang, R.J. Celotta, D.T. Pierce, Phys. Rev. B 23, 1761 (1981)

[17]. J. Ungris, D.T. Pierce, R.J. Celotta, Rev. Sci. Instrum. 57, 1314 (1986)

[18]. T. Okuda, Y. Takeichi, Y. Maeda, A. Harasawa, I. Matsuda, Rev. Sci. Instrum. 79, 123117 (2008)

[19]. T. Okuda, Y. Takaichi, A. Kakizaki, Nihon Butsuri Gakkai-shi (Butsuri) 65, 849 (2010) (in Japanese)

[20]. Shigemasa Suga, Akira Sekiyama, Photoelectron Spectroscopy Bulk and Surface Electronic Structures, Springer, (2014)

[21]. M. K. Brinkley, Angle-resolved photoemission studies of quantum-electronic coherence in metallic thin-film systems, Ph.D. thesis, University of Illinois at Urbana-Champaign (2010)

[22]. M.F. Crommie, C.P. Lutz, and D.M. Eigler. confinement of electrons to quantum corrals on a metal surface. Science, 262:218, 1993.

[23]. J. Bardeen. Tunneling from a many-particle point of view. Phys. Rev. Lett., 6:57–59, 1961.

4. SYMMETRY-ENFORCED TWO-DIMENSIONAL DIRAC FERMIONS IN BISMUTHENE

Two-dimensional (2D) Dirac-like electron gases have attracted tremendous research interest ever since the discovery of free-standing graphene. The linear energy dispersion and nontrivial Berry phase play a pivotal role in the electronic, optical, mechanical, and chemical properties of 2D Dirac materials. The known 2D Dirac materials are gapless only within certain approximations, for example, in the absence of spin−orbit coupling (SOC). In this chapter, we report a route to establishing robust Dirac cones in 2D materials with the nonsymmorphic crystal lattice.

4.1. Introduction

The discovery of graphene and topological insulators has stimulated enormous interest in two-dimensional (2D) electron gas with linear band dispersion. [1−3] The vanishing effective mass and nonzero Berry phase of Dirac fermion-like states give rise to many interesting physical properties such as extremely high mobilities and zero-energy Landau levels. [4] The two-dimensional Dirac cones are generally fragile against perturbations, and so various gapped electronic phases are observed. [5] For example, the weak spin−orbit coupling (SOC) can make graphene a quantum spin Hall insulator. Gapless 2D Dirac fermions can be found on the surfaces of 3D topological insulators. [3] However, when the dimension of the 3D systems is reduced, a tunneling energy gap opens at the Dirac point due to the hybridization of the surface states on the opposite surfaces. Therefore, it is a highly challenging task to find gapless Dirac fermions in intrinsic 2D materials. So far, only a few 2D materials have been theoretically predicted to possess Dirac states, including graphene,

[1,2] silicene, [6] germanene, [7] and some artificial structures. [8−11] Among them, only graphene has been experimentally proven to possess Dirac cones as the spin−orbit gap is negligibly small.

The reason for the rarity of 2D Dirac materials can be seen from a simple co-dimension analysis. The general Hamiltonian of 2D Dirac states is described by $\alpha\sigma_x k_x + \beta\sigma_y k_y$, where σ_i and k_i are Pauli matrices and momentum components, and α and β are constants. The Dirac cone can be easily gapped by any perturbations in the form of $m\sigma_z$, and the resulting gapped system is energetically favored given that the Fermi level is in the gap. The perturbation can be from the intrinsic SOC of the system, as in graphene, or from lattice relaxations which reduce the surface energy of the 2D material. [12] In order to achieve truly gapless Dirac dispersion, geometrical or topological constraints are required to eliminate the gap term. Previous theoretical studies of the relation between lattice symmetry and Dirac states suggested that nonsymmorphic symmetries can enforce Dirac-like band structures. [13−17] The key idea is that the operator algebra involving nonsymmorphic symmetries allows only nontrivial irreducible representations at certain high-symmetry points of the Brillouin zone. [15,17] However, to date, a material realization of symmetry-enforced Dirac fermions in 2D nonsymmorphic materials is still elusive.

In this chapter, we report the existence of 2D Dirac fermions in α-bismuthene ("α-Bi" for short). The Dirac band structure is observed by our micro-angle-resolved photoemission spectroscopy (μ-ARPES) experiment. The Dirac cone is protected by the glided mirror of the nonsymmorphic α-bismuthene lattice and shows that this concept can be generalized to other 2D materials with nonsymmorphic layer groups. The Dirac points are located at certain

high-symmetry momentum points which are entirely determined by the symmetry of the lattice. This correspondence of Dirac states to the lattice symmetry can accelerate discovery of a wide range of 2D Dirac materials. In this chapter, we report our experimental results on α- bismuthene. Then we will present a theoretical analysis of the 2D Dirac cone in this material as well as the first-principles band structure of bismuthene films. Finally, we discuss a guiding rule for the search of 2D Dirac materials.

4.2. Thin film growth and structure characterization

In our experiment, α-Bi was grown by thermal evaporation of bismuth (99.999%) onto the highly oriented pyrolytic graphite (HOPG) substrate. The HOPG substrate was cleaved before deposition, annealed in UHV at 750 K for several hours to remove contaminants, and then kept at room temperature during deposition. In Fig. 4.1.a, a typical low-energy electron microscopy (LEEM) image recorded on α-Bi is shown. α-Bi is relatively well-characterized and consists of two-monolayer thick butterfly-like bases with black phosphorus-like crystallographic structure and the (110) plane (rhombohedral indices) parallel to the substrate [18,19] (see Fig. 4.1.a). On top of α-Bi, additional stripes of α-Bi are usually observed. These can be seen in LEEM images due to quantum oscillations in electron reflectivity for electron energies below 10 eV (as a result of the long inelastic mean free path). In our experiments, we found that highest height contrast for Bi on HOPG is obtained for electron energy equal to 8 eV.

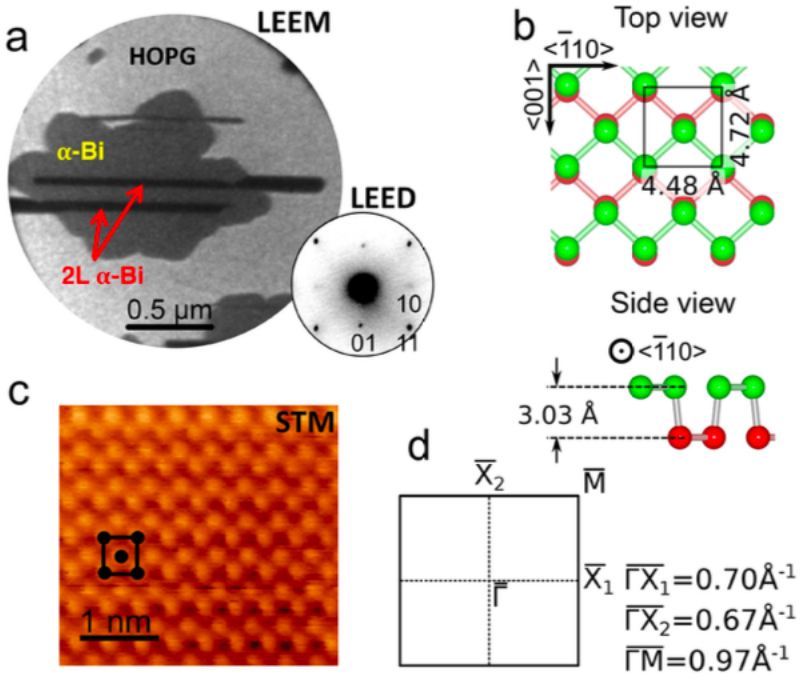

Fig. 4.1. LEEM and scanning transmission microscopy (STM) results recorded on α-bismuthene (a) LEEM image of the α-Bi island. Micro-low-energy electron diffraction (μ-LEED) pattern recorded on α-Bi island is shown in the inset. (b) Lattice structure of α-Bi belonging to the #42-layer group pman: top and side views. The Bi atoms at two different heights are colored in red and green. The dimension of the unit cell after full density functional theory optimization is shown. (c) Atomic-resolution STM image of α-Bi. (d) Brillouin zone of α-Bi.

By using micro-low-energy electron diffraction (μ-LEED) (aperture size 500 nm), we confirm that the crystallographic structure of these islands is of black-phosphorus-type (see top inset in Fig. 4.1.a, recorded on an island shown in Fig. 4.1.a) rather than, for example, possible hexagonal structures. [20,21] Close inspection of the μ-LEED pattern reveals the very weak intensity of the (10) spots, which is the result of glide-line symmetry along the

⟨$1\bar{1}0$⟩ direction [22] (in rhombohedral indices, for a ball-and-stick model, see Fig. 4.1.b). Detailed analysis on the LEED intensity pattern indicates that the two atoms in each layer in the unit cell are at nearly the same height; the surface buckling is small, with a deformation Δz around 0.04 ± 0.005 Å. The geometry of the unit cell from the LEED fitting is shown in Figure 1b. This structure belongs to the #42-layer group (pman). The dimensions of the unit cell from scanning tunneling microscopy (STM) measurements are $(4.5 \pm 0.2) \times (4.8 \pm 0.2)$ Å [2]; see Fig. 4.1.c. The two-atom surface unit cell from STM is consistent with the LEED result. This is further supported by our fully relaxed first-principles calculations (in the framework of density functional theory (DFT)) performed for a free-standing film, yielding a unit cell of 4.48 × 4.72 Å2 (see Fig. 4.1.b). Note that in this structure there is no buckling within the uncertainties of the calculations; that is, the atoms in each layer are exactly parallel to the surface plane; please see a detailed discussion in the Supporting Information. The Brillouin zone is plotted in Fig. 4.1.d, in which $\bar{\Gamma}-\bar{X}1$ is along the ⟨$1\bar{1}0$⟩ direction and $\bar{\Gamma}-\bar{X}_2$ along the ⟨001⟩ direction.

4.3. μ-ARPES results and calculated band structures

In order to understand the electronic properties of α-Bi, we performed μ-ARPES measurements using a spectroscopic photoemission and low-energy electron microscope (SPE- LEEM) [23] on the island shown in Fig. 4.1.a. When operated in the diffraction imaging mode, the SPELEEM microscope can record the ARPES pattern up to $k_{//}$ such that the first and a large portion of the second Brillouin zones of α-Bi are imaged. Results of μ-ARPES experiments are compared with DFT calculations in Fig. 4.2. along the high-symmetry directions of the surface Brillouin zone. Second derivative procedures are used to

enhance the visibility of the band features (smoothing and moving average used before second derivative calculation), as in the central column of Fig. 4.2. α-Bi is a semiconductor with the Fermi level barely touching the top of the valence band, as shown in the ARPES spectra. The most prominent feature of the valence band is that band crossings exist at $\bar{X}_1$ and $\bar{X}_2$. A band degeneracy occurs for every band crossing at these two high-symmetry points. Here, we focus on the band crossings at 0.7 and 0.4 eV (denoted by "DP1" and "DP2", respectively, in Figure 2) as examples and present a detailed analysis of the band dispersion. The conclusions from this analysis apply to every pair of bands that cross at $\bar{X}_1$ and $\bar{X}_2$. Overall, the agreement between theory and experiment is good considering the ARPES spectrum is taken from a single α-Bi island with size about 1 μm × 1 μm. We note that there are no spectral features ascribed to the HOPG substrate because, in the vicinity of Fermi level, HOPG bands are located farther away from the center of the Brillouin zone.

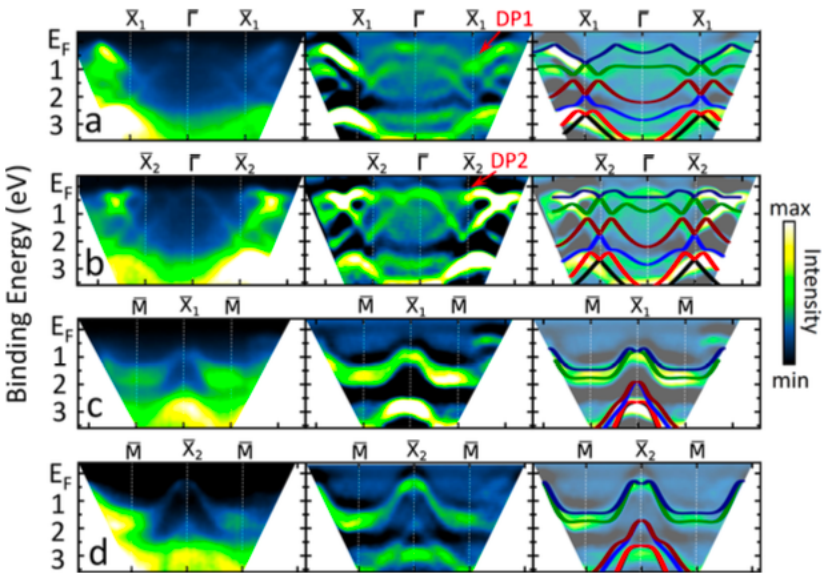

Fig. 4.2. μ-ARPES band structure taken from a single island of α- Bi. (a−d) ARPES band mapping taken at photon energy 27.9 eV along different high-symmetry directions, as indicated in each panel. The raw data are shown in the left column, second derivative enhanced data in the middle, and ARPES result overlaid with first-principles bands in the right column.

The agreement between experiment and theory is seen very clearly in the plots of iso-energy contours (see Fig. 4.3a). The calculated contours are plotted on top of experimental images for comparison. In the first Brillouin zone, there are four small hole pockets at 0.2 eV, two of which are in between $\bar{\Gamma}$ and $\bar{X}_1$ and the other two close to $\bar{X}_2$. In the vicinity of $\bar{X}_2$, the two hole-pockets grow into a star-shaped contour (indicated by arrows in the middle panel of Fig. 4.3a) as the binding energy goes from 0.2 to 0.4 eV. The center of the star corresponds to the Dirac point DP2 located at $\bar{X}_2$. The two pockets between $\bar{\Gamma}$ and $\bar{X}_1$ also grow larger as the binding energy increases about 0.7 eV, they touch the pockets in the second Brillouin zone at $\bar{X}1$, forming the Dirac point DP1 (see the bottom panel of Fig. 4.3a). These pockets eventually merge together into squarish contours for higher binding energy values (see the iso-energy contours at 0.9, 1.2, and 1.4 eV in Fig. 4.3a). This evolution of band contours is consistent with the DFT simulations. The DFT band structure in Fig. 4.3b demonstrates the band crossings DP1 and DP2. Fig. 4.3c,d shows 3D representations of the bands obtained from ARPES and DFT calculation, respectively. To compare with the experimental result, the DFT bands are smeared out by 0.5 eV. All main features in the ARPES data are well reproduced by DFT calculations, strongly suggesting the existence of nonsymmorphic Dirac states. In particular, the band crossing features marked by arrows are nearly identical, which

indicates that a Dirac state indeed exists at $\bar{X}_1$. We note that the Dirac bands at DP1 and DP2 are anisotropic, especially along $\bar{X}_2$–$\bar{M}$ direction. The linear dispersion can be seen only in the close vicinity of $\bar{X}_1$ and $\bar{X}_2$, as shown in Fig. 4.3a,b.

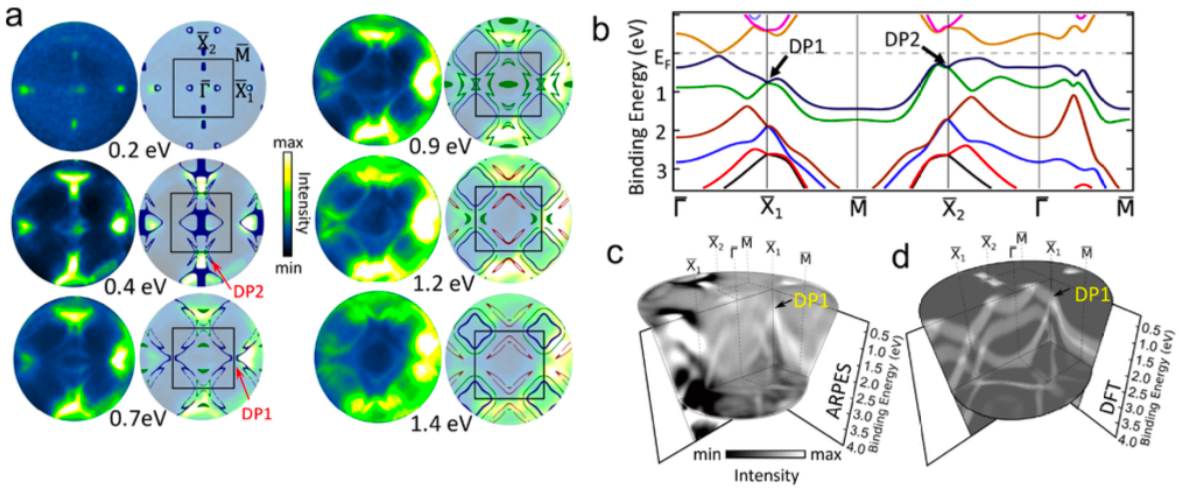

Fig 4.3. μ-ARPES iso-energy contours and first-principles simulations. (a) μ-ARPES iso-energy contours taken at binding energy of 0.2, 0.4, 0.7, 0.9, 1.2, and 1.4 eV. (b) DFT-calculated bands for α-Bi. (c) 3D band representation with two cross-sectional planes $\bar{X}_1$–M–$\bar{X}_1$ and $\bar{X}_1$–$\bar{\Gamma}$–$\bar{X}_1$. (d) Corresponding calculated 3D band contour with smearing of 0.5 eV.

According to the ARPES and first-principles results, Dirac cones exist at $\bar{X}_1 = (\pi,0)$ and $\bar{X}_2 = (0,\pi)$ of the Brillouin zone (for simplicity, the lengths are measured in units of the lattice constants a_x and a_y along $\langle \bar{1}10 \rangle$ and $\langle 001 \rangle$ directions, respectively). We now show that these band degeneracies are protected by the nonsymmorphic lattice symmetry. α-Bi is nonmagnetic and centrosymmetric, so the time reversal (T) and inversion (P) symmetries are preserved. The space−time inversion symmetry PT leads to the two-fold Kramers degeneracy of each band in the Brillouin zone in the presence of SOC. Therefore, the band

degeneracy is 4 for the band crossing points at $\bar{X}_1$ and $\bar{X}_2$. The lattice of α-bismuthene belongs to the #42-layer group (pman), which is described by the three generators:

$$\tilde{M}_z: (x + 1/2, y + 1/2, -z)i\sigma_z$$

$$P: (-x, -y, -z)\sigma_0$$

$$M_x: (-x, y, z)i\sigma_x$$

where σ_i (i = x, y, z) are Pauli matrices for the spin degree of freedom and σ_0 is the 2 × 2 identity matrix. Here, the tilde in $\tilde{M}_z$ indicates that it is a nonsymmorphic glide mirror operation, the mirror reflection, is accompanied by a half- lattice translation parallel to the mirror plane. We shall see that the three symmetries $\tilde{M}_z$, P, and T dictate the existence of Dirac points at $\bar{X}_1$ and $\bar{X}_2$, which are robust under SOC.

We first show that the three symmetries guarantee four-fold band degeneracies at $\bar{X}_1$ and $\bar{X}2$. The key point is that the nonsymmorphic character of $\tilde{M}_z$ leads to a special commutation relation between $\tilde{M}_z$ and P. To see this, we compare the results when these two symmetry operators act on (x, y, z) in the different orders:

$$(x, y, z) \xrightarrow{P} (-x, -y, -z) \xrightarrow{\tilde{M}_z} (-x + 1/2, -y + 1/2, z)$$

$$(x, y, z) \xrightarrow{\tilde{M}_z} (x + 1/2, y + 1/2, -z) \xrightarrow{P} (-x - 1/2, -y - 1/2, z)$$

This means that

$$\tilde{M}_z P = T_{110} P \tilde{M}_z$$

Where $T_{110} = e^{-ikx-iky}$ denotes the translation by one unit cell along both x and y directions. Consequently, at the special high-symmetry points $\bar{X}_1$: (π,0) and $\bar{X}_2$: (0,π), $\tilde{M}_z$ and P anticommuting with each other: $\{\tilde{M}_z, P\} = 0$. Meanwhile, the nonsymmorphic

character also makes the eigenvalues of $\tilde{M}_z$ momentum dependent. As $(\tilde{M}_z)^2 = -T_{110}$ (the minus sign is due to a 2π rotation on spin), we have the $\tilde{M}_z$ eigenvalues $g_z = \pm e^{-ikx/2-iky/2}$. Importantly, at $\bar{X}_1$ and $\bar{X}_2$, $g_z = \pm 1$, which is purely real.

Consider an energy eigenstate $|\Phi(\bar{X}\, i)\rangle$ at $\bar{X}$ i (i = 1, 2), which can be chosen as an eigenstate of $\tilde{M}_z$ with an eigenvalue g_z. As $\bar{X}_i$ is a T-invariant momentum point, $|\Phi(\bar{X}_i)\rangle$ has a degenerate Kramers partner $T|\Phi(\bar{X}_i)\rangle$, which must share the same g_z eigenvalue (because $g_z = \pm 1$ is real). Moreover, because $\{\tilde{M}_z, P\}=0$, $P|\Phi(\bar{X}_i)\rangle$ (and also $TP|\Phi(\bar{X}_i)\rangle$) must be another degenerate partner of $|\Phi(\bar{X}_i)\rangle$ with an opposite $\tilde{M}_z$ eigenvalue $(-g_z)$. Thus, the four states ($|\Phi\rangle$, $P|\Phi\rangle$, $T|\Phi\rangle$, $TP|\Phi\rangle$) always form a degenerate quartet at $\bar{X}_1$ and $\bar{X}_2$. Deviating from $\bar{X}_i$, the four-fold degeneracy will generally be lifted because the k point is no longer invariant under T. We note that the upper equation plays the pivotal role in the formation of band degeneracy. The phase factor from T_{110}, reflecting the nonsymmorphic nature of the lattice, determines the existence and location of the Dirac points. In addition, the above argument is made with explicit consideration of SOC, so these Dirac points are indeed robust against SOC and can be termed as the 2D spin−orbit Dirac points. To further characterize the emergent 2D spin−orbit Dirac fermions and to show that the dispersion is indeed a linear type, we construct an effective k·p model around each Dirac point based on the symmetry constraints. Consider DP1 at $\bar{X}_1$, the symmetry operations in the little group at $\bar{X}_1$ include T. The matrix representations of these operators can be obtained from the standard reference, [24] with $T=-i\sigma_y \otimes \tau_0 K$, $\tilde{M}_z = \sigma_z \otimes \tau_y$, $P=\sigma_0 \otimes \tau_x$, and $Mx = -i\sigma_x \otimes \tau_x$. Here, K is the complex conjugation operator, σ_j and τ_j (j = x, y, z) are the Pauli matrices representing spin and orbital

degrees of freedom, respectively, and σ and τ are the 2 × 2 identity matrices. Subjected to these symmetry constraints, the effective model in the vicinity of DP1 expanded to linear order in the wave vector k' takes the form of

$$\mathcal{H}(\boldsymbol{k}') = v_x k'_x(\cos\theta\ \sigma_x \otimes \tau_z + \sin\theta\ \sigma_0 \otimes \tau_y) + v_y k'_y \sigma_y \otimes \tau_z$$

where the energy and the wave vector $k' = (k'_x, k'_y)$ are measured from DP1, the model parameters v_x, v_y, and θ are real, and their values depend on the microscopic details. The dispersion around DP1 is given by $E = \pm\sqrt{v_x^2 k'^2_x + v_y^2 k'^2_y}$, which indeed corresponds to a linear Dirac cone. This confirms that the emergent fermions are 2D spin−orbit Dirac fermions. The effective model for DP2 at $\bar{X}_2$ can be defined in a similar way. With $T=-i\sigma_y \otimes \tau_0 K$, $\tilde{M}z = \sigma_z \otimes \tau_y$, $P=\sigma_0 \otimes \tau_x$, and $M_x = -i\ \sigma_x \otimes \tau_0$, the effective Hamiltonian can be written as

$$\mathcal{H}(\boldsymbol{k}') = v_x k'_x \sigma_y \otimes \tau_z + v_y k'_y(\cos\theta\ \sigma_x \otimes \tau_z + \sin\theta\ \sigma_0 \otimes \tau_y)$$

Because there is no symmetry operation connecting DP1 and DP2, the model parameters are generally different for DP1 and DP2. For example, from fitting the DFT band structure, at DP1, we find the Fermi velocities $v_x = 3.95 \times 10^5$ m/s and $v_y = 2.12\times10^5$m/s, whereas at DP2,$v_x = 1.19\times10^5$m/s and $v_y = 4.67 \times 10^5$ m/s. The lack of symmetry connection implies that each Dirac point may be tuned separately. For example, a single Dirac point may be tuned close to the Fermi level by lattice deformations that preserve the crystal symmetry. This is in contrast to the case of graphene, where the two Dirac points are symmetry-connected and hence must shift in energy together. The strong spin−orbit coupling in α-Bi is crucial for the formation of the nonsymmorphic Dirac states. To see this, we calculated

the band structure without the inclusion of SOC; the result is shown in Fig. 4.4c. The bands become degenerate along $\bar{X}_1$−$\bar{M}$−$\bar{X}_2$ and, consequently, form a nodal line at the boundary of the Brillouin zone; see Figure 4e. The band degeneracy is also due to the nonsymmorphic symmetry of the lattice. However, this band degeneracy is not robust against spin−orbit coupling. Turning on SOC, the nodal line is gapped everywhere except $\bar{X}_1$ and $\bar{X}_2$. In other words, SOC transforms the system from a nodal-line system into a Dirac fermion state. In the presence of SOC, the Dirac points at $\bar{X}_1$ and $\bar{X}_2$ are under the protection of the glided mirror symmetry. Naturally, breaking this glided mirror symmetry will lead to energy gaps at the Dirac points. Fig. 4.4d shows the band structure of a distorted lattice. The lattice distortion is depicted in the inset of Fig. 4.4d, which destroys the glided mirror symmetry while keeping the space inversion symmetry. In this case, every band still possesses the two-fold Kramers degeneracy, but the Dirac points at $\bar{X}_1$ and $\bar{X}_2$ disappear. This evolution of band surfaces and Dirac/nodal points, as schematically depicted in Fig. 4.4e, indicates that SOC and nonsymmorphic symmetry are two essential pillars supporting the formation of Dirac fermions in α-Bi.

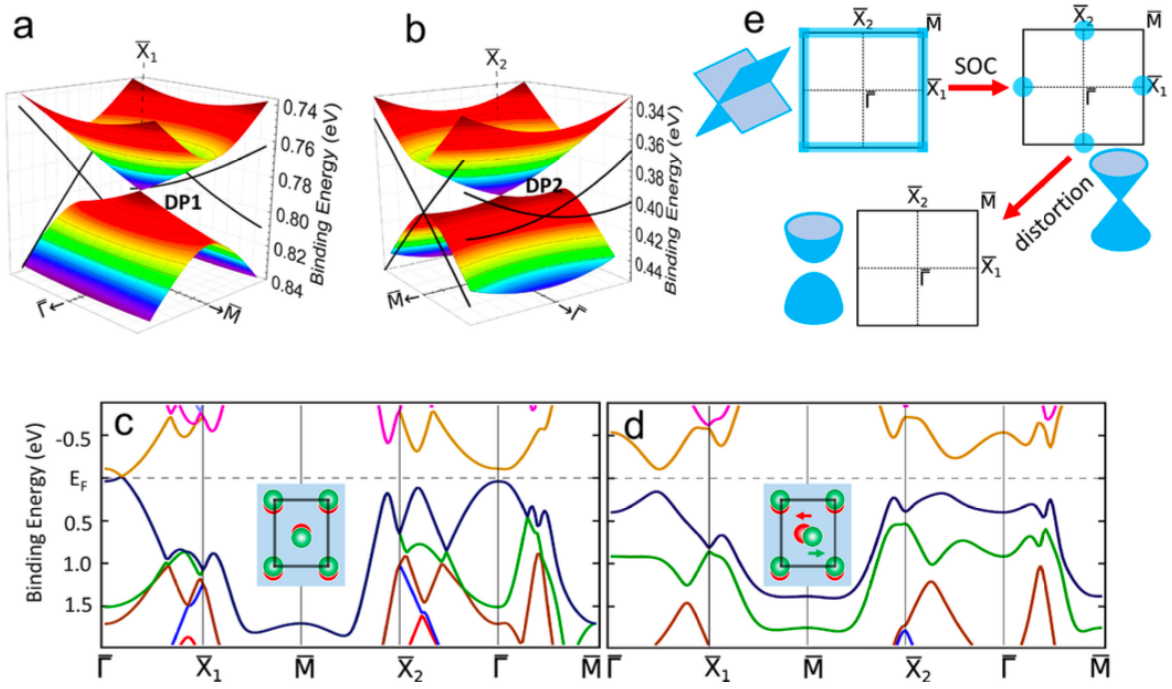

Fig 4.4. SOC and distortion effects on α-Bi band structure. (a,b) DFT band surface calculated in the vicinity of $\bar{X}_1$ and $\bar{X}_2$, respectively. (c) Band structure of α-Bi in the absence of spin−orbit coupling. (d) Band structure of distorted α-Bi. The distortion is shown in the inset. The two atoms are moved along arrow directions by 2% of the unit cell width. (e) Evolution of band configuration from without SOC to with SOC to with both SOC and symmetry-breaking distortion. The Dirac/nodal points are highlighted in blue in the Brillouin zone.

4.4. Further discussion – Monolayer Bismuth case

To illustrate the application of the principle to other cases, we now consider a different nonsymmorphic layer group. The lattice structure of a bismuth monolayer after DFT optimization is shown in Fig. 4.5a, and it belongs to the #15-layer group ($p2_1/m11$). Note the

buckling in this structure i.e. the two atoms in the unit cell are not exactly in plane, as shown in Fig. 4.5a. The layer group has two generators (with spin matrices) as follows:

$$P : (-x, -y, -z)s_0$$
$$\widetilde{C}_{2x} : (x - 1/2, -y, -z)is_x$$

where C_{2x} is a nonsymmorphic 2-fold screw axis operation. The combinations of these two operators in two different orders are given by

$$(x, y, z) \xrightarrow{P} (-x, -y, -z) \xrightarrow{\widetilde{C}_{2x}} (-x - 1/2, y, z)$$
$$(x, y, z) \xrightarrow{\widetilde{C}_{2x}} (x - 1/2, -y, -z) \xrightarrow{P} (-x + 1/2, y, z)$$

Hence, the two combinations are connected by the momentum-dependent phase,

$$P\widetilde{C}_{2x} = T_{100}\widetilde{C}_{2x}P,$$

where $T_{100} = e^{ikx}$. In this case, at M = (π,π) and X_1 = (π,0), we have $\{P,C_{2x}\} = 0$. Meanwhile, the nonsymmorphic character also makes the eigenvalues of C_{2x} momentum dependent. Since $(C_{2x})^2 = -T_{100}$ (the minus sign is due to a 2π rotation on spin), we have the C_{2x} eigenvalues $c_x = \pm ie^{ikx/2}$. Importantly, at both X_1 and M, $c_x = \pm 1$, which are purely real. Suppose $|\Phi\rangle$ is an eigenstate of C_{2x} at X_1 (or M). Following a similar derivation as in the case of α-Bi, $|\Phi\rangle$, $T|\Phi\rangle$, $P|\Phi\rangle$, and $TP|\Phi\rangle$ must be degenerate at X_1 (or M). This is indeed the case we find in the calculated band structure of the bismuth monolayer shown in Fig. 4.5b.

In the absence of spin-orbit coupling, the bands are degenerate and become line nodes along $X_1 - M$, see Fig. 4.5d. To see this, let us consider two operators M_x and C_t, where

$$M_x \equiv \widetilde{C}_{2x}P : (x, y, z) \to (-x - 1/2, y, z)$$
$$C_t \equiv \widetilde{C}_{2x}T : (x, y, z) \to (x - 1/2, -y, -z)$$

Following a similar derivation as in Equations. (11) and (12), we have $M_xC_t = T_{100}C_tM_x$,

where $T_{100} = e^{ikx}$. A generic momentum point $k = (\pi, k_y)$ between X_1 and M is invariant under M_x and C_t, since k_y changes its sign under C_{2x}, P , and T . Meanwhile, $\{M_x, Ct\} = 0$ at k. This anti-commutation relation guarantees the 2-fold band degeneracy at k, which leads to a nodal line along X_1-M in the absence of SOC. Therefore, SOC is crucial for the formation of the Dirac cone. The Dirac bands found in this Bismuth structure are intrinsically of spin-orbit origin, in contrast to the spinless Dirac states in graphene. Just like the case of α-Bi, the band crossing point is protected by the nonsymmorphic lattice symmetry which eliminates the gap-opening effect of spin-orbit coupling in this 2D material. Consequently, breaking lattice symmetry will naturally introduce an energy gap at the Dirac point, as illustrated in Fig. 4.5e, which provides a tunability of the electronic property of this family of 2D Dirac materials. We note that the Dirac states are very close the Fermi level, so this Bi monolayer is a 2D Dirac semimetal. This structure is not energetically favored in its free-standing form, but it can be stabilized with the aid of substrate interactions.

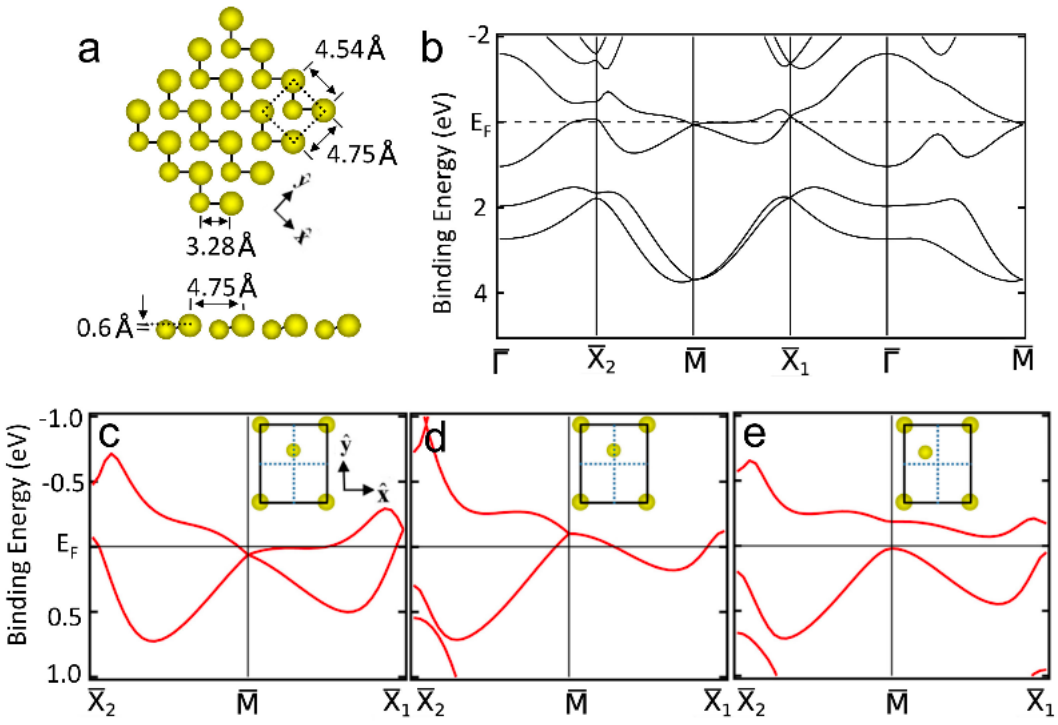

Fig. 4.5: Lattice and band structure of bismuth monolayer. (a), The top and side views of Bi monolayer lattice structure. (b), DFT band structure of Bi monolayer. (c), Zoom-in band structure along X_2-M-X_1. The lattice is shown in the inset. (d), Band structure same as in c but calculated in the absence of spin-orbit coupling. (e), Bands calculated with a distorted lattice. The distortion is schematically shown in the inset.

The nonsymmorphic α-Bi structure can be regarded as a variation of atomic layers truncated along (110) direction from Bi bulk lattice. In the Bi bulk structure, the atoms form a rhombohedral lattice. Therefore, if we look at (110) surface unit cell, d1 is generally not equal to d2 (see Fig. 4.6 for d1 and d2 definition) and the structure violates the nonsymmorphic symmetry. In 2D there is no constraint from the bulk lattice, so the atoms arrange their positions to saturate the dangling orbital of both atoms in the unit cell in the same way. Therefore, the pair of Bi atoms at the corner of the unit cell should be equivalent

to the pair at the center. In other words, d1= d2. This naturally leads to a nonsymmorphic structure in α-Bi and other group-V element monolayers (such P and Sb).

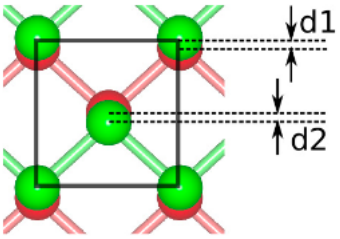

Fig 4.6: Definition of in-plane separation between atoms in Bi(110).

4.5. Conclusions

α-Bismuthene, a two-dimensional spin−orbit material, hosts Dirac fermion states at the high-symmetry momentum points $\bar{X}_1$ and $\bar{X}_2$, as demonstrated by our μ-ARPES measurements and first-principles calculations. The band degeneracy at the Dirac points is strictly protected by the nonsymmorphic symmetry of the lattice. Unlike graphene and other known 2D Dirac materials, the nonsymmorphic symmetry guarantees that the Dirac states in α-bismuthene are robust against spin−orbit coupling. Breaking the lattice symmetry, on the other hand, can lift the band degeneracy at Dirac points and yield gapped phases. Interestingly, a surface buckling in α-bismuthene breaks the space inversion symmetry and turns the system into a 2D elemental ferroelectric. [25] Moreover, the two allotropic phases of bismuthene, namely, α-Bi and β-Bi, possess nontrivial band topology. The β-Bi was first theoretically proposed

to be a quantum spin Hall (QSH) insulator and recently realized in experiment. [26,27] Similar to the β phase, α-Bi has been reported to be a QSH in its flat form. [28] Here, we confirm the α-bismuthene prepared on HOPG is with negligible surface buckling and, therefore, belongs to the QSH topological phase.

The formation mechanism of Dirac bands discussed in this work is intrinsically different from the band crossing induced by nonsymmorphic crystalline symmetry reported in previous works. [29−33] The two bands exchange the eigenvalues of a single nonsymmorphic operator, a glided plane or a screw axis, as they disperse from one high-symmetry momentum to another high-symmetry momentum. Therefore, a band crossing must happen between the two high-symmetry points. By contrast, the Dirac points in α-bismuthene reside at the high- symmetry momenta of the Brillouin zone because these points are invariant under P and T and allow momentum-dependent commutation/anticommutation relations involving the non-symmorphic symmetry operators. In other words, the location of the Dirac points is determined by the nonsymmorphic symmetry operations. [15] This property facilitates the detection of Dirac states in experiments. For example, let us consider a different nonsymmorphic group, the #15-layer group ($p2_1/m11$). A bismuth monolayer structure belongs to this layer group. Because of a screw axis of the lattice, Dirac states are guaranteed to exist at $\bar{X}_1$ and $\bar{M}$ points of the Brillouin zone. The principle demonstrated in this work can be applied to all 2D layered materials with a lattice belonging to one of the 36 nonsymmorphic layer groups. [15,17] This will significantly accelerate the search of 2D Dirac materials and extend “graphene” physics into the territory where strong spin−orbit coupling is present.

Reference

(1) Novoselov, K. S.; Geim, A. K.; Morozov, S. V.; Jiang, D.; Katsnelson, M. I.; Grigorieva, I. V.; Dubonos, S. V.; Firsov, A. A. Two- Dimensional Gas of Massless Dirac Fermions in Graphene. Nature 2005, 438, 197−200.

(2) Zhang, Y.; Tan, Y.-W.; Stormer, H. L.; Kim, P. Experimental Observation of the Quantum Hall Effect and Berry's Phase in Graphene. Nature 2005, 438, 201−204.

(3) Hasan, M. Z.; Kane, C. L. Colloquium: Topological Insulators. Rev. Mod. Phys. 2010, 82, 3045−3067.

(4) Castro Neto, A. H.; Guinea, F.; Peres, N. M. R.; Novoselov, K. S.; Geim, A. K. The Electronic Properties of Graphene. Rev. Mod. Phys. 2009, 81, 109−162.

(5) Zhou, S. Y.; Siegel, D. A.; Fedorov, A. V.; Gabaly, F.; Schmid, A. K.; Neto, A. H. C.; Lee, D.-H.; Lanzara, A. Origin of the Energy Bandgap in Epitaxial Graphene. Nat. Mater. 2008, 7, 259.

(6) Zhao, J.; Liu, H.; Yu, Z.; Quhe, R.; Zhou, S.; Wang, Y.; Liu, C. C.; Zhong, H.; Han, N.; Lu, J.; Yao, Y.; Wu, K. Rise of Silicene: A Competitive 2D Material. Prog. Mater. Sci. 2016, 83, 24−151.

(7) Cahangirov, S.; Topsakal, M.; Akturk, E.; Sahin, H.; Ciraci, S. Two- and One-Dimensional Honeycomb Structures of Silicon and Germanium. Phys. Rev. Lett. 2009, 102, 236804.

(8) Malko, D.; Neiss, C.; Vines, F.; Görling, A. Competition for Graphene: Graphynes with Direction-Dependent Dirac Cones. Phys. Rev. Lett. 2012, 108, 086804.

(9) Zhou, X.-F.; Dong, X.; Oganov, A. R.; Zhu, Q.; Tian, Y.; Wang, H.-T. Semimetallic Two-Dimensional Boron Allotrope with Massless Dirac Fermions. Phys. Rev. Lett. 2014, 112, 085502.

(10) Gomes, K. K.; Mar, W.; Ko, W.; Guinea, F.; Manoharan, H. C. Designer Dirac Fermions and Topological Phases in Molecular Graphene. Nature 2012, 483, 306−310.

(11) Pardo, V.; Pickett, W. E. Half-Metallic Semi-Dirac-Point Generated by Quantum Confinement in TiO2/VO2 Nanostructures. Phys. Rev. Lett. 2009, 102, 166803.

(12) Bian, G.; Wang, X.; Miller, T.; Chiang, T.-C.; Kowalczyk, P. J.; Mahapatra, O.; Brown, S. A. First-Principles and Spectroscopic Studies of Bi(110) Films: Thickness-Dependent Dirac Modes and Property Oscillations. Phys. Rev. B: Condens. Matter Mater. Phys. 2014, 90, 195409.

(13) Young, S. M.; Kane, C. L. Dirac Semimetals in Two Dimensions. Phys. Rev. Lett. 2015, 115, 126803.

(14) Guan, S.; Liu, Y.; Yu, Z.-M.; Wang, S.-S.; Yao, Y.; Yang, S. A. Two-Dimensional Spin-Orbit Dirac Point in Monolayer HfGeTe. Phys. Rev. Mater. 2017, 1, 054003.

(15) Wieder, B. J.; Kane, C. L. Spin-Orbit Semimetals in the Layer Groups. Phys. Rev. B: Condens. Matter Mater. Phys. 2016, 94, 155108. (16) Wieder, B. J.; Bradlyn, B.; Wang, Z.; Cano, J.; Kim, Y.; Kim, H.- S. D.; Rappe, A. M.; Kane, C. L.; Bernevig, B. A. Wallpaper Fermions and the Nonsymmorphic Dirac Insulator. Science 2018, 361, 246−251.

(17) Po, H. C.; Vishwanath, A.; Watanabe, H. Symmetry-Based Indicators of Band Topology in the 230 Space Groups. Nat. Commun. 2017, 8, 50.

(18) Kowalczyk, P. J.; Mahapatra, O.; Brown, S. A.; Bian, G.; Wang, X.; Chiang, T.-C. Electronic Size Effects in Three-Dimensional Nanostructures. Nano Lett. 2013, 13, 43−47.

(19) Scott, S. A.; Kral, M. V.; Brown, S. A. Bi on Graphite: Morphology and Growth Characteristics of Star-Shaped Dendrites. Phys. Rev. B: Condens. Matter Mater. Phys. 2006, 73, 205424.

(20) Koroteev, Y.; Bihlmayer, G.; Chulkov, E.; Blügel, S. First- Principles Investigation of Structural and Electronic Properties of Ultrathin Bi Films. Phys. Rev. B: Condens. Matter Mater. Phys. 2008, 77, 045428.

(21) Hofmann, P. The Surfaces of Bismuth: Structural and Electronic Properties. Prog. Surf. Sci. 2006, 81, 191−245.

(22) Lizzit, S.; Baraldi, A.; Grutter, Ch.; Bilgram, J.H.; Hofmann, Ph. The Surface Phase Transition and Low-Temperature Phase of α- Ga(010) Studied by SPA-LEED. Surf. Sci. 2009, 603, 3222−3226.

(23) Mentes¸ T. O.; Zamborlini, G.; Sala, A.; Locatelli, A. Cathode Lens Spectromicroscopy: Methodology and Applications. Beilstein J. Nanotechnol. 2014, 5, 1873−1886.

(24) Bradley, C. J.; Cracknell, A. P. The Mathematical Theory of Symmetry in Solids; Clarendon Press: Oxford, 1972.

(25) Xiao, C.; Wang, F.; Yang, S. A.; Lu, Y.; Feng, Y.; Zhang, S. Elemental Ferroelectricity and Antiferroelectricity in Group-V Monolayer. Adv. Funct. Mater. 2018, 28, 1707383.

(26) Murakami, S. Quantum Spin Hall Effect and Enhanced Magnetic Response by Spin-Orbit Coupling. Phys. Rev. Lett. 2006, 97, 236805.

(27) Reis, F.; Li, G.; Dudy, L.; Bauernfeind, M.; Glass, S.; Hanke, W.; Thomale, R.; Schäfer, J.; Claessen, R. Bismuthene on a SiC Substrate: A Candidate for a High-Temperature Quantum Spin Hall Material. Science 2017, 357, 287−290.

(28) Lu, Y.; Xu, W.; Zeng, M.; Yao, G.; Shen, L.; Yang, M.; Luo, Z.; Pan, F.; Wu, K.; Das, T.; He, P.; Jiang, J.; Martin, J.; Feng, Y. P.; Lin, H.; Wang, X.-S. Topological Properties Determined by Atomic Buckling in Self-Assembled Ultrathin Bi(110). Nano Lett. 2015, 15, 80−87.

(29) Fang, C.; Fu, L. New Classes of Three-Dimensional Topological Crystalline Insulators: Nonsymmorphic and Magnetic. Phys. Rev. B: Condens. Matter Mater. Phys. 2015, 91, 161105.

(30) Wang, Z.; Alexandradinata, A.; Cava, R. J.; Bernevig, B. A. Hourglass Fermions. Nature 2016, 532, 189−194.

(31) Li, S.; Liu, Y.; Wang, S.-S.; Yu, Z.-M.; Guan, S.; Sheng, X.-L.; Yao, Y.; Yang, S. A. Nonsymmorphic-Symmetry-Protected Hourglass Dirac Loop, Nodal Line, and Dirac Point in Bulk and Monolayer X3SiTe6 (X = Ta, Nb). Phys. Rev. B: Condens. Matter Mater. Phys. 2018, 97, 045131.

(32) Takahashi, R.; Hirayama, M.; Murakami, S. Spinless Hourglass Nodal-Line Semimetals. Phys. Rev. B: Condens. Matter Mater. Phys. 2017, 96, 155206.

(33) Yang, B.-J.; Bojesen, T. A.; Morimoto, T.; Furusaki, A. Topological Semimetals Protected by Off-Centered Symmetries in Nonsymmorphic Crystals. Phys. Rev. B: Condens. Matter Mater. Phys. 2017, 95, 075135.

(34) Hartwigsen, C.; Goedecker, S.; Hutter, J. Relativistic Separable Dual-Space Gaussian Pseudopotentials from H to Rn. Phys. Rev. B: Condens. Matter Mater. Phys. 1998, 58, 3641−3662.

(35) Gonze, X.; Beuken, J.-M.; Caracas, R.; Detraux, F.; Fuchs, M.; Rignanese, G.-M.; Sindic, L.; Verstraete, M.; Zerah, G.; Jollet, F.; Torrent, M.; Roy, A.; Mikami, M.; Ghosez, P.; Raty, J.-Y.; Allan, D. First-Principles Computation of Material Properties: The Abinit Software Project. Comput. Mater. Sci. 2002, 25, 478−492.

5. OBSERVATION ON SYMMETRY-ENFORCED DIRAC FERMIONS IN ANTIMONENE

Nonsymmorphic crystal symmetries can enforce the formation of Dirac nodes, providing another route to establishing symmetry-protected Dirac states in 2D materials. Similar to the bismuthene in last chapter, antimonene can also from the phosphorene structure or the α-antimonene. As this structure contain nonsymmorphic symmetry, we can expect that α-antimonene hold Dirac nodes but because the number of electrons is different in antimonene, a different band dispersion and properties would be found in α-antimonene. In this chapter, we report the symmetry-protected Dirac states in nonsymmorphic α-antimonene (Sb monolayer). The antimonene was synthesized by the method of molecular beam epitaxy. 2D Dirac states with large anisotropy were observed by angle-resolved photoemission spectroscopy. The Dirac states in α-antimonene are spin-orbit coupled in contrast to the spinless Dirac states in graphene. The result extends the graphene physics into a family of 2D materials where spin-orbit coupling is present.

5.1. Introduction

Dirac states with linear band dispersion and a vanishing effective mass have been discovered in condensed matter materials such as graphene, topological insulators, and bulk Dirac/Weyl semimetals [1–4]. The topological phase of Dirac-fermion states leads to many exotic physical properties such as zero-energy Landau levels [5]. The graphene like Dirac materials have been considered as a cornerstone for the development of next-generation electronic devices. However, the two-dimensional Dirac cones are generally unstable because an energy gap can be easily induced by intrinsic or extrinsic perturbations such as spin-orbit

coupling (SOC) and lattice distortions [6]. This leads to the rarity of two-dimensional (2D) Dirac materials, and only a few materials have been proved experimentally to host gapless 2D Dirac states, including graphene [1,2] and the surface of topological insulators [3]. The Dirac states in graphene can be considered to be gapless only by ignoring the small SOC of the system. When the dimension of topological insulators is reduced, a tunneling energy gap opens at the Dirac point, which is due to the hybridization of the surface states on the opposite surfaces [3]. To find gapless Dirac states, geometrical constraints on the crystal lattice are generally needed to protect the nodal points against various gapping mechanisms.

Recently, it has been proposed that nonsymmorphic crystalline symmetries including glide mirrors and screw axes can enforce band crossings and hence induce Dirac-fermion-like states [7–13]. This is because the operators of nonsymmorphic symmetry operations create only high-dimensional irreducible representations at certain symmetry points of the Brillouin zone [9,11–18]. This presents another route to realizing 2D Dirac materials whose Dirac states are robust even in the presence of strong SOC. Here, we report the observation of 2D Dirac states in the α phase of antimonene (monolayer antimony). Bulk Sb is a group-V semimetal with a small overlap between the valence and conduction bands. Despite small electron and hole pockets at the Fermi level, there exists an indirect negative energy gap traversing the whole Brillouin zone and separating the valence and conduction bands [19]. This gapped band structure enables Sb, though semimetallic, to host the same Z_2 topological invariants as topological insulators [3,20]. The large spin-orbit coupling plays a key role in the generation of the nontrivial band topology. In the 2D limit, monolayer Sb, i.e., antimonene, is known to have two allotropic structural phases, namely, the black-phosphorus

(BP)-like α phase and the hexagonal β phase. The lattice of α-antimonene (α-Sb for short) is nonsymmorphic, meaning that α-Sb can host symmetry-protected Dirac states. In this Letter, we synthesized α-Sb by the technique of molecular beam epitaxy (MBE) and detected the 2D Dirac states by angle-resolved photoemission (ARPES) experiments. The results shed light on the search for 2D Dirac materials in the vast territory of 2D nonsymmorphic crystals.

5.2. Thin film growth, crystal structures and calculated band structures

In our experiment, α-Sb was grown on SnSe substrates under an ultrahigh vacuum environment. The SnSe crystals were cleaved in situ and provided an atomically flat surface for the deposition of Sb. The crystallographic structure of α-Sb is shown in Figs. 5.1(a) and 1(b). The surface unit cell is marked by a blue rectangular box. The in-plane lattice constants are 4.49 and 4.30 Å in the x and y directions, respectively. The in-plane nearest-neighbor bond length is 2.90 Å. α-Sb consists of two horizontal atomic sublayers. Each atomic sublayer is perfectly flat according to the first-principles lattice relaxations. For a single layer (1L) of α-Sb, the vertical spacing between the two atomic sublayers is 2.79 Å. For a two-layer (2L) α-Sb film, the vertical distance between the two atomic sublayers within each α-Sb layer is 2.89 Å while the spacing between the two layers of α-Sb is 3.18 Å. The structure of one- and two-layer α-Sb belongs to the No. 42 layer group (pman). The lattice is nonsymmorphic because it is invariant under a glide mirror reflection operation. The glide mirror is parallel to the x-y plane and lies in the middle between the two atomic sublayers of 1L α-Sb. The glide mirror reflection is composed of a mirror reflection and an in-plane translation by (0.5a,0.5b), where a = 4.30Å and b = 4.49Å are the lattice constants in the x and y directions, respectively. For 2L α-Sb, the glide mirror sits in the middle between the

two α-Sb layers. Figures 1(c)–1(e) show the scanning tunneling microscopy (STM) image of two α-Sb/SnSe samples with atomic resolution. The first sample consists of mainly 1L α-Sb islands [see Fig. 5.1(c)]. A line-mode reconstruction (moiré pattern) can be seen on the α-Sb surface, as marked by the green dashed lines. The height profile is taken along the blue arrow [shown in Fig. 5.1(d)] indicates that the height of the 1L α-Sb island on the SnSe surface is 6.5 Å. The second sample possesses both 1L and 2L domains as shown in Fig. 5.1(e).

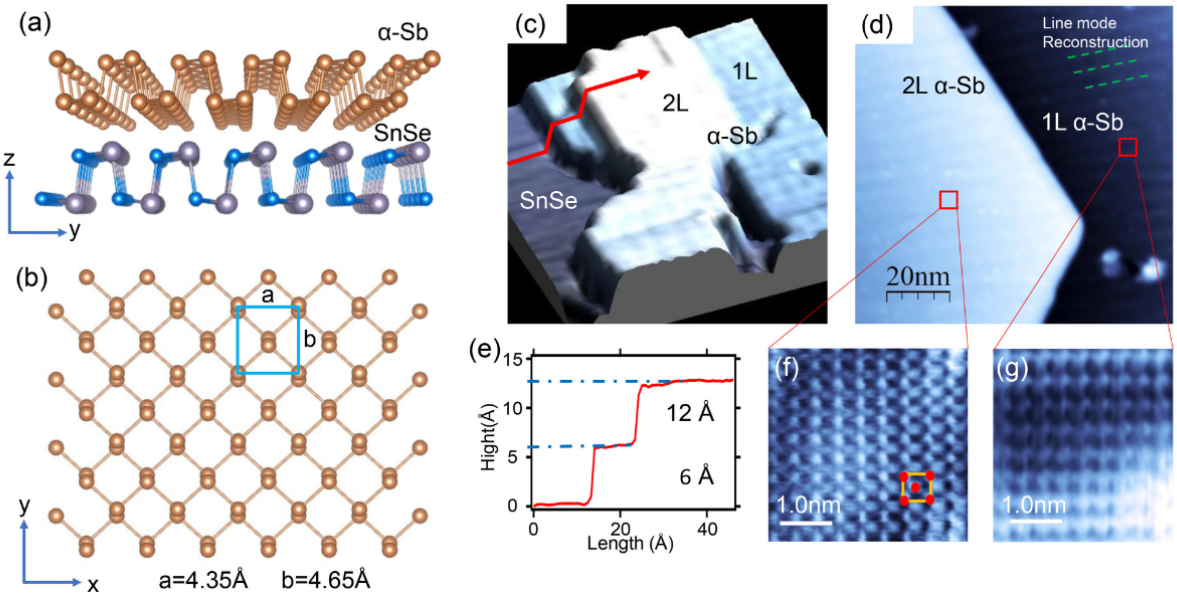

Fig. 5.1. (a) Side view of an α-Sb/SnSe lattice structure. (b) Top view of an α-Sb lattice structure. The unit cell is indicated by the blue rectangular box. The structure belongs to the No. 42 layer group pman. (c) Surface morphology of an α-Sb sample grown on SnSe substrate. (d) STM image of the α-Sb sample showing 1L and 2L domains. (e) The height profile taken along the red arrow in (c). (f), (g) Zoom-in STM images of the 1L and 2L domains shown in (d), respectively.

The glide mirror symmetry of the lattice leads to band degeneracy at high-symmetry points $X_1 = (\pi , 0)$ and $X_2 = (0, \pi)$. A detailed analysis of the location of the Dirac points can be found in a previous work [21]. We performed first- principles calculations for the band structure of 1L and 2L α-Sb films. The ABINIT package [22,23] and a plane-wave basis set were employed in the calculations. The energy cut is 400 eV. Relativistic pseudopotential functions constructed by Hartwigsen, Goedecker, and Hutter (HGH) were used [24]. The SOC of the system is varied from 0 to 300% by linearly scaling the relativistic parts of the Hamiltonian [25]. The calculated band structures of 1L and 2L α-Sb are shown in Figs. 5.2(a) and 5.2(b). The Brillouin zone of α-Sb is plotted in Fig. 5.2(c). Both 1L and 2L α-Sb have a semiconducting behavior, which can be seen in the calculated density of states. There exist band crossings at points X_1 and X_2. The band degeneracy occurs for every band at these two high-symmetry points. Each band splits into two branches as it disperses away from $X_{1,2}$. Therefore, the band crossings at $X_{1,2}$ create 2D Dirac states. The Dirac points at X_1 and X_2 in the top valence band are marked by "D1" and "D2," respectively. The location of the Dirac points is entirely determined by the underlying nonsymmorphic lattice symmetry. We note that the Dirac points in α-Sb are away from the Fermi level. There are a multitude of ways to shift the Fermi level in 2D materials, such as electrostatic gating and chemical doping. Therefore, the Dirac states can be accessed in transport experiments when the Fermi level is appropriately tuned in this monolayer system.

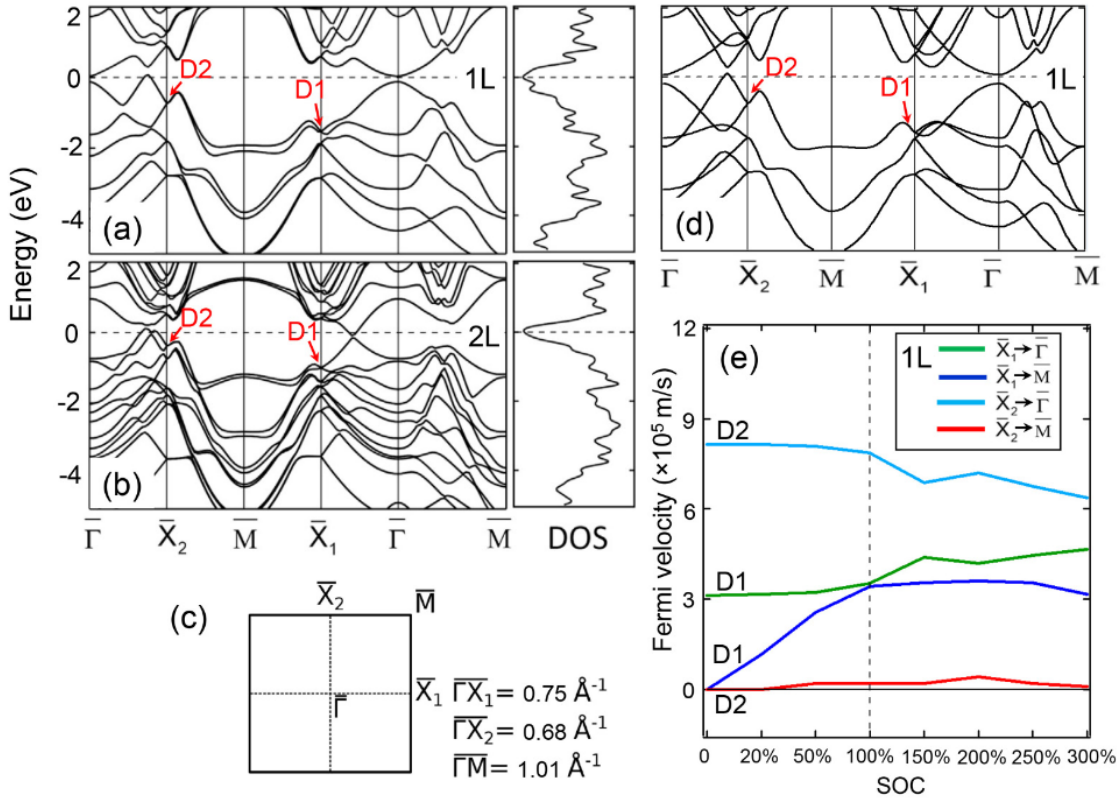

Fig. 5.2. (a) The band structure and density of states of 1L α-Sb. (b) The band structure and density of states of 2L α-Sb. (c) The Brillouin zone of α-Sb. (d) The band structure of 1L α-Sb without SOC. (e) Fermi velocity of the bands at D1 and D2 of 1L α-Sb with various strengths of SOC.

The Dirac bands at $X_{1,2}$ can be described by an effective k · p model constructed around each Dirac point. For D1 at X_1, the matrix representations of the symmetry operations are $T = -i\sigma_y \otimes \tau_0 K$ (time reversal), $M_z = \sigma_z \otimes \tau_y$ (glide mirror reflection), $P = \sigma_0 \otimes \tau_x$ (space inversion), and $M_x = -i\sigma_x \otimes \tau_x$ (mirror reflection with respect to a plane parallel to the y-z plane), where K is the complex conjugation operator, σ_j and τ_j (j = x, y, z) are the Pauli matrices representing spin and orbital degrees of freedom, respectively, and σ_0 and τ_0 are the 2 × 2

identity matrices. These matrices of symmetry operators can be found in the standard reference [26]. Subjected to these symmetry constraints, the effective model in the vicinity of D1 expanded to linear order in the wave vector k' takes the form of

$$\mathcal{H}(\boldsymbol{k}') = v_x k'_x(\cos\theta\,\sigma_x \otimes \tau_z + \sin\theta\,\sigma_0 \otimes \tau_y) + v_y k'_y \sigma_y \otimes \tau_z$$

where the energy and the wave vector $k' = (k_x', k_y')$ are measured from D1, the model parameters v_x and v_y are the Fermi velocities in the x and y directions, respectively, and θ is a real parameter that depends on the microscopic details. The dispersion around D1 is $E = \pm\sqrt{v_x^2 k'^2_x + v_y^2 k'^2_y}$, which indeed corresponds to a linear spin-orbit coupled Dirac cone. According to the first-principles bands, $v_x = 3.74 \times 10^5$ m/s and $v_y = 3.60 \times 10^5$ m/s. The Dirac cone exhibits a minor anisotropy. The effective model for D2 at X_2 can be described in a similar way. With $T=-i\sigma_y \otimes \tau_0 K$, $M_z=\sigma_z \otimes \tau_y$, $P=\sigma_0 \otimes \tau_x$, and $M_x = -i\sigma_x \otimes \tau_x$, the effective Hamiltonian can be written as

$$\mathcal{H}(\boldsymbol{k}') = v_x k'_x \sigma_y \otimes \tau_z + v_y k'_y(\cos\theta\,\sigma_x \otimes \tau_z + \sin\theta\,\sigma_0 \otimes \tau_y)$$

where $v_x = 2.16\times10^4$ m/s and $v_y = 8.35\times10^5$ m/s, according to the first-principles calculation. A huge anisotropy is found in the Dirac bands at D2. To find the SOC effect on the Dirac states, we calculated the band structure with various strengths of SOC and extract the Fermi velocity at D1 and D2 [see Figs. 5.2(d) and 5.2(e)]. Without SOC, the two bands of the Dirac cone become degenerate in the direction of X_1-M-X_2. This can be seen in the above eqs: The terms depending on the spin matrices $\sigma_{x,y,z}$ vanishes in the absence of SOC, leaving only one term with σ_0, which induces the band splitting in X_1-Γ and X_2-Γ directions. Consequently, the bands form a nodal line at the boundary of the Brillouin zone, since the bands are

degenerate along X_1-M-X_2 [see Fig. 5.2(d)]. In this sense, the nodal-line band structure in the absence of SOC also arises from the nonsymmorphic symmetry of the lattice. However, this band degeneracy is not robust against spin-orbit coupling. Turning on SOC, the nodal line is gapped everywhere except X_1 and X_2. The Fermi velocity v_y at D1 and v_x at D2 grows from zero as SOC increases, leading to the formation of Dirac cones. In other words, SOC transforms the system from a nodal-line system into a Dirac-fermion state. It is worth noting that v_x at D2 remains highly suppressed even at artificially enlarged SOC, leading to an anisotropic Dirac cone at D2.

5.3. ARPES and calculated band structures

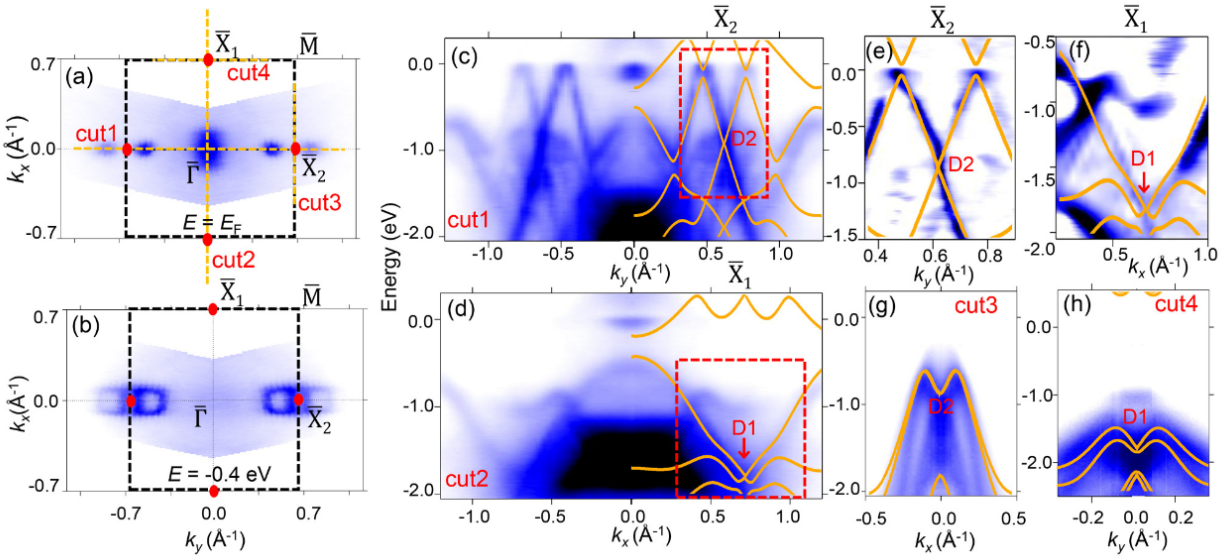

Fig. 5.3. (a), (b) Isoenergy contours of 1L α-Sb taken at E = EF and −0.4 eV, respectively. (c), (d) ARPES spectra taken along the lines of "cut1" and "cut2" marked in (a), respectively. The ARPES spectra are overlaid with the calculated bands. (e), (f) Second derivative of the spectra shown in the red boxes marked in (c) and (d). (g), (h) ARPES spectra taken along "cut3" and "cut4" marked in (a).

The ARPES result taken from the 1L α-Sb sample is shown in Fig. 5.3. The photon energy is 21.2 eV. There are three prominent features on the Fermi surface, namely, one electron pocket at Γ and two hole pockets near X_2 [see Fig. 5.3(a)]. The central pocket disappears in the isoenergy contour at $E = -0.4$ eV , as shown in Fig. 3(b). The band spectrum taken along the X_2-Γ-X_2 and X_1-Γ-X_1 directions are plotted in Figs. 5.3(c) and 3(d). The calculated band dispersion is overlaid on the ARPES spectrum for comparison. The second derivative of the spectra near X_2 and X_1 is shown in Figs. 5.3(e) and 5.3(f) for a better visualization of the band dispersion. The theoretical bands agree with the ARPES spectrum, especially both showing the band crossings at X_1 and X_2. We note that the MBE sample is slightly electron doped due to the charge transfer between the film and the substrate, and the Fermi level of the calculated bands is shifted to match the ARPES spectrum. Fig. 5.3(g) and 5.3(h) show the band dispersion around X_1 and X_2 in a perpendicular direction. In the M-X_2-M direction, the two subbands dispersing away from the Dirac nodes are nearly degenerate, which leads to a huge anisotropy in the Dirac band contours. The anisotropy of Dirac bands is less prominent in the M -X_1-M direction. This is consistent with the calculated band structure. We note that the minor discrepancy between the ARPES spectrum and first-principles bands can be attributed to the substrate effects on the MBE samples. We note that the linear Dirac bands along the X_2-Γ are clearly resolved by ARPES, because the Dirac state at X_2 is isolated in energy from the other occupied states and thus largely unaffected by the presence of the other bands. By contrast, the Dirac point at X_1 is close to the other states in energy, and the Dirac bands are bent in the vicinity of the other bands. This explains the tangled spectrum taken along the X_1-Γ direction. The ARPES results taken from the 2L α-Sb sample are shown in Fig. 5.4. According to the STM characterization, the sample possesses 1L and 2L domains,

therefore we can see contributions from 1L and 2L to the total ARPES spectrum. From a comparison with the calculated bands, we can identify the spectrum from 2L α-Sb films. The ARPES results again show Dirac points (band degeneracy) at X_1 and X_2. The Dirac cone centered at X_2 exhibits a large anisotropy in the band dispersion. The ARPES results along with the first-principles band simulations unambiguously demonstrate the existence of 2D Dirac states in the nonsymmorphic α-Sb films.

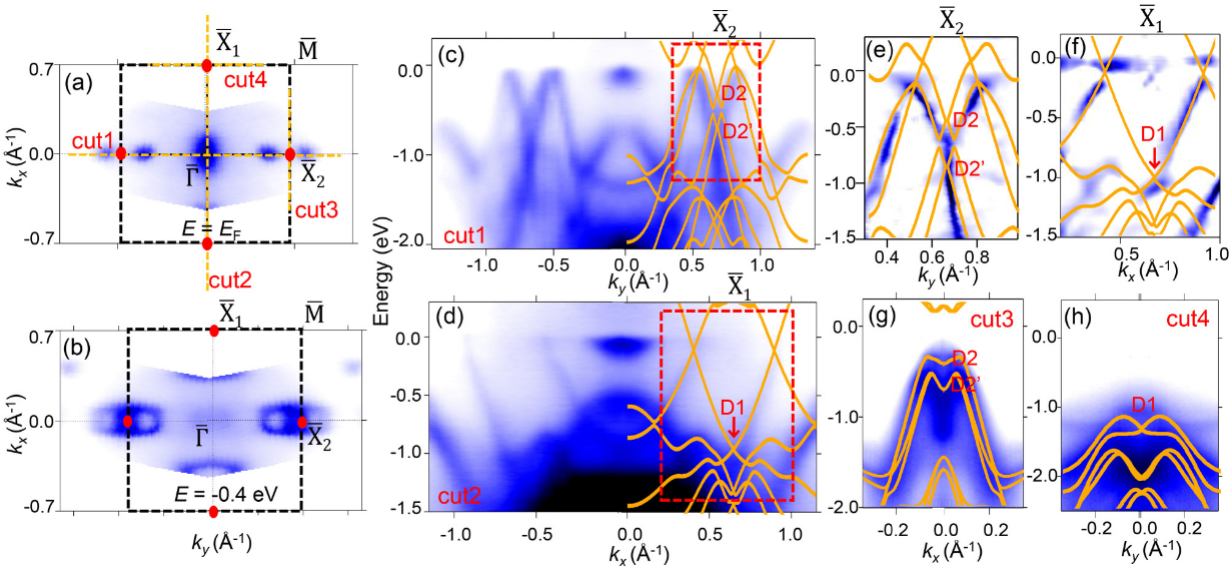

. Fig. 5.4. (**a**), (**b**) Isoenergy contours of 2L α-Sb taken at E = EF and −0.4 eV, respectively. (c), (d) ARPES spectra taken along the lines of "cut1" and "cut2" marked in (a), respectively. The ARPES spectra are overlaid with the calculated bands. (e), (f) Second derivative of the spectra shown in the red boxes marked in (c) and (d). (g), (h) ARPES spectra taken along "cut3" and "cut4" marked in (a).

5.4. Conclusions

Here In summary, our ARPES measurements and first-principles calculations showed that α-Sb hosts Dirac-fermion states at the high-symmetry momentum points X_1 and X_2. The band degeneracy at the Dirac points is protected by the nonsymmorphic symmetry of the lattice. The lattice symmetry guarantees that the Dirac states in α-Sb are robust even in the presence of strong SOC. SOC actually plays an important role in the formation of Dirac states. Without SOC, the two branches of the Dirac cone become degenerate along the $X_{1,2}$-M directions and result in a nodal-line band structure [21]. In this sense, the Dirac states of α-Sb are spin-orbit coupled, in contrast to the spinless ones of graphene. Breaking the lattice symmetry, on the other hand, can lift the band degeneracy at the Dirac points and yield gapped phases [21]. This correspondence principle of lattice symmetry and nodal band structure applies to all 2D nonsymmorphic crystalline materials. The results open a door for exploring different "graphene" physics in a rich material pool of nonsymmorphic materials with strong spin-orbit coupling.

Reference

[1] K. S. Novoselov, A. K. Geim, S. V. Morozov, D. Jiang, M. I. Katsnelson, I. V. Grigorieva, S. V. Dubonos, and A. A. Firsov, Nature (London) 438, 197 (2005).

[2] Y. Zhang, Y.-W. Tan, H. L. Stormer, and P. Kim, Nature (London) 438, 201 (2005).

[3] M. Z. Hasan and C. L. Kane, Rev. Mod. Phys. 82, 3045 (2010).

[4] N. P. Armitage, E. J. Mele, and A. Vishwanath, Rev. Mod. Phys. 90, 015001 (2018).

[5] A. H. Castro Neto, F. Guinea, N. M. R. Peres, K. S. Novoselov, and A. K. Geim, Rev. Mod. Phys. 81, 109 (2009).

[6] S. Y. Zhou, D. A. Siegel, A. V. Fedorov, F. Gabaly, A. K. Schmid, A. H. C. Neto, D.-H. Lee, and A. Lanzara, Nat. Mater. 7, 259 (2008).

[7] S. M. Young and C. L. Kane, Phys. Rev. Lett. 115, 126803 (2015).

[8] S. Guan, Y. Liu, Z.-M. Yu, S.-S. Wang, Y. Yao, and S. A. Yang, Phys. Rev. Mater. 1, 054003 (2017).

[9] B. J. Wieder and C. L. Kane, Phys. Rev. B 94, 155108 (2016).

[10] B. J. Wieder, B. Bradlyn, Z. Wang, J. Cano, Y. Kim, H.-S. D. Kim, A. M. Rappe, C. L. Kane, and B. A. Bernevig, Science 361, 246 (2018).

[11] H. C. Po, A. Vishwanath, and H. Watanabe, Nat. Commun. 8, 50 (2017).

[12] R.-J. Slager, A. Mesaros, V. Juricˇic´, and J. Zaanen, Nat. Phys. 9, 98 (2013).

[13] J. Kruthoff, J. de Boer, J. van Wezel, C. L. Kane, and R.-J. Slager, Phys. Rev. X 7, 041069 (2017).

[14] C. Fang and L. Fu, Phys. Rev. B 91, 161105(R) (2015).

[15] Z. Wang, A. Alexandradinata, R. J. Cava, and B. A. Bernevig, Nature (London) 532, 189 (2016).

[16] S. Li, Y. Liu, S.-S. Wang, Z.-M. Yu, S. Guan, X.-L. Sheng, Y. Yao, and S. A. Yang, Phys. Rev. B 97, 045131 (2018).

[17] R. Takahashi, M. Hirayama, and S. Murakami, Phys. Rev. B 96, 155206 (2017).

[18] B.-J. Yang, T. A. Bojesen, T. Morimoto, and A. Furusaki, Phys. Rev. B 95, 075135 (2017).

[19] Y. Liu and R. E. Allen, Phys. Rev. B 52, 1566 (1995).

[20] G. Bian, T. Miller, and T.-C. Chiang, Phys. Rev. Lett. 107, 036802 (2011).

[21] P. J. Kowalczyk, S. A. Brown, T. Maerkl, Q. Lu, C.-K. Chiu, Y. Liu, S. A. Yang, X. Wang, I. Zasada, F. Genuzio et al., ACS Nano 14, 1888 (2020).

[22] X. Gonze, B. Amadon, P.-M. Anglade, J.-M. Beuken, F. Bottin, P. Boulanger, F. Bruneval, D. Caliste, R. Caracas, M. Côté et al., Comput. Phys. Commun. 180, 2582 (2009).

[23] X. Gonze, Z. Kristallogr. - Cryst. Mater. 220, 558 (2009).

[24] C. Hartwigsen, S. Goedecker, and J. Hutter, Phys. Rev. B 58, 3641 (1998).

[25] G. Bian, X. wang, T. Miller, and T.-C. Chiang, Europhys. Lett. 101, 27004 (2013).

[26] C. J. Bradley and A. P. Cracknell, The Mathematical Theory of Symmetry in Solids (Clarendon Press, Oxford, U.K., 1972).

6. REALIZATION OF UNPINNED TWO-DIMENSIONAL DIRAC STATES IN ANTIMONENE

Two-dimensional (2D) Dirac states with linear dispersion have been observed in graphene and on the surface of topological insulators. 2D Dirac states discovered so far are exclusively pinned at high-symmetry points of the Brillouin zone, for example, surface Dirac states at Γ in topological insulators $Bi_2Se(Te)_3$ and Dirac cones at K and K' points in graphene. The low-energy dispersion of those Dirac states are isotropic due to the constraints of crystal symmetries. In this work, we report the observation of novel 2D Dirac states in antimony atomic layers with phosphorene structure. The Dirac states in the antimony films are located at generic momentum points. This unpinned nature enables versatile ways such as lattice strains to control the locations of the Dirac points in momentum space. In addition, dispersions around the unpinned Dirac points are highly anisotropic due to the reduced symmetry of generic momentum points. The exotic properties of unpinned Dirac states make antimony atomic layers a new type of 2D Dirac semimetals that are distinct from graphene.

6.1. Introduction

Two-dimensional (2D) Dirac states have attracted tremendous research interests since the discovery of graphene and topological insulators [1–5]. The linear dispersion and vanishing effective mass of Dirac fermion states are connected to interesting physical phenomena [4]. To date, gapless 2D Dirac states have only been observed in graphene [1,2] and on the surface of topological insulators [3,6]. The Dirac states in those 2D systems are exclusively pinned at high-symmetry points of the Brillouin zone, such as K(K') of graphene (due to the C3 rotational symmetry). The Dirac states also feature isotropic low-energy dispersion due

to the local rotational symmetry of the crystal lattice. The warping effect, a higher-order correction to the linear dispersion, becomes prominent only for states distant from the Dirac point [7]. These features impose constraints on applications of the massless Dirac states. For example, the two Dirac cones in graphene are pinned at opposite corners of the Brillouin zone. It is difficult to make two valleys effectively coupled in monolayer graphene. Therefore, 2D Dirac states that are unpinned in momentum space are desirable for enabling novel functionalities in Dirac materials.

Recently, it has been theoretically proposed that multiple 2D Dirac states emerge at generic momentum points in the low-energy spectrum of group-Va few-layers with phosphorene-like lattice structure [8]. In this case, highly anisotropic cone is a character of the unpinned Dirac point, because the generic k point has much reduced local symmetry. The unpinned nature makes the Dirac nodes movable in momentum space, e.g., by lattice strains. All these properties lead to tunable transport properties of Dirac states, which are unavailable in conventional 2D Dirac materials. Therefore, the Dirac states in group-Va few-layers are distinct from those in graphene and thus, offer new insights into the Dirac fermion physics at low dimensions. In this work, we report the observation of multiple unpinned Dirac states near the Fermi level in single layer (1L) and double layer (2L) antimony (Sb) films in the phosphorene structural phase.

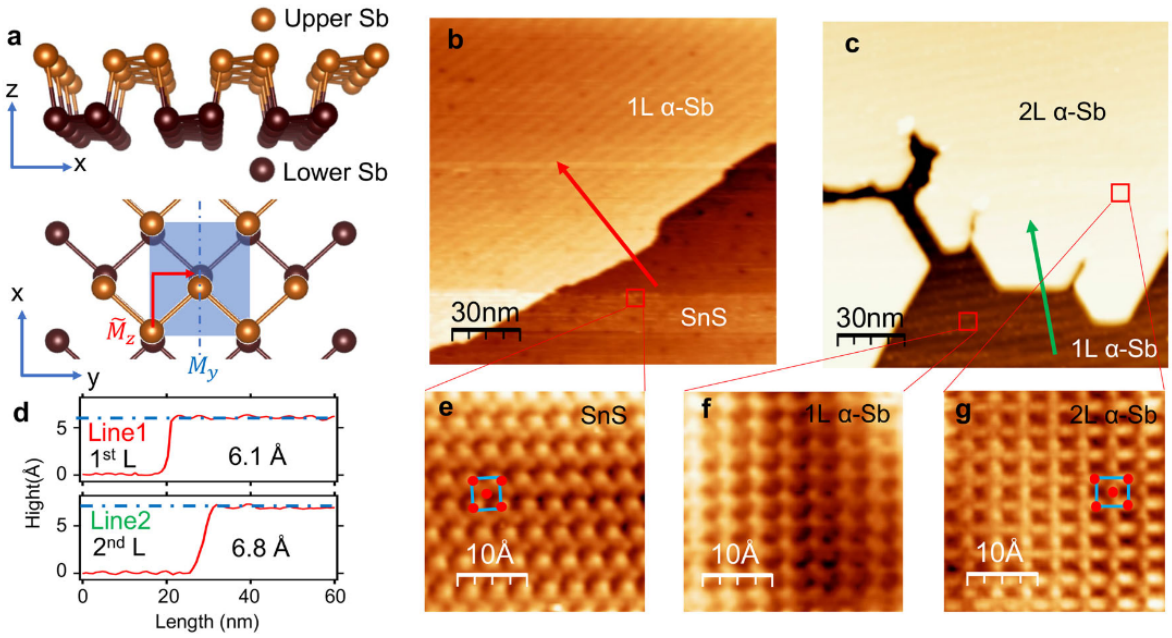

Fig. 6.1 | Lattice structure and STM characterization of α-Sb films. **a** Side and top views of α-Sb lattice structure. **b** STM image of 1L α-Sb grown on SnS substrate. **c** STM image of 1L and 2L α-Sb domains. **d** The height profiles taken along the red arrow in **b** and the green arrow in **c. e–g** Atom-resolved STM images taken from SnS surface, 1L α-Sb and 2L α-Sb domains.

A group-Va pnictogen atom typically forms three covalent bonds with its neighbors. In the 2D limit, two allotropic structural phases, the orthorhombic phosphorene-like phase [9,10] and the hexagonal honeycomb-like phase [11,12], are allowed by this requirement. The two phases are referred to as α and β-phases, respectively, in the literature. In the family of group-Va elements, P, As, Sb and Bi can form phosphorene-like structures [9,10,13–19]. Here we focus on the phosphorene-like α-antimonene (α-Sb for short). As shown in Fig. 6.1a, in the lattice of 1L α-Sb, the three Sb-Sb bonds form a tetrahedral configuration. This results in two

atomic sublayers with a vertical separation comparable to the in-plane bond length. In each atomic sublayer, the bonding between Sb atoms forms zig-zag chains along the y- direction. The unit cell, marked by the blue rectangle in Fig. 1a, has a four-atom basis (two in each atomic plane). The space group of the lattice is D_{2h} (7), which includes space inversion P, a vertical mirror plane M_y perpendicular to y, two two-fold rotational axes C_{2y} and C_{2z}, and a glide mirror $\widetilde{M}_z$ that is parallel to the x–y plane and lies in the middle between the two atomic planes. The glide mirror reflection is composed of a mirror reflection and an in-plane translation by (0.5a, 0.5b) [20], and it interchanges the two atoms connected by the red arrow in Fig. 6.1a. Previous works [20,21] have shown that the glide mirror of bismuthene and antimonene leads to band crossings at certain high symmetry momentum points of the Brillouin zone. However, those nodal points are >0.5 eV away from the Fermi level and thus irrelevant to the transport properties of the materials. In this work, we demonstrate by angle-resolved photoemission spectroscopy (ARPES) the existence of unpinned Dirac states at the Fermi level in α-Sb films, which makes these materials an ideal 2D Dirac semimetal. The Dirac states are located at generic momentum points. The location of Dirac points can be shifted by lattice strains, which is confirmed by our ARPES experiments.

6.2. Thin film growth and lattice structures

We grew α-Sb thin films by the method by molecular beam epitaxy (MBE). α-Sb has been grown on various substrates [22–24]. In this work, we chose SnS as substrate, because SnS(001) surface has similar lattice parameters and lattice symmetry as α-Sb, and thus, favors the formation of α-Sb. The (001) surface lattice constants of SnS are a = 4.35 Å and b = 3.99 Å [25]. The crystallographic structure of the epitaxial sample is shown in Fig. 6.1a.

The in-plane lattice constants of 1L α-Sb are a = 4.42 Å and b = 4.30 Å in the x and y-directions, respectively, while the in-plane nearest-neighbor bond length is 2.85 Å. Figure 6.1b, c show the STM image of two α-Sb/SnS samples. The first sample consists of mainly 1L α-Sb islands, as shown in Fig. 6.1c. The height profile taken along the red arrow (shown in Fig. 6.1d) shows that the apparent height of the 1L α-Sb island on the SnS surface is 6.1 Å. The surface unit cell of SnS substrate can be seen in the zoom-in STM image shown in Fig. 6.1e. The second sample possesses both 1L and 2L domains as shown in Fig. 6.1c. The atom-resolved images taken from the 1L and 2L domains (Fig. 6.1f, g) clearly demonstrate the rectangular surface unit cell of α-Sb. The height profile taken along the green arrow in Fig. 6.1c shows the apparent height of the second layer is 6.8 Å, which is slightly larger than that of the first layer due to the lattice relaxation.

6.3. Monolayer Sb ARPES spectrum and calculated bands

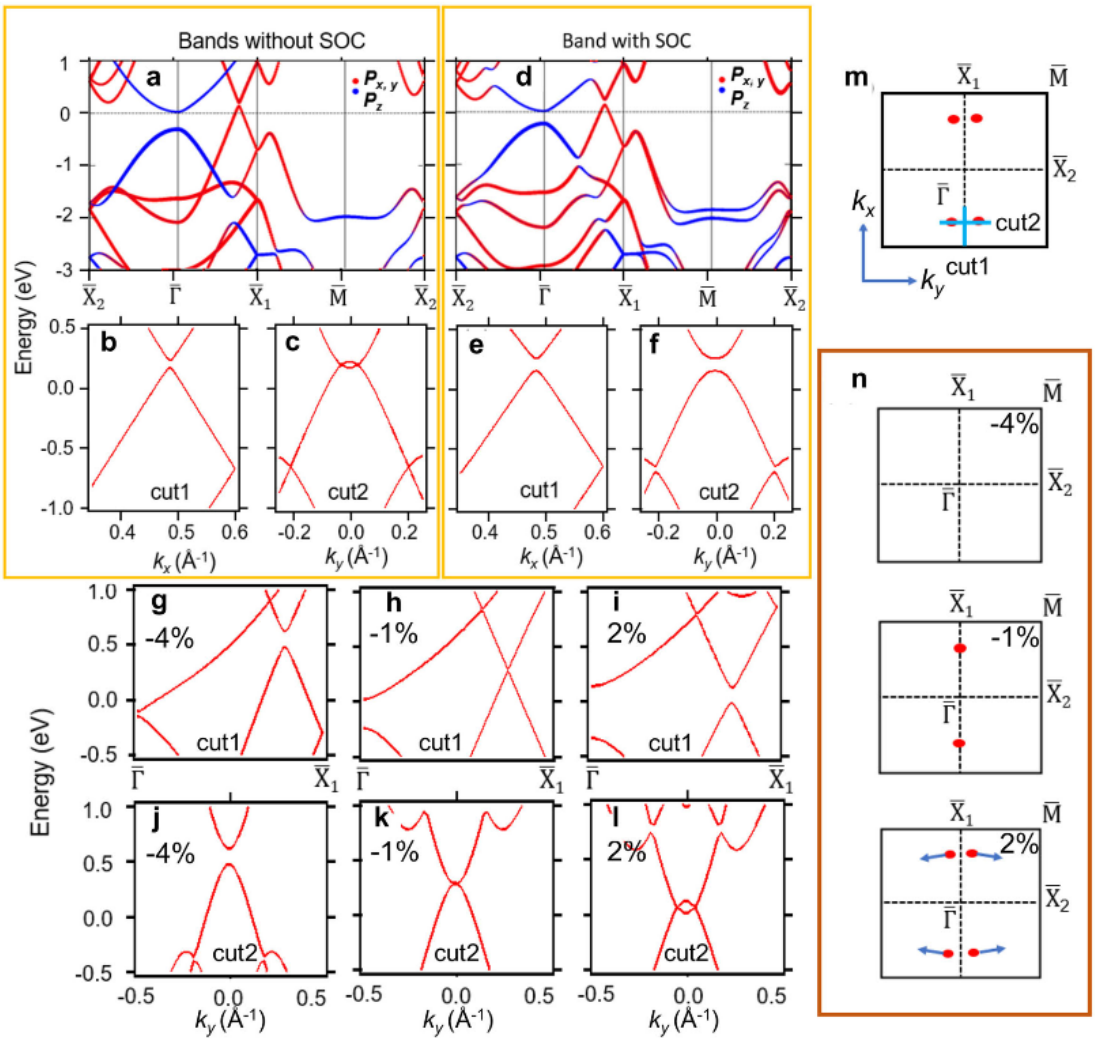

Fig. 6.2 | Calculated band structure of 1L α-Sb. **a** The band structure of 1L α-Sb calculated without the inclusion of SOC. The bands are colored according to their orbital components. **b, c** The calculated band dispersion along 'cut1' and 'cut2' (marked in m) without the inclusion of SOC. **d–f** Same as **a-c**, but calculated with the inclusion of SOC. **g–l** Band structure (without SOC) of 1L α-Sb under uniaxial lattice strains along y-direction. **g, j** Band dispersion along 'cut1' and 'cut2' (marked in m) with − 4% lattice strain in y direction. **h, k and i**, l same as **g, j**, but for lattice strains in ^y direction of − 1% and +2%, respectively. m The Brillouin zone of 1L α-Sb. The Dirac points in the case without SOC are marked by the red dots. **n** The locations of Dirac points under uniaxial lattice strains of

−4%,−1% and +2% in y-direction. The blue arrows indicate the movement of Dirac points as the lattice constant b increases.

To study the electronic band structure, we performed first-principles calculations for the band structure of 1L and 2L α-Sb films. The calculated band structure of 1L α-Sb is shown in Fig. 6.2. In the absence of SOC, the bottom conduction band and the top valence band at Γ" are separated by an energy gap of 0.3 eV, as shown in Fig. 2a. The two bands are dominated of the p_z-orbital character near the zone center8. Between Γ and X_1, there is a small hole pocket at the Fermi level, which is generated by the overlap of a pair of bands of mainly the $p_{x,y}$-orbital character [8]. To see this pocket more clearly, we plot the zoom-in band structure along the lines of 'cut1' and 'cut2' marked in Fig. 6.2m. The conduction and valence bands cross each other and leave a pair of nodal points, which lie 0.15 eV above the Fermi level, as shown in Fig. 6.2b, c. It is worth noting that the Dirac nodes are located at generic momentum points, as schematically shown in Fig. 6.2m. In the absence of SOC, the Dirac nodes are stable due to the protection by the spacetime inversion symmetry (PT), which enforces a quantized Berry phase θ_B for each Dirac point. The Berry phase along a closed loop l encircling each Dirac node is defined as follows,

$$\theta_B = \oint_\ell \boldsymbol{A_k} \cdot \mathrm{d}\boldsymbol{k} = \pm\pi,$$

where Ak is the berry connection of the occupied valence bands8. On the other hand, with the inclusion of SOC, the number of bands is doubled due to the spin degrees of freedom. Gap-opening terms are allowed in the Hamiltonian to lift the band degeneracy at Dirac points. This can be seen in the band structure plotted in Fig. 6.2d–f. Though the hole pockets remain largely unchanged at the Fermi level, the conduction and valence bands are separated

by an SOC-induced energy gap of 70 meV. The gapped band dispersion is similar to the quasi-2D Dirac states observed in bulk crystal ZrSiS [26]. Below the Fermi level, the lower part of the gapped Dirac cone remains nearly linear.

The band dispersion close to the Dirac nodes in absence of SOC can be described by the linear Hamiltonian,

$$\widetilde{H}(\boldsymbol{k}) = v_x k_x \sigma_y + \omega v_y (k_y - \omega k_0)\sigma_x,$$

where k_x is measured from the location of the Dirac points, $\omega = \pm 1$ indicates the opposite chirality of the two Dirac nodes along 'cut2' in Fig. 6.2m, k_0 measures the separation between the two Dirac nodes in k_y direction, $\sigma_{x,y}$ are the Pauli matrices for pseudospin, and $v_{x,y}$ is the group velocity at the Dirac point in k_x and k_y directions, respectively. According to the calculated band structure in Fig. 6.2a–c, $v_x = 8.35 \times 10^5$ m/s and $v_y = 4.08 \times 10^5$ m/s, indicating a highly anisotropic Dirac cone. To further examine the unpinned nature of the Dirac bands, we calculated the band structure under uniaxial lattice strains. The lattice constant b in y direction is changed by −4%, −1% and +2%, where the '+' and '−' signs correspond to lattice expansion and com- pression, respectively. The results are plotted in Fig. 6.2g–l. Under the lattice stain of −4%, the conduction and valence bands are separated in energy, and thus no Dirac nodes are formed as shown in Fig. 6.2g, j. At the critical lattice strain of −1%, the conduction and valence bands touch each other, leading to a quadratic Dirac cone (Fig. 6.2h, k), in which the band dispersion is linear in k_x direction and quadratic in k_y direction. The quadratic Dirac cone signals a topological transition between a semimetallic phase and a band insulator [27]. The quadratic band dispersion occurs when two Dirac points merge in a two-dimensional crystal. This can be seen from the fact that increasing the lattice constant b from the critical value makes the quadratic Dirac node split

into two linear Dirac nodes, as demonstrated in Fig. 6.2i, l. The separation between the two Dirac nodes is sensitive to the magnitude of lattice strains. The arrows in Fig. 6.2n indicates the movement of Dirac nodes when the lattice is further expanded in y direction. These results reveal two prominent features of unpinned Dirac states: (1) the Dirac nodes can freely move in the momentum space by perturbations such as lattice strains; and (2) the dispersions of Dirac bands are intrinsically highly anisotropic due to the reduced symmetry at the location of the generic Dirac points.

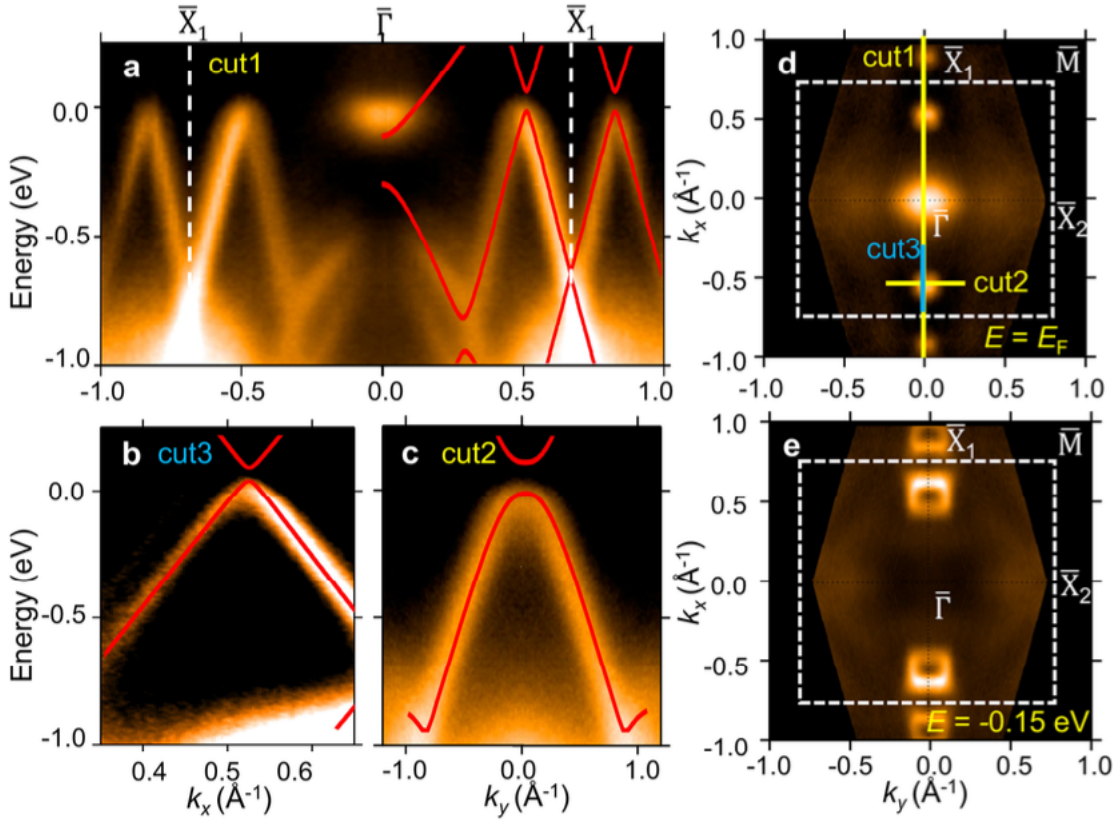

Fig. 6.3 | ARPES spectrum of 1L α-Sb. **a** ARPES spectrum taken along X_1-Γ-X_1. **b, c** Zoom-in spectra taken along 'cut3' and 'cut2' (marked in d), respectively. **d** Fermi surface taken from the 1L α-Sb sample by ARPES. **e** ARPES iso-energy contour taken at E = −0.15 eV.

The ARPES result taken from the 1L α-Sb sample is shown in Fig. 6.3. The photon energy is 21.2 eV. There are three prominent features on the Fermi surface, namely, one electron pocket at Γ and two hole pockets near X_1 (Fig. 6.3d). The band spectrum taken along the X_1 -Γ-X_1 direction is plotted in Fig. 6.3a. The calculated band dispersion is overlaid on the ARPES spectrum for comparison. The theoretical bands agree with the ARPES spectrum, especially in showing the linear bands between Γ and X_1 . The molecular beam epitaxy (MBE) sample is slightly electron-doped due to the charge transfer from the SnS substrate to the α-Sb overlayer, and thus the Fermi level of the calculated bands was shifted to match the ARPES spectrum. We note that the band calculation was performed with freestanding film geometry and experimental lattice constants. The good consistency between the calculated band structure and ARPES spectra indicates that the substrate coupling is weak, and thus, the epitaxial α-Sb film can be considered as nearly freestanding. In the iso-energy contour taken at 0.1 eV below the Fermi level (Fig. 6.3e), there are only a pair of circular pockets sitting close to X_1, which are the cross-sections of the lower Dirac cone. The zoom-in spectra along 'cut2' and 'cut3' are plotted in Fig. 6.3b, c. The ARPES spectra show clearly the linear band dispersion from the lower part of the gapped Dirac cone.

6.4. Bilayer Sb ARPES spectrum and calculated bands

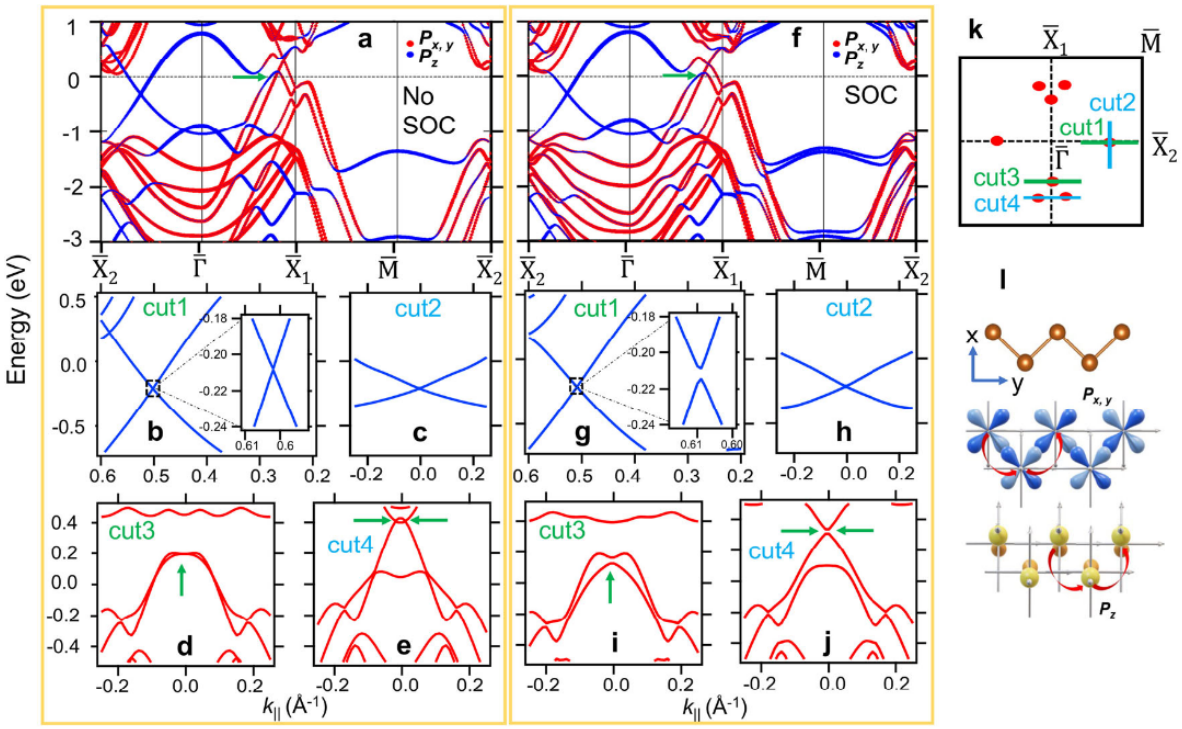

Fig. 6.4 Calculated band structure of 2L α-Sb. **a** The band structure of 2L α-Sb calculated without the inclusion of SOC. **b–e** The calculated band dispersions along 'cut1-4', respectively. The Dirac points in the direction of Γ-X_1 are marked by green arrows in **d** and **e. f–j** Same as **a–e**, but calculated with the inclusion of SOC. **k** The Brillouin zone of 2L α-Sb. The Dirac points in the case without SOC are marked by red dots. **l** Schematic diagrams showing the formation of $p_{x,y}$ and p_z bands.

We also calculated the band structure of 2L α-Sb. The results are summarized in Fig. 6.4. In the absence of SOC (Fig. 6.4a), there are multiple band crossings along the Γ-X_1 direction near the Fermi level. This is because the number of $p_{x,y}$-orbital dominated bands is doubled in the 2L film. The location of Dirac points is schematically plotted in Fig. 6.4k. The zoom-in bands along 'cut3' and 'cut4' in Fig. 6.4d, e clearly show the Dirac states close to the line of Γ-X_1. The Dirac cone in Fig. 6.4d is highly anisotropic. The Dirac node is on the Γ-X1 line and at 0.2 eV above the Fermi level. The two branches of the Dirac cone are nearly degenerate in the direction of 'cut3'. On the other

hand, the bands along 'cut4' (Fig. 6.4e) show a pair of Dirac nodes at 0.4 eV above the Fermi level, which are generated by the small overlap between the conduction and valence bands. The dispersion is similar to the Dirac bands of 1L α-Sb in the absence of SOC. Moreover, there is another band crossing along the Γ-X_2 direction as shown in Fig. 6.4a. The bands at this new nodal point are of p_z orbital character. In Fig. 6.4b, c, the zoom-in bands along 'cut1' and 'cut2' (marked in Fig. 6.4k) show that this new Dirac point is located at a generic momentum point between Γ and X_2, and sit at 0.2 eV below the Fermi level. The Dirac band is gapless in the absence of SOC [8]. The band dispersions calculated with SOC are plotted in Fig. 6.4f, g. Energy gaps are opened at all Dirac nodes marked in Fig. 6.4k. Interestingly, the SOC gap found at the Dirac points of the p_z band (Fig. 4g, h) is very small, only 6 meV. It can be explained by the fact that the p_z band is largely immune to the effects of SOC, since the first-order SOC matrix element of the p_z orbital vanishes, i.e.,

$$\left\langle \Psi_{p_z} | \boldsymbol{L} \cdot \boldsymbol{S} | \Psi_{p_z} \right\rangle = \left\langle \Psi_{p_z} | L_+ S_- + L_- S_+ + L_z S_z | \Psi_{p_z} \right\rangle = 0,$$

where Ψ_{pz} is the wavefunction of the p_z orbital with $L_z = 0$. We note that the p_z orbitals do not hybridize with the $p_{x,y}$ orbitals since they have opposite parities of $\widetilde{M}_z$. The SOC matrix element is nonzero for the $p_{x,y}$ bands due to the mixing of p_x and p_y orbitals as schematically shown in Fig. 6.4l. Therefore, energy gaps can only be opened in the p_z band by higher-order SOC effects induced by the inter-site hoppings [28]. As a result, the SOC gaps are highly suppressed in the p_z band compared to those gaps found in the $p_{x,y}$ bands (Fig. 6.4i, j). Therefore, the unpinned Dirac bands formed by the p_z orbitals is nearly gapless even in the presence of SOC.

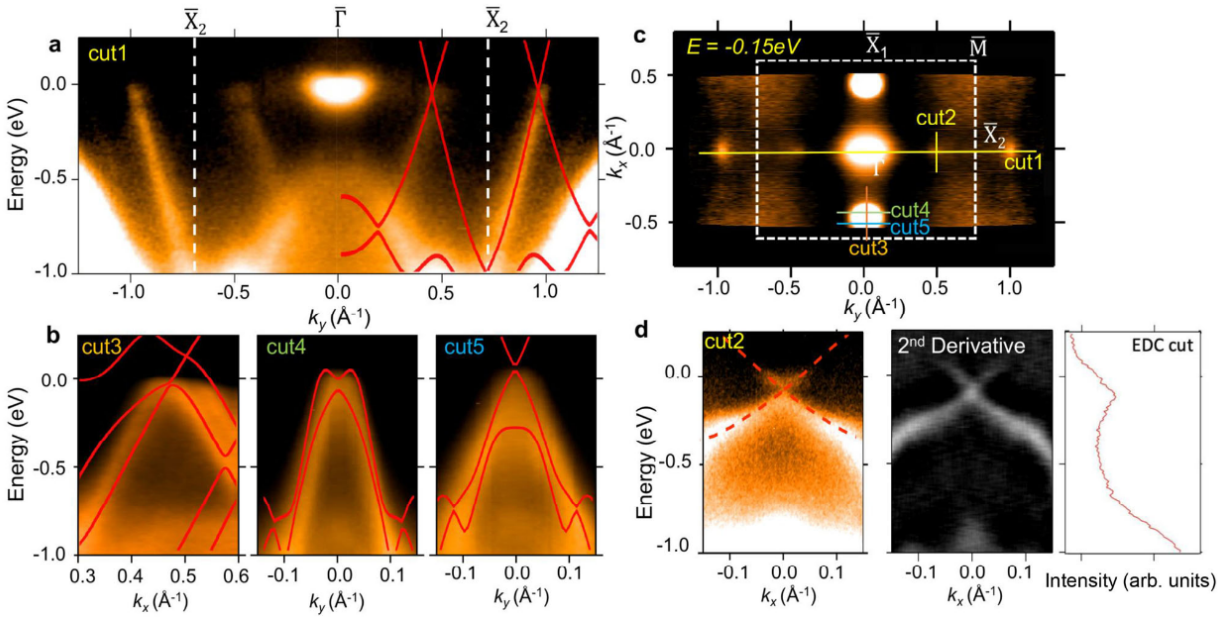

Fig. 6.5 ARPES spectrum of 2L α-Sb. **a** ARPES spectrum taken along X_2-Γ-X_2. **b** ARPES spectra taken along 'cut3-5' (marked in **c**). **c** ARPES iso-energy contour of 2L α-Sb at E = − 0.15 eV. **d** ARPES spectrum taken along 'cut2' showing the Dirac bands of p_z orbital character. The second derivative of the ARPES spectrum along 'cut2' is plotted for better visualization of the Dirac band structure. The energy distribution curve (EDC) taken at the momentum of the band crossing demonstrates the absence of a gap at the Dirac point.

We measured the band structure of the 2L α-Sb sample shown in Fig. 6.1c. The ARPES result is plotted in Fig. 6.5. The Fermi surface contour is plotted in Fig. 6.5c. We note that the sample consists of 1L and 2L domains. The bright pocket located at the zone center is from the 1L domains of the samples. The nodal features of 2L α-Sb at generic momentum points can also be easily identified. The band spectrum along the X_2 -Γ-X_2 direction (Fig. 6.5a) exhibits the linear Dirac band dispersion of 2L α-Sb, which is in good agreement with the calculated bands. The consistency can also be seen in the spectra taken along 'cut3-5'

(Fig. 6.5b). The zoom-in spectrum along 'cut2' is plotted in Fig. 6.5d. Dirac point of the p_z band is at 0.2 eV below the Fermi level. No apparent gap was observed at the Dirac point. The experimental result confirms that the energy gap at the Dirac point of the p_z band is less than the energy resolution of our ARPES instrument (~25 meV).

6.5. The unpinned nature and summary

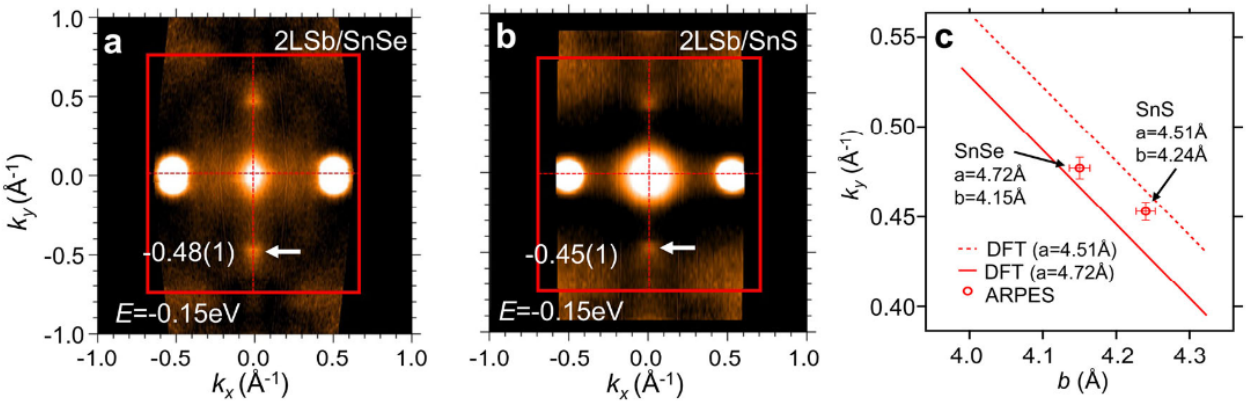

Fig. 6.6 | ARPES iso-energy contours of 2L Sb films grown on SnS and SnSe showing the unpinned nature of Dirac states. **a** ARPES iso-energy contour at E = − 0.15 eV taken from the 2L α-Sb sample grown on SnSe substrate. The Dirac point of the p_z band is marked by the white arrow. **b** Same as a, but from the sample grown on SnS substrate. **c** The location of the Dirac point of the p_z band. The solid line shows the calculated location of the Dirac point for different lattice constant b and a fixed value of a, 4.72 Å. The dashed line is same as the solid line but for a = 4.15 Å. The open circles indicate the experimental results from the SnS and SnSe samples.

To demonstrate the unpinned nature of the Dirac states, we performed ARPES measurements on 2L α-Sb samples grown on a different substrate, SnSe. The epitaxial α-Sb films on SnSe and SeS substrates have different lattice parameters due to the lattice strains caused by the

substrate effects. According to the STM measurements, the in-plane lattice parameters of 2L α-Sb are a=4.72Å, b=4.18Å for the SnSe sample, and a=4.51Å, b = 4.27 Å for the SnS sample. We observed clearly the shift of Dirac points in the SnSe sample compared to the SnS sample. The distance from the Dirac point of the p_z band to the Brillouin zone center is 0.48 $Å^{-1}$ for the SnSe sample and 0.45 $Å^{-1}$ for the SnS sample, as shown in the ARPES iso-energy contours taken from the two samples (Fig. 6.6a, b). The shift of the Dirac point in momentum space due to the lattice strain is also confirmed by the first-principles calculations as shown in Fig. 6.6c. Therefore, our ARPES experiments unambiguously establish the existence of the unpinned Dirac states in α-Sb.

In summary, our ARPES measurements and first-principles calculations clearly demonstrated that α-Sb hosts unpinned Dirac states in both 1L and 2L cases. The Dirac nodes are protected by the spacetime inversion symmetry in the absence of SOC. SOC of the system, on the other hand, induces energy gaps at the Dirac nodes. Surprisingly, we found that the Dirac bands formed by Sb p_z orbitals remain nearly gapless even in the presence of SOC due to the highly suppressed SOC matrix elements. The 2D Dirac nodes at generic k-points are unpinned and have highly anisotropic dispersions, which are experimentally confirmed in this study for the first time. The unpinned nature enables versatile ways such as lattice strains to control the locations and the dispersion of the Dirac states. It opens the door to inducing interactions between Dirac states by moving unpinned states closer in momentum space. The Dirac states with tunable properties and controllable couplings are useful for transport and optical applications [29–31]. All of group-Va elements including P, As, Sb and Bi can form phosphorene-like structures [9,10,13–19]. The conduction and

valence bands of P and As monolayers are far apart in energy (1.2 eV for P and 0.4 eV for As). Consequently, no Dirac states can form near the Fermi level. On the other hand, the conduction and valence bands of Sb and Bi layers overlap in energy and can generate band crossings near the Fermi level. The size of SOC gaps depends on the effective strength of SOC of the system. The strength of atomic spin-orbit coupling is proportional to the fourth power of the atomic number ($\propto Z^4$). So, Bi has a much stronger SOC coupling compared to Sb, resulting in larger SOC gaps at the Dirac points of α-Bi [8,12]. Therefore, α-Sb atomic layers studied in this work provide an ideal platform, compared with other elements in group-Va, for exploring novel properties of unpinned 2D Dirac fermions.

Reference

1. Novoselov, K. S. et al. Two-dimensional gas of massless Dirac fer- mions in graphene. Nature 438, 197–200 (2005).

2. Zhang, Y., Tan, Y.-W., Stormer, H. L. & Kim, P. Experimental obser- vation of the quantum Hall effect and Berry's phase in graphene. Nature 438, 201–204 (2005).

3. Hasan, M. Z. & Kane, C. L. Colloquium : topological insulators. Rev. Mod. Phys. 82, 3045–3067 (2010).

4. Castro Neto, A. H., Guinea, F., Peres, N. M. R., Novoselov, K. S. & Geim, A. K. The electronic properties of graphene. Rev. Mod. Phys. 81, 109–162 (2009).

5. Armitage, N. P., Mele, E. J. & Vishwanath, A. Weyl and dirac semi- metals in three-dimensional solids. Rev. Mod. Phys. 90, 015001 (2018).

6. Qi, X.-L. & Zhang, S.-C. Topological insulators and super- conductors. Rev. Mod. Phys. 83, 1057–1110 (2011).

7. Fu, L. Hexagonal warping effects in the surface states of the topo- logical insulator Bi2Te3. Phys. Rev. Lett. 103, 266801 (2009).

8. Lu, Y. et al. Multiple unpinned Dirac points in group-Va single-layers with phosphorene structure .npjComput.Mater.2,16011(2016).

9. Li, L. et al. Black phosphorus field-effect transistors. Nat. Nano 9, 372–377 (2014).

10. Liu, H. et al. Phosphorene: an unexplored 2D semiconductor with a high hole mobility. ACS Nano 8, 4033–4041 (2014).

11. Ji, J. et al. Two-dimensional antimonene single crystals grown by van der Waals epitaxy. Nat. Commun. 7, 13352 (2016).

12. Bian, G. et al. Survey of electronic structure of Bi and Sb thin films by first-principles calculations and photoemission measurements. J. Phys. Chem. Solids 128, 109–117 (2017).

13. Liu, Q., Zhang, X., Abdalla, L. B., Fazzio, A. & Zunger, A. Switching a Normal Insulator into a Topological Insulator via Electric Field with Application to Phosphorene. Nano Lett. 15, 1222–1228 (2015).

14. Kamal, C. & Ezawa, M. Arsenene: Two-dimensional buckled and puckered honeycomb arsenic systems. Phys. Rev. B 91, 085423 (2015).

15. Zhang, S., Yan, Z., Li, Y., Chen, Z. & Zeng, H. Atomically thin arsenene and antimonene: semimetal-semiconductor and indirect-direct band-gap transitions. Angew. Chem. Int. Ed. 54, 3112–3115 (2015).

16. Wang, X.-S., Kushvaha, S. S., Yan, Z. & Xiao, W. Self-assembly of antimony nanowires on graphite. Appl. Phys. Lett. 88, 233105 (2006).

17. Bian, G., Miller, T. & Chiang, T.-C. Electronic structure and surface- mediated metastability of bi films on si(111)-7 × 7 studied by angle- resolved photoemission spectroscopy. Phys. Rev. B 80, 245407 (2009).

18. Kowalczyk, P. J. et al. Electronic size effects in three-dimensional nanostructures. Nano Lett. 13, 43–47 (2013).

19. Kundu, A. K., Gu, G. & Valla, T. Quantum size effects, multiple dirac cones, and edge states in Ultrathin Bi(110) films. ACS Appl. Mater. Interfaces 13, 33627–33634 (2021).

20. Kowalczyk,P.J.etal.Realizationofsymmetry-enforcedtwo- dimensional deirac fermions in nonsymmorphic α-Bismuthene. ACS Nano 14, 1888–1894 (2020).

21. Lu, Q. et al. Observation of symmetry-protected dirac states in nonsymmorphic α-antimonene. Phys. Rev. B 104, L201105 (2021).

22. Le Ster, M., Maerkl, T., Kowalczyk, P. J. & Brown, S. A. Moiré patterns in van der waals heterostructures. Phys. Rev. B 99, 075422 (2019).

23. Hogan, C. et al. Temperature driven phase transition at the anti- monene/bi2se3 van der waals heterostructure. ACS Nano 13, 10481–10489 (2019).

24. Flammini, R. et al. Evidence ofβ-antimonene at the sb/bi2se3 inter- face. Nanotechnology 29, 065704 (2018).

25. Lu, Q. et al. Unexpected large hole effective masses in snse revealed by angle-resolved photoemission spectroscopy. Phys. Rev. Lett. 119, 116401 (2017).

26. Schoop, L. M. et al. Dirac cone protected by non-symmorphic symmetry and three-dimensional Dirac line node in ZrSiS. Nat. Commun. 7, 11696 (2016).

27. Montambaux, G., Piéchon, F., Fuchs, J.-N. & Goerbig, M. O. Merging of dirac points in a two-dimensional crystal. Phys. Rev. B 80, 153412 (2009).

28. Liu, C.-C. et al. Low-energy effective hamiltonian for giant-gap quantum spin hall insulators in honeycomb x-hydride/halide (x = N − − Bi) monolayers. Phys. Rev. B 90, 085431 (2014).

29. Zhou, S. Y. et al. Origin of the energy bandgap in epitaxial graphene. Nat. Mater. 7, 259 (2008).

30. Xu, S.-Y. et al. Hedgehog spin texture and Berry's phase tuning in a magnetic topological insulator. Nature Physics 8, 616–622 (2012).

31. Hor, Y. S. et al. Development of ferromagnetism in the doped topological insulator bi2−xmnxte3. Phys. Rev. B 81, 195203 (2010).

32. Kresse, G. & Furthmüller, J. Efficient iterative schemes for ab initio total-energy calculations using a plane-wave basis set. Phys. Rev. B 54, 11169–11186 (1996).

33. Perdew,J.P.,Burke,K.&Ernzerhof,M.Generalizedgradient approximation made simple. Phys. Rev. Lett. 77, 3865–3868 (1996).

7. DISCOVERY OF A TWO-DIMENSIONAL WEYL SEMIMENTAL

The discoveries of two-dimensional (2D) Dirac semimetal states in graphene and 3D Weyl semimetals in bulk TaAs have led to an exciting territory of modern condensed matter physics where a multitude of emergent phases are generated from the interplay of quantum mechanics, relativity, and topology. So far, however, a 2D variant of Weyl semimetals remain elusive due to the instability of linear band crossings in reduced dimensions. In this chapter, we report the realization of a 2D Weyl semimetal in monolayer-thick epitaxial bismuthene grown on SnS(Se) substrate. The band gap of bismuthene is eliminated by the space-inversion-symmetry-breaking that is driven by interfacial charge transfer, which leads to a gapless spin-polarized Weyl band dispersion. The spin polarization of the Weyl bands is observed in spin-resolved photoemission measurements. The band topology of the 2D Weyl cones guarantees the existence of 1D Fermi arc edge states. These results establish epitaxial bismuthene as an ideal 2D Weyl semimetal that provides a unique platform for spintronic applications such as high-efficient spin filters and spin-valley separators.

7.1. Introduction

The discovery of Dirac materials, which feature massless states near the Fermi level, has driven the rise of the topological era in condensed matter physics. In particular, graphene, a two-dimensional (2D) Dirac semimetal, has enabled the exploration of relativistic physics in tabletop experiments [1–3]. The fundamental work on graphene set the foundation for future research ranging from topological insulators, valleytronics, to twistronics [4–9]. The subsequent generalization from 2D to 3D platforms prompted the discovery of bulk Dirac

semimetals. This generalization has shed light on the behaviors of higher dimensional massless carriers, tilted Dirac cones, and protected surface states [10–15]. The discovery of Weyl semimetals, which host spin-split massless 3D quasiparticles, is particularly exciting since is the first experimental realization of the Weyl Fermion which was proposed long ago in the context particle physics [15–19]. The chiral nodal points and 2D Fermi arc surface states of 3D Weyl semimetals give rise to exotic properties such as the chiral anomaly, unusual optical conductivity and nonlocal transport [20–30]. Generalization of a 3D Weyl state to 2D gives states that can be considered as a spin-split version of graphene where the spin and valley degrees of freedom are intrinsically entangled in a 2D Weyl semimetal. A minimum summary of Dirac and Weyl semimetals is presented in Fig. 7.1a, which highlights the prediction a subsequent discovery of 3D and 2D Dirac and Weyl states. So far, however, discovery of gapless 2D Weyl semimetals has remained elusive. This is due to the fact that the nodal points of linear bands can be easily gapped by weak perturbations such as spin-orbit coupling (SOC) in reduced dimensions.

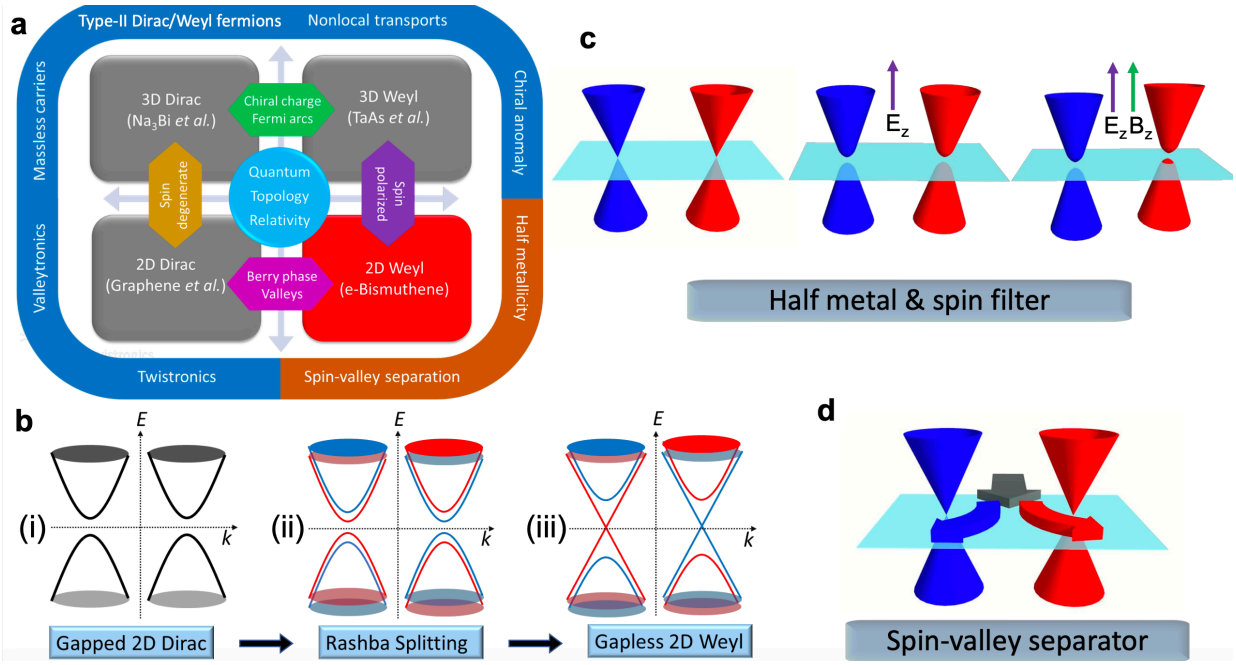

Fig. 7.1: Formation mechanism and applications of 2D Weyl semimetals. **a** Overview of Dirac/Weyl semimetals and their exotic properties. **b** Schematic formation mechanism of 2D Weyl semimetals in epitaxial bismuthene. The red and blue colors indicate two opposite directions of spin polarization. **c** Gapped Weyl cones, half metallic states and spin filter functions generated by external electric and magnetic fields. **d** Spin Hall effects and spin-valley separator.

In this chapter, we report the realization of a 2D Weyl semimetal in epitaxial bismuthene (a single atomic layer of bismuth stabilized in phosphorene structure [31, 32]). The gapless spinful bands are achieved through a self-relaxation procedure as shown in Fig. 7.1b. The first step is to find a 2D Dirac material with narrow SOC gap such as silicene, antimonene, and bismuthene (Fig. 7.1bi) [33–38]. After a suitable material is found, a perturbation can be applied to breaks space-inversion symmetry (Fig. 7.1bii). Such perturbations are commonly found in epitaxial films as the electric potential from the substrate surface naturally breaks

the space inversion symmetry. Like a Rashba system, this perturbation induces a spin splitting in the spin-degenerate bands and narrows down the band gap. The spin-split band structure is energetically favored compared to the spin-degenerate case since the energy gain in the down-moving occupied band is larger than the energy cost in the up-moving occupied bands. In other words, the system tends to relax towards a configuration with a narrower gap. Under a proper combination of the intrinsic gap size and the strength of external perturbation, the band gap is eliminated, leaving a gapless spin-split band structure. The process of removing the gap can take place spontaneously, because the energy of system is lowered as the external perturbation grows in the process of relaxation. Dielectric screening effects help stabilize the gapless nodal point. We will show the existence of gapless 2D Weyl cones can be realized in bismuthene grown on SnS and SnSe substrates.

According to Nielsen-Ninomiya theorem [39], chiral Fermions must appear in pairs, thus resulting in an even number of nodal points in Weyl semimetals. We will show that in epitaxial bisthenene there are only two Weyl nodes, which corresponds to the simplest Weyl semimetal with the minimum number of nodes. The two nodes are also referred to as two valleys in the discussion of Dirac materials. It is unique for 2D Weyl semimetals that the two valleys possess opposite spin polarizations, as shown in Fig. 1b. In other words, the spin and valleys are intrinsically entangled. This unique property makes 2D Weyl semimetals an ideal platform for spintronic applications such as high-efficient spin filters and spin-valley separators. For example, an energy gap can be induced by an external electric field (see the effective Hamiltonian in the next section). An energy shift between the two valleys can be established through the Zeeman effect by an external magnetic field, since the two valleys

are polarized in opposite directions. Tuning the external electric and magnetic field can give rise to a single Fermi surface contour with polarized spins, i.e., a half metallic state (see Fig. 7.1c). The half metal can be utilized as a high-efficient spin filter [40]. Moreover, the Hall coefficients of the two valleys are of opposite signs (see the Supplementary Information), which means the system is naturally a spin Hall semimetal. An in-plane electric field will generate a transverse spin current. Furthermore, the spin current not only makes two spin components accumulate at opposite boundaries but also separate electrons from the two valleys, as shown in Fig. 7.1d. The 2D Weyl semimetal behaves like a spin-valley separator, which is inaccessible in 2D Dirac semimetals such as graphene. Therefore, the 2D Weyl semimetal is a new topological state of condensed matter with unique spin and valley properties. In the following discussion, we will demonstrate the existence of 2D Weyl fermion states in epitaxial bismuthene and discuss the spin texture of the Weyl bands.

7.2. Film growth and lattice structures

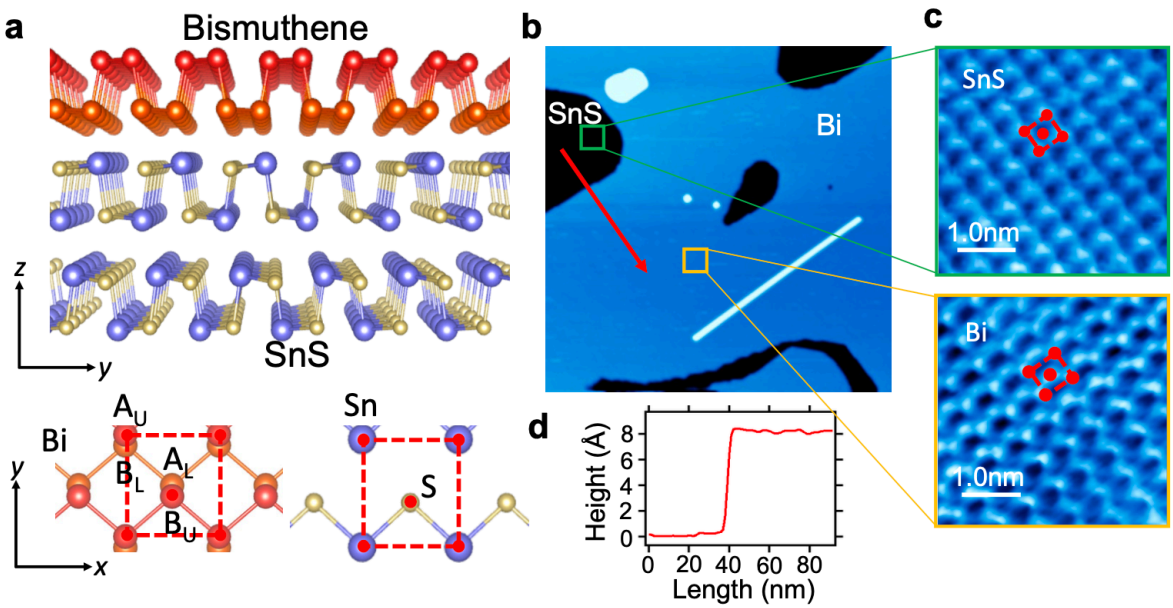

Fig. 7.2: Lattice structure and STM characterization of bismuthene grown on SnS. **a** Side and top views of bismuthene lattice structure. **b** Large-scale STM image of bismuthene grown on SnS substrate. **c** Zoom-in STM images of bismuthene and the surface of SnS. **d** The height profiles taken along the red arrow in **b**.

In our experiment, bismuthene thin films were grown by the technique of molecular beam epitaxy (MBE). The SnS(Se) was chosen as the substrate for SnS(Se) is van der Waals semiconductor and the (001) surface of SnS(Se) has a similar lattice structure as bismuthene. Figure 7.2a schematically shows the lattice structure of the sample. Bi atoms form a single-layer phosphorene structure on the (001) surface of SnS(Se). The Bi atoms have strong sp^3-hybridization character and thus the three Bi−Bi bonds are close to a tetrahedral configuration. This leads to two atomic sublayers (marked with red and orange colors.) The lattice of bismuthene belongs to the Pmna space group (No. 53). The unit cell has a four-atom basis, which are labeled as AU, AL, BU, and BL (see the top view in Fig. 7.2a), where U and L refer to the upper and lower sublayer, respectively. The (001) surface of SnS(Se) has a similar lattice as bismuthene but with S(Se) on A sites and Sn on B sites. The difference in electronegativity of Sn and S(Se) results in an in-plane dipole field along the y-direction, which causes an energy shift of A sites relative to B sites on average. In addition, the surface potential of SnS(Se) creates an electric field perpendicular to the surface and causes a potential difference between the two Bi sublayers. Both the dipole field and the vertical field of the substrate surface breaks the space-inversion symmetry and gives rises to spin splitting in the bands of bismuthene. We performed scanning-tunneling- microscope (STM) measurements to map the surface topography of the Bi sample grown on SnS(Se). The result

is shown in Fig. 7.2b. The observed flat and uniform surface indicates the high structural quality of bismuthene. In our experiment, bismuthene thin films were grown by the technique of molecular beam epitaxy (MBE). The SnS(Se) was chosen as the substrate for SnS(Se) is van der Waals semiconductor and the (001) surface of SnS(Se) has a similar lattice structure as bismuthene. The red squares marked in the zoom-in STM images (Fig. 7.2c) demonstrate the surface unit cell of bismuthene and SnS(Se). We found the in-plane lattice constants (a, b) are (4.49˚A, 4.84˚A) for bismuthene, (4.10˚A, 4.45˚A) for SnS surface, and (4.25˚A, 4.55˚A) for SnSe surface, respectively. The apparent height of bismuthene (including the thickness of bimuthene and the spacing between bismuthene and SnS(001) surface) is 8.0˚A, which can be seen from the height profile (Fig. 7.2d) taken along the red arrow marked in Fig. 7.2b.

7.3. Theoretical model, calculated bands and ARPES spectra

Here we present the first-principles band structures and angle-resolved photoemission spectroscopy (ARPES) spectra to demonstrate the existence of the 2D Weyl states in the epitaxial bismuthene films. The calculated band structure of free-standing bismuthene is shown in Fig. 7.3a. The only prominent band feature near the Fermi level is a gapped Dirac cone located at a generic k point between Γ and X_1. The Dirac bands are dominated by p_z orbitals of Bi atoms. The effective k · p model around the Dirac point can be written as:

$$\mathcal{H}_0^{\mathrm{Dirac}}(\boldsymbol{k}) = \tau_{\pm} v_x k_x \sigma_x + v_y k_y \sigma_y + \lambda_{\mathrm{SOC}} \sigma_z s_z, \qquad (1)$$

where (k_x, k_y) are measured from the Dirac nodes at (±k0, 0), σ_i (i = x,y,z) are Pauli matrices with respect to the basis of $\{|A, p_z\rangle, |B, p_z\rangle\}$ (the p_z orbitals on the two sublattices A and B), s_i (i = x,y,z) are the spin matrices, λ_{SOC} is the effective spin-orbit coupling, $\tau_{\pm} = \pm 1$ represents the chirality of the Dirac nodes located at ($\pm k_0$, 0), and $v_{x,y}$ are Fermi velocity along k_x and k_y directions, respectively. The energy gap induced by spin-orbit coupling is $\Delta E = 2\lambda_{SOC}$

(suppose $\lambda_{SOC} > 0$). λ_{SOC} = 55 meV according to the first-principles results. Every band is doubly degenerate with respect to the spin degree of freedom. The calculated band structure of bismuthene on SnSe is presented in Fig. 7.3b. The states from SnSe can be found only below -1.5 eV and above 0.5 eV, because SnSe is a semi-conductor with a gap of ~2 eV. Therefore, the bands near the Fermi level remain predominantly from Bi p_z orbitals. The presence of SnSe substrate breaks space-inversion symmetry and causes spin splitting in the bands of bismuthene. Particularly, a linear band crossing is formed in the same way as the Weyl cone described in Fig. 7.1b. With the inclusion of the substrate, the low-energy effective Hamiltonian is:

$$\mathcal{H}_0^{\mathrm{Weyl}}(\boldsymbol{k}) = \mathcal{H}_0^{\mathrm{Dirac}}(\boldsymbol{k}) + \lambda_{\mathrm{Dip}}\sigma_z + \lambda_V \sigma_y s_y \quad (2)$$

$$= \tau_{\pm} v_x k_x \sigma_x + v_y k_y \sigma_y + \lambda_{\mathrm{SOC}}\sigma_z s_z + \lambda_{\mathrm{Dip}}\sigma_z + \lambda_{\mathrm{V}}\sigma_y s_y, \quad (3)$$

where λ_{Dip} describes the perturbation induced by the in-plane dipolar field of the SnSe surface, and λ_V is the Rashba coupling induced by the vertical electric field from the SnSe surface. The energy gap at the band crossing is $|\, 2(\lambda_{SOC} - \sqrt{\lambda_{Dip}^2 + \lambda_V^2}) \,|$. The quantity $\sqrt{\lambda_{Dip}^2 + \lambda_V^2}$ reflects the strength of substrate effects on the bands of bismuthene. The band gap vanishes when $\lambda_{SOC} = \sqrt{\lambda_{Dip}^2 + \lambda_V^2}$. The gapless band dispersion is found in the first-principles band calculation with Bi atoms fully relaxed on the SnSe surface. Therefore, the absence of the band gap is a consequence of the spontaneous relaxation of bismuthene lattice on the surface of SnSe. The gapless Weyl band structure was confirmed by our ARPES measurements.

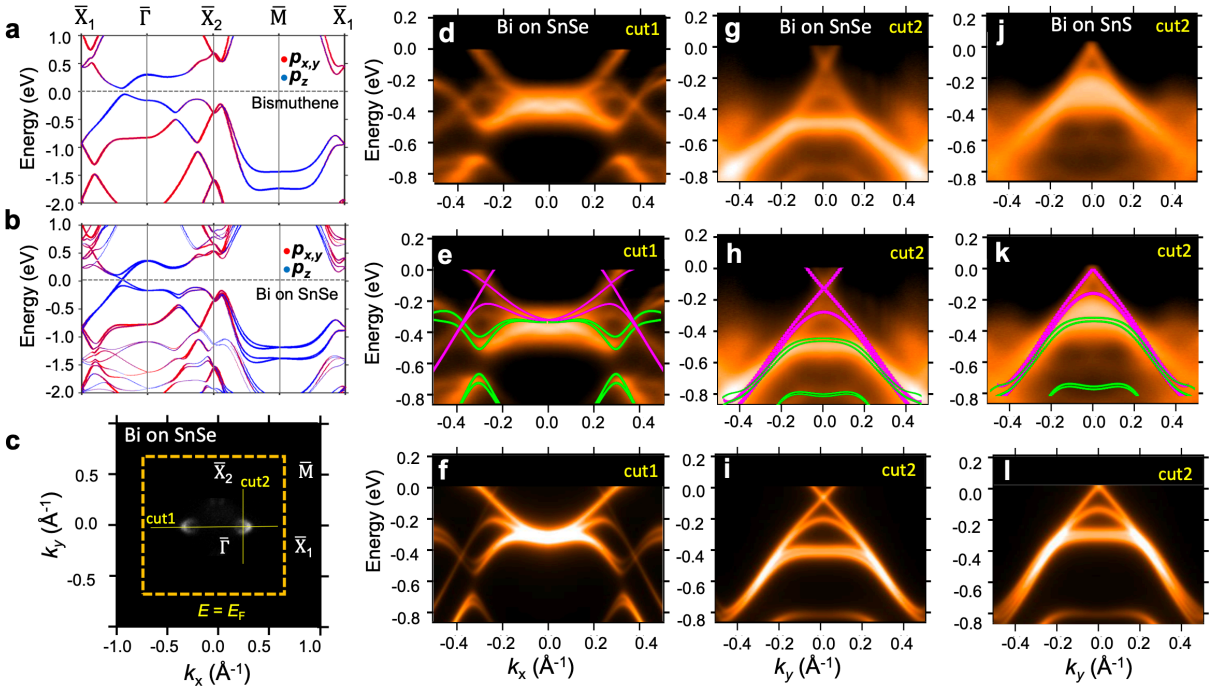

Fig. 7.3: First-principles band structure and ARPES spectra of epitaxial bismuthene. **a** Calculated band structure of free-standing bismuthene. **b** Calculated band structure of bismuthene on SnSe. **c** ARPES Fermi surface taken from bismuthene on SnSe. **d** ARPES spectra of bismuthene taken along the lines of "cut1" and "cut2" marked in **c**. **e** Overlay of calculated band structure on the ARPES spectrum along "cut1" and "cut2". The magenta lines are bands along the direction of Γ-X_1 while the green lines are bands along Γ-X_2. f Calculated spectra with the inclusion of photoemission matrix elements. **g-i** Same as **d-f** but for bands of bismuthene on SnS along "cut2".

The ARPES results taken from the bismuthene/SnSe sample are plotted in Fig. 7.3. The Fermi surface (Fig. 7.3c) contains two circular electron pockets in the direction of $X_1 - \Gamma - X_1$. We note that a similar pair of electron pockets shows up in the direction of $X_2 - \Gamma - X_2$ but with much lower intensity. This extra pair of pockets is due to the existence of Bi domains

rotated by 90◦ in the MBE sample. The ARPES spectra for bismuthene on SnSe taken along the lines of “cut1” and “cut2” (marked in Fig. 7.3c) are plotted in Fig. 7.3d. In the spectra we found the band dispersion along both $\Gamma - X_1$ and $\Gamma - X_2$ directions due to the rotated domains. This can be better seen in Figs. 7.3e,f with overlay of calculated bands on top of the ARPES spectra. The magenta lines are bands along the direction of $\Gamma - X_1$ while the green lines are bands along $\Gamma - X_2$. Only the gapless Weyl cones along $\Gamma - X_1$ stay close to the Fermi level, which means the transport and optical properties of this system are entirely determined by the low-energy Weyl fermion states. The observed Weyl cone is formed by one branch of the spin-split Dirac bands of bismuthene. No apparent gap was found at the nodal point, indicating the existence of 2D Weyl fermion states. The other branch of the spin-split bands can be seen around $E = -0.25$ eV, which is consistent with the calculated bands. We also notice that one linear band of Weyl cone is much dimmer than the other in the spectrum of “cut1”. This can be attributed to the photoemission matrix element effects. Figure 7.3f shows the calculated spectra with the inclusion of the photoemission matrix elements, which agrees well with the ARPES result. The bismuthene/SnSe sample is electron-doped as the nodal point lies 0.1 eV below the Fermi level. The shift of the Fermi level can be attributed to the electron transfer from the SnSe substrate to the epitaxial bismuthene. We also performed ARPES measurements on bismuthene grown on SnS, and the results are plotted in Figs. 7.3j-i. Compared with bismuthene/SnSe, the Fermi level of bimuthene/SnS is slightly lower (due to the difference in electronegativity of Sn and S) and lies right at the Weyl node. Therefore, bismuthene/SnS is a perfect 2D Weyl semimetal with charge neutrality.

7.4. Spin texture and spin resolved ARPES results

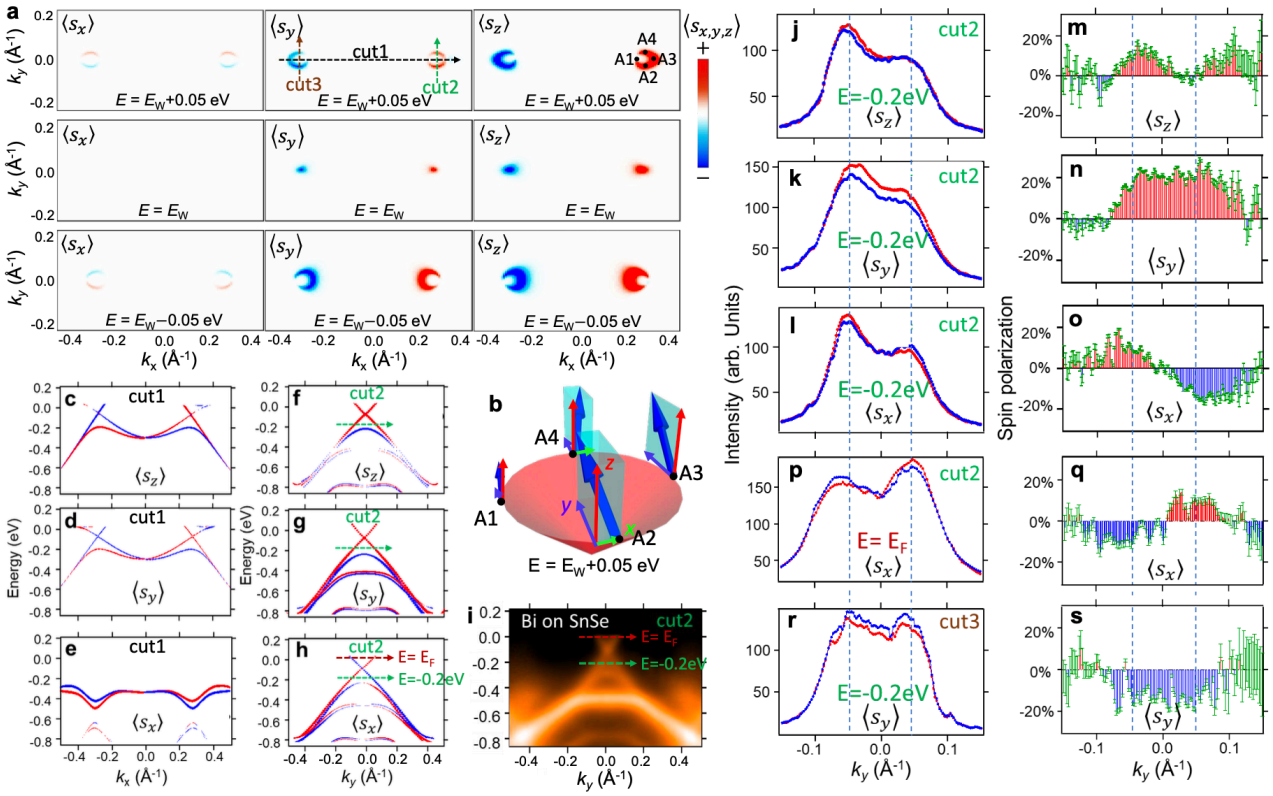

Fig. 7.4: Spin texture of 2D Weyl cones in bismuthene on SnSe. **a** Calculated spin texture of iso-energy contours at E = E_W −0.05 eV, E_W, and E_W +0.05, where EW is the energy of the Weyl nodal points. The calculated spectral intensity is plotted with the inclusion of photoemission matrix elements. **b** Spin orientation of states A1-A4 marked in a. The length of the arrow indicates the magnitude of spin polarization. **c-e** The calculated spin components ⟨s_z⟩, ⟨s_y⟩, and ⟨s_x⟩ of the band structure of bismuthene on SnSe along "cut1" marked in a, respectively. The blue and red colors represent the "spin-down" and "spin-up" states of the corresponding spin component. **f-h** Same as **c-e**, but for the line of "cut2" marked in **a**. **i** ARPES spectrum taken along "cut2" from bismuthene grown on SnSe. **j-l** Spin-resolved momentum distribution curves (MDC) taken along the line (at E = −0.2 eV) marked by the green dashed arrow in **f-h, i.** The blue and red curves are photoemission

intensity recorded in the "spin-down" and "spin-up" channels for $\langle s_z \rangle$, $\langle s_y \rangle$, and $\langle s_x \rangle$, respectively. **m-o** The shaded area with error bars indicate net spin polarization of $\langle s_z \rangle$, $\langle s_y \rangle$, and $\langle s_x \rangle$, respectively, which is calculated based on the spin results in **j-l**. **p,q** Spin-resolved MDC and calculated spin polarization of $\langle s_x \rangle$ at E = EF for "cut2". **r,s** Spin-resolved MDC and calculated spin polarization of $\langle s_y \rangle$ at E = −0.2 eV for "cut3" marked in **a**.

The defining character of Weyl fermion states is the spin polarization of the relativistic electronic states. According to Eq. 3, the dipole term ($\propto \lambda_{Dip}$) together with the SOC term cause the spin polarized in the z direction while the vertical-field term ($\propto \lambda_V$) gives rise to an in-plane spin polarization. As a result, a canted spin texture is expected for the Weyl cone. This is indeed what we found in the first-principles calculations and spin-resolved ARPES measurements. Figure 7.4a shows the calculated spin texture of iso-energy contours at E = E_W −0.05 eV, E_W, and E_W +0.05, where E_W is the energy of the Weyl nodal points. The iso-energy contour is plotted with the inclusion of photoemission matrix elements. A crescent-shaped contour is found above the Weyl nodal point, which agrees the observed Fermi surface shown in Fig. 7.3c. The two valleys of Weyl fermion states possess opposite spin polarizations because the two valleys are partners under the time-reversal symmetry. The calculated $\langle s_x \rangle$ is weaker compared to the other two spin components of $\langle s_y \rangle$ and $\langle s_z \rangle$. The spin orientation of the states "A1"-"A4" marked in Fig. 7.4a is schematically plotted in Fig. 7.4b, which demonstrates the canted spin texture of the Weyl cone. The calculated spin polarization of bands along "cut1" and "cut2" (marked in Fig. 7.4a) are shown in Figs. 7.4c-h. Along "cut1", the Weyl bands near the fermi level carries nonzero s_z and s_y components.

The absence of s_x component is due to the fact that the line of $\Gamma-X_1$ (with $k_y = 0$) is a mirror plane. By contrast, all three spin components show up in the bands along "cut2", which is not a mirror plane. The two linear bands of the Weyl cone in "cut2" have the same sign in the $s_{y,z}$ components but opposite signs in the s_x component. To verify the spin texture of the Weyl fermion states, we performed spin-resolved ARPES measurements on bismuthene /SnSe. Spin-resolved momentum distribution curves (MDC) taken at E = −0.2 eV along a line below the Weyl node (marked in the ARPES spectrum in Fig. 7.4i) are shown in Figs. 7.4j-l. The blue and red dotted lines are photoemission intensity recorded in the "spin-up" and "spin-down" channels for the corresponding spin component, respectively. The spin polarization (defined as $P = \frac{1}{S_{eff}} \frac{I_+ - I_-}{I_+ + I_-}$, where the effective Sherman function $S_{eff} = 0.275$ for our spin detectors) is shown in Figs. 7.4m-o. The observed spin texture is in good agreement with the first-principles results, especially the sign of the three spin components. This unique canted spin texture of the Weyl cone is well described by the effective Hamiltonian in Eq.3 and depends on the value of parameters λ_{Dip} and λ_V. The band dispersion of two Weyl cones can be controlled by applying external electric and magnetic fields. For example, adding a vertical electric field can effectively alter the parameter λ_V and thus open an energy gap at the nodal points. An energy shift can be induced between the two valleys by applying an out-of-plane magnetic field, since the spin of the two valleys is polarized in opposite directions. The spin-valley locking property and the tunability in band dispersion by external fields enable novel functionalities of 2D Weyl semimetals such as half metallicity, high-efficient spin filter, and spin-vally separator as mentioned in the Introduction section.

7.5. Edge states and the nature of 2D Weyl

The 2D Weyl semimetals are a new type of topological matter. The bulk boundary correspondence can be seen in the quantized Berry phase θ_B for bulk Weyl nodes and the protected edge states. The Berry phase along a closed loop l encircling each Weyl node is defined as follows,

$$\theta_B = \oint_\ell \boldsymbol{A}_{\boldsymbol{k}} \cdot \mathrm{d}\boldsymbol{k} = \pm\pi, \tag{4}$$

where A_k is the berry connection of the occupied valence bands [38]. The nonzero winding number of the bulk Weyl bands guarantees the existence of edge state bands (ESB) emanating from the nodal point [41]. To show the edge state dispersion, we calculated the bands of a semi-infinite bismuthene/SnSe heterostructure with an open boundary in the (010) direction. The result is plotted in Fig. 7.5a. There is one ESB connecting directly to the two bulk Weyl nodes, which is 1D analog of Fermi arc (FA) surface states in 3D Weyl semimetals. The connection of the ESBs to the bulk bands is schematically shown in Fig. 7.5b. Besides the 1D Fermi arc, three additional in-gap ESBs exist between the two Weyl nodes, as marked by "A", "B", and "C". (The other ESBs centered at X_1 are irrelevant to the band topology of this system.) We note that the FA band hybridizes with the ESB "B(C)" and opens a tiny gap at the crossing point as shown in Fig. 7.5a. Nevertheless, there is always a continuous ESB connecting directly to both Weyl nodes, indicating the topological nature of the 1D FA band. The robustness of this 1D FA band against perturbations and the spin texture of the edge states are demonstrated in the following section.

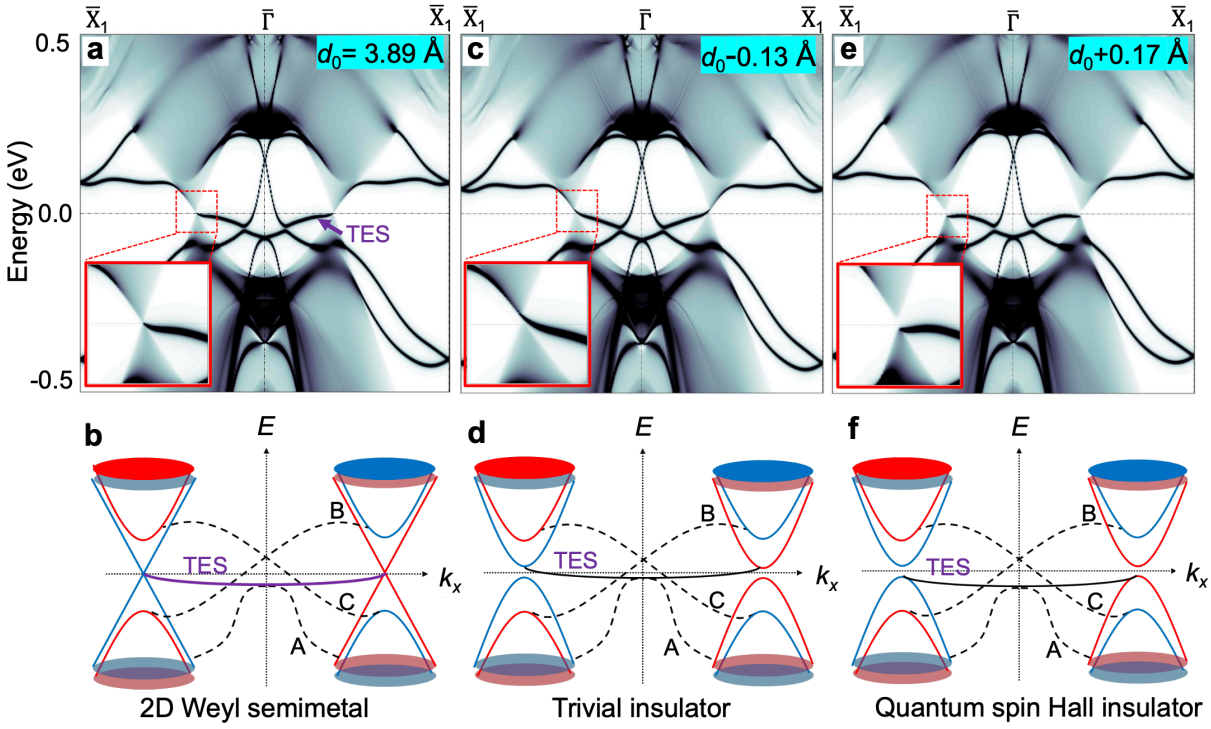

Fig. 5: Bulk-boundary correspondence in 2D Weyl semimetals. **a** The edge bands and bulk bands of a semi-infinite bismuthene film on SnSe with an open boundary in the (010) direction. The bands are weighted with the charge density near the edge. The distance between bismuthene and the surface of SnSe is d_0 = 3.89 Å. **b** Schematic of the connection of edge bands to bulk bands (in red and blue colors). The purple solid curve plots the 1D Fermi-arc edge bands connecting to the two Weyl nodes. The dashed curves are edge bands required by the bulk band topology and time reversal symmetry. **c,d** Same as **a,b,** but for a smaller inter-layer distance d = d_0 − 0.13Å = 3.76 Å. **e,f** Same as **a,b**, but for a larger inter-layer distance d = d_0 + 0.17 Å = 4.06 Å.

The 2D Weyl semimetal is at a critical point in connection to two topologically distinct insulator phases, which can be discerned in the configuration of the ESBs. The FA band and the ESB "A" form a degenerate Kramers pair at Γ as required by the time reversal symmetry.

The ESBs “B” and “C” traverse the bulk band gap and form a Dirac cone on the edge. This edge Dirac cone is related to the Z_2 topological invariant when a bulk band gap is introduced to epitaxial bismuthene. If we increase the substrate perturbation by reducing the distance between bismuthene and the substrate surface, an energy gap is opened at the Weyl nodes, as shown in Fig. 7.5c. The inset shows that the FA band stems from the bulk conduction band. As a result, the ESBs FA and “A” form an edge Dirac cone traversing the bulk band gap (Fig. 7.5d). So, the system has two pairs of edge Dirac bands and thus is equivalent to a topologically trivial insulator with the Z_2 topological invariant $\nu = 0$.

On the other hand, an energy gap can also be opened by reducing the substrate coupling, (e.g., by pulling the substrate slightly away from the substrate, as shown in Fig. 7.5e.) In this case, the FA band emanates from the valence band, and thus it, together with the EBS “A”, forms an edge Dirac cone connecting only to the bulk valence band. Consequently, there is only one edge Dirac cone (from the ESBs “B” and “C”) traversing the bulk band gap, indicating that the system with weakened substrate coupling is in the quantum spin Hall insulator phase. This is consistent with the fact that freestanding bismuthene is a quantum spin Hall insulator. The 1D FA band and its connection to spin-polarized Weyl cones are likely to give rise to exotic transport properties.

7.6. Spin texture and the robustness of the topological states

The edge state bands including the 1D topological edge band are spin polarized, which is shown in the calculated spin texture of edge state bands in Fig. 7.6. The spin components

$\langle s_y \rangle$ and $\langle s_z \rangle$ change the sign as the edge state band disperses, because the spin is not a good quantum number in the presence of SOC.

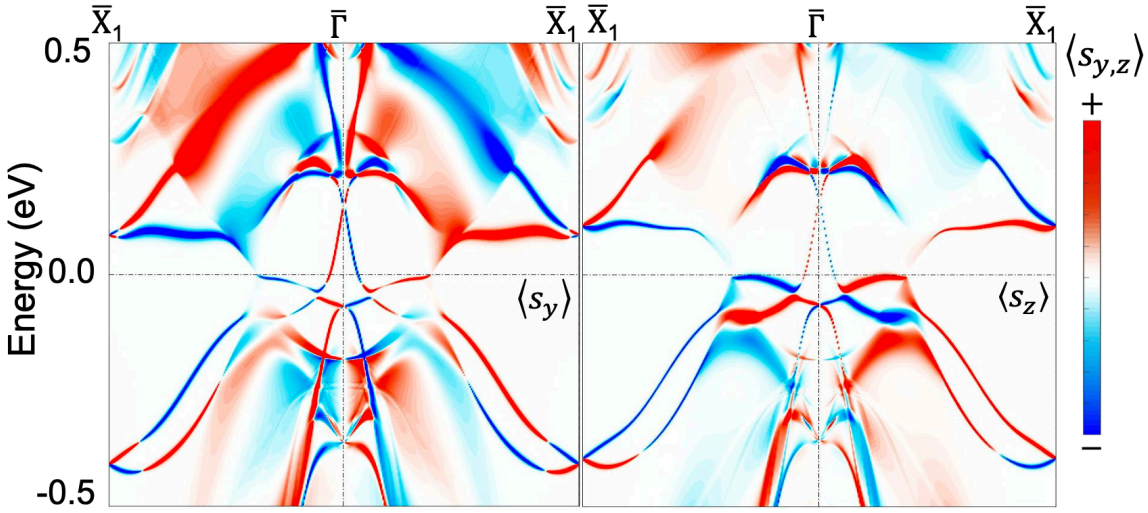

Fig. 7.6: Spin components $\langle s_y \rangle$ and $\langle s_z \rangle$ of the bulk and edge bands shown in Fig. 7.5a. The $\langle s_x \rangle$ component vanishes because Γ-X_1 lies in a mirror plane.

To see the robustness of the topological edge state band, we simulate the band spectrum with altered boundary conditions. Specifically, an onsite potential energy $E_{\text{on site}}$ is added to the two outermost Bi sites on the edge. The calculated edge band spectrum is shown in Fig. 7.7. Though the dispersion of edge bands is sensitive to the boundary condition, one edge state band is always connected to the two bulk Weyl nodes. The result reflects the fact that the connection of the topological edge state band to Weyl nodes is topologically protected.

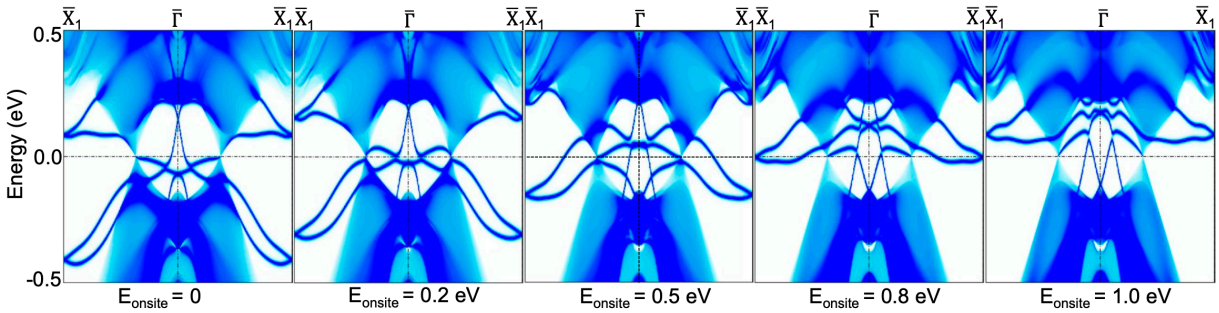

Fig. 7.7: The edge bands and bulk bands of a semi-infinite bismuthene/SnSe heterostructure with an open boundary in the (010) direction. The bands are weighted with the charge density near the edge. An onsite potential energy $E_{on\ site}$ (0, 0.2, 0.5, 0.8, and 1.0 eV) is added to the two outermost Bi sites on the edge.

7.7. Conclusions

The observation of gapless linear dispersion and spin texture of Weyl bands together with the excellent agreement between the measurements with first-principles calculations establish epitaxial bismuthene/SnS(Se) as an ideal 2D Weyl semimetal. This finding identifies the last member in the family of Dirac/Weyl topological semimetals in 2D and 3D. The entangled spin and valley degrees of freedom in 2D Weyl semimetals together with the 1D Fermi arc edge states provide unique opportunities for exploring exotic phenomena such as half metals and tunable spin/valley Hall effects, and their potential device applications.

Reference

[1] Novoselov, K. S. et al. Two-dimensional gas of massless Dirac fermions in graphene. Nature 438, 197–200 (2005).

[2] Zhang, Y., Tan, Y.-W., Stormer, H. L. & Kim, P. Experimental observation of the quantum Hall effect and Berry's phase in graphene. Nature 438, 201–204 (2005).

[3] Castro Neto, A. H., Guinea, F., Peres, N. M. R., Novoselov, K. S. & Geim, A. K. The electronic properties of graphene. Reviews of Modern Physics 81, 109–162 (2009). 0709.1163.

[4] Hasan, M. Z. & Kane, C. L. Colloquium : Topological insulators. Rev. Mod. Phys. 82, 3045–3067 (2010).

[5] Qi, X.-L. & Zhang, S.-C. Topological insulators and superconductors. Rev. Mod. Phys. 83, 1057–1110 (2011).

[6] Li, J. et al. A valley valve and electron beam splitter. Science 362, 1149– 1152 (2018).

[7] Ribeiro-Palau, R. et al. Twistable electronics with dynamically rotatable heterostructures. Science 361, 690–693 (2018).

[8] Cao, Y. et al. Correlated insulator behavior at half-filling in magic-angle graphene superlattices. Nature 556, 80–84 (2018).

[9] Cao, Y. et al. Unconventional superconductivity in magic-angle graphene superlattices. Nature

556, 43–50 (2018).

[10] Liu, Z. K. et al. Discovery of a Three-Dimensional Topological Dirac Semimetal, Na3Bi.

Science 343, 864–867 (2014).

[11] Xu, S.-Y. et al. Observation of fermi arc surface states in a topological metal. Sci-ence 347, 294–298 (2015).

[12] Borisenko, S. et al. Experimental realization of a three-dimensional dirac semimetal. Phys. Rev. Lett. 113, 027603 (2014).

[13] Yan, M. et al. Lorentz-violating type-II Dirac fermions in transition metal dichalcogenide PtTe2. Nature Communications 8, 257 (2017).

[14] Xiong, J. et al. Evidence for the chiral anomaly in the dirac semimetal na3bi. Science 350, 413–416 (2015).

[15] Armitage,N.P.,Mele,E.J.&Vishwanath,A.Weyl and dirac semimetals in three-dimensional solids. Rev. Mod. Phys. 90, 015001 (2018).

[16] Wan, X., Turner, A. M., Vishwanath, A. & Savrasov, S. Y. Topological semimetal and fermi-

arc surface states in the electronic structure of pyrochlore iridates. Phys. Rev. B 83, 205101 (2011).

[17] Xu, S.-Y. et al. Discovery of a weyl fermion semimetal and topological fermi arcs. Sci- ence 349, 613–617 (2015).

[18] Lv, B. Q. et al. Experimental discovery of weyl semimetal taas. Phys. Rev. X 5, 031013 (2015).

[19] Soluyanov, A. A. et al. Type-II Weyl semimetals. Nature 527, 495–8 (2015).

[20] Son, D. T. & Spivak, B. Z. Chiral anomaly and classical negative magnetoresistance of weyl metals. Phys. Rev. B 88, 104412 (2013).

[21] Huang, X. et al. Observation of the chiral-anomaly-induced negative magnetoresistance in 3d weyl semimetal taas. Phys. Rev. X 5, 031023 (2015).

[22] Zhang, C.-L. et al. Signatures of the Adler-Bell-Jackiw chiral anomaly in a Weyl fermion semimetal. Nature Communications 7 (2016).

[23] Liu, C.-X., Ye, P. & Qi, X.-L. Chiral gauge field and axial anomaly in a weyl semimetal. Phys. Rev. B 87, 235306 (2013).

[24] Wei, H., Chao, S.-P. & Aji, V. Excitonic phases from weyl semimetals. Phys. Rev. Lett. 109, 196403 (2012).

[25] Ashby, P. E. C. & Carbotte, J. P. Magneto-optical conductivity of weyl semimetals. Phys. Rev.B 87, 245131 (2013).

[26] Jia, S., Xu, S.-Y. & Hasan, M. Z. Weyl semimetals, Fermi arcs and chiral anomalies. Nature Materials 15, 1140–1144 (2016).

[27] Zyuzin,A.A.&Burkov,A.A. Topological response in weyl semimetals and the chiral anomaly. Phys. Rev. B 86, 115133 (2012).

[28] Parameswaran, S. A., Grover, T., Abanin, D. A., Pesin, D. A. & Vishwanath, A. Probing the chiral anomaly with nonlocal transport in three-dimensional topological semimetals. Phys. Rev. X 4, 031035 (2014).

[29] Gorbar, E. V., Miransky, V. A., Shovkovy, I. A. & Sukhachov, P. O. Nonlocal transport in weyl semimetals in the hydrodynamic regime. Phys. Rev. B 98, 035121 (2018).

[30] Hasan, M. Z. et al. Weyl, Dirac and high-fold chiral fermions in topological quantum materials. Nature Reviews Materials 0123456789 (2021).

[31] Liu, H. et al. Phosphorene: An Unexplored 2D Semiconductor with a High Hole Mobility. ACS Nano 8, 4033–4041 (2014).

[32] Li, L. et al. Black phosphorus field-effect transistors. Nat Nano 9, 372–377 (2014).

[33] Liu, C.-C., Feng, W. & Yao, Y. Quantum spin hall effect in silicene and two-dimensional germanium. Phys. Rev. Lett. 107, 076802 (2011).

[34] Chen, L. et al. Evidence for dirac fermions in a honeycomb lattice based on silicon. Phys. Rev. Lett. 109, 056804 (2012).

[35] Lu, Q. et al. Realization of unpinned two-dimensional dirac states in antimony atomic layers. Nature Communications 13, 4603 (2022).

[36] Reis, F. et al. Bismuthene on a sic substrate: A candidate for a high-temperature quantum spin hall material. Science 357, 287–290 (2017).

[37] Kowalczyk, P. J. et al. Realization of Symmetry-Enforced Two-Dimensional Dirac Fermions in Nonsymmorphic α-Bismuthene. ACS Nano 14, 1888–1894 (2020).

[38] Lu, Y. et al. Multiple unpinned Dirac points in group-Va single-layers with phosphorene structure. npj Computational Materials 2, 16011 (2016).

[39] Nielsen, H. & Ninomiya, M. The adler-bell-jackiw anomaly and weyl fermions in a crystal. Physics Letters B 130, 389–396 (1983).

[40] Tsai, W.-F. et al. Gated silicene as a tunable source of nearly 100spin-polarized electrons. Nature Communications 4, 1500 (2013)..

[41] Bian, G. et al. Topological nodal-line fermions in spin-orbit metal PbTaSe2. Nature Communications 7, 10556 (2016).

[42] Kresse, G. & Furthmu ̈ller, J. Efficient iterative schemes for ab initio total-energy calculations using a plane-wave basis set. Phys. Rev. B 54, 11169–11186 (1996).

[43] Perdew, J. P., Burke, K. & Ernzerhof, M. Generalized gradient approximation made simple. Phys. Rev. Lett. 77, 3865–3868 (1996).

[44] Marzari, N. & Vanderbilt, D. Maximally localized generalized wannier functions for composite energy bands. Phys. Rev. B 56, 12847–12865 (1997).

[45] Souza, I., Marzari, N. & Vanderbilt, D. Maximally localized wannier functions for entangled energy bands. Phys. Rev. B 65, 035109 (2001).

[46] Mostofi, A. A. et al. wannier90: A tool for obtaining maximally-localised wannier functions. Computer Physics Communications 178, 685–699 (2008).

[47] Franchini, C. et al. Maximally localized wannier functions in LaMnO3 within PBE+U, hybrid functionals and partially self-consistent GW: an efficient route to construct ab initio tight- binding parameters for eg perovskites. Journal of Physics: Condensed Matter 24, 235602 (2012).

[48] Lee, C.-C., Fukuda, M., Lee, Y.-T. & Ozaki, T. Realization of intrinsically broken dirac cones in graphene via the momentum-resolved electronic band structure. Journal of Physics: Condensed Matter 30, 295502 (2018).

[49] Bisti, F. et al. Weakly-correlated nature of ferromagnetism in nonsymmorphic cro2 revealed by bulk-sensitive soft-x-ray arpes. Phys. Rev. X 7, 041067 (2017).

8. INTERACTIONS BETWEEN DIRAC STATES AND DIRAC FERMION CLONING

Tuning interactions between Dirac states in graphene has attracted enormous interest because it can modify the electronic spectrum of the 2D material, enhance electron correlations, and give rise to novel condensed-matter phases such as superconductors, Mott insulators, Wigner crystals, and quantum anomalous Hall insulators. Previous works predominantly focus on the flat band dispersion of coupled Dirac states from different twisted graphene layers.

In this chapter, a new route to realizing flat band physics in monolayer graphene under a periodic modulation from substrates is proposed. Graphene/SiC heterostructure is taken as a prototypical example and it is demonstrated experimentally that the substrate modulation leads to Dirac fermion cloning and, consequently, the proximity of the two Dirac cones of monolayer graphene in momentum space. Theoretical modeling captures the cloning mechanism of the Dirac states and indicates that moiré flat bands can emerge at certain magic lattice constants of the substrate, specifically when the period of modulation becomes nearly commensurate with the$(\sqrt{3}\times\sqrt{3})$R30° supercell of graphene. The results show that epitaxial single monolayer graphene on suitable substrates is a promising platform for exploring exotic many-body quantum phases arising from interactions between Dirac electrons.

8.1. Introduction

The discovery of graphene has revolutionized modern condensed matter physics by providing direct access to the physics of Dirac fermions in solid-state systems.[1–3] It also sheds light on the path toward a vast field of novel 2D materials including van der Waals

(vdW) materials and topological materials such as quantum spin Hall insulators. [1,4–10] Single-layer graphene possesses two Dirac cones residing at the opposite corners of the Brillouin zone, leaving them essentially isolated from each other. Stacking graphene layers in the graphite order duplicates Dirac cones in the same valley so that the two valleys remain decoupled. Recently, new physics in graphene-like systems have arisen as a consequence of the creation of strongly coupled Dirac states in artificially engineered structures such as twisted bilayer graphene (TBG). The interaction between Dirac states from the two layers can be effectively tuned by the angle. This leads to emergent collective behaviors of electrons including Mott insulating states, unconventional superconductivity, emergent ferromagnetism, quantum anomalous Hall effects. [11–20] The essential ingredient for these new emergent states is the nearly dispersionless bands at zero energy in the Moiré Brillouin zone. Achieving the required large periodicity of Moiré pattern in real space and the closeness of Dirac cones in momentum space generally requires control over the twist angle between mechanically exfoliated graphene layers. This places stringent constraints on the techniques of sample assembly. Therefore, there is a pressing need for accessing flat band physics in systems without fine tuning of twist angles.

In this chapter, we report an alternative route to enable interactions between Dirac electrons in a single layer of graphene and realize flat bands. This comes from the supporting substrate potential. We observed the cloning of Dirac bands in monolayer graphene epitaxially grown on SiC substates by angle-resolved photoemission spectroscopy (ARPES). The periodic substrate potential brings closer the Dirac states from the two valleys and thus turns on intervalley coupling. This is precisely captured by our tight-binding simulations. Our theory

further indicates that the perturbed graphene system with nearly commensurate epitaxial relations hosts Moiré flat bands similar to those found in the magic-angle twisted bilayer graphene. [11,21] The lattice constant of the substate plays the same role as the twist angle in bilayer graphene in the formation of Moiré flat bands. Dispersionless zero-energy bands occur at certain "magic" lattice constants of the substrate.

8.2. The Moiré lattice and structure characterization

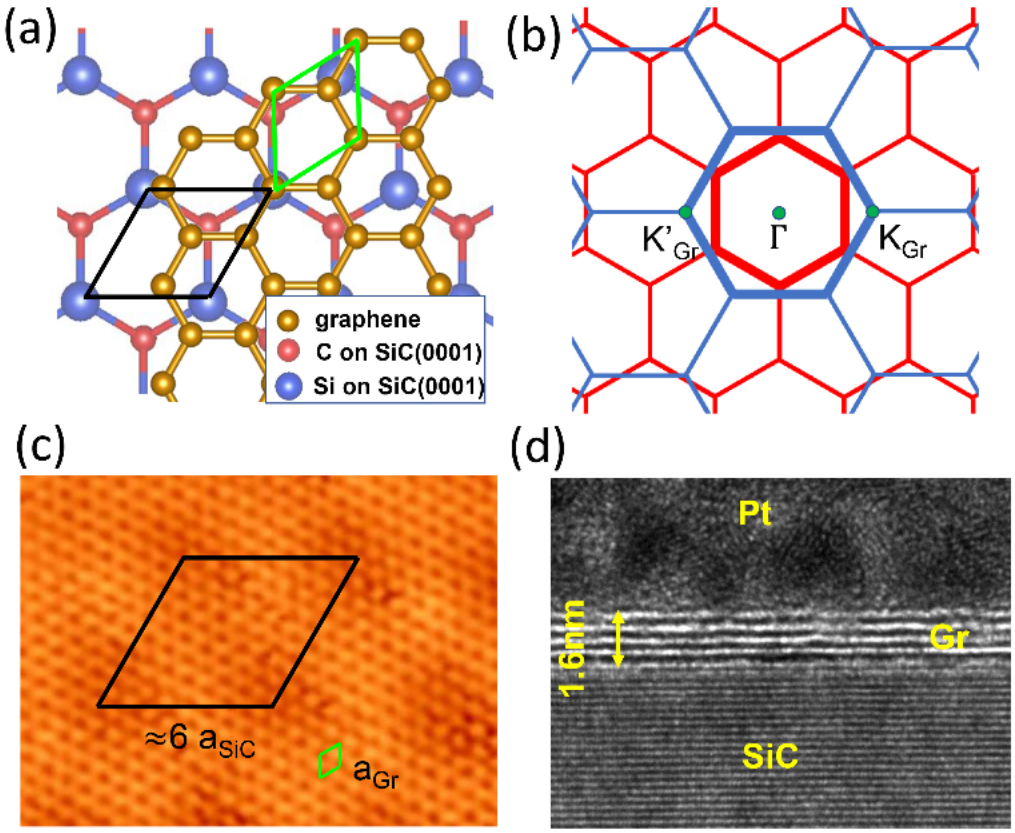

Figure 8.1. Lattice structure and Brillouin zone of graphene/SiC hetero- structure. **a** Lattice structure of graphene and SiC(0001) surface. The unit cell of graphene and SiC surface is depicted by the green and black parallelograms, respectively. **b** Brillouin zone of graphene (blue lines) and SiC(0001) surface (red lines). **c** STM image of graphene with atomic resolution. A moiré pattern is observed

with a period approximately equal to six times the lattice constant of SiC(0001). **d** Cross-sectional TEM image of graphene/SiC heterostructure.

First, we study the substrate effects on the Dirac states of graphene. Our graphene was grown epitaxially on the Si-face of a 6H-SiC substrate. The lattice structure and epitaxial relation between the graphene overlayer and the SiC substrate are plotted in Figure 8.1a. The lattice constant of graphene and SiC(0001) surface is 2.46 and 3.07 Å, respectively. The Brillouin zone of graphene and SiC(0001) is depicted by red and blue lines, respectively, in Figure 8.1b. K_{Gr} and K'_{Gr} represent the location of the two valleys of graphene Dirac states. The atomic-resolution STM image of the graphene sample is shown in Figure 8.1c. A superhexagonal Moiré pattern with a period $\lambda = 6(1 + \delta)a_{SiC}$ is observed due to the incommensurate modulation of the SiC interface layer. [22,23] To examine the structural quality, we performed high-resolution TEM measurements on our graphene samples. A typical TEM image is shown in Figure 8.1d. The sample consists of four well-ordered graphene layers sitting on the carbonized surface of the SiC substrate. A gap between the graphene and the SiC surface is noticeable, indicating a sharp interface between the graphene layers and the substrate. In our experiment, the thickness of graphene layers can be precisely controlled down to a monolayer. We will focus on results obtained from monolayer graphene samples in the following discussion, but the physics discussed here also applies to thicker graphene films.

8.3. ARPES spectrum and the cloning mechanism

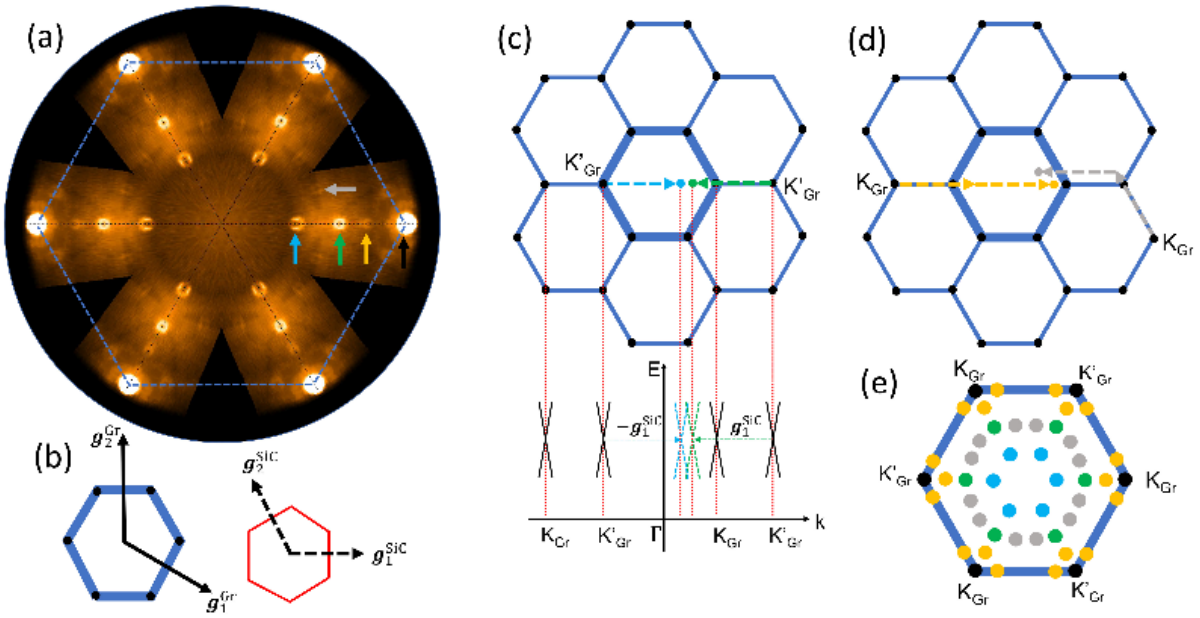

Figure 8.2. ARPES spectrum and momentum-space analysis of Dirac fermion cloning. **a** Fermi surface of graphene/SiC(0001) heterostructure measured by ARPES. **b** Geometrical relation between the Brillouin zones of graphene and SiC(0001) surface. **c** The location of green and blue clones from the first-order perturbations. **d** The location of yellow and gray clones from the second order perturbations. **e** Distribution of first-order and second-order clones in the Brillouin zone of graphene.

The Fermi surface of the graphene sample mapped by ARPES is presented in Figure 8.2a. The Brillouin zone of graphene is marked by the blue dashed lines. At the corners of the Brillouin zone, the K_{Gr} points, we can see bright Fermi surface contours from the Dirac bands of graphene. Note that our sample is n-typed doped with a Fermi level above the Dirac point. Therefore, the Fermi surface contours are small circles surrounding K_{Gr}, as marked by the black arrows. Beside the Dirac states of graphene, there are extra circular contours located inside the Brillouin zone of graphene, which are absent on the Fermi surface of freestanding graphene. These new contours marked by blue, green, yellow, and gray arrows are referred

to as blue, green, yellow, and gray contours (or cones) in the following discussions. The geometric relations between the Brillouin zones of graphene and SiC is depicted in Figure 8.2b. The emergent contour with lesser photoemission intensity is the clones of the graphene Dirac cone generated by the periodic substrate perturbations. Shifting the K'_{Gr} by a reciprocal lattice vector of SiC as shown in Figure 8.2c, we can find the location of the blue and green cones. The yellow and gray contours can be obtained through two successive shifts of the graphene states, see Figure 8.2d. Taking the substrate interaction as a perturbation, we can attribute the blue (green) and yellow (gray) cones to the first-order and second-order perturbation effects, which also explains why the intensity of yellow (gray) cones is apparently lower than that of blue (green) cones. The locations of all the first-order and second-order clones are summarized in Figure 8.2e. It is consistent with the experimental observations shown in Figure 8.2a.

8.4. Theoretical model and calculated band structures

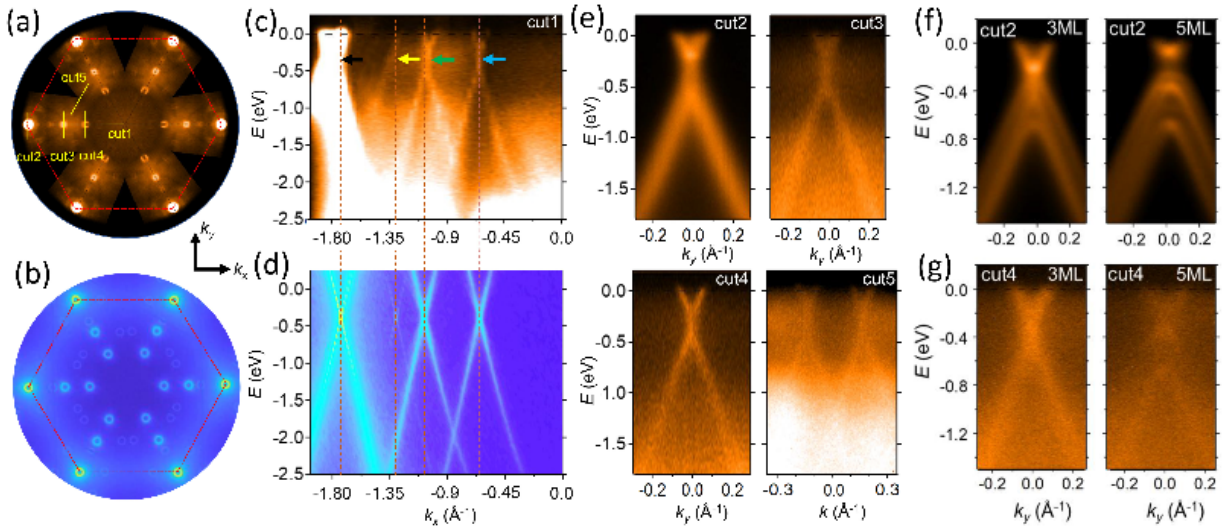

Figure 8.3. ARPES spectra and tight-binding simulation of Dirac bands and their clones. **a** ARPES and **b** tight-binding Fermi surface of graphene/SiC heterostructure. **c** ARPES and **d** tight-binding

spectrum taken along “cut1” marked in **a**. **e** ARPES spectra taken along “cut2-5”. **f** ARPES spectrum of the primary Dirac cone taken along “cut2” from 3-, 5-monolayer graphene films grown on SiC(0001) surface. **g** ARPES spectrum of cloned Dirac bands taken along “cut4” from 3-, 5-monolayer graphene films.

The cloning of Dirac states is rooted in the periodic modulation from the substrate on the electrons in graphene. To understand the mechanism of cloning, we performed a tight-binding simulation in which the substrate effect is approximated by a periodic potential acting on the graphene electrons. The sample is n-type doped, so the fermi level is shifted in the simulation to match the experimental results. There is a good agreement between the experimental and theoretical Fermi surfaces as shown in Figure 8.3a,b. All first-order and second-order clones in the simulation show up at the locations observed in the experimental results. The spectrum along the line of “cut1” (marked in Figure 8.3a) is plotted in Figure 8.3c,d. The brightness of bands indicates the photoemission intensity in the ARPES spectrum and the spectral weight (the probability of finding the electron with the corresponding energy and momentum) in the TB simu- lation. The clones show the same dispersion as the primary Dirac cones but have lower spectral weight compared to the primary cone, consistent with the perturbative picture. This weight reflects the strength of the graphene/substrate inter-action. It is important to note that the width of these clones seen in the spectral line shapes is similar to the main cones, indicating the static nature of the substrate coupling. This is further corroborated by the ARPES spectrum taken along the lines of “cut2”;-“cut5”. Unlike the primary Dirac cones sitting far apart at the corners of the Brillouin zone, the clones are much closer to each other in momentum space. For example, the distance between the yellow and

green clones is 0.21 $Å^{-1}$ while the spacing between neighboring primary cones is 1.7 $Å^{-1}$. The smaller distance between clones enables them to overlap in momentum space, see the iso-energy contours in the Supporting Information. The yellow and green cones cross at E = −1.3 eV while the blue and green cones cross at E = −1.8 eV. Such crossings of Dirac states are unavailable in freestanding graphene films. It is worth noting that there is no gap opened at the crossings of the green and blue bands. This is because both green and blue contours originate from the same valley (see Figure 8.2c) and thus they do not hybridize. Only Dirac bands from different valleys can interact with each other and open hybridization gaps, as discussed below. The cloning of Dirac bands occurs not only in the monolayer graphene but also in thicker films. Figure 8.3f shows the spectra of the primary Dirac cone from 3-ML and 5-ML graphene samples. The number of Dirac bands in the spectra indicates the thickness of the sample. [24,25] Despite of the weaker intensity, the clone bands (the blue cone marked in Figure 8.2a, 8.3c) are still observable in the 3-ML and 5-ML samples as shown in Figure 8.3g. We note that similar π-band replicas have been reported in previous ARPES works. [23,26] However, a detailed theoretical model of the band duplication remains elusive. In this work, we build up a tight-binding model with the inclusion of electron hoppings between atomic orbitals of graphene and SiC substrate. It shows that the periodic substrate modulation not only duplicates the π-band of graphene, but also induces strong couplings between two valleys of graphene. The effect of Dirac fermion cloning has also been observed in the graphene/h-BN heterostructure, in which the superlattice potential leads to the emergence of Moiré minibands, second- generation Dirac cones, and consequently, the self-similar Hofstadter butterfly states in high magnetic fields. [12,13,16,27–29] The emergent states are related to the hybridization of the graphene Dirac cone and its clones in the nearly

commensurate graphene/h-BN lattice. Those experimental results indicate that the duplication of Dirac states is an intrinsic property of graphene heterostructures rather than a final-state photoelectron diffraction effect as suggested in the previous work. [26]

8.5. Tight-binding model and calculated band structures.

Perturbation theory can capture the essential physics of Dirac fermion cloning in the graphene/SiC heterostructure. The substrate potential can be treated as a small perturbation and exerts a periodic modulation to the Dirac states of graphene. [23] Taking W(x) as the potential on the SiC(0001) surface, the eigenfunction up to the second-order is given by:

$$|\Psi_k\rangle = |\Psi_k^0\rangle + \sum_{p\neq k} |\Psi_p^0\rangle \frac{\langle\Psi_p^0|W|\Psi_k^0\rangle}{E_k^0 - E_p^0} + \sum_{p\neq k, l\neq k} |\Psi_p^0\rangle \frac{\langle\Psi_p^0|W|\Psi_l^0\rangle\langle\Psi_l^0|W|\Psi_k^0\rangle}{(E_k^0 - E_p^0)(E_k^0 - E_l^0)} - \sum_{p\neq k} |\Psi_p^0\rangle \frac{\langle\Psi_k^0|W|\Psi_k^0\rangle\langle\Psi_p^0|W|\Psi_k^0\rangle}{(E_k^0 - E_p^0)^2} - \frac{1}{2}|\Psi_k^0\rangle \sum_{p\neq k} \frac{|\langle\Psi_p^0|W|\Psi_k^0\rangle|^2}{(E_k^0 - E_p^0)^2}, \quad (1)$$

where "0" indicates the original wavefunction of the graphene in the absence of the substrate surface potential. The second term in Equation (1) is the first-order correction. To have non-vanishing $< \psi_p^0|W|\psi_k^0 >$, the difference between p and k must align with the period of W(x). Here we simulate the substrate surface potential by using a periodic function in the simplest harmonic form, that is, W(x)=2w(cos($\mathbf{b_1}\cdot\mathbf{x}$)+cos($\mathbf{b_2}\cdot\mathbf{x}$)+cos(−($\mathbf{b_1}$+$\mathbf{b_2}$)·x)). A detailed discussion on the substrate surface potential can be found in next Section. Since the period of W(x) is described by the two reciprocal lattice vectors b_1 and b_2, non-zero spectral weight appears only at p=k±b_1 , k±b_2, and k±(b_1 +b_2). As k represents the momentum of the

Dirac states, there are 12 duplicates of the first order (the green and blue clones in Figure 8.2e) within the Brillouin zone of graphene, which is in agreement with the experimental observation. The strength of the substrate coupling w can be obtained by comparing the photoemission intensities from the primary Dirac cone and the clones. The observed photoemission intensities from the blue clone, the green clone, and the primary Dirac cone at the energy of Dirac nodes have ratios of I_{blue}:I_{green}:$I_{primary}$ =0.48:1.00:61.91. According to Equation (1), the intensity from the cloned states is that from the primary Dirac state multiplied by the spectral weight of (2w / E 0)2 (here we assume the transition pmatrix element is same for primary and cloned Dirac states), where p is the momentum of the cloned Dirac nodes. E0 is 6.65 and 4.39 eV for the blue and green Dirac nodes, respectively. Then, the ratio of the emission from the green and blue nodes is (4.39/6.65)2 = 0.44, which is close to the observed value. The coupling strength w can be estimated by using $w = E_p^0\sqrt{I_{green}/I_{primary}}\,/2$. With $E_p^0 = 4.39eV$ for the green node and I_{green}:$I_{primary}$ = 1:61.91, we find w = 0.279 eV $\approx$ 0.1t, where t = 2.8 eV is the nearest-neighbor hopping parameter of graphene. [1] The observed value of w is consistent with the estimate from the tight-binding simulation. Since t = 2.8 eV is the characteristic energy scale of the graphene band dispersion, it is justified to consider the substrate potential of size w $\approx$ 0.1t as a perturbation in Equation (1). The last three terms of | Ψk> correspond to the second-order perturbations. The second last term on the right side of Equation (1) vanishes due to the fact that $< \psi_k^0|W|\psi_k^0 > = 0$. The last term only induces a renormalization of the primary cone at k. Only the first term of the second-order survives in certain conditions and give rise to clones in momentum space. To have non-vanishing $< \psi_l^0|W|\psi_k^0 >$, the momentum obeys l=k±b_1,

$k\pm b_2$, $k\pm b_1\pm b_2$ Likewise, the momentum of the final wavefunction satisfies $p=k\pm 2b_1$, $k\pm 2b_2$,$k\pm 2(b_1+b_2)$, $k\pm(b_1-b_2)$, $k\pm(2b_1+b_2)$,$k\pm(b_1+2b_2)$. In this regard, the second-order perturbations duplicate 24 Dirac cones (the gray and yellow clones in Figure 8.2e) at various p, consistent with the experimental observation.

The perturbative corrections to the wavefunction in Equation (1) give rise to the clones of Dirac cones. The clones represent a redistribution of spectral weight of the primary Dirac cone in the momentum space. That is why the observed clones share the same band dispersion as the primary Dirac cones. The clones derived from the same primary Dirac cone do not hybridize with each other. On the other hand, the hybridization are allowed for the clone or primary contours from different valleys. The hybridization between two valleys is mediated by the substrate potential. Here the two valleys of monolayer graphene behave like the two sets of Dirac cones from the two layers of TBG. Flat bands can be created under certain substrate conditions, as discussed below.

8.6. The position of the cloned cones and the magic lattice constant

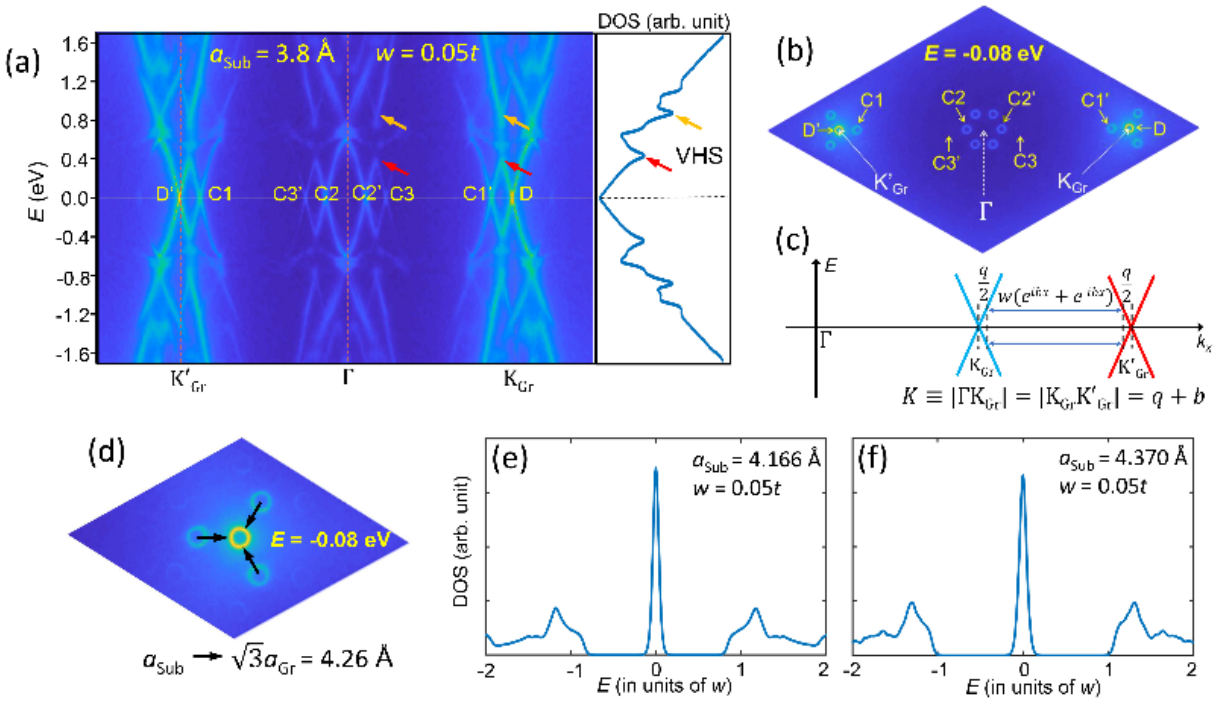

Figure 8.4. Tight-binding simulation of epitaxial graphene with various substrate lattice constants. **a** The tight-binding band structure and density of states with a_{sub} = 3.8Å. **b** Calculated iso-energy contours at E = −0.08eV. **c** Coupling mechanism between the two Dirac cones at K_{Gr} and K'_{Gr}. **d** Schematic of the movement of clone contours C1' as the substrate approaches to the commensurate value $3a_{Gr}$ = 4.26 Å. **e** Calculated density of states for a_{sub} = 4.166Å and w = 0.05t. **f** Same as **e** but for a_{sub} = 4.370Å.

Our ARPES and tight-binding results indicate that the substrate potential creates a periodic modulation of the graphene band structure and thus produces clones of the Dirac states. They effectively shorten the distance between the two valleys by the reciprocal vectors of the substrate. This mechanism yields a direct coupling between the Dirac states from the two valleys when the substrate lattice is nearly commensurate with graphene. To date, various graphene-based heterostructures such as graphene/metals, [30–32] graphene/ boron nitride,

[33–35] and graphene/chalcogenide compounds [4,36–40] have been experimentally realized. To investigate the substrate effects in the nearly commensurate condition, we performed a tight-binding simulation for a generic graphene heterostructure with a hexagonal substrate rotated by 30° relative to the graphene unit cell. The substrate lattice constant is chosen to be 3.8 Å, which is about 10% smaller than the commensurate value $\sqrt{3}a_{Gr} = 4.26$Å. The calculated band structure is shown in Figure 8.4a. At the Fermi level, there are two primary Dirac points (DP) denoted by D and D' and six duplicated DPs denoted by C1, C1', C2, C2', C3, and C3'. The clones of C1–C3 are from the valley of the "D" Dirac cone while those of C1'-C3' are from the other valley. When two Dirac bands from different valleys (for example, C1' and D, or C2 and C2') intersect, an energy gap is opened at the crossing point. The gapped band structure gives rise to van Hove singularities (VHS) in the density of states (DOS) as marked by the yellow and red arrows. The iso-energy contours at E = −0.08 eV are plotted in Figure 8.4b. Close to the zero energy, all the primary and cloned contours are isolated in momentum space and thus contribute to the DOS as independent Dirac cones. Therefore, the DOS vanishes at zero energy as shown in Figure 8.4a. The effective distance between the two primary Dirac points in the presence of substrate perturbations is

$$q = \left| |\mathrm{K'_{Gr}K_{Gr}}| - b \right| = \left| |\Gamma \mathrm{K_{Gr}}| - b \right|, \tag{2}$$

where b is the length of the substrate reciprocal lattice vector, as schematically shown in Figure 8.4c. That is also the separation between DPs C1' and D in Figure 8.4b. As the substrate constant approaches, the commensurate value $\sqrt{3}a_{Gr}$, the clone contours move closer to the the primary cone (see Figure 8.4d) and enhance the coupling between the two

valleys, since the effective coupling is described by a dimensionless parameter $\alpha = \frac{w}{\hbar v_F q}$, where w is the amplitude of the substrate potential and v_F is the Fermi velocity of electrons in graphene. [11] In this simulation, w is set to be 0.05t = 140 meV, a value comparable to that of TBG, w ≈ 110 meV). [11] When the substrate lattice constant is equal to 4.166 and 4.370 Å, a sharp peak shows up at zero energy in DOS and an energy gap of size ≈2w emerges between the conduction and valence bands, as shown in Figures 4e,f. The zero-energy peaks in DOS cannot be described by isolated Dirac cones, therefore there must be dispersionless bands emerging at low energy as a consequence of hybridization of Dirac states from the two valleys.

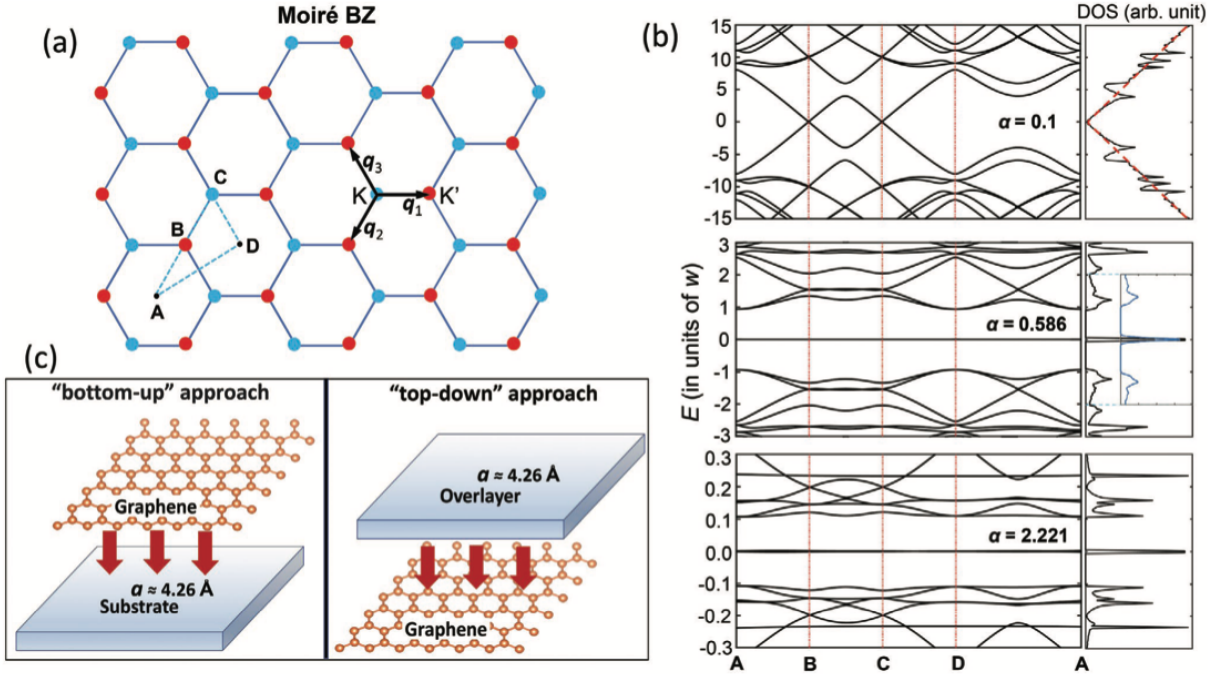

Figure 8.5. Effective model of moiré mini lattice and flat bands. **a** Moiré Brillouin zone of a nearly commensurate graphene heterostructure. **b** Calculated band structure and density of states with α = 0.1, 0.586, and 2.221. The DOS plot in the middle panel includes an inset showing the tight-binding

DOS (the blue curve) from Figure 8.4f. **c** Schematic of the two ways of assembling heterostructures with flat bands.

The effective separation between the two DPs of monolayer graphene in the presence of substrate modulation is described by three vectors, $q_1 = q(1,0), q_2 = q\left(\frac{-1}{2}, \frac{-\sqrt{3}}{2}\right)$, and $q_3 = q\left(\frac{-1}{2}, \frac{\sqrt{3}}{2}\right)$ Repeated hopping between the two valleys generates a k-space honeycomb lattice shown in Figure 8.5a. The unit vectors of this lattice are same as reciprocal vectors of the Moire pattern (MP) of this hybrid structure, namely, $b_1^{MP} = q_1 - q_2$ and $b_2^{MP} = q_1 - q_3$. The low-energy electron dynamics can be described by an effective Hamiltonian,

$$H_{\text{eff}}(\boldsymbol{k}) = \begin{bmatrix} D(\boldsymbol{k}) & T_1 & T_2 & T_3 \\ T_1^{\dagger} & \overline{D}(\boldsymbol{k}-\boldsymbol{q}_1) & 0 & 0 \\ T_2^{\dagger} & 0 & \overline{D}(\boldsymbol{k}-\boldsymbol{q}_2) & 0 \\ T_3^{\dagger} & 0 & 0 & \overline{D}(\boldsymbol{k}-\boldsymbol{q}_3) \end{bmatrix}, \quad (3)$$

Where $D(k)=v_F k\sigma$, $\overline{D}(k)=-v_F k\cdot\sigma^*$, and $T_m = w \exp\left(i\frac{2(m-1)\pi}{3}\sigma_z\right)$, m=1, 2, and 3. Here $\sigma = (\sigma_x, \sigma_y)$, and σ_z are Pauli matrices associated with the A and B sublattices of graphene. D(k) and $\overline{D}$ (k) describe the Dirac cone at K and K', respectively, as the two cones are time-reversal partners. The derivation of the effective Hamiltonian can be found in the following section. Using this effective Hamiltonian, we calculated the band structure along the path A–B–C–D–A and the DOS, see Figure 8.5b. For α = 0.1, the DPs at B and C remain isolated meanwhile an energy gap is opened at the crossing point of two Dirac bands. The DOS shows a nearly linear dependence of energy and several peaks from VHSs, which is consistent with the tight-binding result in Figure 4a. When α increases to 0.586, a pair of absolutely flat bands exist at zero energy inside the bandgap ($\Delta E \approx 2w$). This leads to a sharp zero-energy peak in DOS, which agrees remarkably well with the tight-binding DOS with a_{sub} = 4.370 Å

and w = 0.05t as shown in the inset of Figure 8.5b. The perfect flatness of zero-energy bands is due to the chiral symmetry of the Hamiltonian, since H_{eff} is equivalent to the chirally symmetric continuum model proposed by Tarnopolsky et al. [21] (see the proof in the following section). The inter-valley transition matrices T_m (m = 1, 2, and 3) in H_{eff} contain only the diagonal AA and BB sublattice couplings due to the on-site substrate potential and the fact that the wavefunctions of Dirac states at K and K' are defined with respect to the same A and B sublattices of monolayer graphene. As a result, mono-layer graphene perturbed by an on-site substrate potential is a natural realization of the chirally symmetric model of flat bands. [21] The unique coupling α* = 0.586 corresponds to two "magic" lattice constants according to Equation (2),

$$a^*_{\text{sub}} = \sqrt{3}a_{\text{Gr}} \pm \frac{3wa_{\text{Gr}}}{2\pi t\alpha^*}. \quad (4)$$

Plug in α* = 0.586, a_{Gr} = 2.46 Å, and w = 0.05t, we find that a∗ = 4.161 and 4.361 Å. The magic lattice constants match the values (4.166 and 4.370 Å) we found in the tight-binding simulations. The small discrepancy between two results can be attributed to the finite size of the supercell we used in the tight- binding simulations. The effective Hamiltonian gives rise to a series of magic coupling a* with a periodicity of $\Delta\alpha \simeq 1.5$. [11,41,42] The second magic coupling is a* = 2.221. The band structure with this magic coupling (the bottom panel of Figure 8.5b) exhibits absolute flat bands at zero energy and a smaller bandgap ($\Delta E \approx 0.2w$). The second and higher magic couplings correspond to a very small deviation from the commensurate lattice constant, $\Delta a \lesssim 0.02$ Å. It is technically challenging to detect such small lattice deviations in experiments, just like the smaller twists corresponding the higher magic couplings in the TBG systems. We note that the perfect flatness of the zero-energy bands is

due to the absence of off-diagonal AB sublattice coupling in the model described by Equation (3). A detailed modeling of the substrate interaction indicates that substrate-mediated AB sublattice coupling exists and is smaller (< 50%) in magnitude than the on-site AA(BB) coupling. The band calculation shows that the Moiré bands at zero energy remain highly flat even with the inclusion of off-diagonal AB coupling.

8.7. Derivation of the substrate electrostatic potential from the tight-binding model and experimental evidence

In this section, we present a tight-binding description of the graphene-substrate coupling. In the graphene/SiC heterostructure, there exist a carbon buffer layer between graphene and SiC. The TEM image in Fig. 8.1 of the main text shows that the spacing between the buffer layer and the bottom graphene layer (d_{buffer}) is slightly larger than the interlayer spacing of graphene (d_{gr}), i.e., $d_{buffer} = 1.1 d_{gr} = 1.1 \times 0.335\text{Å} = 3.68\text{Å}$. The structure of the graphene/SiC heterostructure is schematically plotted in Fig. 8.6.

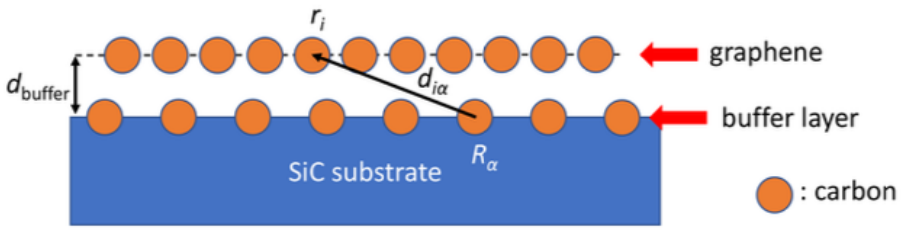

Figure 8.6 Schematic for epitaxial graphene and SiC surface with a carbon buffer layer.

There exists a carbon buffer layer between epitaxial graphene and SiC surface. The Hamiltonian for the substrate coupling is written as H = H0 + Hb + U, where H0 is the tight-binding Hamiltonian for graphene and

$$H_b = V_b \sum_{\alpha} D_{\alpha}^{\dagger} D_{\alpha}, \tag{1}$$

$$U = \sum_{i,\alpha} \lambda_{i\alpha} C_i^{\dagger} D_{\alpha} + (c.c.). \tag{2}$$

Here C_i and D_α are the annihilation operators for electron in graphene and the carbon buffer layer, respectively. For simplicity, we assume that there is one p_z dangling orbital per unit cell of the buffer layer, the lattice constant of the buffer layer is same as that of SiC(0001) surface, and the in-plane hopping within the buffer layer is negligibly small (since the lattice constant of SiC(0001) (3.07 Å) is significantly greater than the nearest-neighbor spacing of graphene (1.42 Å)). The on-site potential V_b describes the energy difference between carbon orbitals in graphene and the buffer layer considering charge transfers due to the polar SiC surface. The value of V_b can be estimated from the energy shift of the Dirac point of graphene relative to the Fermi level, which is found to be $V_b = 0.3$ eV according to the ARPES result in Fig. 8.3. $\lambda_{i\alpha}$ is the transfer integral between the sites r_i in graphene and R_α in the buffer layer. It can be modeled by using the Slater-Koster-type function,

$$\lambda_{i\alpha} = V_{pp\pi}\left[1 - \left(\frac{\boldsymbol{d}_{i\alpha} \cdot \boldsymbol{e}_z}{d_{i\alpha}}\right)^2\right] + V_{pp\sigma}\left(\frac{\boldsymbol{d}_{i\alpha} \cdot \boldsymbol{e}_z}{d_{i\alpha}}\right)^2, \tag{3}$$

$$V_{pp\pi} = V_{pp\pi}^0 \exp\left(-\frac{d_{i\alpha} - a_0}{r_0}\right), \tag{4}$$

$$V_{pp\sigma} = V_{pp\sigma}^0 \exp\left(-\frac{d_{i\alpha} - d_0}{r_0}\right), \tag{5}$$

where $d_{i\alpha} = r_i - R_\alpha$ as shown in Fig. 8.6, e_z is the unit normal vector of the surface, $a_0 \approx$

1.42 Å is the nearest neighbor distance in graphene, and $d_0 \approx 3.68$ Å is the spacing between graphene and the buffer layer. The transfer integrals $V_{pp\pi}^0 \approx -2.7$ eV and $V_{pp\sigma}^0 \approx 0.48$ eV. r_0 is the decay length of the transfer integral and is taken to be $0.319a_0$. Near the K point of graphene, the effective Hamiltonian of graphene is written as

$$H_{\text{eff}} = H_0 + U^{\dagger}(-H_b)^{-1}U \equiv H_0 + H_{\text{int}}, \tag{6}$$

Here $H_{int} = \sum_{ij} \tilde{t}_{ij} C_i^{\dagger} C_j + (c.c.)$,where $\tilde{t}_{ij}$ is the substrate-mediated hopping amplitude. For the low-energy spectrum near $E \approx 0$,

$$\tilde{t}_{ij} = \sum_{\alpha} \frac{\lambda_{i\alpha} \cdot \lambda_{j\alpha}^*}{-V_b}, \tag{7}$$

where the summation is carried out over all sites R_α in the buffer layer. Among all $\tilde{t}_{ij}$ components, the same-site transition amplitude $\tilde{t}_{ij}$ is the largest, because the terms in the numerator in Eqn. 7 are all in phase for $\tilde{t}_{ij}$.

The substrate-mediated hopping $\tilde{t}_{ij}$ monotonically decreases as the distance between sites r_i and r_j grows. The same-site transition amplitude $\tilde{t}_{ii}$ is 2 times greater than the nearest neighbor hopping $\tilde{t}_{<ij>}$ as shown in the result of numerical evaluation in Fig. 8.7. Therefore, the $\tilde{t}_{ij}$ term, which corresponds to an on-site potential, dominates in the cloning mechanism of Dirac states and inter-valley couplings in the nearly commensurate cases.

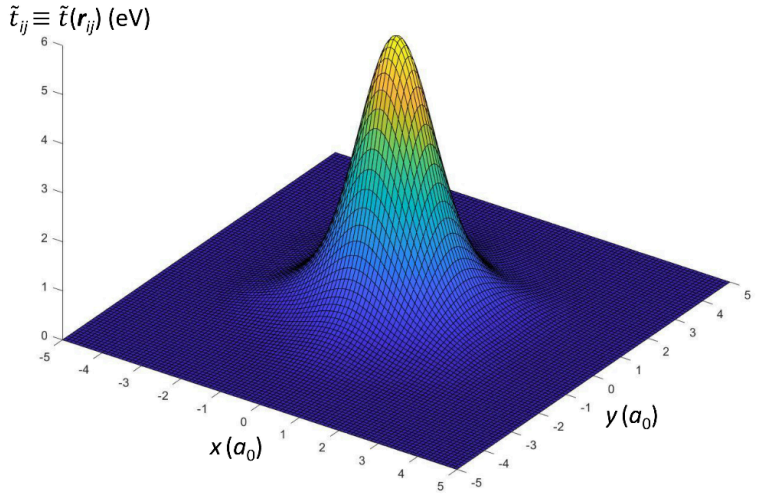

Figure 8.7: Substrate-mediated hopping amplitude $\tilde{t}_{ij}$ (r) as a function of the distance between sites r_i and r_j in graphene. $r_{ij} \equiv r_i - r_j = (x, y)$, where x and y are measured in the unit of a_0, the nearest-neighbor distance in graphene. r_i is fixed in this calculation and is taken to be 0.

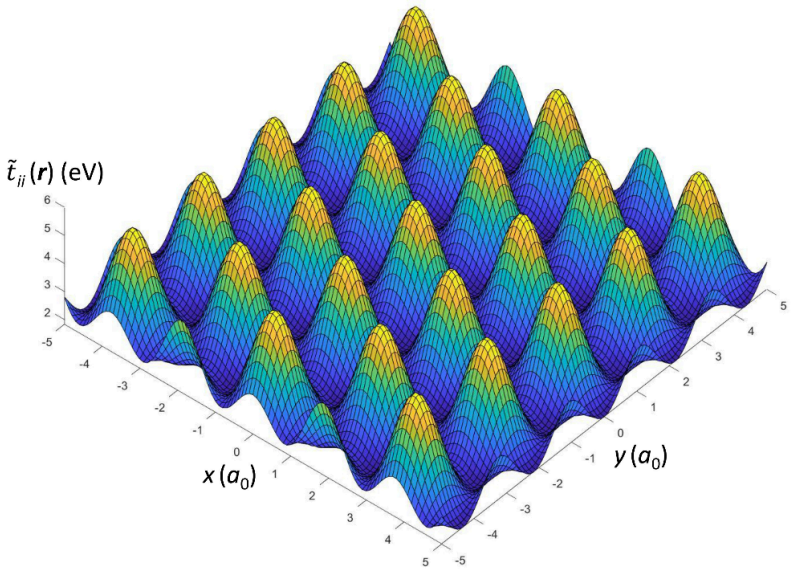

Figure 8.8: Distribution of the same-site transition amplitude $\tilde{t}_{ii}$ (r). r is the position of a carbon atom in the graphene layer.

It is easy to see that $\tilde{t}_{ii}$(r) is a periodic function of r with a periodicity of substrate lattice constants, because of the summation over all sites R_α in the definition of $\tilde{t}_{ii}$. The distribution of $\tilde{t}_{ii}$(r) is plotted in Fig. 8.8. This term is formally indistinguishable from a periodic electrostatic potential, even though its physical origin is in the quantum overlaps of orbitals in adjacent layers. If we keep only the lowest-order spherical harmonics, then we get the on-site electrostatic potential employed,

$$W(\boldsymbol{r}) = \tilde{t}_{ii}(\boldsymbol{r}) = 2w\left(\cos(\boldsymbol{b_1}\cdot\boldsymbol{r}) + \cos(\boldsymbol{b_2}\cdot\boldsymbol{r}) + \cos(-(\boldsymbol{b_1}+\boldsymbol{b_2})\cdot\boldsymbol{r})\right), \tag{8}$$

where $b_{1,2}$ are the reciprocal vectors of substrate surface. The parameter w can be obtained from the max/min values of $\tilde{t}_{ii}$(r). w = (5.72 eV−1.98 eV)/12 = 0.31 eV, which is consistent with the value extracted from the ARPES results, w_{exp} = 0.28 eV.

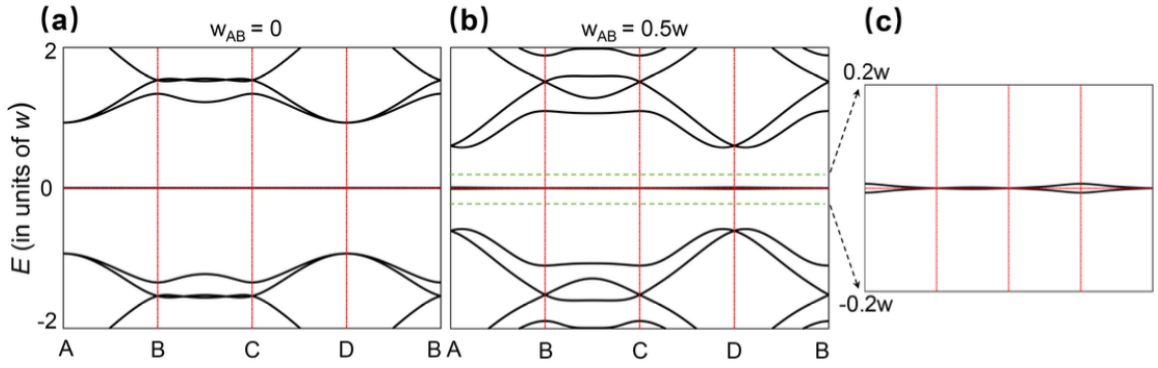

Figure 8.9: Band structure of the effective model with the magic coupling α = 0.586. (a) Bands calculated without the off-diagonal coupling. (b) Bands calculated with the off-diagonal coupling w_{AB} = 0.5w. (c) Zoom-in band dispersion near the Fermi level.

Next, we have studied the effects of substrate-meditated off-site hopping parameters, $\tilde{t}_{ij}$ (i≠ j). The amplitude of $\tilde{t}_{ij}$ decays quickly as the distance between sites r_i and r_j increases. For simplicity, we keep only the nearest-neighbor hopping $\tilde{t}_{<ij>}$, which causes off diagonal couplings between A and B sublattices of graphene. Considering both the on-site and off-site hopping amplitudes, the coupling term in the effective Hamiltion, Eqn.(3) can be written as

$$T_m = w \exp(i\frac{2(m-1)\pi}{3}\sigma_z) + w_{AB}\sigma_y, \quad (9)$$

where m = 1,2,3, and the coupling of AB sublattices w_{AB} is induced by the nearest- neighbor hopping $\tilde{t}_{<ij>}$. Here, w = 0.5w, since $\tilde{t}_{<ij>}$ is half of $\tilde{t}_{ij}$ in magnitude according to the numerical calculation shown in Fig. 8.7. The band structure with the inclusion of off-diagonal couplings is plotted in Fig. 8.9. The off-diagonal coupling has two prominent effects on the band structure. First, the band gap is reduced from 1.87w to 1.16w. Second, the Moiŕe flat bands acquire a small dispersion. The maximum energy of the flat band is 0.01w, less than 1% of the size of the band gap. Therefore, the Moiŕe bands at zero energy remain highly flat even with the inclusion of substrate mediated off-diagonal hopping.

The evidence of monolayer graphene

Figure 8.10 shows the ARPES and STM results taken from 0.5L, 1L, and 2L graphene/SiC samples. In the STM image of 0.5L sample, the surface of SiC is partially covered by graphene islands. In the ARPES spectrum of 0.5L, we found a broadened linear band feature. The STM images of 1L and 2L samples show that the surface of SiC is fully covered by the

graphene layers. The thickness of the graphene layers can be straightforwardly determined by counting the number of Dirac bands in the ARPES spectra.

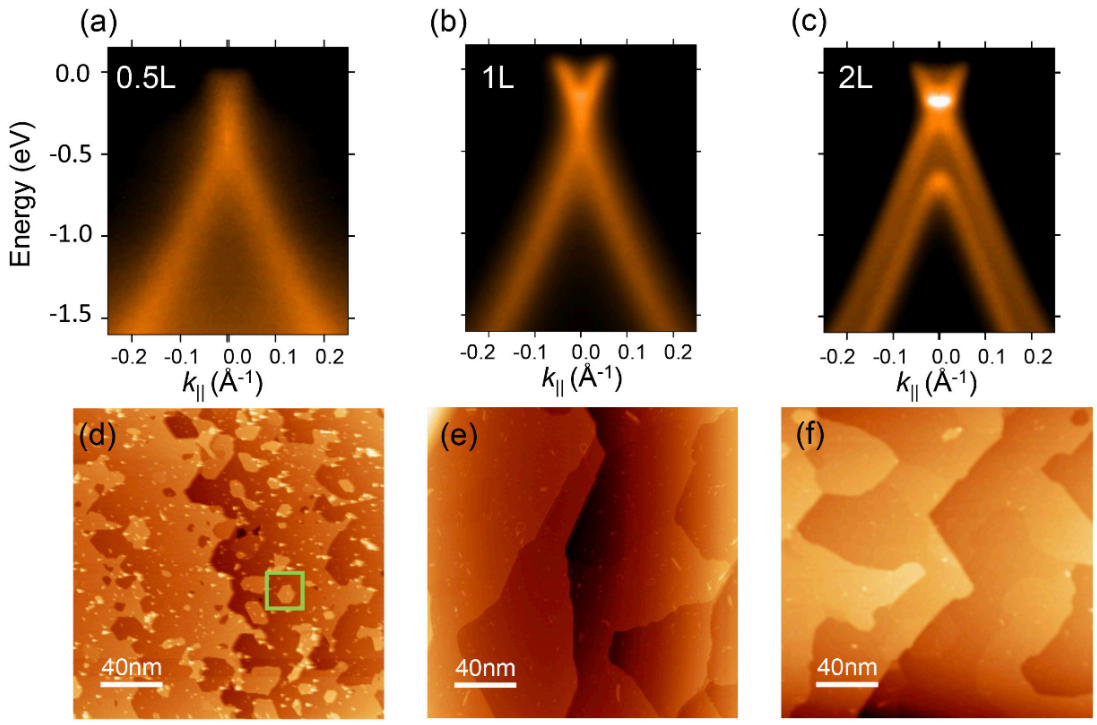

Figure 8.10: (a-c) ARPES spectrum taken from 0.5L, 1L, and 2L graphene/SiC samples, respectively. (d-f) STM topography taken from 0.5L, 1L, and 2L graphene/SiC samples, respectively.

The zoom-in STM topography (of the area marked by the green box in Fig. 8.10(d)) is shown in Figure 8.11. The atom-resolve STM images and their Fourier transformation clearly demonstrate the lattices of SiC surface and monolayer graphene. The thickness of monolayer graphene can also be seen in the height profile plotted in Fig. 8.11(d).

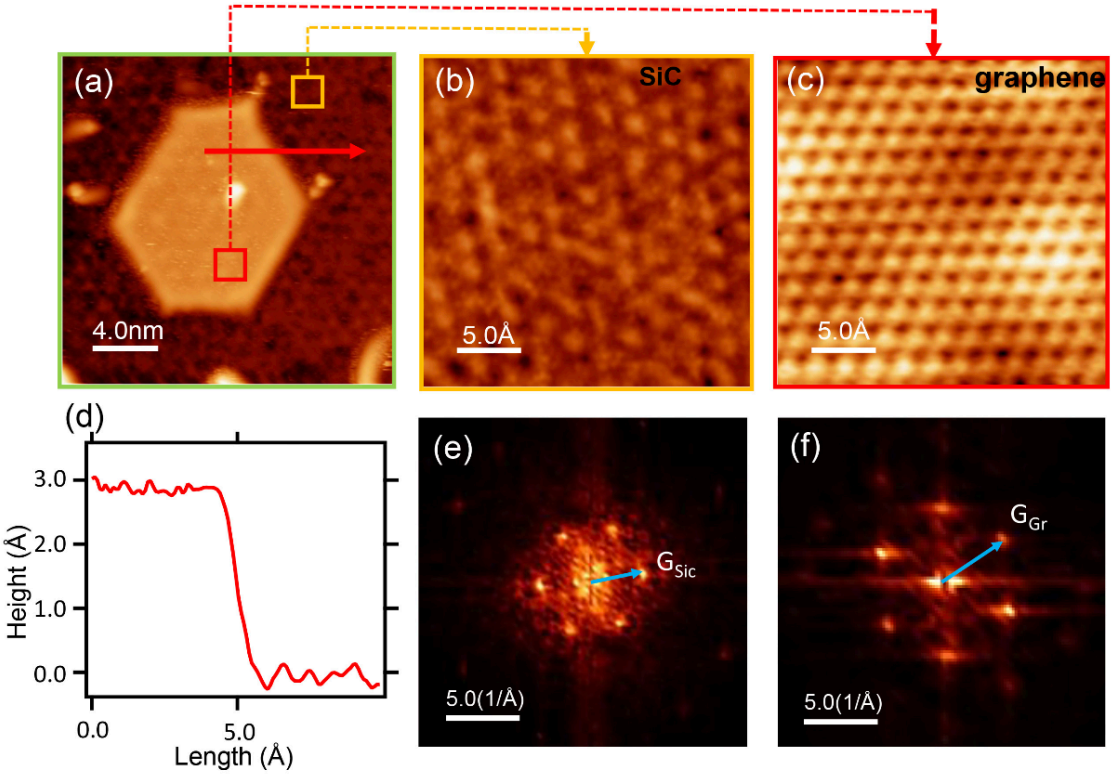

Figure 8.11: (a) Zoom-in STM topography taken from the 0.5L graphene sample. (b, c) Atom-resolved STM images taken from SiC surface and the graphene island, respectively. (d) Height profile taken along the red arrow marked in (a). The observed step height indicates the thickness of graphene island is 1L. (e, f) Fourier transformation of the STM images in (b, c), showing the reciprocal lattice vectors of SiC surface and graphene.

8.8. Comparison of the tight-binding model and the effective TKV model

We calculated the band structure and density of states by using the tight-binding model and the effective TKV model for two magic couplings $\alpha = 0.586$ and 2.221. The results are plotted in Fig. 8.12. There is a good agreement between the tight-binding and TKV results. The small discrepancy between results of the two models in the case of $\alpha = 2.221$ can be

attributed to the finite size of the supercell used in the tight-binding simulation. The size of Moiŕe pattern for α = 2.221 is larger than that for α = 0.586. Therefore, a larger supercell is needed in the tight-binding simulation for α = 2.221 to make the result converge to the bulk value.

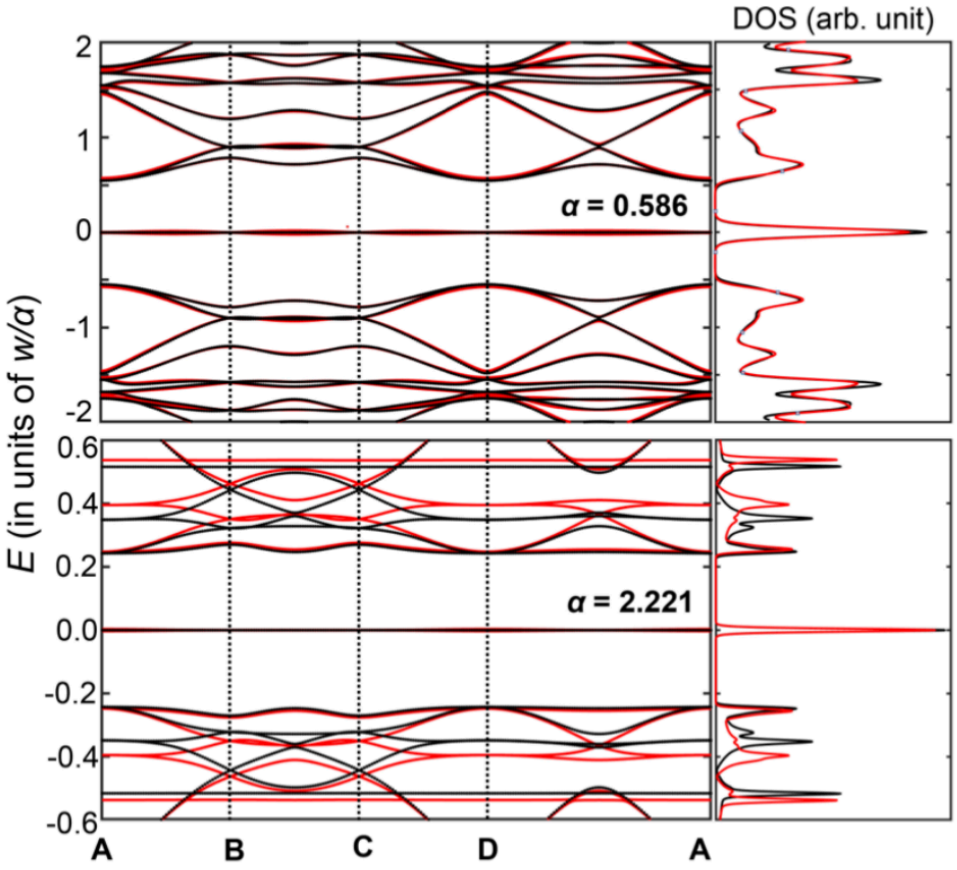

Figure 8.12: Band structure and density of states for α = 0.586 and 2.221. Red and black curves are results of tight-binding model and the effective TKV model, respectively.

8.9. Summary and Outlook

The low-energy dynamics in the graphene heterostructures is essentially governed by the coupling α, and α is determined by the separation q between two adjacent Dirac cones in the Moiré lattice. For w = 0.05t (≈140 meV) and α* = 0.586, q = 0.04 Å−1 ≪ $|\Gamma K_{Gr}| = 1.7 Å^{-1}$, which means the reciprocal lattice vectors of substrate must almost connect the two DPs at K and K' in momentum space, see Figure 8.4c. This places a constraint on the possible substrate lattice constants and orienta- tions. To have flat bands, the largest possible substrate lattice constant corresponds to a ($\sqrt{3} \times \sqrt{3}$)R30° supercell of graphene, that is, $a_{sub} \approx \sqrt{3} a_{Gr}$ = 4.26 Å. This commensurate relation is also known as the Kekulé superlattice. [43] For other commensurate relations between graphene and substrates, the substrate lattice constant has to be $\leq \frac{\sqrt{3}}{3} a_{Gr}$= 2.13 Å, which is very rare in real materials. Therefore, the substrate materials for the flat-band heterostructure must have a surface with C_3 rotation symmetry and lattice constant close to 4.26 Å. In Table 1, we list several materials which can be potentially employed in the proposed heterostructures. The suggested materials are all elemental or binary vdW materials and can be straightforwardly synthesized, for example, by the method of molecular beam epitaxy (MBE). The vdW nature of graphene and the suggested substrate materials facilitates the formation of an atomically sharp interface and thus enhances substrate interaction as well as intervalley couplings. In addition to the conventional assembly method by growing or transferring graphene onto the substrate surface, the proposed flat-band heterostructures can be readily synthesized via a "top–down" approach, as schematically plotted in Figure 8.5c. High-quality graphene layers can be epitaxially grown on the SiC(0001) surface, and the Dirac states of graphene remain isolated due to the large lattice mismatch. Therefore, the graphene/SiC structure can serve as a

supporting substrate for the growth of various materials with nearly commensurate relations as suggested in Table 1. For example, Bi_2Se_3 (a = 4.136 Å) thin layers have been grown on the graphene/SiC(0001) surface. [44]

Our ARPES experiments demonstrated the cloning of Dirac fermions in the graphene/SiC(0001) heterostructure due to the periodic modulation of the substrate potential. Our theoretical calculations showed this modulation effect from the substrate can effectively couple the two valleys of Dirac states in mono- layer graphene in the nearly commensurate condition. The graphene heterostructures can be a promising alternate system for exploring the intriguing flat-band physics that was found in TBG. The criterion for realizing flat bands is a matchup of the surface potential strength and the periodicity of the substrate to reach the magic effective coupling α^*. There are a vast number of possible substrate materials that could be potentially used in this hybrid structure. In addition, the charge and spin orderings in the substrates such as antiferromagnetism in MnTe, [45] superconductivity in $PdTe_2$, [46] and topological surface states in Bi_2Se_3 [44] can further enrich flat-band physics in graphene via proximity effects, systematic investigations of which are left to future works.

Materials	a_{sub} (Å)	Space group	Materials	a_{sub} (Å)	Space group
CuSe	3.980	$P6_3/mmc$	Bi_2Se_3	4.136	$R\text{-}3mH$
InSe	4.000	$R\text{-}3mH$	CdS	4.137	$P6_3/mc$
CrTe	4.005	$P6_3/mmc$	MnTe	4.148	$P6_3/mmc$
$PdTe_2$	4.024	$P\text{-}3m1$	GeTe	4.156	$R\text{-}3mH$
In_2Se_3	4.026	$R\text{-}3mH$	PdTe	4.200	$P6_3/mmc$
$PtTe_2$	4.026	$P\text{-}3m1$	CdSe	4.232	$P6_3/mc$
InSe	4.050	$P6_3/mmc$	Cu_2Te	4.237	$P6/mmm$
As_2Te_3	4.058	$R3mH$	Sb_2Te_3	4.264	$R\text{-}3mH$
GaTe	4.060	$P6_3/mmc$	$SiTe_2$	4.289	$P\text{-}3m1$
ZnTe	4.092	$P3_121$	MgSe	4.319	$P6_3/mmc$
ScTe	4.097	$P6_3/mmc$	HgSe	4.320	$P3_221$
$AuTe_2$	4.107	$P\text{-}3m1$	Sb(111)	4.332	$R\text{-}3mH$
PtTe	4.111	$P6_3/mmc$	HgTe	4.392	$P3_121$
AuSe	4.120	$P6_3/mmc$	Bi_2Te_3	4.403	$R\text{-}3mH$
MnSe	4.120	$P6_3/mc$	MgTe	4.531	$P6_3/mmc$
Cu_2Se	4.132	$R\text{-}3mH$	Bi(111)	4.546	$R\text{-}3mH$

Table 1: Material candidates for flat-band heterostructures. The materials are ordered according to their in-plane lattice constant. Bi(111) and Sb(111) are Bi and Sb films grown in the rhombohedral (111) direction [47].

Reference

[1] A. H. Castro Neto, F. Guinea, N. M. R. Peres, K. S. Novoselov, A. K. Geim, Reviews of Modern Physics 2009, 81, 1 109.

[2] K. S. Novoselov, A. K. Geim, S. V. Morozov, D. Jiang, M. I. Katsnelson, I. V. Grigorieva, S. V. Dubonos, A. A. Firsov, Nature 2005, 438, 7065 197.

[3] Y. Zhang, Y.-W. Tan, H. L. Stormer, P. Kim, Nature 2005, 438, 7065 201.

[4] A. K. Geim, I. V. Grigorieva, Nature 2013, 499, 7459 419.

[5] M. I. Katsnelson, K. S. Novoselov, A. K. Geim, Nature Physics 2006, 2, 9 620.

[6] D. N. Basov, M. M. Fogler, A. Lanzara, F. Wang, Y. Zhang, Rev. Mod. Phys. 2014, 86 959.

[7] F. D. M. Haldane, Phys. Rev. Lett. 1988, 61 2015.

[8] M. Z. Hasan, C. L. Kane, Rev. Mod. Phys. 2010, 82 3045.

[9] X.-L. Qi, S.-C. Zhang, Rev. Mod. Phys. 2011, 83 1057.

[10] Y. Liu, G. Bian, T. Miller, T.-C. Chiang, Physical Review Letters 2011, 107, 16 166803.

[11] R. Bistritzer, A. H. MacDonald, Proceedings of the National Academy of Sciences 2011, 108, 3012233.

[12] L. A. Ponomarenko, R. V. Gorbachev, G. L. Yu, D. C. Elias, R. Jalil, A. A. Patel, A. Mishchenko, A. S. Mayorov, C. R. Woods, J. R. Wallbank, M. Mucha-Kruczynski, B. A. Piot, M. Potemski, I. V. Grigorieva, K. S. Novoselov, F. Guinea, V. I. Fal'Ko, A. K. Geim, Nature 2013, 497, 7451 594.

[13] C. R. Dean, L. Wang, P. Maher, C. Forsythe, F. Ghahari, Y. Gao, J. Katoch, M. Ishigami,

P. Moon, M. Koshino, T. Taniguchi, K. Watanabe, K. L. Shepard, J. Hone, P. Kim, Nature 2013, 497, 7451 598.

[14] Y. Cao, V. Fatemi, A. Demir, S. Fang, S. L. Tomarken, J. Y. Luo, J. D. Sanchez-Yamagishi,

K. Watanabe, T. Taniguchi, E. Kaxiras, R. C. Ashoori, P. Jarillo-Herrero, Nature 2018, 556, 7699 80.

[15] Y. Cao, V. Fatemi, S. Fang, K. Watanabe, T. Taniguchi, E. Kaxiras, P. Jarillo-Herrero, Nature 2018, 556, 7699 43.

[16] E. Wang, X. Lu, S. Ding, W. Yao, M. Yan, G. Wan, K. Deng, S. Wang, G. Chen, L. Ma, J. Jung, A. V. Fedorov, Y. Zhang, G. Zhang, S. Zhou, Nature Physics 2016, 12, 12 1111.

[17] A. L. Sharpe, E. J. Fox, A. W. Barnard, J. Finney, K. Watanabe, T. Taniguchi, M. A. Kastner, D. Goldhaber-Gordon, Science 2019, 365, 6453 605.

[18] M. Serlin, C. L. Tschirhart, H. Polshyn, Y. Zhang, J. Zhu, K. Watanabe, T. Taniguchi, L. Balents, A. F. Young, Science 2020, 367, 6480 900.

[19] G. A. Tritsaris, S. Carr, Z. Zhu, Y. Xie, S. B. Torrisi, J. Tang, M. Mattheakis, D. Larson, E. Kaxiras, 2D Materials 2020, 7 035028.

[20] Z. Song, Z. Wang, W. Shi, G. Li, C. Fang, B. A. Bernevig, arXiv 2018, 123, 3 36401.

[21] G. Tarnopolsky, A. J. Kruchkov, A. Vishwanath, Phys. Rev. Lett. 2019, 122 106405.

[22] M. Conrad, F. Wang, M. Nevius, K. Jinkins, A. Celis, M. N. Nair, A. Taleb-Ibrahimi, A. Tejeda, Y. Garreau, A. Vlad, A. Coati, P. F. Miceli, E. H. Conrad, Nano Letters 2017, 17, 1 341.

[23] L. Huang, Y. Wu, M. T. Hershberger, D. Mou, B. Schrunk, M. C. Tringides, M. Hupalo, A. Kamin- ski, Phys. Rev. B 2017, 96 035411.

[24] S. Y. Zhou, G.-H. Gweon, J. Graf, A. V. Fedorov, C. D. Spataru, R. D. Diehl, Y. Kopelevich, D.-H. Lee, S. G. Louie, A. Lanzara, Nature Physics 2006, 2, 9 595.

[25] Y. Liu, L. Zhang, M. K. Brinkley, G. Bian, T. Miller, T. C. Chiang, Physical Review Letters 2010, 105, 13 1.

[26] C. M. Polley, L. I. Johansson, H. Fedderwitz, T. Balasubramanian, M. Leandersson, J. Adell, R. Yakimova, C. Jacobi, Phys. Rev. B 2019, 99 115404.

[27] M. Yankowitz, J. Xue, D. Cormode, J. D. Sanchez-Yamagishi, K. Watanabe, T. Taniguchi, P. Jarillo-Herrero, P. Jacquod, B. J. LeRoy, Nature Physics 2012, 8, 5 382.

[28] W. Yang, G. Chen, Z. Shi, C.-C. Liu, L. Zhang, G. Xie, M. Cheng, D. Wang, R. Yang, D. Shi, K. Watanabe, T. Taniguchi, Y. Yao, Y. Zhang, G. Zhang, Nature Materials 2013, 12, 9 792.

[29] G. L. Yu, R. V. Gorbachev, J. S. Tu, A. V. Kretinin, Y. Cao, R. Jalil, F. Withers, L. A. Ponomarenko, B. A. Piot, M. Potemski, D. C. Elias, X. Chen, K. Watanabe, T. Taniguchi, I. V. Grig- orieva, K. S. Novoselov, V. I. Fal'ko, A. K. Geim, A. Mishchenko, Nature Physics 2014, 10, 7 525.

[30] E. Rotenberg, A. Bostwick, Synthetic Metals 2015, 210 85.

[31] I. Herna´ndez-Rodr´ıguez, J. M. Garc´ıa, J. A. Mart´ın-Gago, P. L. de Andr´es, J. M´endez, Diamond and Related Materials 2015, 57 58 .

[32] J. Yu, Z. Hao, J. Wang, J. Deng, W. Yu, L. Wang, Y. Luo, Y. Han, C. Sun, B. Xiong, H. Li, Journal of Alloys and Compounds 2019, 783 633 .

[33] M. Yankowitz, Q. Ma, P. Jarillo-Herrero, B. J. LeRoy, Nature Reviews Physics 2019, 1, 2 112.

[34] C. R. Dean, A. F. Young, I. Meric, C. Lee, L. Wang, S. Sorgenfrei, K. Watanabe, T. Taniguchi, P. Kim, K. L. Shepard, J. Hone, Nature Nanotechnology 2010, 5, 10 722.

[35] S. J. Haigh, A. Gholinia, R. Jalil, S. Romani, L. Britnell, D. C. Elias, K. S. Novoselov, L. A. Pono- marenko, A. K. Geim, R. Gorbachev, Nature Materials 2012, 11, 9 764.

[36] Z. Zhang, P. Lin, Q. Liao, Z. Kang, H. Si, Y. Zhang, Advanced Materials 2019, 31, 37 1806411.

[37] S. Aeschlimann, A. Rossi, M. Cha´vez-Cervantes, R. Krause, B. Arnoldi, B. Stadtmu¨ller, M. Aeschli-mann, S. Forti, F. Fabbri, C. Coletti, I. Gierz, Science Advances 2020, 6, 20.

[38] J. Mao, S. P. Milovanovi´c, M. Andelkovi´c, X. Lai, Y. Cao, K. Watanabe, T. Taniguchi, L. Covaci, F. M. Peeters, A. K. Geim, Y. Jiang, E. Y. Andrei, Nature 2020, 584, 7820 215.

[39] L. A. Ponomarenko, A. K. Geim, A. A. Zhukov, R. Jalil, S. V. Morozov, K. S. Novoselov, I. V. Grigorieva, E. H. Hill, V. V. Cheianov, V. I. Fal'ko, K. Watanabe, T. Taniguchi, R. V. Gorbachev, Nature Physics 2011, 7, 12 958.

[40] T. Georgiou, R. Jalil, B. D. Belle, L. Britnell, R. V. Gorbachev, S. V. Morozov, Y.-J. Kim, A. Gholinia, S. J. Haigh, O. Makarovsky, L. Eaves, L. A. Ponomarenko, A. K. Geim, K. S. Novoselov, A. Mishchenko, Nature Nanotechnology 2013, 8, 2 100.

[41] Y. Ren, Q. Gao, A. H. MacDonald, Q. Niu, Phys. Rev. Lett. 2021, 126 016404.

[42] J. Liu, X. Dai, Phys. Rev. B 2021, 103 035427.

[43] J. R. Wallbank, M. Mucha-Kruczyn´ski, V. I. Fal'ko, Phys. Rev. B 2013, 88 155415.

[44] K.-H. Jin, S.-H. Jhi, Physical Review B 2013, 87, 7 075442.

[45] D. Kriegner, H. Reichlova, J. Grenzer, W. Schmidt, E. Ressouche, J. Godinho, T. Wagner, S. Y. Martin, A. B. Shick, V. V. Volobuev, G. Springholz, V. Holy´, J. Wunderlich, T. Jungwirth, K. Vy´borny´, Phys. Rev. B 2017, 96 214418.

[46] S. Das, Amit, A. Sirohi, L. Yadav, S. Gayen, Y. Singh, G. Sheet, Phys. Rev. B 2018, 97 014523.

[47] G. Bian, X. Wang, P. J. Kowalczyk, T. Maerkl, S. A. Brown, T.-C. Chiang, Journal of Physics and Chemistry of Solids 2019, 128 109.

9. TWO-DIMENSIONAL ROOM-TEMPERATURE FERROMAGNETISM IN CRTE2

While the discovery of two-dimensional (2D) magnets opens the door for fundamental physics and next-generation spintronics, it is technically challenging to achieve the room-temperature ferromagnetic (FM) order in a way compatible with potential device applications.

In this chapter, we report the growth and properties of single- and few-layer $CrTe_2$, a van der Waals (vdW) material, on bilayer graphene by molecular beam epitaxy (MBE). Intrinsic ferromagnetism with a Curie temperature (T_C) up to 300 K, an atomic magnetic moment of ~0.21 μ_B/Cr and perpendicular magnetic anisotropy (PMA) constant (K_u) of 4.89×10^5 erg/cm^3 at room temperature in these few-monolayer films have been unambiguously evidenced by superconducting quantum interference device and X-ray magnetic circular dichroism. This intrinsic ferromagnetism has also been identified by the splitting of majority and minority band dispersions with ~0.2 eV at Γ point using angle-resolved photoemission spectroscopy. The FM order is preserved with the film thickness down to a monolayer (T_C ~200 K), benefiting from the strong PMA and weak interlayer coupling. The successful MBE growth of 2D FM $CrTe_2$ films with room-temperature ferromagnetism opens a new avenue for developing large-scale 2D magnet-based spintronics devices.

9.1. Introduction

Two-dimensional (2D) layered magnets exhibit novel phases of quantum matter with abrupt transition in the magnon density of states in atomically thin layers. In a three-dimensional

(3D) system, the magnon density of states are consecutive and chiefly determined by exchange interactions. Therefore, a magnetic phase transition could occur at a finite temperature. By contrast, the long-range magnetic order in 2D systems is fragile against thermal fluctuations according to the Mermin-Wagner theorem [1,2]. The magneto-anisotropy in 2D ferromagnets opens up a large spin-wave excitation gap, quenches thermal fluctuations [3-9] and thus stabilizes the long-range magnetic order in 2D regime. In contrast to defect or dopant induced magnetism, the ferromagnetism occurring in a stoichiometric compound is defined as intrinsic ferromagnetism [10].

While the presence of 2D crystals with intrinsic magnetism has been well established, the intrinsic ferromagnetic (FM) order in the discovered magnetic van der Waals (vdW) materials is generally fragile with a low Curie temperature (T_C). It mainly results from the enhanced spin fluctuation in reduced dimensions or the relatively weak exchange interactions. Note that the interlayer bonding strength in vdW compounds is 2–3 orders of magnitude weaker than that of traditional 3D materials[4], which leads to a low T_C in the bulk form already. It motivates research efforts to enhance the robustness of 2D FM order. The first route is doping a FM host with specific elements, which normally results in a limited increase of T_C but unavoidable clusters and/or disorders from dopants [11,12]. The second one is constructing heterostructures with FM (or ferrimagnetic) metals (or insulators), in which the FM order can be enhanced by proximity effects [13,14]. For instance, the (Fe_3GeTe_2/MnTe) [3] superlattices possess an enhanced coercive field as a result of the proximity effect [12]. However, the penetration depth of proximity effect is usually very small (<5 nm), hindering an effective manipulation of magnetic order. The third method is

doping 2D magnets with electrons via electrolyte gating, and thereby modulating the T_C of ferromagnetism. For example, the T_C of an atomically thin Fe_3GeTe_2 flake is successfully raised to even room temperature [15]. Nevertheless, particular device geometry and gating are required by this means. Apart from the issues mentioned above, most of the 2D magnetic materials reported so far are thin flakes exfoliated from bulk with typical size of several micrometers, which greatly limits the practical applications of those 2D magnets in spintronics. Therefore, there is a pressing need for the realization of stoichiometric 2D materials with intrinsic robust ferromagnetism (e.g. high T_C and strong perpendicular anisotropy) and, importantly, compatibility with large-scale solid state device applications.

Molecular beam epitaxy (MBE) growth is significant as it provides the opportunity to obtain nominally stoichiometric single-crystalline films, explore the role of physical dimensionality as well as fabricate heterostructures and superlattices in a way compatible with conventional microelectronics techniques. One remarkable work is the strong FM order in ML VSe_2 epitaxial film with in-plane easy axis and a large magnetic moment (~15 m_B/V) persisting to even above room temperature, as characterized by magneto-optical Kerr effect (MOKE) and vibrating sample magnetometry (VSM) [16]. However, according to the theoretical calculations, the magnetic moment of ML VSe_2 mostly comes from V ions with an atomic value of ~0.6 m_B [17], which is completely contradictory to the experimentally observed large magnetic moment [16], raising doubts about this presumed FM phase. Most recently, Wong *et al*. has provided the evidence of spin frustration with absence of a long-range magnetic order in ML VSe_2 films from complementary temperature- and field-dependent susceptibility measurements [18], in stark contrast to the previous study. Moreover, the

electronic structure and X-ray magnetic circular dichroism (XMCD) measurements of ML VSe_2 conducted by Feng *et al*. reveal no signatures of FM order [19]. These studies suggest that the existence of 2D FM order in VSe_2 remains to be further confirmed. Therefore, layer-controlled growth of stoichiometric large-scale 2D FM films with strong perpendicular magnetic anisotropy (PMA) and direct proof for the intrinsic ferromagnetism by unambiguous techniques would be mandatory. Notably, an above-room-temperature T_C has been reported in 1T-$CrTe_2$ in its bulk form [20]. Very recently, above-room-temperature ferromagnetism has been observed in the exfoliated thin flakes of $CrTe_2$ (10 nm, or ~17 ML) [21,22]. Their properties were found to be rather similar to that of the bulk with in-plane magnetic anisotropy, but with enhanced coercivity compared with its bulk counterpart. However, the magnetic response (e.g., T_C and PMA) of $CrTe_2$ epitaxial thin films with thickness down to ML limit has not been explored so far.

Here, we succeed in synthesizing mono- and few-layer $CrTe_2$ films by MBE and observed intrinsic long-range 2D ferromagnetism. The robust ferromagnetism and strong PMA of $CrTe_2$ films persist up to 300 K, as evidenced by both superconducting quantum interference device (SQUID) and XMCD characterizations. In addition, the splitting of the majority and minority bands (~0.2 eV at Γ point) with distinct photon-energy responses has been observed by *in-situ* angle-resolved photoemission spectroscopy (ARPES) measurements, suggesting the magnetic band structure of $CrTe_2$ with spin-splitting. Furthermore, the $CrTe_2$ thin films retain a robust ferromagnetism with high T_C down to a ML, indicating a weak dimensionality effect. These results establish $CrTe_2$ ultrathin films as a promising 2D ferromagnet for exotic low-dimensional spintronics applications.

9.2. Preparation of CrTe2 film and crystal structure characterization

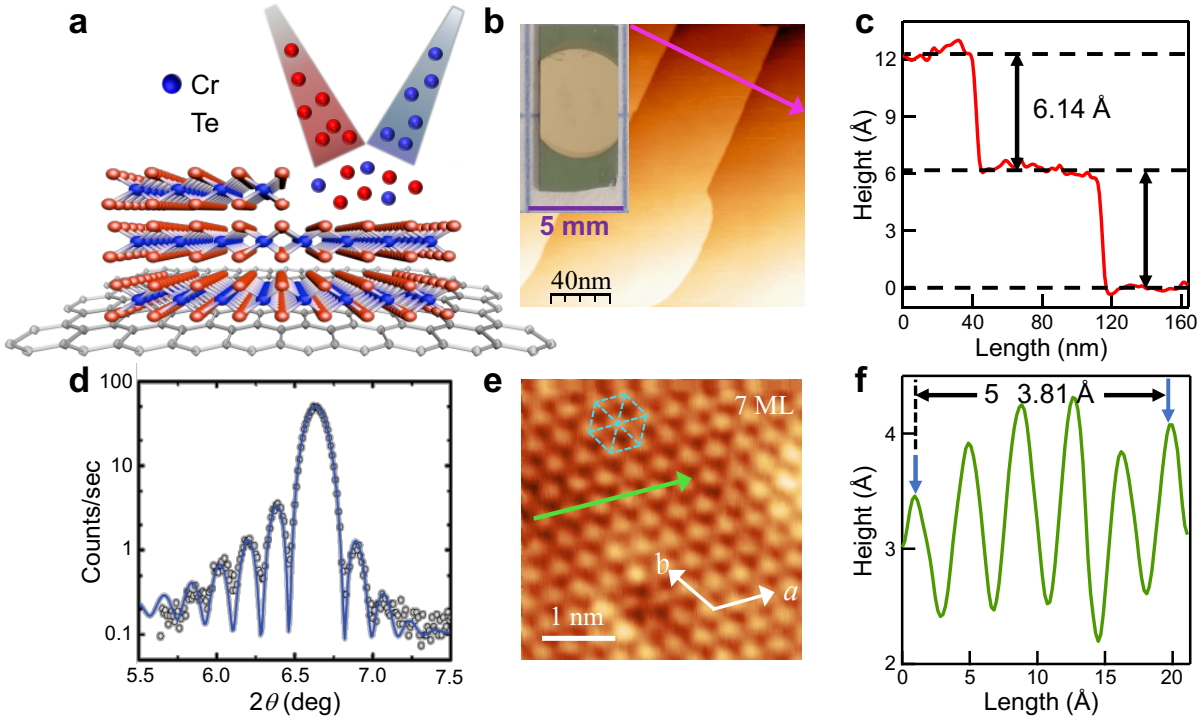

Fig. 9.1 Crystal structure and STM characterizations of epitaxially grown $CrTe_2$ thin films. **a** Schematic illustration of MBE growth process of $CrTe_2$ films on graphene. **b** The STM topology image (200 × 200 nm^2) of a 7 ML $CrTe_2$ fabricated on graphene/SiC. U = +1 V, I_t = 200 pA. Inset on the left is an optical image. **c** The line-scan profile taken along the pink line in b, with an average step height of ~6.14 Å. **d** XRD spectrum showing Laue fringes around the (001) $CrTe_2$ reflections. The solid fitting curve indicates the thickness of 39 layers, the roughness of 2 layers and the lattice constant c = 6.13 Å. **e** Atomically resolved STM image (4 × 4 nm^2) with a hexagonal structure. U = -1.5 mV, I_t = -440 pA. **f** The line-scan along the green arrow in e, showing a lattice periodicity of ~3.81 Å.

$CrTe_2$ is a layered trigonal crystal structure with a unit cell of a hexagonal Cr layer sandwiched between Te layers, as schematically illustrated in Fig. 9.1a. In our experiment, a bilayer graphene on SiC substrate was used to support a layer-by-layer growth of $CrTe_2$ films. The optical image of a single-crystal $CrTe_2$ film with large size (~4 mm × 5 mm) is shown in the inset of Fig. 9.1b. The microscopic topography taken from the surface of a few-layer $CrTe_2$ film by *in-situ* scanning tunneling microscopy (STM) shows atomically flat terrace (Fig. 9.1b). Figure 1c exhibits the step height between adjacent layers with a uniform value of 6.14 Å, which is consistent with the thickness of the unit cell of $CrTe_2$ crystal in 1T phase. One of the atomic resolution image taken by STM on the same sample is presented in Fig. 1e, showing the hexagonal lattice structure. The lattice constant obtained from the line profile in Fig. 1f is 3.81 Å, which is very close to the corresponding bulk $CrTe_2$ lattice parameter (3.79 Å) [20]. STM measurements carried out on several $CrTe_2$ thin films with different thicknesses (mono- to few-layer) show similar terraces, indicating the layer-by-layer growth mode and homogeneously well-structured thin films.

There are various stable stoichiometries reported for chromium chalcogenides [e.g., CrT [23,24], Cr_2Te_3 [25,26], and Cr_5Te_8 [27,28]] depending on the Cr vacancies that occur in intercalation. However, none of them belongs to layered compounds with interlayer vdW gap, except for $CrTe_2$. The layered surface morphology with a uniform step height characterized by STM suggests that the films are in a single phase with vdW gap. The atomic-resolution high-angle annular dark-field scanning transmission electron microscopy (HAADF-STEM) images show the $\sqrt{3}a \times a$ arrangement, revealing that $CrTe_2$ thin films correspond to the 1T phase with an octahedral (O_h) symmetry. Both TEM and STM

characterizations manifest the epitaxial nature and crystallographic orientation of as-grown $CrTe_2$ films. A typical X-ray diffraction (XRD) 2*q*-*w* scan was employed to further identify the crystal structure (Fig. 9.1d). The diffraction pattern with perpendicular constant c = 6.13 Å is matched to the (001) crystal planes of 1T-type hexagonal structure explored experimentally (a = 3.79 Å, c = 6.10 Å) [20], rather than those of the 2H phase (a = 3.49 Å, c = 13.64 Å) [29]. We note that the magnetic exchange coupling is sensitive to the lattice parameters. For example, bulk 1T-$CrSe_2$ with lattice constants of a= 3.39 Å and c = 5.92 Å shows an antiferromagnetic (AFM) order [30], in contrast to the FM phase in $CrTe_2$. With STM, TEM and XRD characterizations, the formation of $CrTe_2$ films with 1T phase and their single-crystalline nature has been confirmed. The reflectivity curves show Laue fringes, attesting to the structural coherence of the film. The chemical states and band structure of the as-synthesized samples were determined by X-ray absorption spectroscopy (XAS) and ARPES as included in the following part, respectively, which further identify the metallic 1T-phase in these few-layer $CrTe_2$ films.

9.3. Magnetic properties in CrTe2 thin film

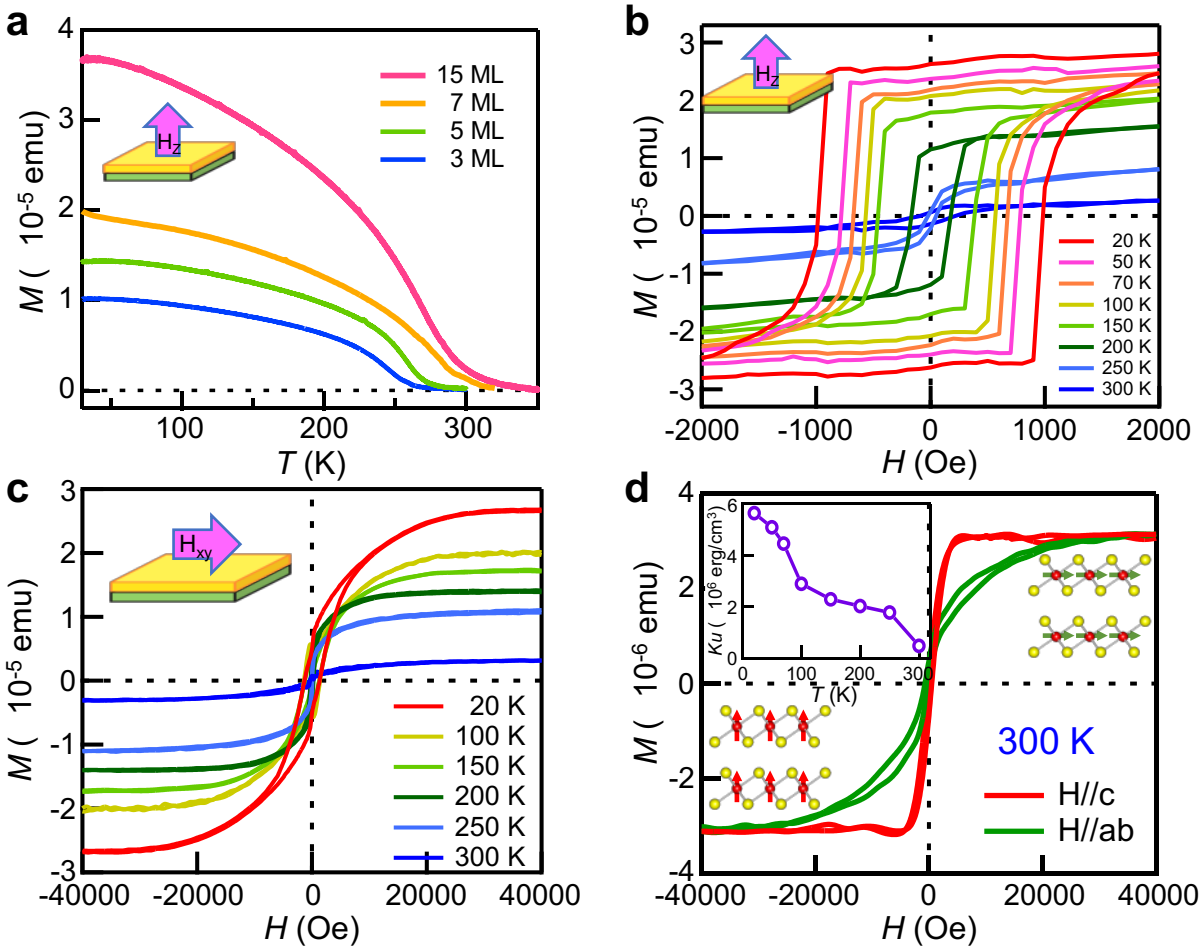

Fig. 9.2 SQUID measurements of the $CrTe_2$ films. **a** Temperature dependent magnetization curves of the films with various thicknesses under field-cooled mode. The magnetic field is applied along the out-of-plane direction with a magnitude of 1000 Oe. The high T_C is preserved with thickness decreasing to 3 ML. **b, c** Magnetic hysteresis loops of 7 ML $CrTe_2$ at different temperatures with external fields along the perpendicular (**b**) and parallel orientation (**c**) with respect to sample plane, indicating a strong out-of-plane magnetic anisotropy. **d** Enlarged hysteresis loops of 7 ML $CrTe_2$ at 300 K, where the intrinsic ferromagnetism and PMA still maintains. Top inset: temperature dependence of K_u for 7 ML $CrTe_2$, where the K_u is preserved at 300 K, despite the lower intensity with the increase of temperature.

Magnetic properties of $CrTe_2$ thin films with both in-plane and out-of-plane configurations were examined by SQUID, as shown in Fig. 9.2. The temperature dependent magnetization (**M-T**) curves of $CrTe_2$ thin films with different thicknesses under an out-of-plane magnetic field of 1000 Oe were measured, as shown in Fig. 9.2a. It shows a general trend of decreasing with the increase of temperature, demonstrating a FM nature. It indicates that the T_C is close to the room temperature with the specific values depending on the thickness. The magnetization of 7 ML $CrTe_2$ film is still observable at 300 K, indicating the FM order at room temperature. The magnetization curve exhibits a long "tail" near $T_{C,}$ which is commonly observed in ferromagnets [4,11,31]. It can be explained by a positive-feedback mean-field modification of the classical Brillouin magnetization theory [32].

The magnetization-magnetic field (**M-H**) hysteresis loops acquired from the 7 ML $CrTe_2$ film at different temperatures are included in Fig. 9.2b and 9.2c. The sharp distinction between out-of-plane (Fig. 9.2b) and in-plane (Fig. 9.2c) **M-H** loops demonstrates a strong out-of-plane anisotropy of the magnetization with a large PMA constant ($K_u = \frac{H_k M_s}{2}$) of 5.63×10^6 erg/cm^3 at 20 K. The K_u in $CrTe_2$ thin films is comparable to the typical PMA systems such as Co/Pd and Co/Pt [33-36], which is vital for obtaining 2D FM order and is also considerably desirable for vdW heterostructures-based spintronics. The film also exhibits rather large coercivities (e.g., ~1000 Oe at 20 K), indicative of a hard magnetic phase. Well-defined hysteresis loops are observed at elevated temperatures up to 300 K (Fig. 9.2d) with the easy axis along the out-of-plane direction and hard axis along the in-plane one. The existence of PMA in the ultrathin 7 ML film is confirmed, supporting the FM order at room temperature. The in-plane magnetic hysteresis loops, similar to those reported in the

FM vdW $Cr_2Ge_2Te_6$ thin films [37] and typical PMA systems such as $Mn_{2.5}Ga$ [38] and Co/Pt [39], can be attributed to the shape anisotropy favoring in-plane easy axis for thin films [40,41]. Control experiments on the field dependent magnetization of SiC/graphene substrate show a typical diamagnetic behavior. Therefore, the possibility of magnetic contribution from magnetic impurities in the substrate can be ruled out. In order to clarify the thickness dependence of the magnetic properties, we have measured the field dependent magnetization curves of 3 ML and 5 ML $CrTe_2$ thin films under out-of-plane and in-plane configuration. The squarish FM hysteresis loops in the out-of-plane magnetic field suggest the robust FM order with the easy axis perpendicular to the thin films, which is essential for the applications of FM devices. Compared with other 2D magnets from literature [3,4,42,43], the $CrTe_2$ films perform a relatively high T_C (above room temperature) and strong magnetic anisotropy with a few atomic layers. Notably, a large K_u (4.89×10^5 erg/cm^3) is maintained at 300 K, comparable to the value of bulk $CrGeTe_3$ at 1.8 K (4.7×10^5 erg/cm^3) [44]. The strong PMA in $CrTe_2$ few-layer films is different from the in-plane magnetic anisotropy observed in bulk $CrTe_2$ [20] and exfoliated flakes (thicker than 10 nm) [21]. Here, the thickness dependent magnetic anisotropy suggests that the reduced symmetry at the interface plays an important role in determining the PMA in $CrTe_2$ thin films [45]. As the magnetic film thickness approaches a few nm, the interfacial magnetism and inversion symmetry breaking give rise to the PMA [46]. This is a consequence of magneto-crystalline anisotropy from spin-orbit interactions, that apparently have a stronger effect in the more anisotropic film limit [33,41,45]. In addition, based on density functional theory (DFT) calculations, it has been found that the FM Cr-Cr intrasublattice exchange interactions dominate in $CrTe_2$ thin films, and the total energy minima is at perpendicular direction [47]. In general, the magnetic

moments of $CrTe_2$ thin films are aligned in the perpendicular direction, due to the magneto-crystalline anisotropy and the anisotropy of exchange interactions.

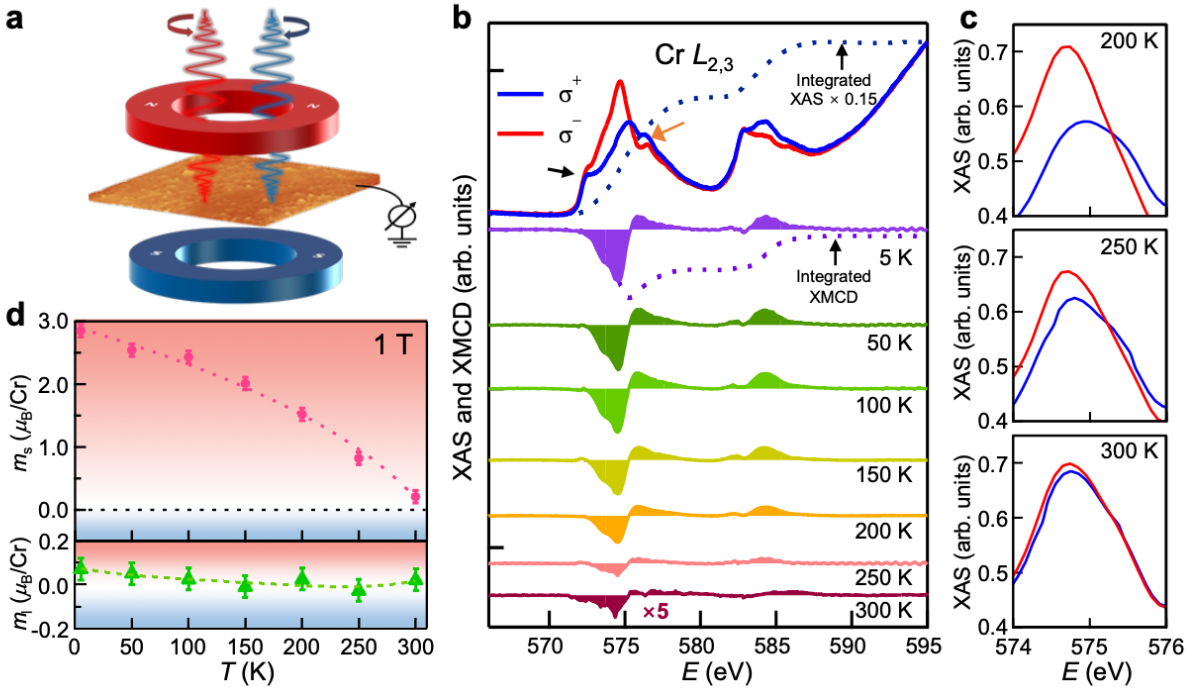

Fig. 9.3 XAS and XMCD characterization of 7 ML $CrTe_2$ films. **a** Schematic geometry of XMCD experimental setup. **b** Typical pairs of XAS and XMCD spectra of 7 ML $CrTe_2$ from 5 K to 300 K and the integrals at 5 K, where the dichroism at Cr L_3 edge can be traced to 300 K (spectra at different temperatures are offset for clarify). **c** The partially enlarged XAS of Cr L_3 edge at 200 K, 250 K, and 300 K. **d** m_s and m_l versus temperature derived from **b** using sum rules. The error bars reflect the uncertainties in the background estimation for the XMCD sum rules analysis.

To examine the local electronic character and magnetic ground states of $CrTe_2$ films, XAS and XMCD measurements at the Cr $L_{2,3}$ absorption edges were performed, as schematically

shown in Fig. 9.3a. This element-specific magnetic characterization technique can also exclude any possible magnetic impurities. The XAS spectra of Cr present multiplet structures around photon energies of 575 eV and 584 eV (Fig. 9.3b), which stem from the excitations from Cr $2p_{3/2}$ and Cr $2p_{1/2}$ core levels, respectively. A small peak (~2 eV away from L_3 peak of Cr) marked with the black arrow comes from Te $5d_{5/2}$ core level, which slightly overlaps with the peak of Cr $2p_{3/2}$ with almost no magnetic contribution [48]. A small peak at the higher energy side (marked with orange arrow) of the main feature in Fig. 9.3b is related to the distribution of atomic multiplet.

Due to the O_h coordination, the $3d$ orbitals of Cr split into e_g and t_{2g} states with energy separation of nominal 10 Dq. The t_{2g} states are lower in energy than the e_g states. In this case, the Cr^{3+} (d^3) configuration with half-filled t_{2g} states causes the reduction of free energy [49], which is in good agreement with the reported theoretical value of magnetic moment, 3 μ_B/Cr atom [50]. The observed XAS spectral line shape is in line with that of spinel $Cu(Cr,Ti)_2Se_4$ polycrystals with trivalent Cr cations on O_h sites [51], further providing a spectroscopic fingerprint of 1T-type $CrTe_2$ with predominately Cr^{3+} cations. In this case, approximately three electrons are removed from the Cr atoms, and distributed over the Te.

The Cr $L_{2,3}$ XMCD spectra in the bottom panel of Fig. 9.3b highlight the emergence of intrinsic ferromagnetism from Cr atoms. XMCD and XAS measurements were repeated at elevated temperatures, and the dichroism of 7 ML thin film at Cr L_3 edge is evident up to 300 K. The characteristic peaks in the spectra remain at the same energy as the temperature rises, despite the attenuation of intensity. For greater clarity, partial enlarged left- and right-circularly polarized XAS of Cr L_3 edge at 200 K, 250 K and 300 K are exhibited in Fig. 9.3c.

There is an obvious difference between the XAS under distinct X-ray helicity even at 300 K, directly confirm the intrinsic FM order coming from the Cr^{3+} cations in the $CrTe_2$ films. The XMCD spectra have been analyzed in terms of element-specific magnetic moments according to the sum rules [52,53]. The spin moment (m_s) and orbital moment (m_l) can be obtained by sum rule:

$$m_s = -n_h \frac{6\int_{L_3}(\sigma^+ - \sigma^-)dE - 4\int_{L_{2,3}}(\sigma^+ - \sigma^-)dE}{\int_{L_{2,3}}(\sigma^+ + \sigma^-)dE} \times \mathrm{SC} - \langle T_z \rangle \quad (1)$$

$$m_l = -\frac{4}{3} n_h \frac{\int_{L_{2,3}}(\sigma^+ - \sigma^-)dE}{\int_{L_{2,3}}(\sigma^+ + \sigma^-)dE} \quad (2)$$

where n_h, SC and $\langle T_z \rangle$ are the number of *d* holes, spin correction factor (estimated to be 2.0 $\pm$0.2 for Cr) [13,54] and the averaged magnetic dipole term, respectively. Based on the trivalent Cr, we assume n_h = 7. The magnetic dipole term, $\langle T_z \rangle$ can be neglected due to its rather small contribution (<5%) in the Cr t_{2g}^3 configuration. An arctangent step-like function was employed in the fitting of the threshold of XAS spectra in order to exclude the nonmagnetic contribution [55,56].

The calculated m_s and m_l from 5 to 300 K are summarized in Fig. 9.3d. The derived m_s demonstrates a Curie-like behavior. A remarkably large value of m_s (2.85$\pm$0.10 μ_B/Cr) is found at 5 K. The m_s retains a sizable value of 0.82$\pm$0.10 μ_B/Cr at 250 K and drops to 0.21$\pm$0.05 μ_B/atom at 300 K, confirming a FM phase transition near this temperature. On the other hand, m_l is relatively small of around 0.08$\pm$0.05 μ_B/atom, consistent with a half-filled t_{2g} level in O_h crystal field of 1T-$CrTe_2$. The m_l plays an important role in the magneto-crystalline anisotropy and the perpendicular orientation of the moments that underlies the

FM order in this 2D system. The atomic magnetic moment of $CrTe_2$ is determined to be ~3 μ_B/atom. The observed FM behavior cannot be attributed to the Cr clusters, since bulk Cr is AFM and therefore would give a zero XMCD intensity.

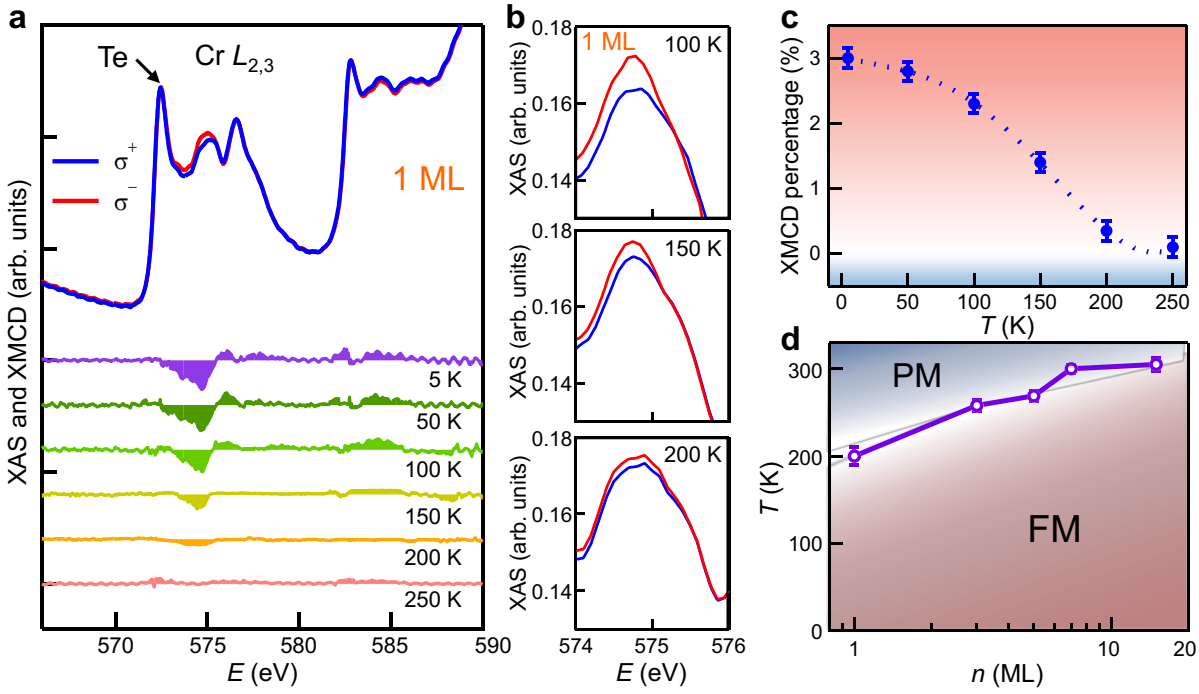

Fig. 9.4 XAS and XMCD characterization of $CrTe_2$ films with thickness of monolayer. **a** Typical pairs of XAS and XMCD spectra of 1 ML $CrTe_2$ thin film at various temperatures, where the dichroism at Cr L_3 edge is observable up to 200 K. **b** The partially enlarged XAS spectra near the Cr L_3 edge, where the difference between left- and right-circularly polarized XAS is evident. **c** XMCD percentage as a function of temperature derived from **a**. The error bars indicate the uncertainties in the background estimation for the XMCD percentage calculation. **d** Compiled thickness–temperature phase diagram with the T_C obtained from XMCD and SQUID measurements. The error bars are the uncertainties in determining the T_C.

The magnetic response of 1 ML $CrTe_2$ film is worth exploring. It is difficult to detect magnetization in such ultrathin films by SQUID, since the magnetic signal of 1 ML $CrTe_2$ is too weak compared with an overwhelmingly larger background signal from the substrate and beyond the resolution of SQUID. Therefore, we did element-specific XMCD characterization of 1 ML $CrTe_2$ film (Fig. 9.4a). There is a noticeable difference in the XAS spectra between left- and right-handed circularly polarized setups (Fig. 9.4b). Although the dichroism is small compared with 7 ML sample, the clear XMCD signals appear near the absorption peaks. It suggests that the intrinsic ferromagnetism of 1 ML $CrTe_2$ film originates from the spin polarization of Cr 3*d* electrons. Accurate calculation of the magnetic moment remains a challenge since the contribution of Te capping layer to the XAS spectra is so large for 1 ML sample. The XMCD percentage increases with the reduced temperature (Fig. 9.4c), in line with a typical FM behavior. The nonzero XMCD percentage persists when temperature approaches 200 K and disappears above 250 K, indicating that 1 ML $CrTe_2$ has a T_C of ~200 K. The T_C has been obtained by using a critical power-law function $\alpha(1-T/T_C)^{\beta}$ to fit **M-T** curves without the inclusion of the paramagnetic tail [42]. In order to investigate the dimensionality effect of the ferromagnetism in $CrTe_2$ stemming from thermal fluctuation, we plot the thickness dependent T_C obtained from XMCD and SQUID measurements in Fig. 9.4d. The T_C of $CrTe_2$ decreases mildly as the film thickness is reduced, in contrast to the other known 2D magnets such as $Cr_2Ge_2Te_6$ [4] and Fe_3GeTe_2 [15]. The high T_C in the 2D limit demonstrates the robustness of ferromagnetism in the epitaxial $CrTe_2$ thin films.

The electronic band structure of $CrTe_2$ thin films has been mapped by ARPES with two different photon energies of 21.2 eV and 40.8 eV at 107 K. The band dispersions of 7 ML $CrTe_2$ measured at $h\nu$ = 21.2 eV along high symmetry crystallographic direction M-Γ-K in the surface Brillouin zone are shown in Fig. 9.5a. Near the Γ point, the main features include two hole-like valence bands aligned close to the Fermi level, which shares identity with the typical features of 1T-$ZrTe_2$ [57]. Near the M point, there are two electron pockets with bottom locating at -1.2 eV and -1.8 eV, respectively. The Fermi surface map shows two circular pockets centered at Γ point surrounded by six triangular pockets at K points. Below the Fermi level, the pockets around K points begin to merge with the expanded pockets at Γ point. The well-defined band structure indicates the high structural quality of the MBE-fabricated films.

9.4. ARPES band spectrum and calculated bands

The origin of the band dispersions has been investigated by first-principle DFT calculations based on $CrTe_2$ slab [18]. The mean free path of photoelectrons excited by photons of 21.2 eV and 40.8 eV is between 0.5 and 1 nm. Therefore, to compare with the experimental spectra, we simulated the band structure with a surface weight of each Bloch wavefunction. The higher intensity in the image means greater weight of wavefunction near the slab surface. Figure 9.4b shows the calculated spin-polarized band structure, with the majority and minority spin bands plotted in blue and red, respectively. Both magnetization and spin orbit coupling (SOC) are taken into account in the calculation, and the magnetic moments are set along out-of-plane direction. According to the orbital and surface projection analysis of the band structure, the metallicity is a consequence of the hybridization of Te-5*p* and Cr-3*d*

orbitals crossing the Fermi level at the center of the Brillouin zone, which is confirmed by the calculated density of states. The hybridization of Te and Cr states was also verified in previous DFT calculations [20]. There is an overall agreement between the experimental (Fig. 9.5a) and calculated band dispersions (Fig. 9.5b), except for the absence of two hole pockets from minority band near Γ point.

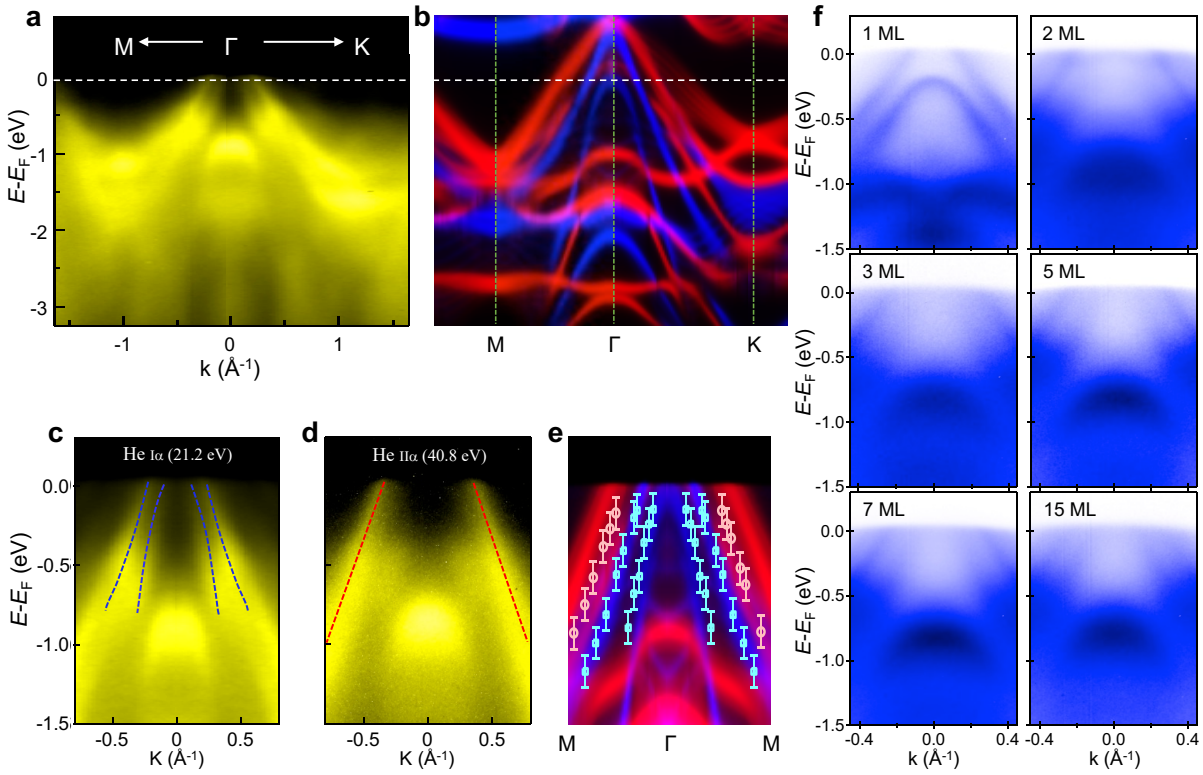

Fig. 9.5 Band structure of $CrTe_2$ ultrathin films. **a**, **b** Plots of valence-band dispersion (**a**) and the first-principles calculations (**b**) of 7 ML $CrTe_2$ with the inclusion of spin polarization along the high symmetry direction M-Γ-K. The minority and majority spin bands are plotted in red and blue colors, respectively. The major features seen in the left panel are well reproduced in the right one. **c-e** Comparison of the valence-band dispersion near the Fermi level taken by He Iα (21.2 eV) (**c**), He IIα photons (40.8 eV) (**d**) with theoretical bands (**e**) along the high symmetry direction M-Γ-M. The

blue and red dashed lines indicate the position of hole pockets measured by He Iα and He IIα photons, respectively. The light blue/red markers represent the positions of MDC peaks. The error bars represent uncertainties in locating peak positions. **f** ARPES intensity maps of 1 ML, 2 ML, 3 ML, 5 ML, 7 ML and 15 ML, respectively. The spectra of various thicknesses were taken along the high symmetry direction M-Γ-M.

To compare experiment and theory in greater detail, the dispersion of hole pockets detected by different photon energies is plotted in Fig. 9.5c and Fig. 9.5d. Note that the two hole pockets near the Fermi level in Fig. 9.5c are mainly from the majority bands. Interestingly, the minority hole pocket shows up in the spectrum taken at $h\nu$ = 40.8 eV (Fig. 9.5d) while the majority ones disappear. It suggests the emission from the minority spin pockets was suppressed in the measurement at $h\nu$ = 21.2 eV as a consequence of matrix element effect [58]. The band dispersion can be traced by fitting the peak position in the momentum distribution curves (MDC), as marked by blue and red dashed lines in Fig. 9.5c and 9.5d, respectively. Combining the band structure near Fermi energy (E_F) taken by He Iα and He IIα photons together, as shown in Fig. 9.5e, the electronic structure is clearly metallic in both the majority and minority spin channels, and agrees well with DFT calculations. Relatively small renormalizations are needed to match with ARPES results, indicating moderate-to-weak correlations. The experimental band structure of $CrTe_2$ is in sharp contrast with the band structure calculated without the inclusion of spin polarization, where hole pockets near E_F are degenerate at Γ point as in the cases of VTe_2 [59] and VSe_2 [18,19]. There are no exchange splitting of band dispersion in MBE grown VSe_2 films, indicating the absence of

ferromagnetism [18,19]. By contrast, the splitting of majority and minority bands (~0.2 eV at Γ point) in $CrTe_2$ films corroborates the FM ground state, which highlights the unique interplay of ferromagnetism and electronic structure in $CrTe_2$. In addition, the calculated magnetic moment of Cr is 2.89 μ_B/atom, in good agreement with the SQUID and XMCD measurements. For a comparison with the ARPES spectra, we also calculated the electronic band structure of 2H-$CrTe_2$, which are different from those observed in the ARPES spectra and the calculated 1T-$CrTe_2$ band structure in the low-energy bands. Another significant difference between 1T and 2H phase is that the 1T-$CrTe_2$ exhibits a FM ground state along *c*-axis, while the 2H-$CrTe_2$ is PM as a result of the fully occupied d_{z^2} orbital of tetravalent Cr. The observed FM band structure and FM properties corroborate the 1T phase of the epitaxial $CrTe_2$ films.

We have further studied the thickness dependence of hole pocket features. The evolution of the band structure for the films with a thickness ranging from 1 ML to 15 ML is shown in Fig. 9.5f. For the 1 ML film, there are two parabolic bands with a maximum above and below the Fermi level, respectively. When film thickness increases to 2 ML, one of the parabolic band overlaps with another one near the Fermi level, sharing similar feature with the case of few-layer $ZrTe_2$ [57] and $HfTe_2$ [60]. With further increasing the film thickness, the Fermi level moves towards the valence band with the band shape invariant. To understand the thickness-dependent electronic structure, we carried out first-principles calculations of 1T-$CrTe_2$ with different thicknesses. There is an excellent agreement between our experiment and theory. In particular, the hole-like band near E_F and a relatively flat Cr 3*d* orbital band are similar to that of calculated 1T-$CrTe_2$ with the inclusion of spin polarization. For the 1

ML film, the two parabolic hole pockets are well reproduced by the majority spin projections of the bands, which highlights the FM nature. These results demonstrate that the epitaxial 1T structure and ferromagnetism have been established since 1 ML deposition, in line with the corresponding STM images. The layer-by-layer growth mode of the $CrTe_2$ ultrathin films enables us to further explore the interplay between electronic structure and extraordinary magnetic properties on the basis of thin-film electronic devices.

9.5. Conclusions

To summarize, we have successfully synthesized high-quality mono- to few-layer $CrTe_2$ via MBE method, for the first time. The epitaxial $CrTe_2$ ultrathin films with thickness up to 7 ML possess room-temperature intrinsic ferromagnetism, large magnetic moments (~3 μ_B/atom), strong perpendicular anisotropy and magnetic spin-split band structure. The high T_C is preserved with the thickness down to one ML due to the strong magnetic anisotropy and the weak interlayer coupling. The FM $CrTe_2$ films can be employed as a spin injector when hybridized with other 2D materials such as topological insulator and topological semimetals for exploring novel spin physics. At the same time, this work provides a tremendous potential for the future 2D magnet-based spintronics technologies, as the films can readily reach wafer size with MBE growth technique.

Reference

[1] *Mermin, N. D. & Wagner, H. Absence of Ferromagnetism or Antiferromagnetism in One- or Two-Dimensional Isotropic Heisenberg Models. Phys. Rev. Lett.* ***17****, 1133-1136 (1966).*

[2] *Gibertini, M., Koperski, M., Morpurgo, A. F. & Novoselov, K. S. Magnetic 2D materials and heterostructures. Nat. Nanotechnol.* ***14****, 408-419 (2019).*

[3] *Huang, B. et al. Layer-dependent ferromagnetism in a van der Waals crystal down to the monolayer limit. Nature* ***546****, 270-273 (2017).*

[4] *Gong, C. et al. Discovery of intrinsic ferromagnetism in two-dimensional van der Waals crystals. Nature* ***546****, 265-269 (2017).*

[5] *Song, T. et al. Giant tunneling magnetoresistance in spin-filter van der Waals heterostructures. Science* ***360****, 1214–1218 (2018).*

[6] *Zhong, D. et al. Van der Waals engineering of ferromagnetic semiconductor heterostructures for spin and valleytronics. Sci. Adv.* ***3****, e1603113 (2017).*

[7] *Seyler, K. L. et al. Ligand-field helical luminescence in a 2D ferromagnetic insulator. Nat. Phys.* ***14****, 277-281 (2017).*

[8] *Wang, Z. et al. Electric-field control of magnetism in a few-layered van der Waals ferromagnetic semiconductor. Nat. Nanotechnol.* ***13****, 554-559 (2018).*

[9] *Jiang, S., Shan, J. & Mak, K. F. Electric-field switching of two-dimensional van der Waals magnets. Nat. Mater.* ***17****, 406-410 (2018).*

[10] *Shabbir, B. et al. Long range intrinsic ferromagnetism in two dimensional materials and*

dissipationless future technologies. Appl. Phys. Rev. ***5****, 041105 (2018).*

[11] May, A. F., Calder, S., Cantoni, C., Cao, H. & McGuire, M. A. Magnetic structure and phase stability of the van der Waals bonded ferromagnet $Fe_{3-x}GeTe_2$*. Phys. Rev. B* ***93****, 014411 (2016).*

[12] Liu, S. et al. Wafer-scale two-dimensional ferromagnetic Fe_3GeTe_2 *thin films grown by molecular beam epitaxy. Npj 2D Mater. Appl.* ***1****, 30 (2017).*

[13] Liu, W. et al. Enhancing magnetic ordering in Cr-doped Bi_2Se_3 *using high-*T_C *ferrimagnetic insulator. Nano Lett.* ***15****, 764-769 (2015).*

[14] He, Q. L. et al. Tailoring exchange couplings in magnetic topological-insulator/antiferromagnet heterostructures. Nat. Mater. ***16****, 94-100 (2017).*

[15] Deng, Y. et al. Gate-tunable room-temperature ferromagnetism in two-dimensional Fe_3GeTe_2*. Nature* ***563****, 94-99 (2018).*

[16] Bonilla, M. et al. Strong room-temperature ferromagnetism in VSe_2 *monolayers on van der Waals substrates. Nat. Nanotechnol.* ***13****, 289-293 (2018).*

[17] Ma, Y. D. et al. Evidence of the Existence of Magnetism in Pristine VX_2 *Monolayers (X = S, Se) and Their Strain-Induced Tunable Magnetic Properties. ACS nano* ***6****, 1695 (2012).*

[18] Wong, P. K. J. et al. Evidence of Spin Frustration in a Vanadium Diselenide Monolayer Magnet. Adv. Mater. ***31****, 1901185 (2019).*

[19] Feng, J. et al. Electronic Structure and Enhanced Charge-Density Wave Order of Monolayer VSe_2*. Nano Lett.* ***18****, 4493-4499 (2018).*

[20] *Freitas, C. D. et al. Ferromagnetism in layered metastable 1T-$CrTe_2$. J. Phys.: Condens. Matter* ***27****, 176002 (2015).*

[21] *Sun, X. et al. Room temperature ferromagnetism in ultra-thin van der Waals crystals of 1T-$CrTe_2$. Nano Res.* ***13****, 3358-3363 (2020).*

[22] *Purbawati, A. et al. In-plane magnetic domains and Neel-like domain walls in thin flakes of the room temperature $CrTe_2$ van der Waals ferromagnet. ACS Appl. Mater. Inter.* ***12****, 30702-30710 (2020).*

[23] *Kanazawa, K. et al. Structural and magnetic properties of hexagonal $Cr_{1-\delta}Te$ films grown on CdTe(001) by molecular beam epitaxy. J. Crys. Grow.* ***415****, 31-35 (2015).*

[24] *Zhao, D. et al. Observation of unconventional anomalous Hall effect in epitaxial CrTe thin films. Nano Res.* ***11****, 3116-3121 (2017).*

[25] *Chen, J. et al. Evidence for Magnetic Skyrmions at the Interface of Ferromagnet/Topological-Insulator Heterostructures. Nano Lett.* ***19****, 6144-6151 (2019).*

[26] *Roy, A. & Guchhait, S. Perpendicular Magnetic Anisotropy and Spin Glass-like Behavior in Molecular Beam Epitaxy Grown Chromium Telluride Thin Films. ACS nano* ***9****, 3772–3779 (2015).*

[27] *Wang, Y. et al. Magnetic anisotropy and topological Hall effect in the trigonal chromium tellurides Cr_5Te_8. Phys. Rev. B* ***100****, 024434 (2019).*

[28] *Liu, Y. & Petrovic, C. Anomalous Hall effect in the trigonal Cr_5Te_8 single crystal. Phys. Rev. B* ***98****, 195122 (2018).*

[29] *Bastos, C. M. O., Besse, R., Da Silva, J. L. F. & Sipahi, G. M. Ab initio investigation of structural stability and exfoliation energies in transition metal dichalcogenides based on Ti-, V-, and Mo-group elements. Phys. Rev. Mater.* ***3****, 044002 (2019).*

[30] *Freitas, D. C. Antiferromagnetism and ferromagnetism in layered 1T-$CrSe_2$ with V and Ti replacements. Phys. Rev. B* ***87****, 014420 (2013).*

[31] *Li, Y. F. et al. Electronic structure of ferromagnetic semiconductor $CrGeTe_3$ by angle-resolved photoemission spectroscopy. Phys. Rev. B* ***98****, 125127 (2018).*

[32] *Harrison, R. G. Calculating the spontaneous magnetization and defining the Curie temperature using a positive-feedback model. J. Appl. Phys.* ***115****, 033901 (2014).*

[33] *Ikeda, S. et al. A perpendicular-anisotropy CoFeB-MgO magnetic tunnel junction. Nat. Mater.* ***9****, 721-724 (2010).*

[34] *Wu, Y., Xu, X. G., Miao, J. & Jiang, Y. Perpendicular Magnetic Anisotropy in Co-Based Full Heusler Alloy Thin Films. Spin* ***5****, 1540012 (2016).*

[35] *Richter, N. et al. Temperature-dependent magnetic anisotropy in the layered magnetic semiconductors CrI_3 and $CrBr_3$. Phys. Rev. Mater.* ***2****, 024004 (2018).*

[36] *Yakushiji, K. et al. Ultrathin Co/Pt and Co/Pd superlattice films for MgO-based perpendicular magnetic tunnel junctions. Appl. Phys. Lett.* ***97****, 232508 (2010).*

[37] *Mogi, M. et al. Ferromagnetic insulator $Cr_2Ge_2Te_6$ thin films with perpendicular remanence. APL Mater.* ***6****, 091104 (2018).*

[38] *Wu, F. et al. Epitaxial $Mn_{2.5}Ga$ thin films with giant perpendicular magnetic anisotropy for*

spintronic devices. Appl. Phys. Lett. ***94****, 122503 (2009).*

[39] Emori, S. & Beach, G. S. D. Optimization of out-of-plane magnetized Co/Pt multilayers with resistive buffer layers. J. Appl. Phys. ***110****, 033919 (2011).*

[40] Lado, J. L. & Fernández-Rossier, J. On the origin of magnetic anisotropy in two dimensional CrI_3*. 2D Mater.* ***4****, 035002 (2017).*

[41] Lau, Y.-C. et al. Giant perpendicular magnetic anisotropy in Ir/Co/Pt multilayers. Phys. Rev. Mater. ***3****, 104419 (2019).*

[42] Fei, Z. et al. Two-dimensional itinerant ferromagnetism in atomically thin Fe_3GeTe_2*. Nat. Mater. 1 Mermin, N. D. & Wagner, H. Absence of Ferromagnetism or Antiferromagnetism in One- or Two-Dimensional Isotropic Heisenberg Models. Phys. Rev. Lett.* ***17****, 1133-1136 (1966).*

[43] Tan, C. et al. Hard magnetic properties in nanoflake van der Waals Fe_3GeTe_2*. Nat. Commun.* ***9****, 1554 (2018).*

[44] Zeisner, J. et al. Magnetic anisotropy and spin-polarized two-dimensional electron gas in the van der Waals ferromagnet $Cr_2Ge_2Te_6$*. Phys. Rev. B* ***99****, 165109 (2019).*

[45] Dieny, B. & Chshiev, M. Perpendicular magnetic anisotropy at transition metal/oxide interfaces and applications. Rev. Mod. Phys. ***89****, 025008 (2017).*

[46] Lee, A. J. et al. Interfacial Rashba-Effect-Induced Anisotropy in Nonmagnetic-Material-Ferrimagnetic-Insulator Bilayers. Phys. Rev. Lett. ***124****, 257202 (2020).*

[47] Fujisawa, Y. et al. Tailoring magnetism in self-intercalated $Cr_{1+\delta}Te_2$ *epitaxial films. Phys.*

Rev. Mater. ***4****, 114001 (2020).*

[48] Ye, M. et al. Carrier-mediated ferromagnetism in the magnetic topological insulator Cr-doped $(Sb,Bi)_2Te_3$*. Nat. Commun.* ***6****, 8913 (2015).*

[49] Hu, T., Li, R. & Dong, J. Characterization of few-layer 1T-$MoSe_2$ *and its superior performance in the visible-light induced hydrogen evolution reaction. J. Chem. Phys.* ***139****, 174702 (2013).*

[50] Otero Fumega, A., Phillips, J. & Pardo, V. Controlled Two-Dimensional Ferromagnetism in 1T–$CrTe_2$*: The Role of Charge Density Wave and Strain. J. Phys. Chem. C* ***124****, 21047-21053 (2020).*

[51] Noh, H. J. et al. Valence values of the cations in selenospinel $Cu(Cr,Ti)_2Se_4$*. EPL* ***78****, 27004 (2007).*

[52] Chen, C. T. et al. Experimental confirmation of the X-ray magnetic circular dichroism sum rules for iron and cobalt. Phys. Rev. Lett. ***75****, 152-155 (1995).*

[53] van der Laan, G. & Thole, B. T. Strong magnetic x-ray dichroism in 2p absorption spectra of 3dtransition-metal ions. Phys. Rev. B ***43****, 13401-13411 (1991).*

[54] Liu, W. et al. Atomic-Scale Magnetism of Cr-Doped Bi_2Se_3 *Thin Film Topological Insulators. ACS nano* ***9****, 10237-10243 (2015).*

[55] Liu, W. Q. et al. Atomic-Scale Interfacial Magnetism in Fe/Graphene Heterojunction. Sci. Rep. ***5****, 11911 (2015).*

[56] Liu, W. et al. Experimental Observation of Dual Magnetic States in Topological Insulators.

Sci. Adv. ***5****, eaav2088 (2019).*

[57] Tsipas, P. et al. Massless Dirac Fermions in $ZrTe_2$ Semimetal Grown on InAs(111) by van der Waals Epitaxy. ACS nano ***12****, 1696-1703 (2018).*

[58] Belopolski, I. et al. Discovery of topological Weyl fermion lines and drumhead surface states in a room temperature magnet. Science ***365****, 1278–1281 (2019).*

[59] Wang, Y. et al. Evidence of charge density wave with anisotropic gap in a monolayer VTe_2 film. Phys. Rev. B ***100****, 241404 (2019).*

10. GIANT TOPOLOGICAL HALL EFFECT IN FM/TI HETEROSTRUCTURES

Discoveries of interfacial topological Hall effect (THE) provide an ideal platform for exploring physics arising from the interplay between topology and magnetism. The interfacial topological Hall effect is closely related to the Dzyaloshinskii-Moriya interaction (DMI) at interface and topological spin textures. However, it is difficult to achieve a sizable THE in heterostructures due to the stringent constraints on the constituents of THE heterostructures such as strong spin-orbit coupling (SOC).

In this chapter, we report the observation of a giant THE signal of 1.39 μΩ·cm in the van der Waals heterostructures of $CrTe_2/Bi_2Te_3$ fabricated by molecular beam epitaxy, a prototype of two-dimensional (2D) ferromagnet (FM)/topological insulator (TI). This large magnitude of THE is attributed to an optimized combination of 2D ferromagnetism in $CrTe_2$, strong SOC in Bi_2Te_3, and an atomically sharp interface. Our work reveals $CrTe_2/Bi_2Te_3$ as a convenient platform for achieving large interfacial THE in hybrid systems, which could be utilized to develop quantum science and high-density information storage.

10.1. Introduction

Over the past decade, real-space magnetic chiral spin textures have generated enormous attention for featuring Berry curvature physics and inherent magnetic stability. [1-3] Generally, the topological spin texture with scalar spin chirality in real-space provides an emergent field , which acts on charge carriers and consequently generates the topological Hall effect (THE). [4,5] This real-space THE is distinct from the intrinsic anomalous Hall

effect (AHE) in ferromagnets (FMs), which results from the Berry phase in momentum space. Magnetic skyrmions were firstly observed in noncentrosymmetric chiral-lattice magnets like B20-type MnSi/MnGe [6-8] and $Fe_{0.5}Co_{0.5}Si$, [9] which showed prominent THE responses in transport measurements. Since then, the THE has been considered as an experimental signature of the topological spin texture of skyrmions.

The occurrence of the delicate spin texture of skyrmions depends on the strength of the Dzyaloshinskii-Moriya interaction (DMI). A practical way to generate DMI is to construct heterostructures with spin ordering and strong spin-orbit coupling (SOC). Inversion symmetry is always broken at the interface of two dissimilar materials in a heterostructure, which is essential for generating DMI. Advances in fabricating artificial structures based on thin-film deposition techniques enable construction of heterostructures with essential ingredients for interfacial DMI and skyrmions. Néel-type skyrmions have been probed in hybrid systems, including FM/heavy-metal (HM), [2,10-12] FM/topological insulator (TI), [13-15] TI/magnetic insulator (MI)[16] and HM/MI heterostructures. [5,17] These hybrid systems with magnetic skyrmions are summarized in Figure 10.1. For instance, a two-dimensional (2D) skyrmion lattice was revealed in monolayer Fe on Ir surface, originating from the co-interplay of four-spin interaction and DMI. [12] Moreover, interfacial DMI and skyrmions have been observed in $(BiSb)_2Te_3$/GdFeCo heterostructures, [15] benefiting from the strong SOC in TIs. Among all the research framework of interfacial hybrid systems with interfacial magnetic skyrmions, 2D FM/TI, a van der Waals (vdW) heterostructure, remains largely unexplored. Compared with conventional hybrid systems involving three-dimensional (3D) metals, vdW heterostructures hold many advantages, including reduced

sample dimension (with thickness down to a few atomic layers), flexibility in stacking order, and the atomically sharp interface between vdW components. Those features favor the formation of strong interfacial DMI and chiral spin textures such as skyrmions. Therefore, optimization of vdW heterostructures provides a promising opportunity for exploring interfacial skyrmion physics.

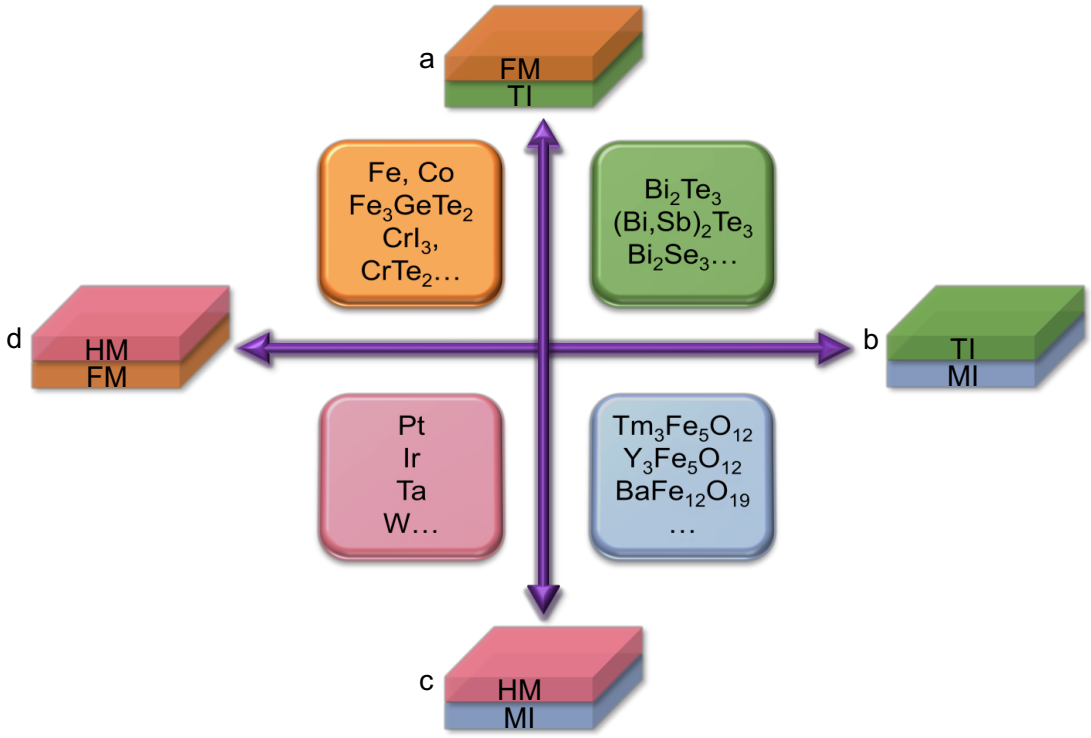

Figure 10.1. Research frameworks of interfacial magnetic skyrmions in hybrid systems. **a-d** Four categories of heterostructures with interfacial magnetic skyrmions, including FM/TI (Cr_2Te_3/Bi_2Te_3) [13] **a**, TI/MI ($Bi_2Se_3/BaFe_{12}O_{19}$) [16] **b**, HM/MI ($Pt/Tm_3Fe_5O_{12}$) [5,17] **c**, and HM/FM (Ir/Fe/Co/Pt) [10,11] **d**. The orange, green, blue and pink squares represent FM, TI, MI and HM, respectively.

2D vdW magnets with intrinsic ferromagnetic order preserved in monolayer limit provide opportunities for probing the THE. The strong uniaxial magnetic anisotropy (K) of 2D

magnets is vital for the formation of 2D ferromagnetism. However, it also raises the threshold of DMI for generating the chiral spin texture ($D_c = 2\sqrt{2JK}/\pi$, where D_c represents the critical DMI value and J is the exchange interaction coefficient). [18] TI can serve as the other component in a bilayer heterostructure to provide strong SOC that can modulate spins in real space. [15] In addition, the topological surface states (SS) of TI could mediate the interfacial DMI. [19,20] It has been demonstrated that Néel-type skyrmions exist in mechanically exfoliated 1T'-WTe_2/Fe_3GeTe_2 heterostructures. [21] Very recently, room-temperature intrinsic ferromagnetism has been observed in $CrTe_2$ epitaxial films, [22] indicating that $CrTe_2$ is a promising spin host for THE heterostructures. Furthermore, the epitaxial thin films are critically significant for spintronics device applications as they offer the opportunity to fabricate wafer-size heterostructures and superlattices with thickness down to atomic layers. As a prototypical TI, Bi_2Te_3 features a single Dirac cone, which can act as nontrivial SS to mediate DMI. [23-25] Moreover, compared with Ta, W and Pt compounds, Bi_2Te_3 possesses a much larger SOC, [26,27] due to the facts that Bi is the heaviest nonradioactive element and the atomic SOC is proportional to the fourth power of atomic number, Z^4. Besides robust spin order in $CrTe_2$ and strong SOC in Bi_2Te_3, $CrTe_2$ and Bi_2Te_3 also share three crucial features for realizing strong interfacial DMI: 1) vdW interlayer coupling, 2) simple telluride compounds, and 3) hexagonal surface lattice symmetry, which facilitates the formation of an atomically sharp interface between the two compounds. Therefore, $CrTe_2$/Bi_2Te_3 heterostructure presents an optimal condition for stabilizing interfacial THE.

In this chapter, we report the realization of an optimal THE heterostructure, $CrTe_2/Bi_2Te_3$, as demonstrated by angle-resolved photoemission spectroscopy (ARPES) and scanning tunneling microscopy (STM) and magneto-transport measurements. The epitaxial heterostructure was grown by molecular beam epitaxy (MBE) with thickness down to a few atomic layers. A pronounced THE resistivity of ~ 1.39 μΩ·cm was observed at 10 K, much larger than the typical THE strength ~0.1 μΩ·cm of previous THE bilayer heterostructures. The observed THE signals in $CrTe_2/Bi_2Te_3$ persist up to 100 K, indicating a highly robust topologically non-trivial chiral spin texture at the interface.

10.2. Preparation of 2D FM/TI heterostructures

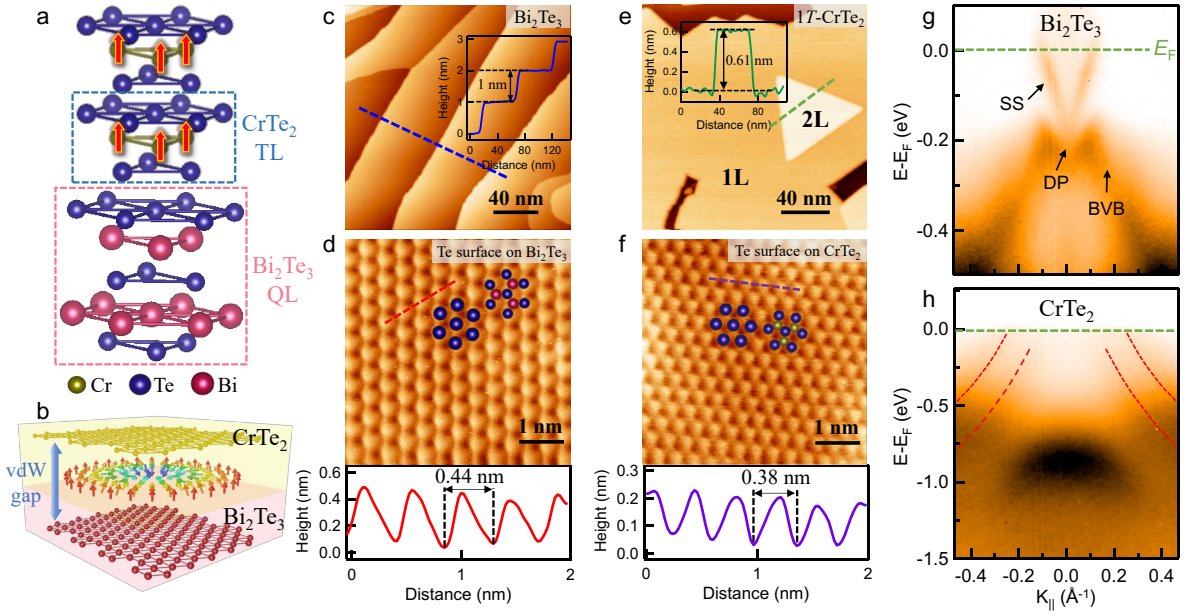

Figure 10.2. Atomic-scale growth and ARPES characterization of $CrTe_2/Bi_2Te_3$ heterostructure. **a** Crystal structure of the $CrTe_2/Bi_2Te_3$ heterostructure. **b** Schematic picture of $CrTe_2/Bi_2Te_3$ bilayer with vdW gap. **c,e** Surface morphologies of 10 QL Bi_2Te_3 **c** and 2 TL $CrTe_2$ grown on Bi_2Te_3 **e** (tunneling condition V = 1000 mV, I = 0.01 nA). Inset: Cross-sectional profile of QL Bi_2Te_3 and TL $CrTe_2$ flakes along the blue and green dashed line, respectively. **d,f** Atomically resolved Te surfaces

of Bi_2Te_3 **d** and $CrTe_2$ **f** with corresponding atomic lattice structures (V = 10 mV, I = 0.2 nA). The panel below indicates the lattice unit distance calculated from line-cut profile. **g,h** ARPES spectra of Bi_2Te_3(111) **g** as well as $CrTe_2$ thin film on Bi_2Te_3 **h** taken with a photon energy of 21.2 eV.

Quintuple layers (QLs) of Bi_2Te_3 thin films were firstly grown on sapphire (Al_2O_3) substrates (see Methods), followed by 10 trilayers (TLs) of $CrTe_2$ on top. 1T-$CrTe_2$ has a layered trigonal crystal structure with the space group of $p\bar{3}m1$ and lattice constants a=3.8 Å and c=6.1 Å. [28] A schematic of $CrTe_2/Bi_2Te_3$ bilayer is shown in Figure 10.2a, in which the red arrows represent the magnetic moments of Cr. Few-layer $CrTe_2$ is a ferromagnetic material with strong perpendicular magnetic anisotropy (PMA). The magnetic moments of Cr atoms in adjacent layers are ferromagnetically coupled with an atomic value of ~3 μ_B/atom. 2D crystalline thin films were characterized by STM (Figure 10.2c-10.2f). Bi_2Te_3 and $CrTe_2$ surfaces are identified *via* comparisons of their respective step edge heights and atomic lattice distances. Figure 10.2c and 10.2e are the large-scale STM images of atomically flat Bi_2Te_3 and $CrTe_2$ thin films with height profiles (inset) showing different layers. The hexagonal atomic lattices of the top Te layer of Bi_2Te_3 and $CrTe_2$ with a spacing of 0.44 nm and 0.38 nm are shown in Figure 10.2d and 10.2f, respectively. A typical layer-by-layer growth mode of $CrTe_2/Bi_2Te_3$ bilayers with atomically flat surfaces and the same Te terminated layers endows the system with emergent phenomenon and tunable functionality. ARPES measurements were performed to visualize the band structure of the heterostructures. The band spectra of Bi_2Te_3 and $CrTe_2$ thin films along M–Γ–M direction are shown in Figure 10.2g and 10.2h, respectively. The "M" shape bulk valence band (BVB)

of Bi_2Te_3 locates at the bottom. The clear linear band dispersion confirms the massless Dirac SS, which do not disperse with photon energy. The Dirac point is located at ~0.25 eV below the Fermi level. These typical features are in agreement with previous works. [23,29] In the spectrum of $CrTe_2$, two hole-pockets locate near the Fermi level. These two pockets are from the majority and minority spin bands of $CrTe_2$, which is consistent with the first-principles results. [22] The spin band structure confirms the intrinsic ferromagnetism in $CrTe_2$ thin layers. The coexistence of intrinsic topological SS with strong SOC and magnetic states at the interface establishes that the $CrTe_2/Bi_2Te_3$ bilayer is a viable platform to study the THE.

10.3. THE -- Berry phase effect in real space

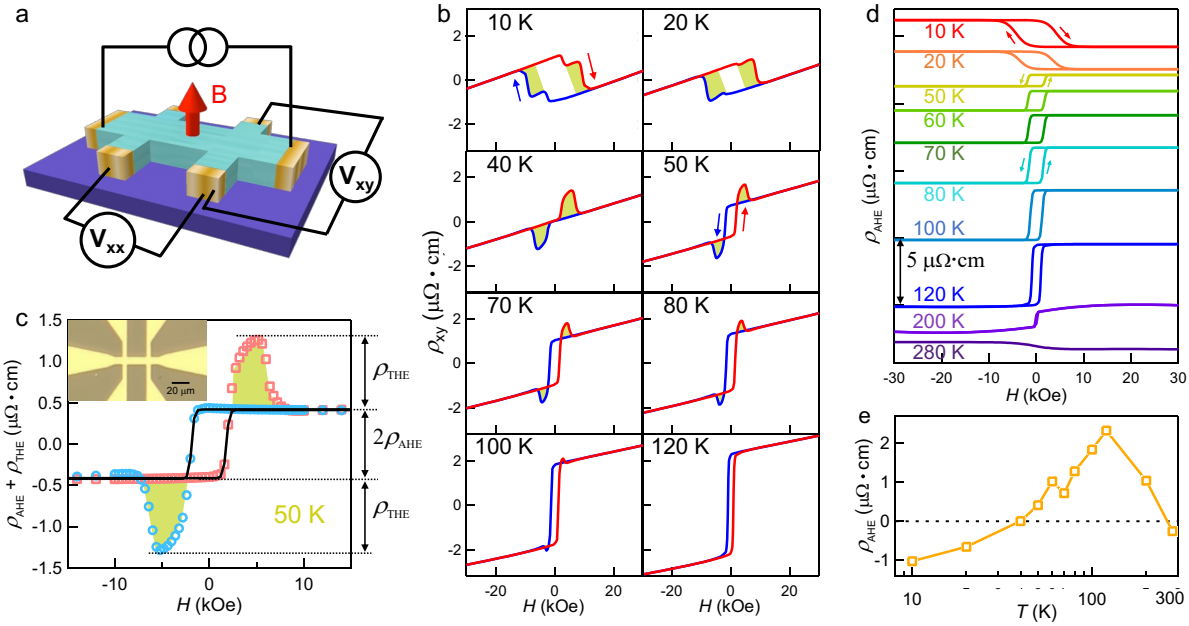

Figure 10.3. Hall resistivity of $CrTe_2/Bi_2Te_3$ bilayer with a perpendicular magnetic field. **a** Schematic diagram of the experimental set up for transport measurements. **b** Magnetic-field dependence of ρ_{xy} at various temperatures for the $CrTe_2/Bi_2Te_3$ sample. Curves are antisymmetrized to remove the ρ_{xx}

component. The positive slope at high field indicates hole carriers. Red (blue) curve represents the process of increasing (decreasing) magnetic field. The humps on the shoulder of AHE loops are highlighted in light green. **c** Detailed view of the Hall resistivity at 50 K with subtraction of ordinary Hall term. Contribution from AHE (black solid lines) and THE term (light green area) is marked, where the AHE contribution is fitted by a $M_0 \tanh(\frac{H}{a_0} - H_0)$ function to represent the magnetization, where M_0, a_0 and H_0 is a fitting parameter. Inset: An optical image of a Hall bar device with a 20 μm scale bar. **d** Field-dependent anomalous Hall loops of the bilayer at different temperatures obtained by fitting with function of $M_0 \tanh(\frac{H}{a_0} - H_0)$. An unexpected transition of AHE component occurs with temperature decreasing below 50 K. **e** The magnitude of the AHE (ρ_{AHE}) at different temperatures extracted from **d**.

The $CrTe_2/Bi_2Te_3$ bilayers were patterned into a Hall bar geometry for magnetotransport measurements. The schematic diagram of the experimental setup is illustrated in Figure 10.3a. Figure 10.3b shows the Hall resistivity (ρ_{xy}) as a function of the magnetic field. At low temperatures, the hysteresis loops show a pronounced square shape, which is a hallmark of robust ferromagnetism with strong out-of-plane magnetic anisotropy. The remanent ρ_{xy} and coercive field (H_C) vanish at around 280 K, indicating a Curie temperature (T_C) near this temperature.

The positive slope at high field suggests dominant hole carriers, echoing the electronic structure of $CrTe_2$ where the hole pockets in the valence band cross the Fermi level. Apart from that, an anomaly in ρ_{xy} is noticed below 120 K. There is a sharp antisymmetric peak near H_C followed by a smooth suppression at the high field region. The emergent hump and dip features indicate an additional contribution to the Hall signal, which shares similarity

with the THE response. When the spin-polarized electrons at the interface pass through a chiral spin texture, they pick up the real-space Berry phase by aligning their spins with the local magnetic moments, giving rise to the THE contribution to the Hall resistivity.

In general, the Hall resistivity of a ferromagnetic conductor consists of three contributions: an ordinary Hall effect (OHE) term due to the Lorentz force acting on the charge carriers, the AHE term proportional to the magnetization and the THE term resulting from the real-space Berry phase. Therefore, ρ_{xy} can be expressed as:

$$\rho_{xy}(H) = R_0 H + R_s M + \rho_{\mathrm{THE}},$$

where R_0 is the ordinary Hall coefficient determined from a linear fitting of ρ_{xy} at high magnetic fields, R_s is the anomalous Hall coefficient of the ferromagnetic component, and ρ_{THE} is the topological Hall contribution. The THE and AHE contributions should be extracted to understand the temperature evolution of THE and AHE. Two main approaches are employed to single out THE component. The first one is using a step function, $M_0 \tanh\left(\frac{H}{a_0} - H_0\right)$ to extract the AHE contribution. [18] At a high magnetic field, all the spins align ferromagnetically, leading to the absence of spin chirality. Under this circumstance, ρ_{xy} is only from the AHE and ordinary Hall term. When the magnetization starts to change orientation near H_C, the ρ_{xy} curve deviates from AHE behavior and develops a broad hump over AHE loops. An example of the AHE background subtraction based on the fitting function of $M_0 \tanh\left(\frac{H}{a_0} - H_0\right)$ is exhibited in Figure 10.3c. The topological Hall term is highlighted by green areas. The other method is taking the difference of resistivity between upward and downward field scans. [30] Considering the positive field region at 50 K, the $CrTe_2/Bi_2Te_3$ system is in a topologically trivial ferromagnetic state without any spin

chirality during the downward field sweep. When the sweep direction changes from downward to upward, the system evolves into an intermediate chiral spin texture during the process of magnetic transitions. Therefore, ρ_{THE} can be extracted by taking the difference between the hysteresis loops under upward and downward field sweeps. We have used both methods to extract the THE contribution, and the fitting results are equivalent.

10.4. Temperature and field evolution of AHE and THE

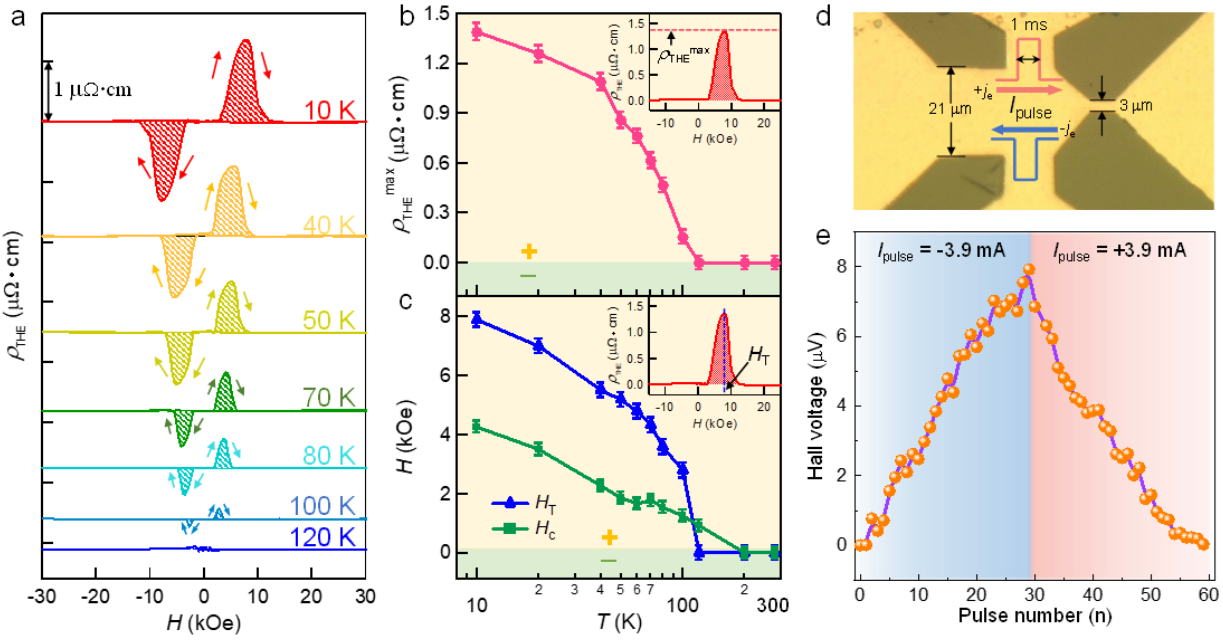

Figure 10.4. Interfacial coupling induced topological Hall effect and effective manipulation of magnetic skyrmions. **a** Typical pairs of magnetic-field dependence of the topological Hall resistivity at various temperatures generated after subtracting the AHE term (loops at different temperatures are offset vertically for clarity). **b,c** Temperature-dependent topological Hall effect. Red and blue solid symbols represent the amplitude (ρ_{THE}^{max}) and the field (H_T) at which the topological Hall resistivity reaches its maximum (top inset), respectively. Green squares are the H_C of AHE, which scale quite

well with H_T. **d** An optical image of a Hall bar device structure, in which a geometrical constriction is introduced for giving rise to an inhomogeneous current distribution. **e** Hall voltages recorded after repeated 1-ms-long current pulses (j_e=±3.9 mA).

After subtracting the OHE and THE term, the net AHE signal is displayed in Figure 10.3d. Nonlinear field dependence of ρ_{AHE} with a negative value emerges at 280 K. Upon cooling, a pronounced hysteresis loop appears, indicating the formation of ferromagnetic order. In particular, the AHE changes its polarity as temperature decreases below 50 K (Figure 10.3e), at which ρ_{xy} is dominated by the THE contribution. We now discuss possible origins of the polarity change of AHE in $CrTe_2/Bi_2Te_3$. Since the magnetization (M) is positive at a high positive magnetic field, the negative AHE is definitely due to the sign-change of R_s. R_s is the ratio of the anomalous Hall resistivity to the M, which consists of contributions from extrinsic dynamical processes such as skew scattering and side-jump, and intrinsic Berry curvature of the band structure. The extrinsic mechanisms depend on the impurities, scattering time, and density of states at the Fermi level. [31] On the other hand, the intrinsic AHE is related to the integral of the Berry curvature over the Fermi sea. [32] Similar sign-change behavior of AHE was previously observed in ferromagnetic $SrRuO_3$ crystals and $Cr_x(Bi_{1-y}Sb_y)_{2-x}Te_3/(Bi_{1-y}Sb_y)_2Te_3$ heterostructures, which is theoretically shown to result from the magnetic monopoles in momentum space [32] and Rashba splitting of bulk bands, [33] respectively. In addition, temperature-dependent sign-change of ρ_{AHE} has been reported in Co/Pd multilayers, [34] in which the phonons/magnons scattering has a crucial contribution. The variation of momentum-space Berry curvature around the Fermi level is also a possible explanation for the polarity change of AHE in $CrTe_2/Bi_2Te_3$ at low

temperatures. Considering that the longitudinal resistivity of $CrTe_2$ increases with temperature, the enhanced ρ_{AHE} with temperature is likely due to the growing electron-phonon or magnons scattering. When the temperature further increases above 120 K, ρ_{AHE} is reduced due to the suppressed magnetization at high temperatures. The interplay of ferromagnetism, topology and spin-dependent scattering leads to complex AHE behaviors.

The magnetic-field dependence of the THE shows a hysteresis behavior in Figure 10.4a. At 10 K, THE reaches its maximum at 7.9 kOe and decays gradually to zero at high fields. The THE signal persists up to 100 K, despite the decreased intensity at high temperature. Above this temperature, only AHE is present. Note that the THE features with a similar critical temperature can be reproduced in another $CrTe_2/Bi_2Te_3$ bilayer sample. To further study the characteristics of the Hall anomaly, we extracted the peak value of ρ_{THE} (ρ_{THE}^{max}), H_C and peak position of humps (H_T) in Figure 10.4b. ρ_{THE}^{max}, the maximal amplitude of THE signal, manifests a pronounced value of 1.39 μΩ·cm at 10 K, and decreases monotonically at elevated temperatures. Notably, the observed ρ_{THE}^{max} in $CrTe_2/Bi_2Te_3$ is the largest among interfacial and bulk skyrmion systems known to date, including Ir/Fe/Co/Pt (0.03 μΩ·cm), [11] $SrIrO_3/SrRuO_3$ (0.2 μΩ·cm), [35] $Pt/Y_3Fe_5O_{12}$ (0.3 μΩ·cm) [36] and bulk MnSi (0.04 μΩ·cm), [7] as summarized in Table 1. We note that the THE amplitude observed in this work is lower than the magnetic bubbles system $Ca_{0.99}Ce_{0.01}MnO_3$ (120 μΩ·cm). [4] The amplitude of the topological Hall resistivity reflects the strength of the coupling between electric current and the spin structure. [37] For metallic systems, the reduced electron mean free path and the large charge carrier density usually lead to a significant reduction of THE contribution to Hall resistivity because the conductivity is sensitive to the disorder. [38]

However, in $CrTe_2/Bi_2Te_3$ systems, the nontrivial SS of TI provides nearly dissipationless spin transport, which enhances the electron mean free path. Additionally, the atomically sharp interface between vdW layers is also favorable for enhancing interfacial DMI and hence the THE.

Table 1. Maximal THE amplitude (ρ_{THE}^{max}) in various skyrmion systems from literatures[α]

Material	Maximal THE (μΩ·cm)	Ref.	System
$CrTe_2/Bi_2Te_3$	1.39	[*]	Interfacial skyrmion
Fe_3GeTe_2/WTe_2	1.3	[21]	Interfacial skyrmion
Cr_2Te_3/Bi_2Te_3	0.53	[13]	Interfacial skyrmion
$Pt/Y_3Fe_5O_{12}$	0.3	[36]	Interfacial skyrmion
$SrIrO_3/SrRuO_3$	0.2	[35]	Interfacial skyrmion
Ir/Fe/Co/Pt	0.03	[11]	Interfacial skyrmion
$Fe_{0.7}Co_{0.3}Si$	0.5	[9]	Bulk skyrmion
MnGe	0.16	[6]	Bulk skyrmion
MnSi	0.04	[7]	Bulk skyrmion

[α] Typical values of ρ_{THE}^{max} from reports. Our work [*] has demonstrated a relatively large ρ_{THE}^{max} among them.

The temperature dependence of H_T and H_C are summarized in Figure 10.4c. The curve of H_T at which ρ_{THE} reaches its maximum follows the trend of H_C, suggesting that the spin chirality is induced when the magnetic moments of Cr atoms start to be reversed. Note that the THE response is developed when carriers pass through the emergent magnetic field, that is, a fictitious field derived from the Berry phase in real-space. The topological Hall feature is the strongest at low temperature, then monotonically decreases at elevated temperatures and disappears above 100 K. Although this critical temperature is lower than that of magnetic

skyrmion multilayers composed of heavy-metal thin films (usually above room temperature), it is significantly higher than typical TI-based skyrmion systems, like $MnTe/(Bi,Sb)_2Te_3$ (20 K), [14] Mn-Bi_2Te_3 (14 K) [19] and Cr_2Te_3/Bi_2Te_3 (20 K). [13] It is comparable with other vdW interfacial DMI systems, such as Fe_3GeTe_2/WTe_2 (100 K). [21] Moreover, the sign of THE remains positive in the entire temperature window, irrespective of the sign change of AHE. It indicates that the origin of THE is entirely different from that of AHE. The THE is associated with the DMI strength, while AHE is related to the resistivity and magnetization.

How electric currents can manipulate chiral spin textures in hybrid systems remains elusive. To investigate it, experimental depinning and motion of spin chirality by applying current pulses were conducted in the $CrTe_2/Bi_2Te_3$ system, as exhibited in Figure 10.4e. Upon passing a current of $-j_e$ through the device, the left of the device develops dense chiral spin textures, giving rise to an increased Hall voltage, and vice versa. This is a strong evidence of skyrmions as similar Hall voltage change was observed when current was used to pulse skyrmions. [38] Since the current can only shrink and elongate the topologically trivial magnetic textures, it clearly follows that the topologically nontrivial spin textures in $CrTe_2/Bi_2Te_3$ system with well-defined chirality can be efficiently manipulated, including depinning and motion. In order to rule out the Joule heating effect, we have carried out the control experiment with pulse width of 0.01 ms. The curve is almost the same as the case for the 1 ms pulse width. These results show that Joule heating has a negligible effect on the current-induced skyrmion depinning and motion experiment. [39]

10.5. Quantitative agreement between transport and theoretical simulations.

Combining the THE signals for all temperatures and magnetic fields, a phase diagram is plotted in Figure 10.5a. As temperature decreases, the THE amplitude increases and can exist in a stronger magnetic field. It is because THE is induced by the thermodynamic stability of the chiral spin texture, which is enhanced by lowering the temperature. Therefore, a stronger magnetic field is needed to eliminate this nontrivial spin texture. The large amplitude of THE at low temperatures manifests a stronger fictitious magnetic field induced by Berry phase effects in real space. The emergence of THE humps across a wide range of temperature from 10 K to 100 K, suggests that the topological spin structure is robust. The THE effect exists only below the T_C of $CrTe_2$, which rules out the possibility of spin chirality driven by thermal fluctuation. [18] Moreover, the THE is absent in the transport properties of pure $CrTe_2$ thin films, [22] implying the important role of TI in the formation of spin chirality.

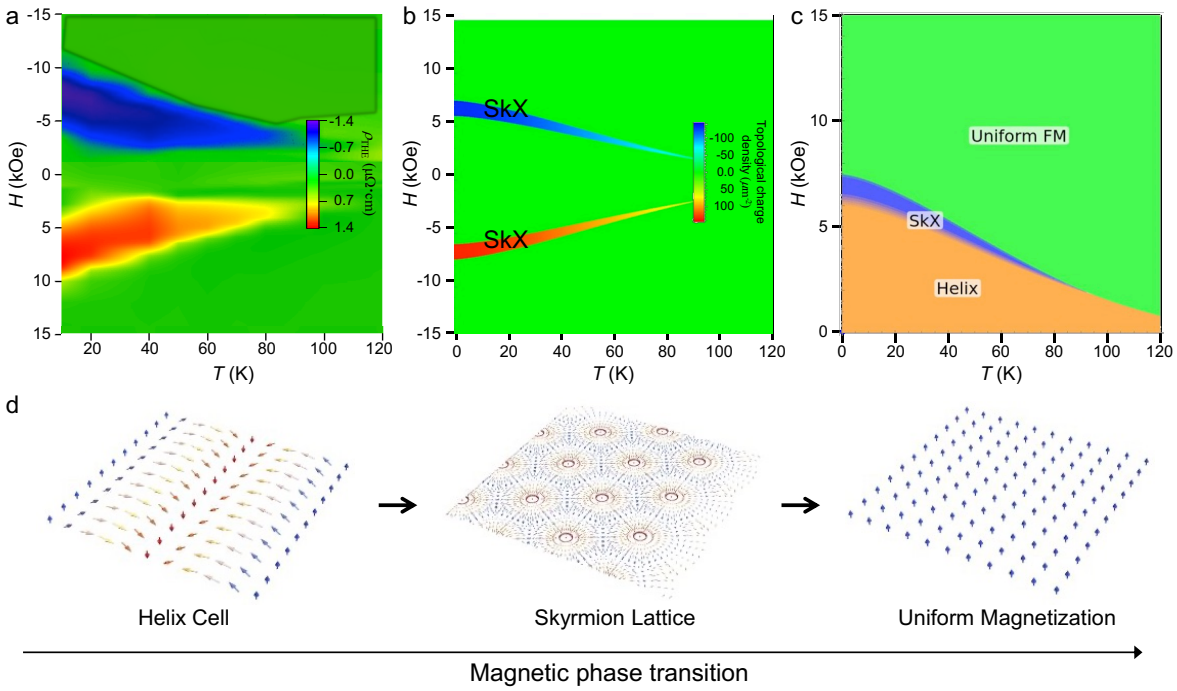

Figure 10.5. Topological Hall resistivity, topological charge density, magnetic phase diagram and spin ordering. **a** Experimental color map of ρ_{THE} in the temperature-magnetic field plane. A larger THE amplitude at lower temperature indicates a higher density of Néel skyrmions. **b** Calculated topological charge density as a comparison with the measured topological Hall resistivity. **c** Calculated magnetic phase diagram in the plane of temperature and out-of-plane magnetic field. The colored regions correspond to the uniform FM (green), the helix (orange), and the skyrmion lattice (SkX; blue) phases, respectively. **d** Schematic spin structures of helix phases, closely-packed hexagonal SkX, and uniform ferromagnetic phase.

To understand spin chirality and the experimental phase diagram in $CrTe_2/Bi_2Te_3$ hybrid system, we calculated the energy landscapes of various magnetic states, which arise from the competition between exchange coupling, uniaxial anisotropy, and DMI in this system. [40] Figure 10.5c shows a magnetic phase diagram in the plane of magnetic field and temperature calculated by using zero-temperature saturation magnetization (M_0 = 362 emu/cm^3), experimental perpendicular anisotropy coefficient ($K_u = 3.16\times10^5$ J/m^3), and taking the DMI coefficient[41] as $D(T) = D_0\left[1-\left(\frac{T}{T_c}\right)^{\frac{3}{2}}\right]^5$ with $D_0 = 6\times10^{-3}$ J/m^{-2} and the T_C of $CrTe_2$ being 280 K. The Ginzburg-Landau model [42] is employed in the calculation At low magnetic fields, a helical phase with zero net out-of-plane magnetization is energetically favorable. When the out-of-plane magnetic field is increased to a window of intermediate field strength, a skyrmion lattice phase prevails over the helical phase as the out-of-plane magnetization in the skyrmion core areas lowers the Zeeman energy. Further increasing the magnetic field leads to a ferromagnetic phase (Figure 10.5d) with magnetization uniformly aligned with the external magnetic field.

To compare with the experimental phase diagram for the THE resistivity, we also calculated topological charge density as a function of the magnetic field and temperature (Figure 10.5b) based on the same materials parameters used in the calculation of Figure 10.5c. Comparing with Figure 10.5a, we find the calculated magnetic-field window for finite topological charge density is relatively narrower, which could be attributed to the following reasons. In our theoretical calculation, we only considered closely-packed hexagonal skyrmion lattice whereas in reality there may exist other topological spin structures such as a disordered skyrmion phase [43] that may contribute to the measured THE as well. In addition, derivation from the linear dependence of the topological Hall resistivity on the topological charge density may take place in the presence of strong SOC [44] and diffusive scattering. [45] Except for the width of THE window on magnetic field axis for a particular value of temperature, the calculated diagram of topological charge density is in good agreement with the experimental phase diagram of THE.

The spin-chiral structure responsible for the observed interfacial THE is most likely the Néel-textured magnetic skyrmions stabilized by DMI. In contrast to Bloch-type skyrmions in bulk DMI materials with ρ_{THE} typically between 5~100 nΩ·cm and narrow temperature-field range near T_C, [6,7] Néel-type skyrmions usually exhibit a more pronounced ρ_{THE} and a wider temperature-field range, [46] as seen in $CrTe_2/Bi_2Te_3$. Similar THE behaviors induced by Néel-type magnetic skyrmions were also observed in Cr_2Te_3/Bi_2Te_3, [13] Pt/TmIG, [5] $La_{0.7}Sr_{0.3}MnO_3/SrIrO_3$ [47] and $(Bi,Sb)_2Te_3$/MnTe heterostructures. [14]

In order to rule out the possibility of two-channel AHE responses, [48,49] which could lead to similar hump-dip features in Hall resistivities, we did two-channel AHE fitting using a double-tanh function. A simple linear superposition of two magnetic hysteresis loops can't

match the ρ_{xy}-H curves, especially for the hump-like features. It suggests that the hump features are not due to the mixed magnetic signals from two AHE responses with different H_C.

10.6. Calculation of skyrmion size.

In skyrmion systems, reducing the skyrmion size is critical to maximizing its potential for device applications of energy-efficient and high-density information storage. A single skyrmion can be treated as one magnetic flux quantum, $\phi_0 = h/e$, where h is the Plank constant and e is the electronic charge. When charge carriers flow through a conductor, the skyrmion density (n_{sk}) gives rise to an emergent electromagnetic field. Therefore, ρ_{THE} can be represented by the following formula [38]

$$\rho_{\mathrm{THE}} = PR_0 n_{\mathrm{sk}} \emptyset_0,$$

where R_0 is the ordinary Hall coefficient representing the total density of mobile charge and n_{sk} is the 2D skyrmions density (assuming each skyrmion carries a topological charge $|Q_{\mathrm{sk}}| = 1$, and skyrmions form a regular 2D lattice). P denotes the spin polarization of carriers. Assuming P = 1, we can estimate the length scale of one single skyrmion ($n_{sk}^{-1/2}$) to be around 34 nm, which is the upper limit of skyrmion size. This value is comparable to that of bulk B20 alloys [6-8,50] and $SrRuO_3$-$SrIrO_3$ bilayers. [35,51] Since the skyrmion density is proportional to the magnitude of the emergent magnetic field, skyrmions with smaller size are essential to optimize the relationship between spin dynamics and electric charge. Most recently, magnetic bubbles have aroused researchers' enthusiasm owing to the observation of an extremely large THE in (Ca,Ce)MnO_3, [4] ten thousand times larger than

the THE in MnSi.[7] However, the size of magnetic bubbles is typically around 0.1-10 μm, which is too large for practical applications in information storage. Unlike magnetic bubbles, the skyrmions stabilized by the DMI scale around sub-100-nm, either in bulk or interface. Here, the estimated maximum value of skyrmion size in $CrTe_2/Bi_2Te_3$ system is ~34 nm, much smaller than the size of magnetic bubbles. Furthermore, skyrmions can easily be moved by a low-threshold electric current/field, while magnetic bubbles require a large external magnetic field to manipulate.

The observed THE magnitude is the largest among all the bilayer systems hosting skyrmions. [6,11,36,36,52] The pure vdW staking in $CrTe_2/Bi_2Te_3$ heterostructures explored in this work is totally different from the traditional magnetic bilayer systems. The vdW coupling between adjacent layers in $CrTe_2/Bi_2Te_3$ heterostructures facilitates the layer-by-layer stacking and the formation of a clean interface, without suffering from interfacial hybridization and diffusion, strain, surface reconstruction and electronic redistribution. [53] Common Te atoms in both of TI and 2D FM permit the topological SS to extend into the 2D FM. Combined with the out-of-plane spin-polarized $CrTe_2$ surface, efficient magnetic exchange coupling could be introduced at the $CrTe_2/Bi_2Te_3$ interface, giving rise to a gapped TI SS and the dissipationless chiral edge conductive channel. As the DMI is largely determined by magnetic interactions within a single atomic layer, the atomically sharp vdW interface together with anisotropic exchange interaction and dissipationless spin carrier, as well as the strong SOC in Bi_2Te_3 provide an optimal environment for the formation of interfacial DMI. The DMI energy parameter can be defined as: $E_{DMI} = Dt$ with $D = 6\times10^{-3}$ J/m^{-2} and t (6 nm) representing the thickness of $CrTe_2$ layer. This leads to an enhanced DMI strength in $CrTe_2/Bi_2Te_3$ of 36 pJ/m, which is one or two orders larger than that of traditional heavy-

metal skyrmion systems such as Pt/TmIG (0.02 pJ/m) [5] and Ir/Co/Pt (0.96 pJ/m). [54] These results indicate that the interfacial DMI at 2D FM/TI heterostructures is one of the promising ways to produce large THE, and therefore a higher recording density.

10.7. Conclusions

In summary, we have synthesized high-quality $CrTe_2/Bi_2Te_3$ bilayers, a prototype vdW 2D FM/TI heterostructure by MBE, which shows the largest THE among bilayer systems. It is driven by an enhanced interfacial DMI as a consequence of an optimal combination of strong SOC in Bi_2Te_3, and an atomically sharp interface with asymmetric exchange interaction. It is also worth noting that the 2D FM/TI hybrid system possesses topologically nontrivial spin textures in both real space and momentum space, namely, chiral spin textures and spin-polarized topological SS of TI. This work provides a platform to explore and manipulate the interplay among magnetism, spin textures, and Berry phase in a class of unexplored bilayers for the development of energy-efficient nanoscale spintronic devices.

Reference

[1].Rossler, U. K.; Bogdanov, A. N.; Pfleiderer, C. Spontaneous Skyrmion Ground States in Magnetic Metals. Nature 2006, 442, 797-801.

[2].Bode, M.; Heide, M.; von Bergmann, K.; Ferriani, P.; Heinze, S.; Bihlmayer, G.; Kubetzka, A.; Pietzsch, O.; Blugel, S.; Wiesendanger, R. Chiral Magnetic Order at Surfaces Driven by Inversion Asymmetry. Nature 2007, 447, 190-193.

[3].Tewari, S.; Belitz, D.; Kirkpatrick, T. R. Blue Quantum Fog: Chiral Condensation in Quantum Helimagnets. Phys. Rev. Lett. 2006, 96, 047207.

[4].Vistoli, L.; Wang, W.; Sander, A.; Zhu, Q.; Casals, B.; Cichelero, R.; Barthélémy, A.; Fusil, S.; Herranz, G.; Valencia, S.; Abrudan, R.; Weschke, E.; Nakazawa, K.; Kohno, H.; Santamaria, J.; Wu, W.; Garcia, V.; Bibes, M. Giant Topological Hall Effect in Correlated Oxide Thin Films. Nat. Phys. 2018, 15, 67-72.

[5].Shao, Q.; Liu, Y.; Yu, G.; Kim, S. K.; Che, X.; Tang, C.; He, Q. L.; Tserkovnyak, Y.; Shi, J.; Wang, K. L. Topological Hall Effect at above Room Temperature in Heterostructures Composed of a Magnetic Insulator and a Heavy Metal. Nat. Electron. 2019, 2, 182-186.

[6].Kanazawa, N.; Onose, Y.; Arima, T.; Okuyama, D.; Ohoyama, K.; Wakimoto, S.; Kakurai, K.; Ishiwata, S.; Tokura, Y. Large Topological Hall Effect in a Short-Period Helimagnet MnGe. Phys. Rev. Lett. 2011, 106, 156603.

[7].Neubauer, A.; Pfleiderer, C.; Binz, B.; Rosch, A.; Ritz, R.; Niklowitz, P. G.; Boni, P. Topological Hall Effect in the A Phase of MnSi. Phys. Rev. Lett. 2009, 102, 186602.

[8].Mühlbauer, S.; Binz, B.; Jonietz, F.; Pfleiderer, C.; Rosch, A.; Neubauer, A.; Georgii, R.; Böni, P. Skyrmion Lattice in a Chiral Magnet. Sicence 2009, 323, 915-919.

[9].Yu, X. Z.; Onose, Y.; Kanazawa, N.; Park, J. H.; Han, J. H.; Matsui, Y.; Nagaosa, N.; Tokura, Y. Real-Space Observation of a Two-Dimensional Skyrmion Crystal. Nature 2010, 465, 901-904.

[10].Raju, M.; Yagil, A.; Soumyanarayanan, A.; Tan, A. K. C.; Almoalem, A.; Ma, F.; Auslaender, O. M.; Panagopoulos, C. The Evolution of Skyrmions in Ir/Fe/Co/Pt Multilayers and Their Topological Hall Signature. Nat. Commun. 2019, 10, 696.

[11].Soumyanarayanan, A.; Raju, M.; Gonzalez Oyarce, A. L.; Tan, A. K. C.; Im, M. Y.; Petrovic, A. P.; Ho, P.; Khoo, K. H.; Tran, M.; Gan, C. K.; Ernult, F.; Panagopoulos, C. Tunable Room-Temperature Magnetic Skyrmions in Ir/Fe/Co/Pt Multilayers. Nat. Mater. 2017, 16, 898-904.

[12].Heinze, S.; von Bergmann, K.; Menzel, M.; Brede, J.; Kubetzka, A.; Wiesendanger, R.; Bihlmayer, G.; Blügel, S. Spontaneous Atomic-Scale Magnetic Skyrmion Lattice in Two Dimensions. Nat. Phys. 2011, 7, 713-718.

[13].Chen, J.; Wang, L.; Zhang, M.; Zhou, L.; Zhang, R.; Jin, L.; Wang, X.; Qin, H.; Qiu, Y.; Mei, J.; Ye, F.; Xi, B.; He, H.; Li, B.; Wang, G. Evidence for Magnetic Skyrmions at the Interface of Ferromagnet/Topological-Insulator Heterostructures. Nano Lett. 2019, 19, 6144-6151.

[14].He, Q. L.; Yin, G.; Grutter, A. J.; Pan, L.; Che, X.; Yu, G.; Gilbert, D. A.; Disseler, S. M.; Liu, Y.; Shafer, P.; Zhang, B.; Wu, Y.; Kirby, B. J.; Arenholz, E.; Lake, R. K.; Han, X.; Wang, K. L. Exchange-Biasing Topological Charges by Antiferromagnetism. Nat. Commun. 2018, 9, 2767.

[15].Wu, H.; Gross, F.; Dai, B.; Lujan, D.; Razavi, S. A.; Zhang, P.; Liu, Y.; Sobotkiewich, K.; Forster, J.; Weigand, M.; Schutz, G.; Li, X.; Grafe, J.; Wang, K. L. Ferrimagnetic Skyrmions in Topological Insulator/Ferrimagnet Heterostructures. Adv. Mater. 2020, 32, e2003380.

[16].Li, P.; Ding, J.; Zhang, S. S.; Kally, J.; Pillsbury, T.; Heinonen, O. G.; Rimal, G.; Bi, C.; DeMann, A.; Field, S. B.; Wang, W.; Tang, J.; Jiang, J. S.; Hoffmann, A.; Samarth, N.; Wu, M. Topological Hall Effect in a Topological Insulator Interfaced with a Magnetic Insulator. Nano Lett. 2021, 21, 84-90.

[17].Ahmed, A. S.; Lee, A. J.; Bagues, N.; McCullian, B. A.; Thabt, A. M. A.; Perrine, A.; Wu, P. K.; Rowland, J. R.; Randeria, M.; Hammel, P. C.; McComb, D. W.; Yang, F. Spin-Hall Topological Hall Effect in Highly Tunable Pt/Ferrimagnetic-Insulator Bilayers. Nano Lett. 2019, 19, 5683-5688.

[18].Wang, W.; Daniels, M. W.; Liao, Z.; Zhao, Y.; Wang, J.; Koster, G.; Rijnders, G.; Chang, C. Z.; Xiao, D.; Wu, W. Spin Chirality Fluctuation in Two-Dimensional Ferromagnets with Perpendicular Magnetic Anisotropy. Nat. Mater. 2019, 18, 1054-1059.

[19].Liu, C.; Zang, Y.; Ruan, W.; Gong, Y.; He, K.; Ma, X.; Xue, Q. K.; Wang, Y. Dimensional Crossover-Induced Topological Hall Effect in a Magnetic Topological Insulator. Phys. Rev. Lett. 2017, 119, 176809.

[20].Wakatsuki, R.; Ezawa, M.; Nagaosa, N. Domain Wall of a Ferromagnet on a Three-Dimensional Topological Insulator. Sci. Rep. 2015, 5, 13638.

[21].Wu, Y.; Zhang, S.; Zhang, J.; Wang, W.; Zhu, Y. L.; Hu, J.; Yin, G.; Wong, K.; Fang, C.; Wan, C.; Han, X.; Shao, Q.; Taniguchi, T.; Watanabe, K.; Zang, J.; Mao, Z.; Zhang, X.; Wang, K. L. Néel-Type Skyrmion in WTe2/Fe3GeTe2 van der Waals Heterostructure. Nat. Commun. 2020, 11, 3860.

[22].Zhang, X.; Lu, Q.; Liu, W.; Niu, W.; Sun, J.; Cook, J.; Vaninger, M.; Miceli, P. F.; Singh, D. J.; Lian, S.-W.; Chang, T.-R.; He, X.; Du, J.; He, L.; Zhang, R.; Bian, G.; Xu, Y. Room-Temperature Intrinsic Ferromagnetism in Epitaxial CrTe2 Ultrathin Films. Nat. Commun. 2021, 12, 2492

[23].Chen, Y. L.; Analytis, J. G.; Chu, J.-H.; Liu, Z. K.; Mo, S.-K.; Qi, X. L.; Zhang, H. J.; Lu, D. H.; Dai, X.; Fang, Z.; Zhang, S. C.; Fisher, I. R.; Hussain, Z.; Shen, Z.-X. Experimental Realization of a Three-Dimensional Topological Insulator, Bi2Te3. Science 2009, 325, 178-181.

[24].Hsieh, D.; Xia, Y.; Qian, D.; Wray, L.; Dil, J. H.; Meier, F.; Osterwalder, J.; Patthey, L.; Checkelsky, J. G.; Ong, N. P.; Fedorov, A. V.; Lin, H.; Bansil, A.; Grauer, D.; Hor, Y. S.; Cava, R. J.; Hasan, M. Z. A Tunable Topological Insulator in the Spin Helical Dirac Transport Regime. Nature 2009, 460, 1101-1105.

[25]. Hasan, M. Z.; Kane, C. L. Topological Insulators. Rev. Mod. Phys. 2010, 82, 3045-3067.

[26].Fan, Y.; Upadhyaya, P.; Kou, X.; Lang, M.; Takei, S.; Wang, Z.; Tang, J.; He, L.; Chang, L. T.; Montazeri, M.; Yu, G.; Jiang, W.; Nie, T.; Schwartz, R. N.; Tserkovnyak, Y.; Wang, K. L. Magnetization Switching through Giant Spin-Orbit Torque in a Magnetically Doped Topological Insulator Heterostructure. Nat. Mater. 2014, 13, 699-704.

[27].Xia, Y.; Qian, D.; Hsieh, D.; Wray, L.; Pal, A.; Lin, H.; Bansil, A.; Grauer, D.; Hor, Y. S.; Cava, R. J.; Hasan, M. Z. Observation of a Large-Gap Topological-Insulator Class with a Single Dirac Cone on the Surface. Nat. Phys. 2009, 5, 398-402.

[28].Freitas, C. D.; Weht, R.; Sulpice, A.; Remenyi, G.; Strobel, P.; Gay, F. Ferromagnetism in Layered Metastable 1T-CrTe2. J. Phys.: Condens. Matter 2015, 27, 176002.

[29].Li, Y. Y.; Wang, G.; Zhu, X. G.; Liu, M. H.; Ye, C.; Chen, X.; Wang, Y. Y.; He, K.; Wang, L. L.; Ma, X. C.; Zhang, H. J.; Dai, X.; Fang, Z.; Xie, X. C.; Liu, Y.; Qi, X. L.; Jia, J. F.; Zhang, S. C.; Xue, Q. K. Intrinsic Topological Insulator Bi2Te3 Thin Films on Si and Their Thickness Limit. Adv. Mater. 2010, 22, 4002-4007.

[30].Jiang, J.; Xiao, D.; Wang, F.; Shin, J. H.; Andreoli, D.; Zhang, J.; Xiao, R.; Zhao, Y. F.; Kayyalha, M.; Zhang, L.; Wang, K.; Zang, J.; Liu, C.; Samarth, N.; Chan, M. H. W.; Chang, C. Z. Concurrence of Quantum Anomalous Hall and Topological Hall Effects in Magnetic Topological Insulator Sandwich Heterostructures. Nat. Mater. 2020, 19, 732-737.

[31].Nagaosa, N.; Sinova, J.; Onoda, S.; MacDonald, A. H. Anomalous Hall Effect. Rev. Mod. Phys. 2010, 82, 1539-1592.

[32].Fang, Z.; Nagaosa, N.; Takahashi, K. S.; Asamitsu, A.; Mathieu, R.; Ogasawara, T.; Yamada, H.; Kawasaki, M.; Tokura, Y.; Terakura, K. The Anomalous Hall Effect and Magnetic Monopoles in Momentum Space. Science 2003, 302, 92-95.

[33].Yasuda, K.; Wakatsuki, R.; Morimoto, T.; Yoshimi, R.; Tsukazaki, A.; Takahashi, K. S.; Ezawa, M.; Kawasaki, M.; Nagaosa, N.; Tokura, Y. Geometric Hall Effects in Topological Insulator Heterostructures. Nat. Phys. 2016, 12, 555-559.

[34].Keskin, V.; Aktaş, B.; Schmalhorst, J.; Reiss, G.; Zhang, H.; Weischenberg, J.; Mokrousov, Y. Temperature and Co Thickness Dependent Sign Change of the Anomalous Hall Effect in Co/Pd Multilayers: An Experimental and Theoretical Study. Appl. Phys. Lett. 2013, 102, 022416.

[35].Matsuno, J.; Ogawa, N.; Yasuda, K. Interface-Driven Topological Hall Effect in SrRuO3-SrIrO3 Bilayer. Sci. Adv. 2016, 2, e1600304.

[36].Liu, Q. B.; Meng, K. K.; Zheng, S. Q.; Wu, Y. C.; Cai, Y. Z.; Wu, Y.; Chen, J. K.; Miao, J.; Xu, X. G.; Jiang, Y. Strain-Induced Large Topological Hall Effect in Pt/YIG Bilayers. arXiv:1810.07384v1, 2018, https://arxiv.org/abs/1810.07384v1 (accessed on Oct 17, 2018).

[37].Ritz, R.; Halder, M.; Franz, C.; Bauer, A.; Wagner, M.; Bamler, R.; Rosch, A.; Pfleiderer, C. Giant Generic Topological Hall Resistivity of MnSi under Pressure. Phys. Rev. B 2013, 87, 134424.

[38].Maccariello, D.; Legrand, W.; Reyren, N.; Garcia, K.; Bouzehouane, K.; Collin, S.; Cros, V.; Fert, A. Electrical Detection of Single Magnetic Skyrmions in Metallic Multilayers at Room Temperature. Nat. Nanotechnol. 2018, 13, 233-237.

[39].Ding, J.; Liu, C.; Kalappattil, V.; Zhang, Y.; Mosendz, O.; Erugu, U.; Yu, R.; Tian, J.; DeMann, A.; Field, S. B.; Yang, X.; Ding, H.; Tang, J.; Terris, B.; Fert, A.; Chen, H.; Wu, M. Switching of a Magnet by Spin-Orbit Torque from a Topological Dirac Semimetal. Adv. Mater. 2021, 33, 2005909.

[40].Skoropata, E.; Nichols, J.; Ok, J. M. Interfacial Tuning of Chiral Magnetic Interactions for Large Topological Hall Effects in LaMnO3/SrIrO3 Heterostructures. Sci. Adv. 2020, 6, eaaz3902

[41].Schlotter, S.; Agrawal, P.; Beach, G. S. D. Temperature Dependence of the Dzyaloshinskii-Moriya Interaction in Pt/Co/Cu Thin Film Heterostructures. Appl. Phys. Lett. 2018, 113, 092402.

[42].Banerjee, S.; Rowland, J.; Erten, O.; Randeria, M. Enhanced Stability of Skyrmions in Two-Dimensional Chiral Magnets with Rashba Spin-Orbit Coupling. Phys. Rev. X 2014, 4, 031045.

[43].Karube, K.; White, J. S.; Morikawa, D.; Dewhurst, C. D.; Cubitt, R.; Kikkawa, A.; Yu, X.; Tokunaga, Y.; Arima, T.; Rønnow, H. M.; Tokura, Y.; Taguchi, Y. Disordered Skyrmion Phase Stabilized by Magnetic Frustration in a Chiral Magnet. Sci. Adv. 2018, 4, eaar7043.

[44].Denisov, K. S.; Rozhansky, I. V.; Averkiev, N. S.; Lahderanta, E. A Nontrivial Crossover in Topological Hall Effect Regimes. Sci. Rep. 2017, 7, 17204.

[45].Zhang, S. S. L.; Heinonen, O. Topological Hall Effect in Diffusive Ferromagnetic Thin Films with Spin-Flip Scattering. Phys. Rev. B 2018, 97, 134401

[46].Qin, Q.; Liu, L.; Lin, W.; Shu, X.; Xie, Q.; Lim, Z.; Li, C.; He, S.; Chow, G. M.; Chen, J. Emergence of Topological Hall Effect in a SrRuO3 Single Layer. Adv. Mater. 2019, 31, 1807008.

[47].Li, Y.; Zhang, L.; Zhang, Q.; Li, C.; Yang, T.; Deng, Y.; Gu, L.; Wu, D. Emergent Topological Hall Effect in La0.7Sr0.3MnO3/SrIrO3 Heterostructures. ACS Appl. Mater. Inter. 2019, 11, 21268-21274.

[48].Fijalkowski, K. M.; Hartl, M.; Winnerlein, M.; Mandal, P.; Schreyeck, S.; Brunner, K.; Gould, C.; Molenkamp, L. W. Coexistence of Surface and Bulk Ferromagnetism Mimics Skyrmion Hall Effect in a Topological Insulator. Phys. Rev. X 2020, 10, 011012.

[49].Wang, L.; Feng, Q.; Lee, H. G.; Ko, E. K.; Lu, Q.; Noh, T. W. Controllable Thickness Inhomogeneity and Berry Curvature Engineering of Anomalous Hall Effect in SrRuO3 Ultrathin Films. Nano Lett. 2020, 20, 2468-2477.

[50].Tonomura, A.; Yu, X.; Yanagisawa, K.; Matsuda, T.; Onose, Y.; Kanazawa, N.; Park, H. S.; Tokura, Y. Real-Space Observation of Skyrmion Lattice in Helimagnet MnSi Thin Samples. Nano Lett. 2012, 12, 1673-1677.

[51].Meng, K. Y.; Ahmed, A. S.; Bacani, M.; Mandru, A. O.; Zhao, X.; Bagues, N.; Esser, B. D.; Flores, J.; McComb, D. W.; Hug, H. J.; Yang, F. Observation of Nanoscale Skyrmions in SrIrO3/SrRuO3 Bilayers. Nano Lett. 2019, 19, 3169-3175.

[52].Porter, N. A.; Sinha, P.; Ward, M. B.; Dobrynin, A. N.; Brydson, R. M. D.; Charlton, T. R.; Kinane, C. J.; Robertson, M. D.; Langridge, S.; Marrows, C. H. Giant Topological Hall Effect in Strained Fe0.7Co0.3Si Epilayers. arXiv:1312.1722, 2013, https://arxiv.org/abs/1312.1722 (accessed on Dec 5, 2013).

[53].Gong, C.; Zhang, X. Two-Dimensional Magnetic Crystals and Emergent Heterostructure Devices. Science 2019, 363, 706.

[54].Moreau-Luchaire, C.; Mouta, S. C.; Reyren, N.; Sampaio, J.; Vaz, C. A.; Van Horne, N.; Bouzehouane, K.; Garcia, K.; Deranlot, C.; Warnicke, P.; Wohlhuter, P.; George, J. M.; Weigand, M.; Raabe, J.; Cros, V.; Fert, A. Additive Interfacial Chiral Interaction in Multilayers for Stabilization of Small Individual Skyrmions at Room Temperature. Nat. Nanotechnol. 2016, 11, 444-448.

11. EPITAXY OF TWO-DIMENSIONAL FERROMAGNETIC FILMS ON AMORPHOUS SUBSTRATE

Two-dimensional (2D) van der Waals (vdW) magnets have opened landmark horizons in the study of fundamental low-dimensional magnetism and the development of intriguing spintronic device architectures. Such compounds are typically fabricated by time-consuming mechanical exfoliation from their bulk counterparts, which are crystal inhomogeneous and incompatible with large-scale industrial applications. Moreover, Si wafers with dielectric substrates are required for batch production, which poses great challenges for the growth of large 2D magnetic thin films with high quality and spatial homogeneity.

In this chapter, we overcome these problems and synthesize centimeter-scale $CrTe_2$ with a Bi_2Te_3 seed layer on amorphous silicon nitride (SiN_x) and crystalline Si substrates via molecular beam epitaxy engineering. This route allows fine-tuning of the crystal structures of $CrTe_2$ on-demand and obtains large-area granular $CrTe_2$ atomic layers on SiN_x films with the highest coercivity ever reported for 2D magnetic thin films/flakes (11.5-kilo-oersted). The boosted coercivity originates from the weak intergranular exchange coupling, which is demonstrated in the field-dependent Néel-type stripe domain dynamics by Lorentz transmission electron microscopy (L-TEM). Remarkably, our devices made from granular $CrTe_2$ films exhibit granular giant magnetoresistance (GMR) and topological Hall effect (THE), revealing rich physics in terms of spin-dependent electron scattering and formation of topological spin textures such as skyrmions at the interface. This work demonstrates a promising avenue for the high-scale production of 2D magnetic films on amorphous substrates, which would enable the batch fabrication of real-world magnetoelectronic and spintronic devices.

11.1. Introduction

The recent discovery of intrinsic magnetic order in two-dimensional (2D) van der Waals (vdW) magnets has opened up exciting avenues for exploring novel phases of matter and developing devices with unique functionalities [1-5]. Such layered materials have the advantages of polarizing spin/valley degrees of freedom and breaking the time-reversal symmetry of adjacent materials through the proximity effect [6]. Exotic phenomena such as skyrmions, chiral domain walls, quantum anomalous Hall effect, axion insulator states, and other quantum and topological phases have been identified in 2D magnetic materials and heterostructures [7-12]. Due to the benefit of the atomic thickness, external perturbations such as electric fields, free carrier doping, layer stacking, and strain may efficiently control or switch the intrinsic magnetism of 2D magnets [13-16]. Among the known vdW compounds, $CrTe_2$ stands out as a promising candidate because of the above-room-temperature magnetic order and strong perpendicular magnetic anisotropy (PMA) as a result of the correlation between its atomic lattice structure and spin texture [17-21].

For the realization of 2D magnet-based devices in industrial production, effective synthesis protocols with desired morphology and quality have yet to be demonstrated [22,23]. 2D magnetic films are typically synthesized by mechanical exfoliation from bulk crystals and transferred onto the target substrate. The exfoliated thin flakes have a typical size of a few μm and are spatially inhomogeneous, which are incompatible with industrial applications. Alternatively, the molecular beam epitaxy (MBE) technique can produce wafer-scale and contamination-free 2D magnetic films on single-crystalline substrates [18,19,24,25]. In this case, the crystal symmetry and lattice match between epitaxial films and substrates are

critical. Furthermore, high-temperature processes (above 400 °C) are typically required to clean the substrate surface, which are not compatible with the thermal budget of CMOS devices [26]. Therefore, efforts and focuses on large-scale growth of 2D magnetic materials with low-temperature processes and compatibility with Si technology are required.

Here we report the crystallinity-selective synthesis of centimeter-scale $CrTe_2$ thin films with the Bi_2Te_3 seed layer on amorphous silicon nitride (SiN_x)/Si substrates by the MBE technique. SiN_x is a high-k dielectric with outstanding mechanical, thermal, and electronic insulating properties [27,28]. The atomically flat surfaces and sharp interfaces are mapped by scanning tunneling microscopy (STM) and scanning transmission electron microscopy (STEM) techniques. Thanks to the weak intergranular exchange coupling and substantial intrinsic PMA, $CrTe_2$ exhibits a robust ferromagnetic (FM) order with a Curie temperature (T_C) up to 184 K and a coercivity ($\mu_0 H_C$) of 11.5-kilo-oersted, which is the largest reported for 2D magnets up to date. The sizable $\mu_0 H_C$ is also verified in the anomalous Hall measurements. In addition, a granular giant magnetoresistance (GMR) with a magnitude of 4.5% at 180 K is detected in the fabricated $CrTe_2$ devices, as a result of the spin-dependent scattering of electrons at the interface of $CrTe_2/Bi_2Te_3$. Lorentz transmission electron microscopy (L-TEM) reveals the Néel-type domain walls with an estimated large Dzyaloshinskii–Moriya interaction (DMI) energy parameter of 6.72 $pJ \cdot m^{-1}$. Our findings highlight crystallinity engineering as a promising route to modulate the intrinsic magnetism of vdW magnets towards device manufacturing.

11.2. Synthesis of polycrystalline $CrTe_2$ on SiN_x/Si via crystallinity engineering

Due to the lack of lattice order, it is difficult to grow single-crystalline, epitaxy films on an amorphous substrate. The amorphous substrate, on the other hand, allows us to design and engineer the crystallinity of the layers to be grown. An overview of the Bi-assisted epitaxy growth method is schematically given in Fig. 11.1a. First, starting with an amorphous SiN_x/Si substrate, we grow a Bi layer with a hexagonal structure, which can alleviate the lattice mismatch and provide a crystalline template for the succeeding staking [29]. It should be noted that Bi atoms form polycrystalline grains with different in-plane rotation angles, as evidenced by atomic-resolution STM characterizations (Fig. 11.1b). Second, the Bi_2Te_3 layer is deposited. In this step, Bi and Te atoms nucleate and form islands, inheriting the same hexagonal symmetry from the Bi layer. Due to the high deposition temperature (200 °C), Te atoms can easily sublimate and diffuse into the Bi precursor film and form the Bi_2Te_3 layer [30]. The Bi_2Te_3 layer acts as a buffer and promotes an atomically flat surface for the growth of the subsequent layer. Third, we grow the 2D vdW $CrTe_2$ layer, which follows a one-to-one grain growth on Bi_2Te_3. As a result, $CrTe_2$ exhibits the same hexagonal symmetry as Bi_2Te_3 with in-plane grain rotations. Finally, a Te capping layer is deposited on the stack to prevent oxidation.

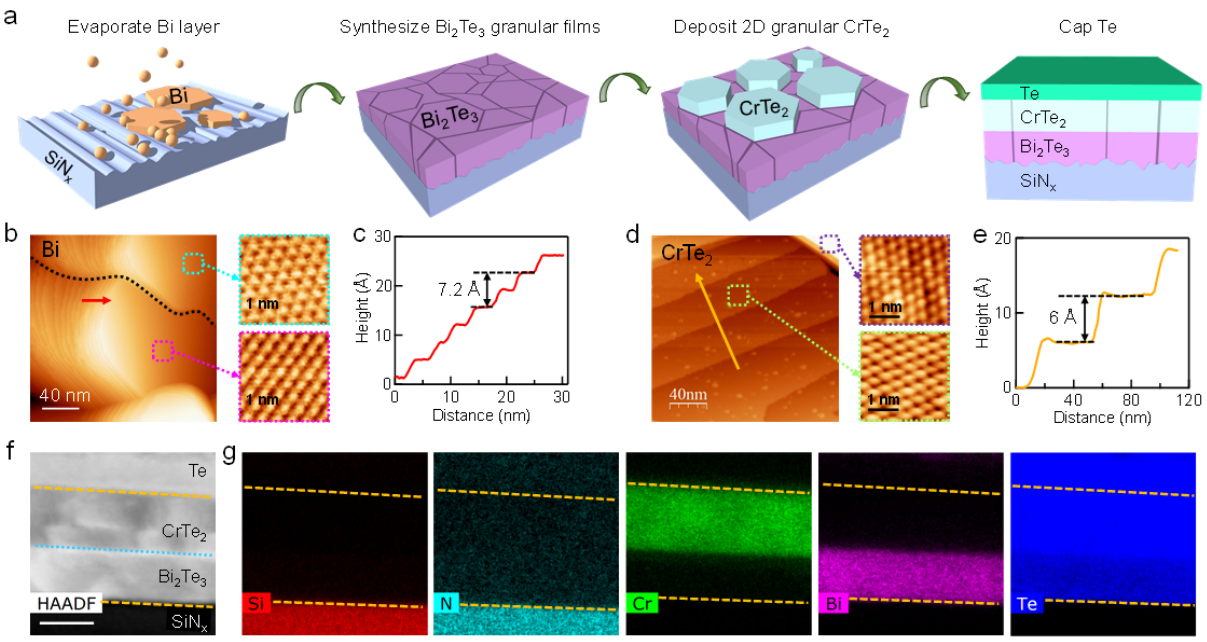

Fig. 11.1 Growth and characterizations of 2D $CrTe_2$ films on amorphous substrates. **a**, Schematics of the MBE growth procedure. Bi_2Te_3 works as a buffer layer to promote epitaxial growth of $CrTe_2$. The final structure from top to bottom is Te/$CrTe_2$/Bi_2Te_3/SiN_x/Si (001). **b**, Topographic and atomically resolved STM images of the as-grown hexagonal Bi layer with grain boundaries on SiN_x/Si substrate. Bi grains show various atomic orientations. **c**, Line profile along the red arrow in (b), with a step height of ~3.6 Å. **d**, Surface morphology and atomically resolved Te surfaces of epitaxial $CrTe_2$ with a highly ordered hexagonal structure. The atomic arrangement of $CrTe_2$ grains shows different in-plane orientations. **e**, Cross-sectional profile drawn along the yellow arrow in (d). The steps are 6 Å high, corresponding to the thickness of monolayer $CrTe_2$. **f**, Typical HAADF-STEM image of the prepared heterostructure from a cross-sectional view. The dashed lines indicate the boundaries of $CrTe_2$/Bi_2Te_3 with Te cap and SiN_x substrate. Scale bar: 20 nm. **g**, EDX color maps of Si, N, Cr, Bi, and Te, respectively. Cr element is uniformly distributed in the $CrTe_2$ film, without spreading to Bi_2Te_3 and SiN_x layers.

To get a glimpse of the growth mechanisms of epi-layers on amorphous substrates, microscopic characterization (*i.e.*, STM and TEM) of epitaxial films during the epitaxial growth was carried out. Figure 11.1b presents a topographic image taken after growing a Bi film on the amorphous substrate. Several terraces and edges are observed. Atomically resolved images of Bi grains show an ordered hexagonal structure. The line profile in Fig. 11.1c shows that the height of each edge is ~3.6 Å, which is corresponding to the interlayer distance of Bi bilayers. These results indicate that the geometric structure of the Bi layer on the SiN_x/Si substrate is identical to that of the (111) surface of Bi single crystals reported previously [31]. Moreover, closer observation of the atomic-resolution STM images shows that the atomic arrangement in the two adjacent grains forms different in-plane angles in the as-grown hexagonal Bi terraces (Fig. 11.1b). It suggests the significant existence of grain boundaries. Indeed, the surface within grains appears atomically flat with no or very few surface steps, while higher step bunches are occasionally formed near the grain boundaries. After the growth of 20 nm Bi_2Te_3, the epi-layer becomes flat with a uniform step height of 10 Å, related to the standard 1 quintuple layer (QL) [32]. With the assistance of the buffer layer, the deposited 21 nm $CrTe_2$ film shows terraces with a uniform step height of ~6 Å (Fig. 11.1d,e), demonstrating the atomically flat $CrTe_2$ epi-layer with a layer-by-layer growth mode [18]. The topographic STM image of $CrTe_2$ verifies the presence of phase boundaries. Further conclusive evidence can be found by resolving the grains. The atomic arrangement in adjacent $CrTe_2$ grains presents a hexagonal structure with different in-plane angles, suggesting the polycrystalline $CrTe_2$ epitaxial films with grain boundaries. A cross-sectional view of the high-angle annular dark-field (HAADF) image for the heterostructure is

exhibited in Fig. 11.1f. Together with the energy dispersive X-ray spectroscopy (EDX) mapping (Fig. 11.1g), different layers show clear and sharp interfaces between without interlayer diffusion. Therefore, STM and EDX characterizations demonstrate the epitaxial growth of the $CrTe_2$ films with grains that have different in-plane rotations via the Bi_2Te_3 seeding layer on amorphous substrates. As will be detailed below, this crystallinity-selective synthesis has produced 2D $CrTe_2$ films on amorphous substrates with exotic magnetic properties and emergent functionalities.

11.3. Significant enhancement of coercivity through weak intergranular exchange coupling

Having identified the granular feature of $CrTe_2$ with various in-plane rotations at the atomic scale, we then characterize its magnetic properties. The FM nature of the grown 21 nm $CrTe_2$ film is well demonstrated by zero-field-cooled (ZFC) and field-cooled (FC) out-of-plane (OOP) magnetization curves. Isothermal magnetization curves obtained under a magnetic field applied parallel to the *c* axis (*H*//*c*) and the *ab* plane (*H*//*ab*) are illustrated in Fig. 11.2a,b. The polycrystalline $CrTe_2$ displays broad FM hysteresis loops along the *c* axis. On the contrary, the in-plane (IP) curves show a hard-axis signature, suggesting the robust FM order and the strong PMA of $CrTe_2$. PMA can be quantified by the anisotropy field $\mu_0 H_A = \mu_0 H_s + 4\pi M_s$, in which μ_0 is the permeability of the vacuum, H_s is the saturation field, and M_s is the saturation magnetization. H_s and M_s can be extracted from hysteresis loops. In Fig.11.2c, we plot $\mu_0 H_A$ of the polycrystalline and single-crystalline $CrTe_2$ as a comparison.

It is discovered that as the temperature rises, both of them exhibit a decreasing trend with a comparable PMA magnitude.

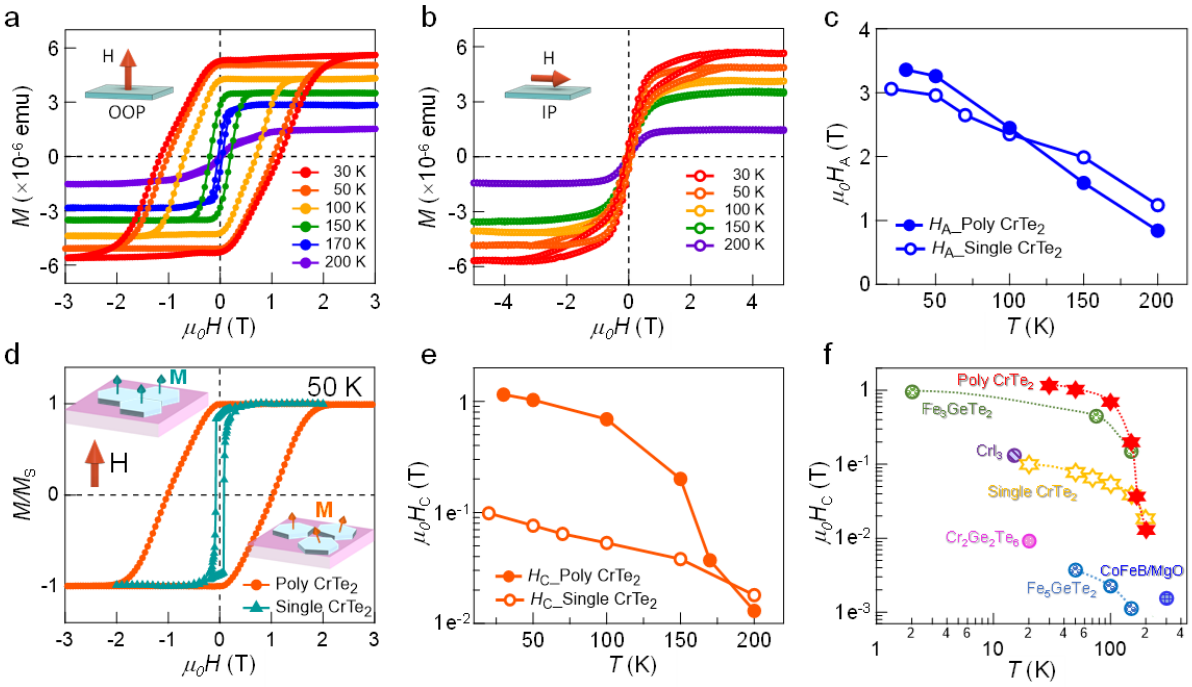

Fig. 11.2 Intrinsic ferromagnetism and PMA of 2D $CrTe_2$. **a**,**b**, Isothermal field-dependent magnetization at indicated temperatures with *H*//*c* axis (a) and *H*//*ab*-plane (b), respectively. **c**, Extracted $\mu_0 H_A$ as a function of temperature. **d**, Enlarged view of normalized hysteresis loops of polycrystalline and single-crystalline $CrTe_2$ on SiN_x/Si and SiC substrates, respectively. The insets are the corresponding magnetizing schematics. **e**, Variation of $\mu_0 H_C$ with respect to the temperature. **f**, Comparison of $\mu_0 H_C$ of $CrTe_2$ in this work with other FM PMA systems.

Apart from PMA, it is crucial to gain insight into $\mu_0 H_C$, as one of the key properties of functional magnetic materials. Figure 11.2d presents the OOP hysteresis loop of a polycrystalline $CrTe_2$ thin film, and the hysteresis loop of $CrTe_2$ on a single-crystalline SiC substrate is plotted for comparison. It can be seen that the polycrystalline $CrTe_2$ thin film

exhibits a broad and sheared hysteresis loop, which is expected to result from the gradual evolution of the domain structures. On the contrary, the single-crystalline one displays a square-shaped hysteresis loop with a near-vertical jump, indicative of a single hard magnetic phase. Furthermore, their hysteresis loops exhibit quite different $\mu_0 H_C$, namely 1.03 T for polycrystalline $CrTe_2$ and 0.076 T for single-crystalline $CrTe_2$ at 50 K. A close view of $\mu_0 H_C$ of these two samples with respect to the temperature is displayed in Fig. 11.2e. Though both $\mu_0 H_C$ decrease with increasing temperature and become close at 200 K, $\mu_0 H_C$ of the polycrystalline $CrTe_2$ is 10 times larger than that of the single-crystalline counterpart [18]. The large $\mu_0 H_C$ in polycrystalline $CrTe_2$ can be explained by the weak intergranular exchange coupling [33], considering the isolated grains and domain-wall pinning at grain boundaries [34,35]. In fact, the crystallinity-selective synthesis with isolated grains and weak exchange coupling can be utilized as an effective route to achieving large $\mu_0 H_C$ and high storage density in recording media.

Note that the large $\mu_0 H_C$ could make related devices highly immune to external magnetic noises, which is desirable for memory applications. To benchmark the $\mu_0 H_C$ values of polycrystalline $CrTe_2$ with other typical 2D and 3D magnets, we have compiled $\mu_0 H_C$ as a function of temperature for various FM systems from literature (Fig. 11.2f) [36-43]. One can see that the polycrystalline $CrTe_2$ manifests the largest $\mu_0 H_C$ among all the reported 2D magnetic thin films/flakes, which presents a highly promising platform for developing ultrahigh-density and low-power memory devices based on 2D magnetism.

11.4. Field-driven Néel-type domain dynamics

L-TEM imaging was employed to directly visualize magnetic domains to understand the magnetic spin texture in $CrTe_2$. The bright and dark contrasts are formed in the L-TEM images due to the process that the electron beam converges or diverges (see Fig.11.3a). When an electron beam passes through an orthogonal magnetic induction, it deflects due to the Lorentz force and generates magnetic contrasts. The perpendicular magnetic domains are invisible on the imaging plane, resulting from the parallel alignment between the perpendicular magnetization and the electron beam. Therefore, it is necessary to tilt the sample to introduce a projected component that is perpendicular to the beam. The comparison of L-TEM images at different tilting angles is a well-established approach for detecting the spin configuration of the Néel-type magnetic texture [44]. As schematically shown in Fig. 11.3a, tilting the sample to the opposite α angles ($\alpha = \pm 20°$) relative to the electron beam gives rise to a reversal of magnetic contrast corresponding to IP magnetization.

As the temperature is lowered to 100 K, left-bright and right-dark stripe contrasts show up at $\alpha = -20°$ (Fig. 11.3b). Different from the maze-like domain structure in single-crystalline PMA materials, the worm-like domains appear in the granular $CrTe_2$. Remarkably, the stripe contrasts in the L-TEM image disappear at $\alpha = 0°$ and reappear with opposite contrasts (left-dark and right-bright) at $\alpha = +20°$, suggestive of Néel-type domain walls. To understand the domain evolution at different sample tilting angles, line profiles are plotted for the observed worm-like domains in Fig. 11.3c. A valley-and-peak pattern emerges in the domain wall at -20°, corresponding to the left-bright and the right-dark regions mentioned above. In

contrast, it evolves into the opposite peak-and-valley pattern at an inverted tilting angle (+20°). For α = 0°, the valley-and-peak pattern is no longer visible. These findings reveal the presence of Néel-type magnetic domains in the granular $CrTe_2$.

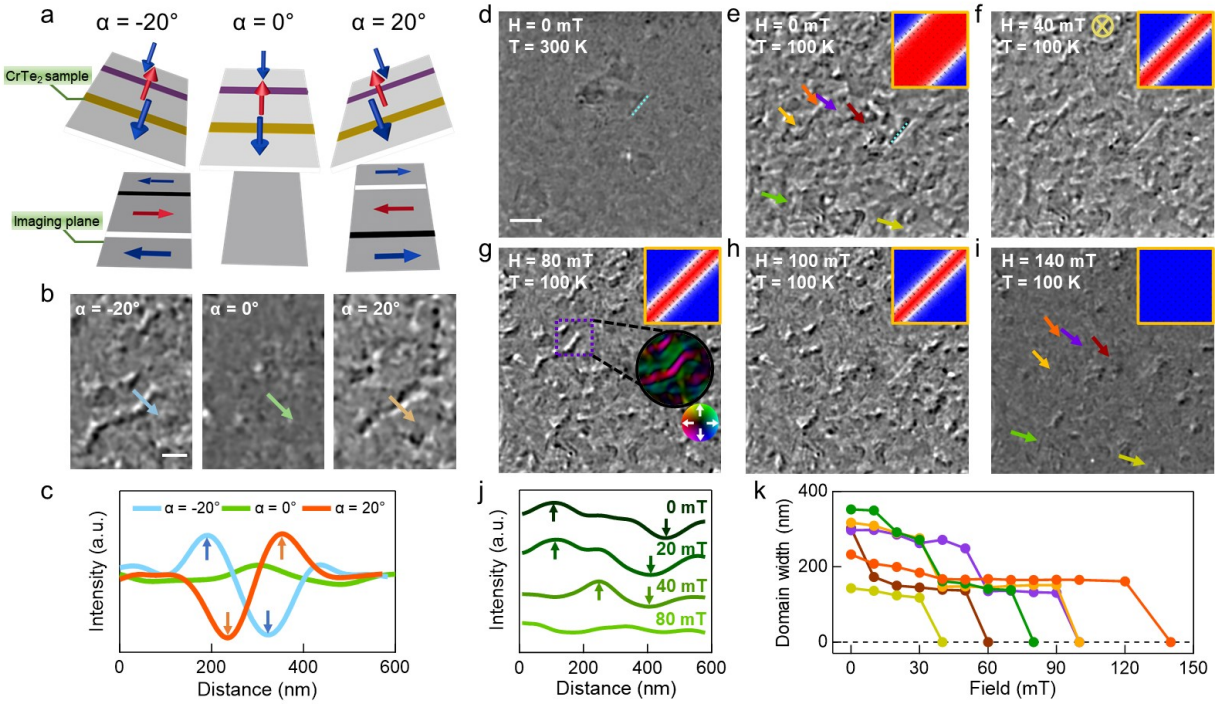

Fig. 11.3 Capturing Néel-type magnetic domain dynamics by L-TEM imaging. **a**, Schematics of L-TEM imaging of Néel-type magnetic stripe domains. On the sample surface, blue and red arrows represent the OOP magnetization. The yellow and purple area represents the position of Néel domain walls. On the imaging plane, blue and red arrows represent the projected IP component of the magnetic moments. Bright and dark contrasts are formed in the domain wall region. **b**, Experimental L-TEM images of $CrTe_2/Bi_2Te_3$ at 100 K with tilted sample angles of -20°, 0°, and 20° in a 600 Oe perpendicular magnetic field. The light blue, green, and orange arrows represent the direction of line scanning. Scale bar: 500 nm. **c**, Line profiles of L-TEM contrast intensity across the magnetic domains at different tilting angles. **d**, L-TEM images measured at 300 K, with sample tilted by -20°. Scale bar: 1 μm. **e**, Formation of magnetic worm-like domains at 100 K following a ZFC protocol. The light blue dashed lines mark the same sample position in (d) and (e). **f-i**, Evolution of magnetic domains as a function of the perpendicular magnetic field. The green, yellow, orange, purple, red, and olive arrows indicate the Néel-type domains at the same positions. The top right corner inset

shows the simulated magnetic domains. The red stripe represents the central domain, which is surrounded by adjacent domain walls (marked by white lines). The outer blue regions are corresponding to the opposite magnetic domains. In (g), a reconstructed magnetic induction map of the selected region is highlighted by a purple dashed box. The color wheel represents the IP magnetization orientation. **j**, Intensity profiles of magnetic contrasts across a worm-like domain (marked by the green arrow) under various magnetic fields. **k**, Relation between the Néel-type worm-like domain width and applied field within regions marked by colorful arrows.

To understand the magnetic field-dependent domain dynamics, L-TEM imaging at different magnetic fields was studied. At room temperature, the L-TEM image does not show any magnetic contrasts as the sample is in the paramagnetic (PM) state (see Fig. 11.3d). When temperature reduces to 100 K, $CrTe_2$ enters the FM state with Néel-type domains. Figure 11.3e-i shows the evolution of the worm-like domains as a function of the perpendicular magnetic field. As the field increases from 0 to 1000 Oe, the width of the worm-like domain gets narrower. Meanwhile, the density of worm-like domains decreases. The bottom inset of Fig. 11.3g shows an IP magnetic induction map of the selected worm-like domain, which is reconstructed based on the transport intensity equation [45]. These findings further confirm the magnetic characteristics of the worm-like structures seen in L-TEM images. With the magnetic field reaching 1400 Oe, the magnetic contrast becomes invisible because of the formation of a uniform field-polarized state. To gain a deeper insight into the field modulation of magnetic domains, micromagnetic simulations were performed to reproduce the process, which verifies the existence of Néel-type magnetic domains (See methods for details). Moreover, the simulations demonstrate that a DMI strength of 6.72 $pJ \cdot m^{-1}$, which is 3 to 6 times that of heavy metal/magnet systems [46,47], is required to stabilize the Néel-type magnetic domain walls under magnetic fields; otherwise, the stripe domains tend to

change into Bloch-type ones. Figure 11.3j plots the line-scanning intensity profiles of the magnetic domain marked by the green arrow (in Fig. 11.3e) at various magnetic fields. The bright and dark contrasts are corresponding to the peak and valley in the line scanning curves. As indicated by the arrows, the width of the worm-like domain, inside of which the magnetization orientation is antiparallel with the external field, shrinks and eventually disappears with the increase of the magnetic field. In addition, the field-driven evolution of Néel-type worm-like domains has been studied in other regions (marked by colorful arrows), which shows field-dependent behavior with an FM ground state. Figure 11.3k summarizes the width of various worm-like domains as a function of the magnetic field. One can see that the domain width decreases with increasing field, however, these magnetic domains in $CrTe_2$ switch incoherently at different switching fields. This, as we describe below, is connected to the weak exchange coupling between different grains.

11.5. Granular GMR effect in $CrTe_2$ devices

To demonstrate the potential application of polycrystalline $CrTe_2$ for developing spintronic devices, we fabricated Hall bar devices and studied the electrical properties at various temperatures. As shown in Fig. 11.4a, a clear anomalous Hall effect with square-shaped hysteresis loops emerges below 180 K, which is a hallmark of robust ferromagnetism with strong PMA. The anomalous Hall resistance (R_{AHE}) shows a nonmonotonic dependence with the temperature and peaks at around T_C (Fig. 11.4c). The suppressed R_{AHE} below T_C has been reported in the $CrTe_2/Bi_2Te_3$ system before [48], which is expected to result from the variation of momentum-space Berry curvature and the reduced electron-phonon or magnon

scattering. The reduced R_{AHE} above T_C indicates that $CrTe_2$ enters into the PM phase. The magnetoresistance (MR) measured at different temperatures with the OOP magnetic field is shown in Fig. 11.4b. At low temperatures, butterfly-shaped curves with two peaks corresponding to the $\mu_0 H_C$ values are observed, as MR is greatest near the switching fields. The magnitude of MR curves at 10 K is ~0.8% at 3 T, comparable with that of the single-crystalline $CrTe_2$ thin flakes [49]. As commonly observed in FM materials, the negative MR is attributed to the suppression of spin scattering by a magnetic field [50].

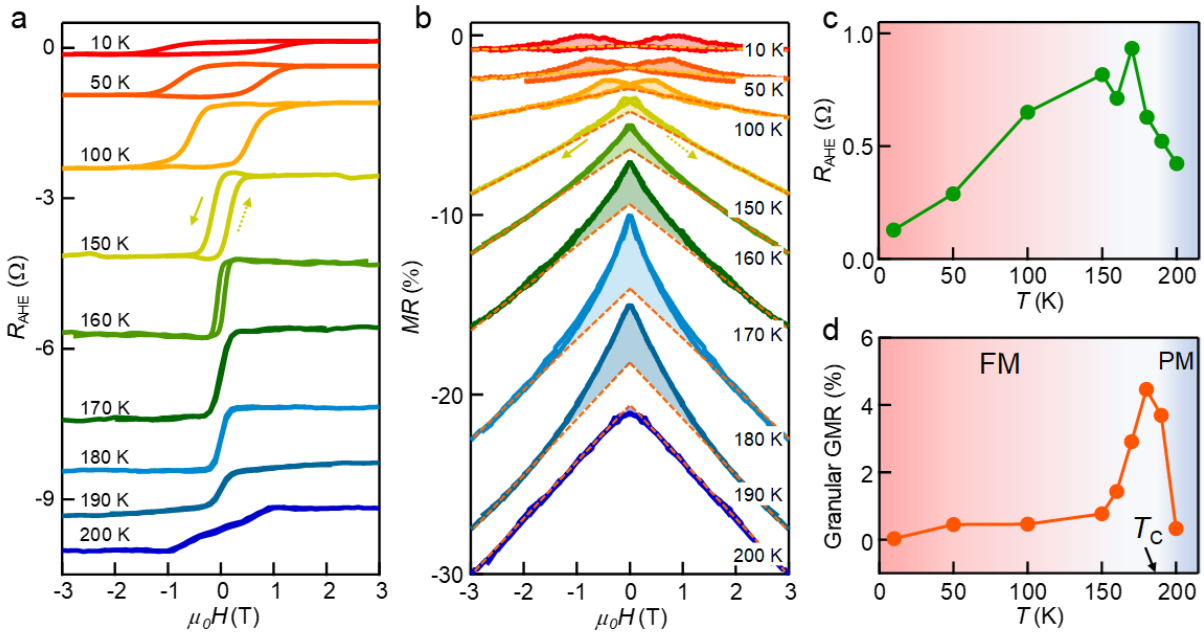

Fig. 11.4 Granular GMR effect in $CrTe_2$ Hall bar devices. **a**, Field-dependent anomalous Hall loops at various temperatures. The magnetic field is applied along the OOP direction. **b**, Temperature evolution of the MR curves of $CrTe_2$ devices. Orange dashed lines are linear fitting of MR at high field. The shaded regions highlight the net granular GMR. **c**,**d**, Temperature dependence of R_{AHE} and the granular GMR ratio derived from transport measurements. The FM and PM phases are color-coded by light red and blue, respectively.

Apart from the negative MR, an interesting observation is the nonlinear part of the MR curves at low fields. As presented in Fig. 11.4b, the prominent characteristic is a fast decline in resistance at low fields, followed by a gradual linear negative MR at high fields. The shaded regions highlight the nonlinear components of the MR curves. We extract the nonlinear MR values and plot them in Fig. 11.4d. The granular GMR ratio is defined as $\frac{\Delta R}{R_0} = (R_{max} - R_0)/R_0$, where R_0 is the zero-field resistance and is obtained by extrapolating this linear portion to zero field [51]. The temperature-dependent GMR ratio displays an apparent increase once approaching T_C, while it drops from the peak value of 4.5% at 180 K to 0.3% at 200 K in the PM state. The observed nonlinear MR is absent in the single-crystalline $CrTe_2$, [21] hinting at a new MR mechanism in the polycrystalline one. Considering the granular feature of polycrystalline $CrTe_2$, our results can be explained by the granular GMR effect [52,53] that strong spin-dependent electron scattering happens at the $CrTe_2$ and Bi_2Te_3 interfaces, which are both granular films. The relationship between the temperature dependence of R_{AHE} and the granular GMR ratio is further investigated (Fig. 11.4c,d). Both R_{AHE} and granular GMR peak near T_C, where thermal spin fluctuations could play an important role in the magneto-transport response of $CrTe_2$. Different from the low-temperature behavior, where low-frequency magnons are the primary magnetic contribution to transport characteristics, spin fluctuations dominate near T_C and reach a maximum. Regarding the granular GMR, spin fluctuations get quenched under an external field, which suppresses spin-dependent scattering and results in a large negative MR. This quantitative agreement between R_{AHE} and the GMR ratio, therefore, reveals the granular GMR effect in polycrystalline $CrTe_2$, in which spin-dependent scattering of polarized electrons dominates at the grain boundaries [54].

11.6. Conclusions

As shown in our work, grain boundaries can significantly affect the magnetic properties of $CrTe_2$ magnets. For instance, the grain boundaries serve to pin and block the switching of the magnetic domains. They can diminish the exchange coupling between adjacent grains, leading to incoherent switching of magnetic domains [34]. This is in strong contrast with the coherent magnetization reversal mode [55], in which one nucleating site could lead to the reversal of an entire macroscopic magnetization. Therefore, the enhanced $\mu_0 H_C$ of $CrTe_2$ thin films on amorphous substrates results from the pinning of magnetic moments at the grain boundaries, the large PMA, as well as the weak exchange coupling. Note that the large magnetic anisotropy and $\mu_0 H_C$ are key features of ultrahigh-density functional magnetic materials owing to good thermal stability.

Apart from the substantial $\mu_0 H_C$, the influence of grain boundaries is also reflected in the evolution of Néel-type magnetic domains in a microscopic view. Considering the weak intergranular exchange coupling, the worm-like domains switch incoherently with magnetic fields. Additionally, it is also evident in the granular GMR effect in $CrTe_2$ devices, where spin-dependent electron scattering occurs at the interface of $CrTe_2$ and Bi_2Te_3. The intriguing GMR mechanism makes $CrTe_2$ promising for engineering spin-valve devices. Furthermore, the topological Hall effect (THE) suggests the existence of skyrmions in our devices. Along with the measured Néel-type stripe domains, these nontrivial spin textures are valuable for building beyond-CMOS devices.

Key ingredients in terms of the grain boundaries, the intrinsic high-temperature ferromagnetism, and the electrical behavior of 2D $CrTe_2$ magnets can be precisely controlled

through crystallinity engineering. Our results set a versatile and reliable approach enabling the hetero-integration of highly mismatched material systems, and provide a protocol for the growth of large-scale high-quality 2D magnets on arbitrary substrates. The challenge however is the extension of our methods to a broad variety of layered magnets at different temperatures and on-demand applications (e.g., quantum computers, memories) which is achievable based on the guidelines provided in our work.

Reference

[1] Gong, C. et al. Discovery of intrinsic ferromagnetism in two-dimensional van der Waals crystals. Nature 546, 265-269 (2017).

[2] Gong, C. & Zhang, X. Two-dimensional magnetic crystals and emergent heterostructure devices. Science 363, 706 (2019).

[3] Huang, B. et al. Layer-dependent ferromagnetism in a van der Waals crystal down to the monolayer limit. Nature 546, 270-273 (2017).

[4] Kim, H. H. et al. Evolution of interlayer and intralayer magnetism in three atomically thin chromium trihalides. PNAS 116, 11131-11136 (2019).

[5] Sun, Z. et al. Giant nonreciprocal second-harmonic generation from antiferromagnetic bilayer CrI3. Nature 572, 497-501 (2019).

[6] Mak, K. F., Shan, J. & Ralph, D. C. Probing and controlling magnetic states in 2D layered magnetic materials. Nat. Rev. Phys. 1, 646-661 (2019).

[7] Wu, Y. et al. Néel-Type Skyrmion in WTe2/Fe3GeTe2 van der Waals Heterostructure. Nat. Commun. 11, 3860 (2020).

[8] Deng, Y. et al. Quantum anomalous Hall effect in intrinsic magnetic topological insulator MnBi2Te4. Science 367, 895–900 (2020).

[9] Jiang, J. et al. Concurrence of Quantum Anomalous Hall and Topological Hall Effects in Magnetic Topological Insulator Sandwich Heterostructures. Nat. Mater. 19, 732-737 (2020).

[10] Liu, C. et al. Robust axion insulator and Chern insulator phases in a two-dimensional antiferromagnetic topological insulator. Nat. Mater. 19, 522-527 (2020).

[11] Gao, A. et al. Layer Hall effect in a 2D topological axion antiferromagnet. Nature 595, 521-525 (2021).

[12] Ge, J. et al. High-Chern-number and high-temperature quantum Hall effect without Landau levels. Nat. Sci. Rev. 7, 1280-1287 (2020).

[13] Deng, Y. et al. Gate-tunable room-temperature ferromagnetism in two-dimensional Fe3GeTe2. Nature 563, 94-99 (2018).

[14] Jiang, S., Li, L., Wang, Z., Mak, K. F. & Shan, J. Controlling magnetism in 2D CrI3 by electrostatic doping. Nat. Nanotechnol. 13, 549-553 (2018).

[15] Wang, Z. et al. Electric-field control of magnetism in a few-layered van der Waals ferromagnetic semiconductor. Nat. Nanotechnol. 13, 554-559 (2018).

[16] Tang, B. et al. Phase engineering of Cr5Te8 with colossal anomalous Hall effect. Nat. Electron. 5, 224-232 (2022).

[17] Xian, J. J. et al. Spin mapping of intralayer antiferromagnetism and field-induced spin reorientation in monolayer CrTe2. Nat. Commun. 13, 257 (2022).

[18] Zhang, X. et al. Room-temperature intrinsic ferromagnetism in epitaxial CrTe2 ultrathin films. Nat. Commun. 12, 2492 (2021).

[19] Ou, Y. et al. ZrTe2/CrTe2: an epitaxial van der Waals platform for spintronics. Nat. Commun. 13, 2972 (2022).

[20] Saha, R. et al. Observation of Néel-type skyrmions in acentric self-intercalated Cr1+δTe2. Nat. Commun. 13, 3965 (2022).

[21] Meng, L. et al. Anomalous thickness dependence of Curie temperature in air-stable two-dimensional ferromagnetic 1T-CrTe2 grown by chemical vapor deposition. Nat. Commun. 12, 809 (2021).

[22] Fang Ren et al. Van der Waals epitaxy of nearly single-crystalline nitride films on amorphous graphene-glass wafer. Sci. Adv. 7, eabf5011 (2021).

[23] Lemme, M. C., Akinwande, D., Huyghebaert, C. & Stampfer, C. 2D materials for future heterogeneous electronics. Nat. Commun. 13, 1392 (2022).

[24] Weijong Chen et al. Direct observation of van der Waals stacking–dependent interlayer magnetism. Science 366, 983–987 (2019).

[25] Liu, S. et al. Wafer-scale two-dimensional ferromagnetic Fe3GeTe2 thin films grown by molecular beam epitaxy. Npj 2D Mater. Appl. 1, 30 (2017).

[26] Choi, S. H. et al. Large-scale synthesis of graphene and other 2D materials towards industrialization. Nat. Commun. 13, 1484 (2022).

[27] Yeo, Y.-C., King, T.-J. & Hu, C. Direct tunneling leakage current and scalability of alternative gate dielectrics. Appl. Phys. Lett. 81, 2091-2093 (2002).

[28] Tsai, S. J. et al. Approaching Defect-free Amorphous Silicon Nitride by Plasma-assisted Atomic Beam Deposition for High Performance Gate Dielectric. Sci. Rep. 6, 28326 (2016).

[29] Bian, G., Miller, T. & Chiang, T. C. Electronic structure and surface-mediated metastability of Bi films on Si(111)-7×7 studied by angle-resolved photoemission spectroscopy. Phys. Rev. B 80, 245407 (2009).

[30] Ao, D. W. et al. Novel Thermal Diffusion Temperature Engineering Leading to High Thermoelectric Performance in Bi2Te3-Based Flexible Thin-Films. Adv. Sci. 9, e2103547 (2022).

[31] Nagao, T. et al. Nanofilm allotrope and phase transformation of ultrathin Bi film on Si(111)-7x7. Phys. Rev. Lett. 93, 105501 (2004).

[32] Li, Y. Y. et al. Intrinsic Topological Insulator Bi2Te3 Thin Films on Si and Their Thickness Limit. Adv. Mater. 22, 4002-4007 (2010).

[33] Liao, J.-W. et al. Simultaneous enhancement of anisotropy and grain isolation inCoPtCr-SiO2perpendicular recording media by a MnRu intermediate layer. Phys. Rev. B 82, 014423 (2010).

[34] Livingston, J. D. A review of coercivity mechanisms. J. Appl. Phys. 52, 2544-2548 (1981).

[35] Wu, W. et al. Formation of pancakelike Ising domains and giant magnetic coercivity in ferrimagnetic LuFe2O4. Phys. Rev. Lett. 101, 137203 (2008).

[36] Verzhbitskiy, I. A. et al. Controlling the magnetic anisotropy in Cr2Ge2Te6 by electrostatic gating. Nat. Electron. 3, 460-465 (2020).

[37] Richter, N. et al. Temperature-dependent magnetic anisotropy in the layered magnetic semiconductors CrI3 and CrBr3. Phys. Rev. Mater. 2, 024004 (2018).

[38] Niu, W. et al. Probing the atomic-scale ferromagnetism in van der Waals magnet CrSiTe3. Appl. Phys. Lett. 119, 172402 (2021).

[39] Ikeda, S. et al. A perpendicular-anisotropy CoFeB-MgO magnetic tunnel junction. Nat. Mater. 9, 721-724 (2010).

[40] Alahmed, L. et al. Magnetism and spin dynamics in room-temperature van der Waals magnet Fe5GeTe2. 2D Mater. 8, 045030 (2021).

[41] Ribeiro, M. et al. Large-scale epitaxy of two-dimensional van der Waals room-temperature ferromagnet Fe5GeTe2. npj 2D Mater. Appl. 6, 10 (2022).

[42] Zeisner, J. et al. Magnetic anisotropy and spin-polarized two-dimensional electron gas in the van der Waals ferromagnet Cr2Ge2Te6. Phys. Rev. B 99, 165109 (2019).

[43] Tan, C. et al. Hard magnetic properties in nanoflake van der Waals Fe3GeTe2. Nat. Commun. 9, 1554 (2018).

[44] Jiang, W. et al. Quantifying chiral exchange interaction for Néel-type skyrmions via Lorentz transmission electron microscopy. Phys. Rev. B 99, 104402 (2019).

[45] McCray, A. R. C., Cote, T., Li, Y., Petford-Long, A. K. & Phatak, C. Understanding Complex Magnetic Spin Textures with Simulation-Assisted Lorentz Transmission Electron Microscopy. Phys. Rev. Appl. 15, 044025 (2021).

[46] Woo, S. et al. Observation of room-temperature magnetic skyrmions and their current-driven dynamics in ultrathin metallic ferromagnets. Nat. Mater. 15, 501-506 (2016).

[47] Li, P. et al. Topological Hall Effect in a Topological Insulator Interfaced with a Magnetic Insulator. Nano Lett. 21, 84-90 (2021).

[48] Zhang, X. et al. Giant Topological Hall Effect in van der Waals Heterostructures of CrTe2/Bi2Te3. ACS nano 15, 15710−15719 (2021).

[49] Sun, X. et al. Room temperature ferromagnetism in ultra-thin van der Waals crystals of 1T-CrTe2. Nano Res. 13, 3358-3363 (2020).

[50] H. Y. Hwang, S-W. Cheong, N. P. Ong & Batlogg, B. Spin-Polarized Intergrain Tunneling in La2/3Sr1/3MnO3. Phys. Rev. Lett. 77, 2041-2044 (1996).

[51] J. M. D. Coey, A. E. Berkowitz, Ll. Balcells & Putris, F. F. Magnetoresistance of Chromium Dioxide Powder Compacts. Phys. Rev. Lett. 80, 3815 (1998).

[52] P. Xiong et al. Extraordinary Hall Effect and Giant Magnetoresistance in the Granular Co-Ag System. Phys. Rev. Lett. 69, 3220 (1992).

[53] Xiao, J. Q., Jiang, J. S. & Chien, C. L. Giant magnetoresistance in nonmultilayer magnetic systems. Phys. Rev. Lett. 68, 3749-3752 (1992).

[54] N. D. Mathur et al. Large low-field magnetoresistance in La0.7Ca0.3MnO3 induced by artificial grain boundaries. Nature 387, 266-268 (1997).

[55] Sun, Q. C. et al. Magnetic domains and domain wall pinning in atomically thin CrBr3 revealed by nanoscale imaging. Nat. Commun. 12, 1989 (2021).

[56] Vansteenkiste, A. et al. The design and verification of MuMax3. AIP Adv. 4, 107133 (2014).

[57] Donahue, M., Porter, D., Lau, J. & McMichael, R. Interagency report NISTIR 6376. National institute of standards and technology, Gaithersburg. NIST J. Res. 114, 57-67 (1999).

12. SUMMARY AND OUTLOOK

In this thesis, three 2D Dirac or Weyl systems are discussed. They are 1. 2D Dirac fermions on black phosphorous structures, 2. The intersection between 2D Dirac fermions in the Moiré system, 3. 2D Weyl candidate in the 2D ferromagnetic $CrTe_2$ films and its heterostructures.

In the first system, we start at the non-symmorphic symmetry of the black phosphorous structures, which protects the degenerate points along the high symmetry lines or points at the boundary of the Brillouin zone (BZ). Monolayer (1 ML) and bilayer (2 ML) α-Bi and α-Sb, a black phosphorous structure, are grown by the MBE system, and the Dirac points sitting at the X_1 and X_2 points of the BZ are measured by the in-situ ARPES, which agree with our density functional theory (DFT) calculation. Second, the unpinned Dirac states are found in the ARPES and DFT results near the Fermi energy (EF). Later research indicates this kind of degeneracy is protected by the sublattice symmetry. The new kind of Dirac states is not discussed before and contains some novel properties such as the movability in the whole BZ and the anisotropy energy dispersion, which shows various good qualities for 2D electronics. We further studied the monolayer bismuthene under substrate perturbation. The substrate perturbation, in this case, breaks the space-inversion symmetry and makes the band structures form a linear and spin-polarized band sitting at the Fermi surface. This finding identifies the last member in the family of Dirac/Weyl topological semimetals in 2D and 3D. The entangled spin and valley degrees of freedom in 2D Weyl semimetals, together with the 1D Fermi arc edge states, provide unique opportunities for exploring exotic phenomena such as half metals and tunable spin/valley Hall effects and their potential device applications.

In the second system, cloned Dirac Fermions are measured by ARPES on the graphene-silicon carbide (SiC) heterostructures. In this case, the Dirac states of graphene are perturbed by the substrate (SiC) periodic lattice penitential. The results can also be understood as a Moiré system. In twist graphene, Dirac states on the top graphene layer could be coupled with the lower graphene layer and, interestingly, could form some dense correlated Dirac states. These dense correlated states could be the fertile soil for superconductivity. In our work, the lattice mismatch act in the same role as the twisted angle and adjust the electron structure of graphene Dirac states. We also propose some magic lattice constants that could hold such dense correlated Dirac states for further research.

In the third system, we firstly grow a new 2D magnetic matter: $CrTe_2$, the curie temperature of this material is even higher than room temperature (300k) for the thicker film (>7 ML). When the film reaches the 2D limit (1~2 ML), the curie temperature is still higher than 200K, which leads to a significant possibility for electronic or spintronic applications. In this system, we also find a giant topological Hall effect on the Bi_2Te_3/ $CrTe_2$ heterostructures, which is related to the Skyrmions in the interface. In addition, we raise a new growth method that can let $CrTe_2$ form small single crystals on an amorphous substrate. The GMR effect and THE are observed. Using this method, we can produce 2D magnetic devices in a large size and amorphous substrate.

Our recent ARPES and DFT studies show the bulk $CrTe_2$ crystal is a magnetic Weyl material containing many Weyl points. As the $CrTe_2$ has a strong inter-layer electron coupling, the k_z-dependent high-resolved ARPES measurements are needed. On the other hand, although when the thickness becomes thinner, some of the Weyl points will open a small gap, the

enhancement of the Berry couverture near those Weyl points won't vanish and make a significant contribution to its anomalous Hall effect, to further test those electronic properties, detailed transport measurements are needed.

The other aspect of the next step of research is to find a method that can protect the α-Bi and α-Sb in the atmosphere. Bi and Sb are stable, and they won't easily react with oxygen. However, bismuthene and antimonene are only two layers of Bi and Sb atoms, so the physical properties would be easily affected by surface absorption, so a protection layer is necessary. The protection layer that won't change the physical properties of the bismuthine and antimonene needs to be discovered in the future so that the bismuthine and antimonene can form real electronic or spintronic devices.

13. AUTHOR'S PUBLICATION LIST

[1] **Qiangsheng Lu**, Jacob Cook, Xiaoqian Zhang, Kyle Y Chen, Matthew Snyder, Duy Tung Nguyen, PV Reddy, Bingchao Qin, Shaoping Zhan, Li-Dong Zhao, Pawel J Kowalczyk, Simon A Brown, Tai-Chang Chiang, Shengyuan A Yang, Tay-Rong Chang, Guang Bian,
Nature Communications 13, Article number: 4603 (2022) "Realization of unpinned two-dimensional Dirac states in antimony atomic layers"

[2] **Qiangsheng Lu**, Ching‐Kai Chiu, Congcong Le, Jacob Cook, Xiaoqian Zhang, Xiaoqing He, Mohammad Zarenia, Mitchel Vaninger, Paul F. Miceli, Chang Liu, Tai‐Chang Chiang, Giovanni Vignale, Guang Bian,
Adv. Mater. 2022, 2200625 "Dirac Fermion Cloning, Moiré Flat Bands and Magic Lattice Constants in Epitaxial Monolayer Graphene"

[3] **Qiangsheng Lu**, Minghui Wu, Di Wu, Cheng Chang, Yan-Ping Guo, Chun-Sheng Zhou, Wei Li, Xiao-Ming Ma, Gan Wang, Li-Dong Zhao, Li Huang, Chang Liu, and Jiaqing He,
Phys. Rev. Lett. 119, 116401, (2017) "Unexpected Large Hole Effective Masses in SnSe Revealed by Angle-Resolved Photoemission Spectroscopy"

[4] Xiaoqian Zhang, **Qiangsheng Lu** (co‐first author), Wenqing Liu, Wei Niu, Jiabao Sun, Jacob Cook, Mitchel Vaninger, Paul F. Miceli, David J. Singh, Shang-Wei Lian, Tay-Rong Chang, Xiaoqing He, Jun Du, Liang He, Rong Zhang, Guang Bian and Yongbing Xu,
Nature Communications 12, 2492 (2021) " Room‐temperature intrinsic ferromagnetism in epitaxial CrTe2 ultrathin films"

[5] Xiaoqian Zhang, Siddhesh C. Ambhire, **Qiangsheng Lu** (co-first author), Wei Niu, Jacob Cook, Jidong Samuel Jiang, Deshun Hong, Laith Alahmed, Liang He, Rong Zhang, Yongbing Xu, Steven S.-L. Zhang, Peng Li, and Guang Bian,

ACS Nano 2021, 15, 10, 15710–15719 ”Giant Topological Hall Effect in van der Waals Heterostructures of CrTe2/Bi2Te3”

[6] Xiaoqian Zhang, Wenqing Liu, Wei Niu, **Qiangsheng Lu**, Wei Wang, Ali Sarikhani, Chunhui Zhu, Jiabao Sun, Mitchel Vaninger, Paul. F. Miceli, Jianqi Li, David J. Singh, Yew San Hor, Liang He, Rong Zhang, Guang Bian, Dapeng Yu and Yongbing Xu,
Adv. Funct. Mater. 2022, 2202977 ” Self‐intercalation tunable interlayer exchange coupling in a synthetic van der Waals antiferromagnet.”

[7] Pawel J. Kowalczyk, Simon A. Brown, Tobias Maerkl, **Qiangsheng Lu**, Ching-Kai Chiu, Ying Liu, Shengyuan A.Yang, Xiaoxiong Wang, Ilona Zasada, Francesca Genuzio, Tevfik Onur Menteş, Andrea Locatelli, Tai-Chang Chiang, and Guang Bian,
ACS Nano 2020, 14, 2, 1888‐1894 ” Realization of Symmetry‐Enforced Two‐Dimensional Dirac Fermions in Nonsymmorphic α‐Bismuthene”

[8] **Qiangsheng Lu**, Kyle Y. Chen, Matthew Snyder, Jacob Cook, Duy Tung Nguyen, P. V. Sreenivasa Reddy, Tay‐Rong Chang, Shengyuan A. Yang, and Guang Bian,
Phys. Rev. B 104, L201105, (2021) ” Observation of symmetry‐protected Dirac states in nonsymmorphic α‐antimonene”

[9] A. Rafi M. Iasir, Todd Lombardi, **Qiangsheng Lu**(co-first author), Amir M. Mofrad, Mitchel Vaninger, Xiaoqian Zhang, and David J. Singh,
Phys. Rev. B 101, 045107 (2020) ”Electronic and magnetic properties of perovskite selenite and tellurite compounds: CoSeO3, NiSeO3, CoTeO3, and NiTeO3”

[10] Tay-Rong Chang, **Qiangsheng Lu**, Xiaoxiong Wang, Hsin Lin, T. Miller, Tai-Chang Chiang, and GuangBian,
Crystals 2019, 9(10), 510 ”Band Topology of Bismuth Quantum Films”

[11] Xiaoqian Zhang, Huanfeng Xu, Bolin Lai, **Qiangsheng Lu**, Xianyang Lu, Yequan Chen, Wei Niu, Chenyi Gu, Wenqing Liu, Xuefeng Wang, Chang Liu, Yuefeng Nie, Liang He, and Yongbing Xu,
Scientific Reports 8, 8074 (2018) "Direct observation of high spin polarization in Co2FeAl thin films."

[12] Alec Pickett, Aiswarya A. Mohapatra, Suman Ray, **Qiangsheng Lu**, Guang Bian, Kartik Ghosh, Satish Patil, and Suchismita Guha,
ACS Appl. Electron. Mater. 2019, 1, 11, 2455 − 2462 " UV-Ozone Modified Sol-Gel Processed ZnO for Improved Diketopyrrolopyrrole-Based Hybrid Photodetectors"

[13] A. R. Mazza, A. L. Miettinen, A. A. Daykin, X. He, T. R. Charlton, M. Conrad, S. Guha, **Q. Lu**, Guang Bian, E. H. Conrad, and P. F. Miceli,
Nanoscale 11, 14434 (2019) " Revealing interfacial disorder at the growth - front of thick many - layer epitaxial graphene on SiC: a complementary neutron and x - ray scattering investigation."

[14] Wei Wang, Xiaoqian Zhang, Yafei Zhao, Huanfeng Xu, **QiangSheng Lu**, Chang Liu, Xiaoying Hu, Ion Cristian Edmond Turcu, Liang He, Wenqin Zou, and Yongbing Xu,
AIP Advances 8, 125110 (2018) " The metal - insulator transition in ZrTe5 induced by temperature."

[15] Zhonghui Nie, Ion Cristian Edmond Turcu, Yao Li, Xiaoqian Zhang, Liang He, Jian Tu, Zhiqiang Ni, Huangfeng Xu, Yequan Chen, Xuezhong Ruan, Fabio Frassetto, Paolo Miotti, Nicola Fabris, Luca Poletto, Jing Wu, **Qiangsheng Lu**, Chang Liu, Thorsten Kampen, Ya Zhai, Wenqing Liu,
Appl. Sci. 2019, 9(3), 370 " Spin - ARPES EUV Beamline for Ultrafast Materials Research and Development"

[16] Angus Huang, Adam D. Smith, Madison Schwinn, **Qiangsheng Lu**, Tay-Rong Chang, Weiwei Xie, Horng-Tay Jeng, and Guang Bian,
Phys. Rev. Materials 2, 054205 (2018) "Multiple topological electronic phases in superconductor MoC."

[17] Guang Bian, Madison Schwinn and **Qiangsheng Lu**,
Int. J. Nanotechnol. 15, 641 (2017) " Electronic and structural properties of few-layer antimonene."

[18] **Qiangsheng Lu**, P. V. Sreenivasa Reddy, Alessandro R. Mazza, Matthew Brahlek, Weikang Wu, Shengyuan A. Yang, Jacob Cook, Clayton Conner, Xiaoqian Zhang, Amarnath Chakraborty, Hung-Ju Tien, Shang-Wei Lien, Tai-Chang Chiang, Giovanni Vignale, Tay-Rong Chang, Rob G. Moore, and Guang Bian
(submitted) "Discovery of a Two-Dimensional Weyl Semimetal"

[19] **Qiangsheng Lu**, Jacob Cook, Tay-Rong Chang, Xiaoxiong Wang, Tai-Chang Chiang, and Guang Bian,
(submitted) (2022) "Observation of Exposed and Hidden Au Quantum Well States in Au/Ag Heterostructures."

[20] Bin Li, **Qiangsheng Lu** (co-first author), Shuigang Xu, Yipu Xia, Wingkin Ho, Ning Wang, Chang Liu, Maohai Xie,
(submitted) arXiv:1611.04688 (2022) "Induced robust topological order on an ordinary insulator hetero-structured with a strong topological insulator."

[21] Jacob Cook, Dorri Halbertal, **Qiangsheng Lu**, Mathew Snyder, Yew San Hor, Dmitri N. Basov, and Guang Bian,
(submitted) arXiv: 2206.07035 (2022) "Moiré modulated lattice strain and thickness-dependent lattice expansion in epitaxial ultrathin films of PdTe2"

[22] Jacob Cook, Sougata Mardanya, **Qiangsheng Lu**, Clayton Conner, James McMillen, Chi Chen, Mathew Snyder, Xiaoqian Zhang, Tay-Rong Chang, Guang Bian

(submitted) arXiv preprint arXiv:2209.14296 “Observation of Gapped Topological Surface States and Isolated Surface Resonances in PdTe Ultrathin Films.”

VITA

Qiangsheng (pronounced as Johnson) Lu was born in Xi’ an, Shanxi, China, in 1994. In Chinese, his name is 陆强声. He attended elementary school at the Elementary School Affiliated Xi’ an University of Architecture and Technology and graduated from the Middle and High School Affiliated Xi’an Jiaotong University in 2013. Later, he entered the Southern University of Science and Technology, Shenzhen, Guangdong, China, and studied condescend matter physics from 2013 to 2017. During his undergraduate period, he joined Liu Chang’s group and focused on angle-resolved photoemission spectroscopy. After receiving a degree of Bachelor in 2017, he entered the University of Missouri, Columbia, MO, and became a graduate student.

Permanent e-mail address: qiangshenglu@gmail.com

This thesis was typed by the author, Qiangsheng Lu.